CIVIL ENGINEERING JOURNAL

číslo 2/2023

Obsah:

STRESS AND DEFORMATION ANALYSIS OF A U-SHAPED THIN AQUEDUCT BASED ON SHELL ELEMENT

Zhao Chuan[1], Zhang Luo[2], Feng Sa[1], Zhou Qiang[2], Zeng Peng[2] and Yu Rui[1]

1. Sichuan Academy of Water Conservancy, Chengdu, Sichuan 610072, China; zhaochuanvip@163.com
2. Sichuan Dujiangyan Dongfengqu Management Department, Chengdu, Sichuan 610057, China

ABSTRACT

To study the stress and deformation characteristics of Jigongzui U-shaped thin shell aqueduct structure, shell element in ANSYS is proposed to establish the three-dimensional finite element model of the aqueduct for numerical calculation, and the relevant mechanical parameters are obtained by detecting the depth of concrete carbonization. The simulated results show that: (1) The concrete carbonization depth of Jigongzui aqueduct reached 20mm, accounting for about 20% of the total thickness of the channel wall; (2) With the increase of aqueduct water level, the deformation and stress of the aqueduct body gradually increase. The maximum deflection in the middle of the span is 6.98mm, which is less than the limit value of the specification, but the tension in some areas at the bottom of the middle of the span is obvious, exceeding the allowable tensile strength. It is suggested to strengthen the aqueduct body by pasting high-performance fiber materials to improve the stress distribution of the aqueduct body; (3) Shell element has fast calculation speed and high efficiency when simulating similar U-shaped thin shell aqueduct, which can be popularized in simulating similar thin shell structures.

KEY WORDS

Thin aqueduct, Shell 181, Finite element method, Deflection, Tensile strength, Stress

INTRODUCTION

The reinforced concrete U-shaped thin shell aqueduct in Jigongzui aqueduct has been in operation for 53 years since its construction completed in 1968, exceeding the requirement of 50 years of reasonable service life specified in the code for design of reasonable service life and durability of water resources and hydropower projects (SL 654-2014) [1], and limited by the conditions of the time, the design standard is low and the construction quality is poor. After years of operation and natural aging, due to environmental erosion, natural disasters and other problems, concrete structures have different degrees of wear, aging, cracking and corrosion. Therefore, it is particularly important to evaluate the stress-strain characteristics of the aqueduct after many years of operation.

Liu Tao [2] carried out water filling test and bearing capacity safety evaluation of Kizi River rectangular aqueduct by using finite element method, and revealed the variation law of deflection and strain of aqueduct under various water loads; Liu Xiaojuan [3] established a typical U-shaped aqueduct of Xinnan main canal by using the solid element solid 65 of ANSYS, and studied the stress and deformation state of the U-shaped aqueduct structure under different operating conditions. The results accord with the general law; Huang Junbao [4] used three-dimensional laser scanning technology to copy the real scene of the aqueduct, established a three-dimensional point cloud model of the aqueduct, and evaluated the safety of the aqueduct as a whole; Xia

Fuzhou [5] put forward the index system and method of safety evaluation of beam aqueduct structure, and then formulated the safety grade scoring standard of aqueduct structure.

At present, the safety evaluation of the existing aqueduct structure is mainly based on on-site detection, theoretical calculation and finite element analysis. Among them, the aqueduct is often regarded as a simply supported beam structure in theoretical calculation, and the typical section is selected for analysis, so it is difficult to comprehensively study the stress and deformation characteristics of the aqueduct structure as a whole [6-8]. The finite element calculation can reconstruct the three-dimensional model, and objectively reflect the deformation and mechanical characteristics of each part of the aqueduct engineering structure by applying various external loads. It has certain advantages in the safety evaluation of the aqueduct structure. Based on the existing finite element analysis results of aqueduct, most studies use solid element modelling and meshing for numerical calculation. When the aqueduct span is long and the accuracy requirements are high, tens of thousands or even hundreds of thousands of meshes will be generated, which will greatly reduce the calculation efficiency.

In view of this, aiming at the characteristic attribute of thin wall of Jigongzui U-shaped thin shell aqueduct project, this paper proposes to use shell 181 shell element for modelling and carry out finite element simulation analysis and calculation, so as to reduce the number of grids and improve the calculation efficiency. At the same time, it explores the current health status of Jigongzui U-shaped thin shell aqueduct and puts forward corresponding reinforcement measures, The purpose is to ensure the safe operation of aqueduct structure engineering.

PROJECT OVERVIEW

Jigongzui aqueduct is located in Sanxing Town, Shuangliu District, Chengdu of China, with a design flow of 15.2m³/s. The corresponding water depth is 2.6m, the trough body type is reinforced concrete U-shaped thin shell, and the support form is reinforced concrete bent. The maximum span of the aqueduct body is 16m, and the gradient in the trough is 1/1200. It was built in 1968. Groove body depth: the measured groove depth is 280cm, the net width is 400cm, and the depth width ratio of groove body is 0.7. Typical cross-sectional structural dimensions of Jigongzui aqueduct: thickness of trough wall t is 0.1m, inner diameter of trough shell R_0 is 2.00 m, height of straight section f is 0.80m, net spacing of tie rods 2m, height of tie rods H_1 is 0.2m and width of tie rods b_1 is 0.2m. Figure 1 shows the current situation of Jigongzui U-shaped thin shell aqueduct project of Dongfeng canal in Sichuan Province of China.

Fig.1 — Current situation of Jigongzui U-shaped thin shell aqueduct project

MATERIALS AND METHODS

As the Jigongzui aqueduct in this case is a thin shell aqueduct designed to save the amount of concrete, the thickness of the aqueduct body is only 0.1m, while the middle span of the aqueduct reaches 16m, which is a typical one-layer "thin shell" structure. Therefore, to improve the

calculation efficiency, shell element 181 in ANSYS finite element software is used for modelling, calculation and analysis.

Shell 181 element is suitable for analyzing thin to medium thickness shell structures. It is a 4-node element with 6 degrees of freedom per node: displacement degrees of freedom in the x, y, and z directions, and rotational degrees of freedom around the X, Y, and Z axes. (If the membrane option is applied, the unit will only have a degree of freedom of movement.). The degenerate triangle option is only used when meshing the cell as a filling cell. Shell element is also very suitable for linear, large rotation angle and large strain nonlinear applications. It supports complete and reduced integration methods in the element range. The coordinate system is shown in Figure 2 below. The element is defined by four nodes I, J, K and L. the expression of the element is through logarithmic strain and real stress. The thickness and other information can be defined through the definition of real constant or section. The real constant option is only used for single-layer shells [9-11].
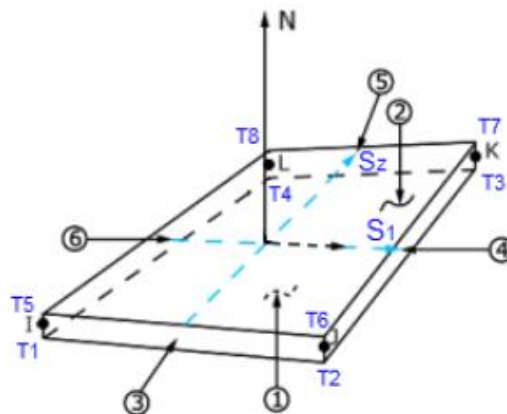

Fig. 2 — Geometric coordinate system of shell 181 shell element

Moreover, the change in shell thickness is to accommodate non-linear analysis. Within the application range of this element, both complete integration and reduced order integration are applicable. The Shell 181 element illustrates the effect of the following (load stiffness) distribution of pressure. The Shell 181 element can be applied to modelling materials of multi-layer structures, such as composite laminated shells or sandwich structures. In the modelling process of composite shells, the accuracy depends on the first shear deformation theory. Shell 181 uses the non-conforming mode method to improve the accuracy of the deflection governing problem, and its accuracy of calculating deformation has been verified in some cases through the Ansys tutorial.

Due to the problems of Jigongzui aqueduct after years of operation and natural aging, environmental erosion and natural disasters, the concrete structure has different degrees of wear, aging, cracking and corrosion. The carbonization depth detection of the body of Jigongzui aqueduct is carried out, as shown in Figure 3. The carbonation depth of concrete outside the tank body is basically more than 10mm, and the carbonation depth of concrete inside the tank body is between 5mm and 10mm. The total carbonation depth accounts for about 20% of the tank body thickness (0.1m). The calculated value of concrete strength grade meets the concrete C25 strength grade required by the specification. After inquiry, the reinforcement ratio of this project is about 5%, and the relevant parameters are shown in Table 1.

Fig. 3 — Detection of carbonization depth of Jigongzui aqueduct body

Tab.1 - Mechanical parameters of reinforced concrete for groove body and tie rod structure

Concrete strength grade	Density（kN/m3）	Standard value of axial tensile strength (N/mm2)	Standard value of axial compressive strength (N/mm2)	Elastic Modulus 104N/mm2	Poisson's ratio
C25	25	1.78	16.7	2.8	0.167
Strength grade of reinforcement	weight /m （kg, D is the diameter of reinforcement bar，mm）	Design value of tensile strength (N/mm2)	Design value of compressive strength (N/mm2)	Elastic Modulus 104N/mm2	Poisson's ratio
HPB235	0.00617D2	210	210	21	0.3

Equivalent treatment of aqueduct reinforced concrete: the aqueduct body structure is composed of materials with different material properties and different mechanical properties. The material properties of reinforcement bar and concrete are calculated as a whole, and the structures with different materials and heterogeneity are transformed into homogeneous model structures [12-14]. Then according to the longitudinal deformation coordination conditions:

$$A_{cs}E_{cs} = A_cE_c + A_sE_s \qquad (1)$$

Where E_{cs} and A_{cs} equivalent elastic modulus and equivalent area of reinforced concrete; E_c and A_c - elastic modulus and area of concrete; E_s and A_s - elastic modulus and area of reinforcement bar.

Since the carbonation depth of the aqueduct accounts for about 20% of the thickness of the aqueduct body, the parameters of the aqueduct are reduced by 20% in the analysis. After calculation, the current comprehensive elastic modulus of Jigongzui U-shaped aqueduct is E = 2.97 × 1010pa, Poisson's ratio is 0.2.

This paper focuses on the stress and deformation characteristics of the whole body of Jigongzui U-shaped thin shell aqueduct project. Therefore, ANSYS R19.0 is adopted to establish the aqueduct model by shell element is shown in Figure 4. The 9 horizontal tie rods at the upper part are simulated by beam188 element, with a length × Width (0.2m × 0.2m), and corresponding mechanical parameters are given at the same time. According to the aqueduct safety evaluation report, the mechanical effect in the midspan of the aqueduct is the most obvious. To facilitate the analysis of the stress-strain characteristics in the midspan under different working conditions, and the aqueduct is a left-right symmetrical structure, three points a, B and C at different heights on one side of the midspan cross section are selected as the monitoring points, and the node labels are 567, 2495 and 2168 respectively. The point distribution is shown in the figure below. To solve the linear contact problem between different elements, multipoint constraint (MPC) method is

selected to realize the degree of freedom coupling between contact node elements. The node elements at both ends of the aqueduct are subject to longitudinal (Z-direction) constraints, which can carry out transverse and vertical deformation. The structural elements at the bottom of both ends are fixed boundaries, which are constrained in X, Y and Z directions.
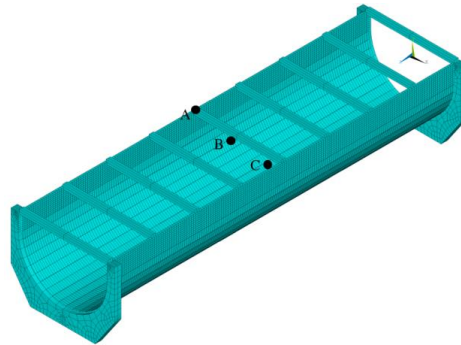

Fig. 4 — Three dimensional finite element model of Jigongzui aqueduct

The working conditions of calculation and analysis are defined as three categories: (1) Empty tank under gravity; (2) Water depth of the half trough under the action of gravity (water depth 1.4m); (3) Full tank depth under gravity (water depth 2.8m). Other external loads, such as crowd load and wind load, are not considered in this analysis. The water pressure inside the aqueduct is a triangular load perpendicular to the action surface. Sfgrad and SF are applied inside the aqueduct through the surface load pressure gradient APDL command, and the gravity acceleration g is 9.81N/kg.

RESULTS ANALYSIS

Deformation Analysis

When the aqueduct is empty without water, after long-term deformation, and the initial displacement of aqueduct will be reset to zero during water filling calculation. Then the water pressure gradient loads of half tank depth (water depth 1.4m) and full tank depth (water depth 2.8m) are applied to the model, and the displacement nephogram of the aqueduct structure under two different water depth conditions is obtained through numerical simulation calculation, as shown in Figure 5 and Figure 6, including horizontal transverse channel displacement Ux, vertical displacement Uy, longitudinal along channel displacement Uz and comprehensive displacement Usum.

The analysis shows that when the Jigongzui U-shaped aqueduct is in half tank water depth (water depth 1.4m), the transverse displacement Ux of the aqueduct is symmetrically distributed, and the wall shell of the aqueduct body tends to expand outward in the middle of the span, but the total transverse deformation is very small, and the maximum value is only 0.83mm. The vertical displacement Uy in the gravity direction shows that the main vertical deformation area is located at the bottom of the middle span of the aqueduct, the direction is vertical downward, decreases to the longitudinal ends gradually, and the maximum vertical displacement is 3.15mm. In the longitudinal direction of the aqueduct, the longitudinal displacement Uz is mainly distributed in the upper part of both ends of the aqueduct close to the pull rod, and the direction is deformed towards the middle of the span, but the total longitudinal deformation of the aqueduct is also very small, and the maximum value is only 0.86mm. The displacements in the three directions are synthesized into Usum. The comprehensive displacement nephogram is basically consistent with the vertical displacement uy. The obvious deformation area is located at the bottom of the mid span trough body and gradually decreases to both sides, with the maximum value of 3.15mm.

(a)Ux

(b)Uy

(c)UZ

(d)Usum
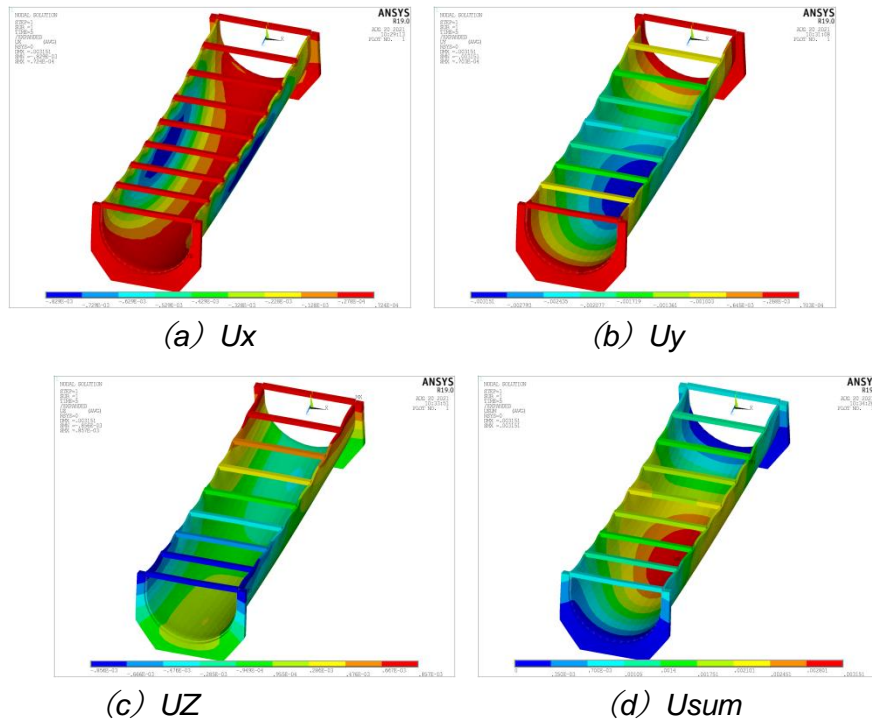
Fig. 5 — Displacement nephogram of Jigongzui aqueduct with water depth of 1.4m

(a)Ux

(b)Uy

(c)UZ

(d)Usum
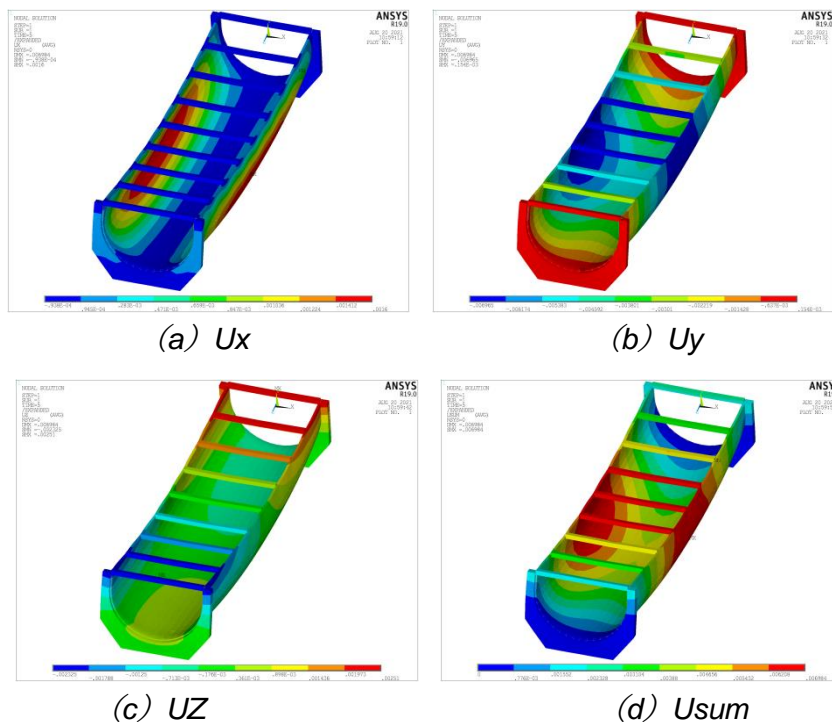
Fig. 6 — Displacement nephogram of Jigongzui aqueduct with water depth of 2.8m

When the Jigongzui U-shaped aqueduct is filled with water to the full depth of 2.8m, the transverse displacement Ux of the aqueduct is symmetrically distributed, and the wall shell of the aqueduct body tends to expand further outward in the middle of the span. The total transverse deformation is slightly larger than that when the water depth is 1.4m, and the maximum value is 1.60mm. The vertical displacement Uy in the gravity direction shows that the main vertical deformation area is located on both sides of the middle span of the aqueduct. The direction is

vertical downward and gradually decreases to both longitudinal ends. The maximum vertical displacement is 6.97mm, which is more than twice that when the water depth is 1.4m (3.15mm); In the longitudinal direction of the aqueduct, the displacement Uz along the aqueduct is mainly distributed in the upper part of both ends of the aqueduct close to the pull rod, and the direction is towards the middle of the span and deformed. The total longitudinal deformation of the aqueduct increases compared with the water depth of 1.4m, and the maximum value reaches 2.51mm. The comprehensive displacement Usum cloud diagram is basically consistent with the vertical displacement Uy. The obvious deformation area is located on both sides of the mid span groove body, and decreases to both sides gradually, with the maximum value of 6.98mm, which is 121% higher than 3.15mm when the water depth is 1.4m. It shows that the vertical displacement in the middle of the span of Jigongzui U-shaped aqueduct is the most obvious after it is filled with water. According to the relevant provisions of article in the code for design of hydraulic concrete structures [15], when the calculated span is greater than 10m, the deflection limit value of flexural members shall not exceed l0/600. If the span of Jigongzui aqueduct is 16m, the deflection limit value is 26mm, and the deflection value does not exceed the limit value when it is full of water depth, and there is enough safety reserve. It is considered that the numerical calculation results of deflection meet the requirements of the specification.

Stress Analysis

Figure 7, 8 and 9 respectively show the stress distribution diagram under the three working conditions of empty groove, half groove water depth (water depth 1.4m) and full groove water depth (water depth 2.8m), including the first principal stress σ1, third principal stress σ3 and von Mises stress. With the first major principal stress σ1 as an example, when the slot is empty, the bottom of the middle span of the slot body is tensioned, and the maximum value at point C (node No. 2168) is 0.79MPa. When the water is filled to 1.4m, the first principal stress at point C increased to 1.89MPa and the aqueduct is filled with water to 2.8m, the first principal stress at point C increased to 4.98MPa, and the tensile area at the bottom of the middle span of the groove body is increased. It shows that when the tank is full of water depth, the tension at the bottom of the middle span of the tank body is obvious, and the local tensile stress exceeds the tensile strength of the concrete, which will lead to local tensile failure. The distribution range and variation trend of normal form equivalent stress are basically consistent with the first principal stress.

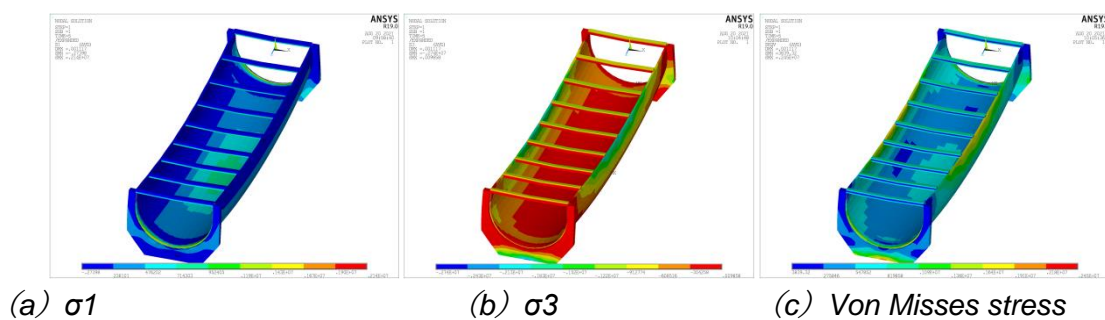(a) σ1　　　　　　　　(b) σ3　　　　　　　　(c) Von Misses stress

Fig. 7 — Stress distribution of Jigongzui aqueduct in empty state

(a) σ1　　　　　　　　(b) σ3　　　　　　　　(c) Von Misses stress
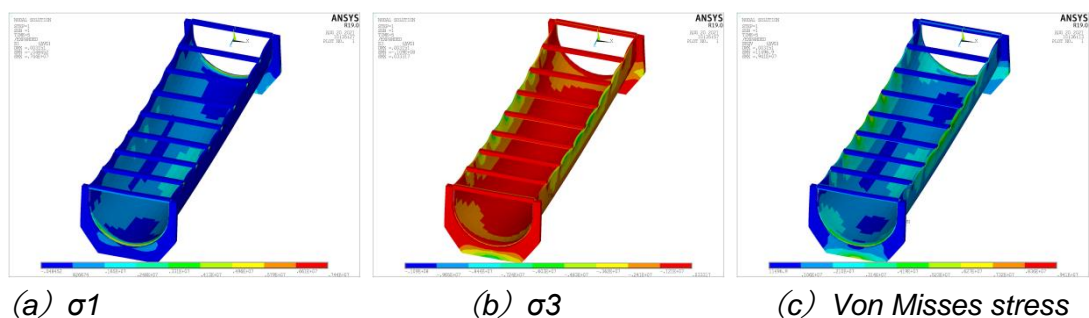
Fig. 8 — Stress distribution of 1.4m deep Jigongzui aqueduct (half trough depth)

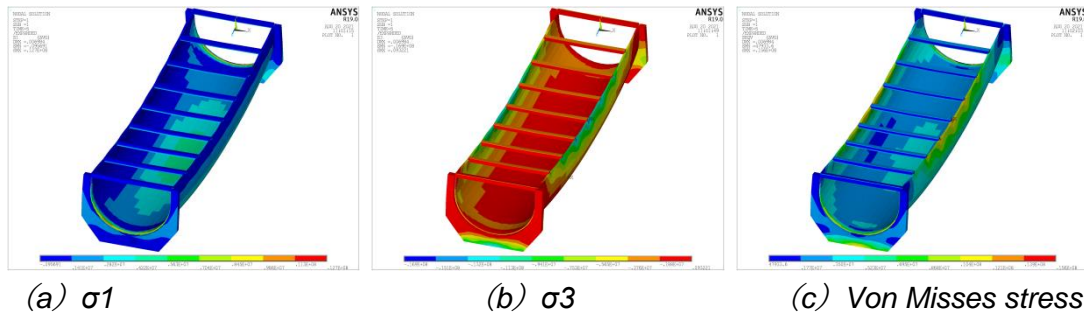(a) σ1　　　　　　　　　(b) σ3　　　　　　　　　(c) Von Misses stress

Fig. 9 — Stress distribution of Jigongzui aqueduct with water depth of 2.8m (full water depth)

Von Mises stress diagram can clearly describe the distribution of stress in the whole model, so as to quickly determine the most dangerous area in the model. Figure 10 indicates the normal form equivalent stress of the three monitoring points in the cross section of the middle span of the structure of Jigongzui aqueduct. It is found that with the increase of the internal water depth of the aqueduct, the normal form equivalent stress values of the three monitoring points also gradually increase, and the value of point a is the largest. However, it can be seen from (c) in Figure 7 ~ Figure 9 that this is the stress concentration phenomenon between the tie rod and the trough wall, and the distribution range is very small. Point B in the middle increases from 0.47MPa to 3.09MPa, while point C at the bottom increases from 0.69MPa to 4.44MPa. Therefore, it can be determined that the most dangerous area after the aqueduct is filled with water is located at the bottom of the span. It is necessary to take corresponding reinforcement measures to improve the stress distribution at the bottom of the aqueduct, such as pasting high-performance fiber materials carbon fiber cloth and carbon fiber board at the corresponding positions, so as to improve the longitudinal bearing capacity of the aqueduct body and ensure the normal operation of the aqueduct engineering structure.
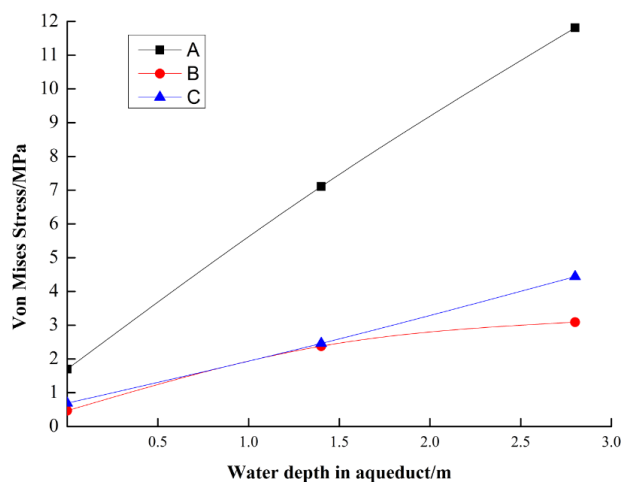
Fig. 10 — Von Mises stress at mid monitoring point of Jigongzui aqueduct under multiple working conditions

CONCLUSIONS

Taking the Jigongzui U-shaped thin shell aqueduct in Dujiangyan Irrigation Area in service as an example, the carbonation depth of the aqueduct is measured on site, and the shell element is proposed to establish the three-dimensional finite element model of the aqueduct engineering structure. The stress and deformation characteristics of the aqueduct under the three working conditions of empty slot, half slot water depth (water depth 1.4m) and full slot water depth (water depth 2.8m) are analyzed quantitatively. The following conclusions are obtained for reference.

(1)   The carbonation depth of concrete outside the tank body is basically more than 10mm, and the carbonation depth of concrete inside the tank body is between 5mm and 10mm. The total carbonation depth accounts for about 20% of the total thickness of the tank wall.

(2)   With the increase of aqueduct water level, the deformation of aqueduct body gradually increases, mainly vertical deformation. When the tank is full of water depth, the deflection value does not exceed the limit value, and the deflection calculation results meet the requirements of code for design of hydraulic concrete structures.

(3)   With the increase of aqueduct water level, the stress of aqueduct body increases gradually. When the groove is full of water depth, the tensile area at the bottom of the midspan tends to expand, and the tensile stress in some areas exceeds the tensile strength of concrete, so there is the possibility of tensile failure. It is necessary to take some reinforcement measures at the bottom of the aqueduct body to improve the longitudinal bearing capacity of the aqueduct body and ensure the normal operation of the aqueduct structure.

(4)   Compared with the traditional three-dimensional solid element structure, using shell element 181 to simulate U-shaped thin shell aqueduct has faster calculation speed and higher efficiency. It has certain advantages in the safety evaluation of similar thin shell aqueduct structures, and can be applied and popularized.

This paper only analyzes and discusses the current situation of Jigongzui U-shaped thin shell aqueduct. Combined with the safety evaluation report, it is found that there are certain potential safety hazards in the aqueduct engineering structure, and puts forward the way of pasting high-performance fiber materials for reinforcement. In the future work, the reinforcement effect of the modification scheme will be further studied.

ACKNOWLEDGMENTS

CONFLICTS OF INTEREST

Authors declare that they have no conflicts of interest.

REFERENCES

[1]   Ministry of water resources of the people's Republic of China Code for design of reasonable service life and durability of water conservancy and hydropower projects: SL 654-2014 [S] Beijing: China water resources and Hydropower Press, 2014.
[2]   Liu Tao, He Jianxin, Liu Liang, et al Water filling test and bearing capacity safety evaluation of Kizilsu river aqueduct [J] Hydropower energy science, 2021,39 (04): 100-104.
[3]   Liu Xiaojuan, Zhang Hongjun, Feng Sa. Three dimensional finite element analysis of stress and deformation of Xinnan main canal aqueduct structure [J] Engineering construction, 2021,53 (04): 32-37.
[4]   Huang Junbao, Deng Chengfa Performance safety evaluation of old aqueduct structure based on three-dimensional laser scanning [J] China rural water resources and hydropower, 2020 (03): 142-145.
[5]   Xia Fuzhou, Qian Liyun, Zhang Jun Study on structural safety and evaluation index system of large aqueduct [J] China Rural Water Conservancy and hydropower, 2011 (08): 121-123.

[6]   Ji richen, Su Xiaofeng, Yan Juan Study on the influence of water quality on the transverse seismic performance of large beam aqueduct [J] Journal of earthquake engineering, 2013,35 (3): 569-574.

[7]   Shang Feng, Zhu Yanzhi, Zheng Yongzhi Safety evaluation and disease treatment of in-service reinforced concrete aqueduct [J] Water conservancy and hydropower technology, 2018,49 (12): 208-214.

[8]   Huang Tao, Zhang Guoxin, Li Jiang, et al Causes of cracks in an aqueduct in cold area and influence of reinforcement corrosion on durability [J] Water conservancy and hydropower technology, 2019,50 (12): 120-129.

[9]   Shen Xiaoming, Huang Yong Study on Design of prestressed concrete U-beam aqueduct [J] China water transport, 2019,19 (11): 253-254.

[10]   Kate E. Porter, Stephanie E. Ordonez-Sanchez, Robynne E. Murray, et al. Flume testing of passively adaptive composite tidal turbine blades under combined wave and current loading[J]. Journal of Fluids and Structures, 2020, 93(1):11-15.

[11]   Holmlund P, Qvarlander S, Malm J, et al. Can pulsatile CSF flow across the cerebral aqueduct cause ventriculomegaly? A prospective study of patients with communicating hydrocephalus[J]. Fluids and barriers of the CNS, 2019, 16(1):40-41.

[12]   Deng Chengfa, Yu Junjun, Lai Sheng, et al Safety evaluation and analysis of datangkou open web double arch aqueduct [J] Hydropower and energy science, 2019,37 (7): 70-73.

[13]   Zhang Jianwei, Wen Jiaqi, Huang Jinlin, et al Determination of simulation parameters of aqueduct and its nonlinear contact wind-induced vibration analysis [J] Journal of North China University of water resources and hydropower (NATURAL SCIENCE EDITION), 2019,40 (2): 77-83.

[14]   Liu Shuai, Zhai juyun Stress and deformation monitoring and simulation analysis of large prestressed beam aqueduct [J] People's Yellow River, 2020,42 (1): 126-130.

[15]   Ministry of water resources of the people's Republic of China Code for design of hydraulic concrete structures: SL191-2008 [S] Beijing: China water resources and Hydropower Press, 2008.

STUDY ON EARTHQUAKE DESTRUCTION MODE OF THE LARGEST CANAL CROSSING HIGHWAY BRIDGE BASED ON IEM BOUNDARY IN SOUTH-TO-NORTH WATER DIVERSION

Xinyong Xu[1,2,3], Honghao Zhang[1], Jinchang Liang[1], Xuhui Liu[1], Chenlong Xie[4] and Jianwei Zhang[1,2,3]

1. *North China University of Water Resources and Electric Power, School of Water Conservancy, Zhengzhou 450046, China; xuxinyong@ncwu.edu.cn*
2. *Collaborative Innovation Center of Water Resources Efficient Utilization and Protection Engineering, Henan Province, Zhengzhou 450046, China*
3. *Henan Hydraulic Structure Safety Engineering Technology Research Center, Zhengzhou 450046, China*
4. *Shanghai Investigation, Design & Research Institute Co., Ltd., Shanghai 200092, China*

ABSTRACT

To study the dynamic failure mechanism and damage development law of highway bridge structure under the boundary effect in the process of seismic dynamic duration, the Wenchang Highway Bridge with the largest canal crossing in the South-to-North Water Diversion is taken as an example for seismic design analysis. Based on the finite element and infinite element coupling theory, the infinite element method boundary is introduced, the concrete damage plasticity is introduced, and the half-space free field model is established to study the energy dispersion phenomenon of waves in the boundary and the absorption effect of the infinite element method boundary on wave energy is verified. Under different peak acceleration intensities, the seismic response analysis of the bridge structure was carried out. The results show that: Under the action of selected artificial waves, the damage location of the bridge mainly concentrated in the junction of the box girder supported by the pier, the bottom of the pier and the junction of the pier and beam. The damage tends to develop downward near the bottom of the box girder. The damage at both ends of the beam extends from both ends to the middle. And the bottom and top of the pier have penetrating damage. These are weak points in seismic design. At a horizontal peak acceleration of 0.6 g, in addition to damage to the pier column, damage also occurred to the bottom of the box girder. Therefore, when the horizontal peak acceleration of the seismic wave is greater than 0.6g, the failure of the bottom of the box girder is paid attention to. Moreover, the IEM boundary has a good control effect on the far-field energy dissipation of the wave, which is simpler and more efficient than the viscous–spring boundary.

KEYWORDS

Cross channel highway bridge for South-to-North Water Diversion, Infinite element method boundary, FE-IE coupling, Plastic damage constitutive, Earthquake damage evolution

INTRODUCTION

In China, the South-to-North Water Diversion(SNWD) is a major national infrastructure project for the deployment of water resources. Since its commissioning, it has effectively alleviated the severe water shortage in the Yellow-Huai-Hai plains of northern China. Study [1] has shown that the middle route of the SNWD has significant positive benefits for the sustainable stabilization and restoration of groundwater in northern China. The middle route of the SNWD is 1432 km long and

spans numerous rivers, highways, railroads, valleys, washes and other projects in the whole area. Many bridges crossing the SNWD are in high seismicity regions. To ensure the safety of these bridges after an earthquake, seismic analysis of them is necessary to clarify their seismic failure characteristics.

The Wenchang Highway Bridge is the largest cross-canal highway bridge in the middle route of the SWND. Its structure is a high-pier and large-span cast-in-place concrete box girder bridge. Its site is located in a 7-degree fortification intensity area. As a bridge spanning major national livelihood projects, its seismic performance is not only related to the safety of water quality, but also to the impact of structural safety. Therefore, it's particularly significant to study the dynamic failure mechanism and damage development law of the bridges crossing the SNWD.

There have been many research results on bridge seismic problems. Based on the damage index, Xie and Sun [2] analyzed the seismic damage and failure mode of the cable-stayed bridge. They concluded that the seismic frequency has a significant impact on structural damage. Deng et al. [3] found that the chain collision effect between the main bridge and multiple approach bridges at the expansion joints will affect the seismic performance of the whole bridge. Zhu and Jiang [4] comprehensively considered the energy and deformation requirements, discussed the seismic method of bridge single pier based on damage performance. Tongaonkar et al. [5] suggested that the interaction between piles and soil will significantly affect the displacement response of the isolated bearing. Shi et al. [6] analyzed the seismic damage mode of the high pier and long-span bridge during the typical construction stage. Combined with the failure limit of each component, Guo et al. [7] analyzed the failure mode of multi-span simply supported beams under earthquake action. Wang et al. [8] analyzed the dynamic response and failure law of the bridge under the combined action of earthquake and blasting. Farahmand-Tabar et al. [9] evaluated the performance of cable-stayed arch Bridges under orthotropic three-component earthquakes. Li et al. [10] studied the effect of soil spatial variability on the seismic performance of SCCS bridges. Li and Xu [11] proposed a hybrid seismic control system combining three-dimensional hybrid seismic isolation bearings and longitudinal fluid viscous dampers. Chu et al. [12] used the modified Morison equation to calculate the hydrodynamic pressure, and analyzed the influence of the water immersion depth on the dynamic response of the arch bridge. Deng et al. [13] took a typical multi-span continuous girder bridge with a pedestal abutment as the research object to analyze the longitudinal seismic performance of the bridge under different abutment stress conditions. Addessi et al. [14] evaluated and monitored the nonlinear dynamic response of the structure from the aspects of top shift time course, global damage index evolution and damage variable distribution.

Throughout the above research, the law of seismic damage of bridge structure is mainly considered, and the influence of infinite foundation on seismic calculation is not fully considered. The energy propagation of seismic wave and the reflection effect of wave on the boundary has an important impact on obtaining reasonable results for the dynamic calculation.

When solving structural dynamics problems, the infinite domain foundation simulation is the key of calculation and analysis. Lysmer and Kuhlemeyer [15] proposed the earliest simple viscous boundary, but it is not suitable for the multi-dimensional wave problems of complex structures. Deek et al. [16] studied the soil-structure interaction effect, striving to solve the transient SSI effect. Liu et al. [17] derived viscoelastic boundary equation based on wave equation and verified accuracy and stability of the three-dimensional viscoelastic artificial boundary. He et al. [18] simplified the implementation method of viscoelastic boundary, which greatly improved the calculation efficiency. Liao et al. [19] proposed and improved the transmission boundary formula, which moderately improves the accuracy, but the implementation process is complex. The infinite element method (IEM) boundary is a method proposed to overcome the problem of infinite domain solved by finite element method. It has inherent coordination with finite element method, and has some advantages than other numerical methods for solving infinite domain problems. Ungless [20] first proposed the concept of the infinite element in 1973. In 1982, Chow et al. [21] proposed the resonant infinite solid element and introduced the infinite element study into the propagation analysis of waves in solids. Bettess [22] put forward the concept of mapping infinite element for the

first time. Asheghabadi et al. [23] compared the calculation results under two boundary conditions of the IEM boundary and viscous boundary and found that the IEM boundary can be realized in less calculation time. Qi et al. [24] verified the applicability of the IEM boundary. Compared with viscoelastic boundary, the IEM boundary can better filter the scattered waves. Zhang et al. [25] applied this method to foundation structure dynamic interaction analysis earlier. As a method to solve three-dimensional multi-directional mapping problems, the IEM boundary has not been widely used in engineering.

Based on the commercial software ABAQUS, modeling and analysis are carried out. In this paper, the IEM boundary is used for seismic wave input. In order to explore the dynamic failure mechanism and damage development law of the concrete highway bridge under ground motion, the concrete damage plasticity (CDP) theory is introduced. This study hopes to provide references and a scientific basis for the large cross canal highway bridges' seismic design.

INFINITE ELEMENT METHOD BOUNDARY

The IEM boundary absorbs the seismic wave energy by introducing a built-in damper on the model boundary to weaken the reflection and scattering effect of the seismic wave at the boundary.

Considering that the medium is endowed with linear elastic properties, its equilibrium equation is

$$-\rho\ddot{u} + \frac{\partial}{\partial x} \cdot \sigma = 0 \tag{1}$$

where ρ is the density, kg/m^3; $\ddot{u}$ is the acceleration, m/s^2; σ is stress, Pa; x is the location. Assuming that the material is isotropic and linear elastic, the stress σ can be expressed as

$$\sigma = \lambda \prod : \varepsilon + 2G\varepsilon \tag{2}$$

where ε is the strain; λ is lame constant, $\lambda = \frac{E\nu}{(1+\nu)(1-2\nu)}$; G is shear modulus, $G = \frac{E}{2(1+\nu)}$ (E is Young's modulus, ν is Poisson's ratio); ε is assumed to be a small strain.

$$\varepsilon = \frac{1}{2}\left\{\frac{\partial u}{\partial x} + \left[\frac{\partial u}{\partial x}\right]^T\right\} \tag{3}$$

The governing equation of motion is expressed as

$$\rho\ddot{u}_i = G\frac{\partial^2 u_i}{\partial x_j \partial x_j} + (\lambda + G)\frac{\partial^2 u_j}{\partial x_i \partial x_j} \tag{4}$$

Assuming that the plane wave moves along the X-axis, equation (5) expresses the longitudinal wave, and equations (6) and (7) express the shear wave.

$$u_x = f(x \pm c_p t), u_y = u_z = 0 \tag{5}$$
$$u_y = f(x \pm c_s t), u_x = u_z = 0 \tag{6}$$
$$u_z = f(x \pm c_s t), u_x = u_y = 0 \tag{7}$$

where $c_p = \sqrt{\frac{\lambda+2G}{\rho}}$, $c_s = \sqrt{\frac{G}{\rho}}$, "-" indicates forward propagation along X, "+" indicates backward propagation along X.

The infinite element absorbs the radiation energy of plane body wave by introducing damping coefficient d_p and d_s on the boundary. It is assumed that the infinite element material is linear elastic, and the stress generated by damping is shown in formula (8) ~ (10)

$$\sigma_{xx} = ma - d_p\dot{u}_x \tag{8}$$

$$\sigma_{xy} = -d_s\dot{u}_y \tag{9}$$

$$\sigma_{xz} = -d_s \dot{u}_z \tag{10}$$

where for longitudinal waves, the stress at the boundary (x = L) is $\sigma_{xx} = (\lambda + 2G)(f_1' + f_2')$. The rest of the stress components are $\sigma_{ij} = 0$. The speed is $\dot{u}_x = -c_p(f_1' - f_2')$, and can be concluded from the above formula

$$(\lambda + 2G - d_p c_p)f_1' + (\lambda + 2G + d_p c_p)f_2' = 0 \tag{11}$$

When $f_2 = 0$ and $f_2' = 0$, we can ensure that no reflection stress wave is generated at the boundary under any incident condition. Therefore, the longitudinal wave and the shear wave damping form can be calculated by the following formula.

$$d_p = \frac{\lambda + 2G}{c_p} = \rho c_p \tag{12}$$

$$d_s = \rho c_s \tag{13}$$

IEM achieves FEM-IEM coupling by processing boundary. The IEM boundary is equivalent to the absorption boundary. In order to ensure that the seismic wave has no reflection under any incident condition, the damping coefficients are introduced into the element itself.

PROJECT OVERVIEW

In this study, the Wenchang Highway Bridge, the largest cross canal highway bridge in the middle route of SNWD, is selected as a case, as shown in Figure 1.
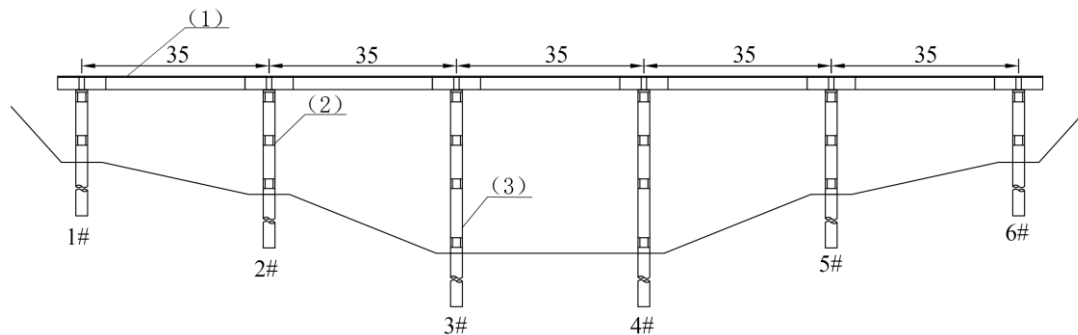
(1) Box girder; (2) Cross beam; (3) Pier

Fig. 1 - General Arrangement of Wenchang Highway Bridge (Unit: m)

The total length of the box girder bridge is 175m with 5 spans. The double box girder's width is 28 m and the height is 2.71m. The model material parameters are shown in Table 1.

Tab. 1 - The Bridge's Material Parameters

Material	Box girder (C50)	Pier (C30)	Foundation soil layer	Foundation rock layer
Young's modulus (GPa)	34.5	30	0.04	10
Density (kg/m^3)	2430	2400	1796	2100
Poisson ratio	0.2	0.2	0.3	0.3
Tensile strength (Mpa)	1.83	1.39	-	-
Compressive strength (Mpa)	24.4	13.8	-	36.1

FINITE ELEMENT MODEL

Figure 2 depicts the whole 3D bridge numerical simulation structure model, and the FEM-IEM coupling foundation model is established (Figure 3), where the seismic wave acceleration is applied at the bottom of a compartment at the FE-IE coupling. The definition of the overall coordinates is as follows: take the center of the box girder bottom as the coordinate origin. The x-axis is the channel flow direction, and the downstream direction is positive; the y-axis is the vertical direction, and the upward direction is positive; the z-axis is the longitudinal axis direction of the bridge deck, and the north direction is positive.
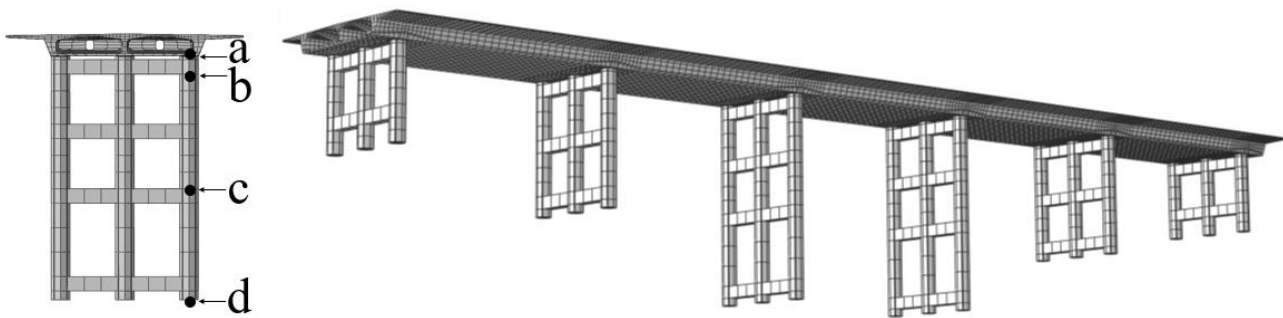
Local 3#   *Overall structure of the bridge*
Fig. 2 - Three-Dimensional Finite Element Calculation Model
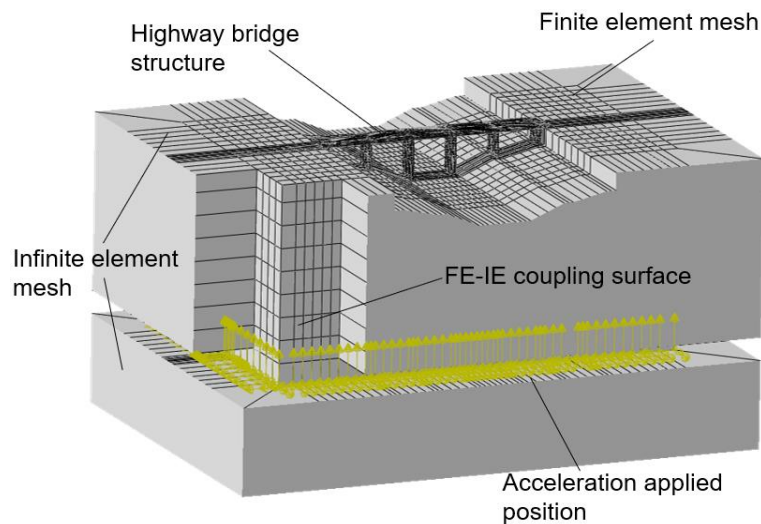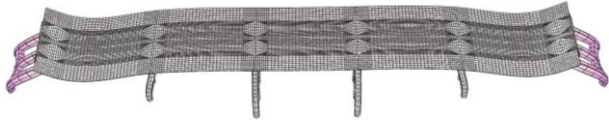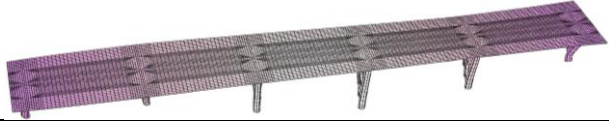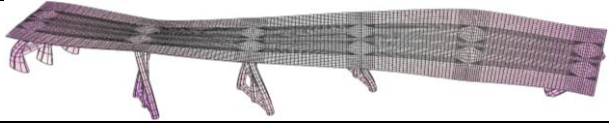
Fig. 3 - FEM-IEM Coupling Foundation Model

MODAL ANALYSIS OF BRIDGE STRUCTURE

Table 2 shows the first four vibration modes of the bridge structure. In this paper, Rayleigh damping is used for the analysis, and take the damping ratio corresponding to the frequency of the structure as 5%, and determine the damping constants according to the first two natural frequencies of the structure as 0.681Hz and 0.697Hz, and the damping constants $\alpha = 0.216$ and $\beta = 0.011$.

Tab. 2 – The first four frequencies and vibration modes of the bridge structure

Mode Number	Modal	Vibration Modes
1	0.681Hz	Transverse
2	0.697Hz	Transverse
3	0.700Hz	Transverse
4	0.714Hz	Vertical

SELECTION OF SEISMIC WAVE

According to the site type and seismic area division of the bridge, the seismic fortification intensity of this site is VII and the site type is class I. The horizontal peak acceleration of the corresponding rare earthquake is 0.2g, and the vertical peak acceleration is 2/3 of the horizontal direction.

Since there are few natural seismic waves recorded at the location of the bridge, the seismic wave input that occurred in the past cannot truly simulate the failure of the bridge, and the artificial wave can well match the characteristics of the target response spectrum, so the artificial wave is fitted according to the basic data of the project and the characteristics of the seismic wave. The RH1TG040 artificial seismic wave is chosen for computation based on the spectral proximity principle. Its peak acceleration is 0.2g. The acceleration time history curve in the main direction is shown in Figure 4, and the ground motion input interval is 0.02 s. This calculation's total duration is 30 s. The acceleration response spectrum is shown in Figure 5, where the black line represents the target response spectrum and the red line represents the RH1TG040 response spectrum. In order to show the failure law of the bridge structure, the horizontal peak acceleration of artificial seismic waves was adjusted to 0.2g, 0.4g, 0.6g, 0.8g and 1.0g, and the seismic response analysis of the structure at different intensities was carried out.
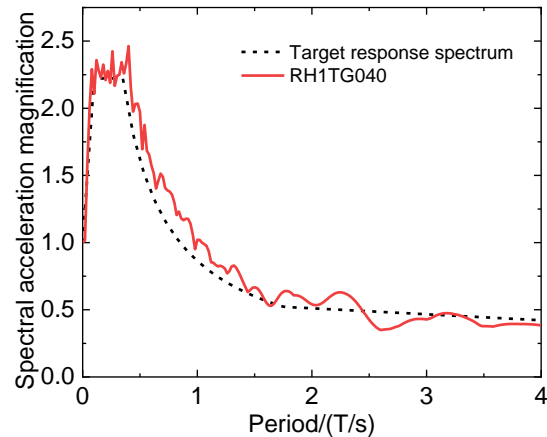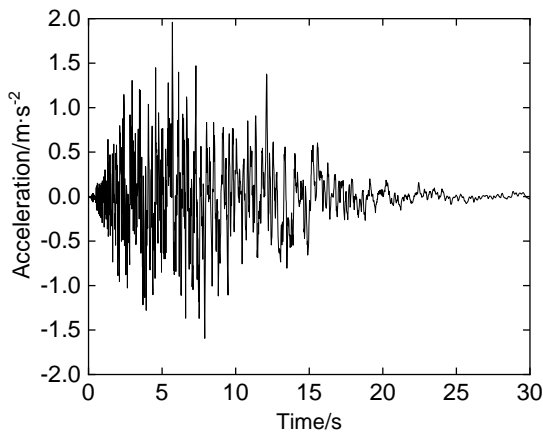
Fig. 4 - Ground Acceleration Time History Curve *Fig. 5 - Acceleration response spectrum curves*

SEISMIC RESPONSE LAW AND DAMAGE MECHANISM OF THE BRIDGE

Acceleration response law of bridge structure

Select 3# bridge box girder bottom plate point a, pier top point b, pier mid-point c and pier bottom point d as the representative characteristic points respectively for bridge seismic dynamic response analysis, and artificial waves with a peak acceleration of 0.2g in the horizontal ground motion are selected for analysis, and the characteristic points are shown in Figure 2.

(a) Transverse direction (point a)   *(b) Along the bridge (point a)*

(c) Transverse direction (point b)   *(d) Along the bridge (point b)*

Fig. 6 - Comparison Diagram of Acceleration Time History of Characteristic Points

(e) Transverse direction (point c)   *(f) Along the bridge (point c)*

(g) Transverse direction (point d)   *(h) Along the bridge (point d)*

Fig. 6 - Comparison Diagram of Acceleration Time History of Characteristic Points

Through the acceleration time history of the bridge structure in Figure 6, we can get the following conclusions. (1) The acceleration development trend of each characteristic point under the IEM boundary is basically the same, and the maximum response appears in the earthquake lasting about 6 s. This is about the same time as the earthquake's peak acceleration. (2) In the process of the strong earthquake, considering the plastic damage and the law of velocity change, compared with the results without considering the damage, the accumulation of plastic damage occurs in the material, and the real-time change of concrete elastic modulus leads to more frequent fluctuation changes. (3) The higher the height of the structure where the feature point is located, the greater the acceleration. The lower position's response of the pier is less than the higher position's and the middle of the box girder.

Displacement response law of bridge structure

The above comparison of the acceleration time history curve results considering nonlinear and linear elasticity shows the rationality of considering plastic damage, and considering plastic damage in engineering practice can more realistically reflect the ground motion response characteristics of bridges. Figure 7 depicts the displacement variation law of each characteristic point of the bridge under differe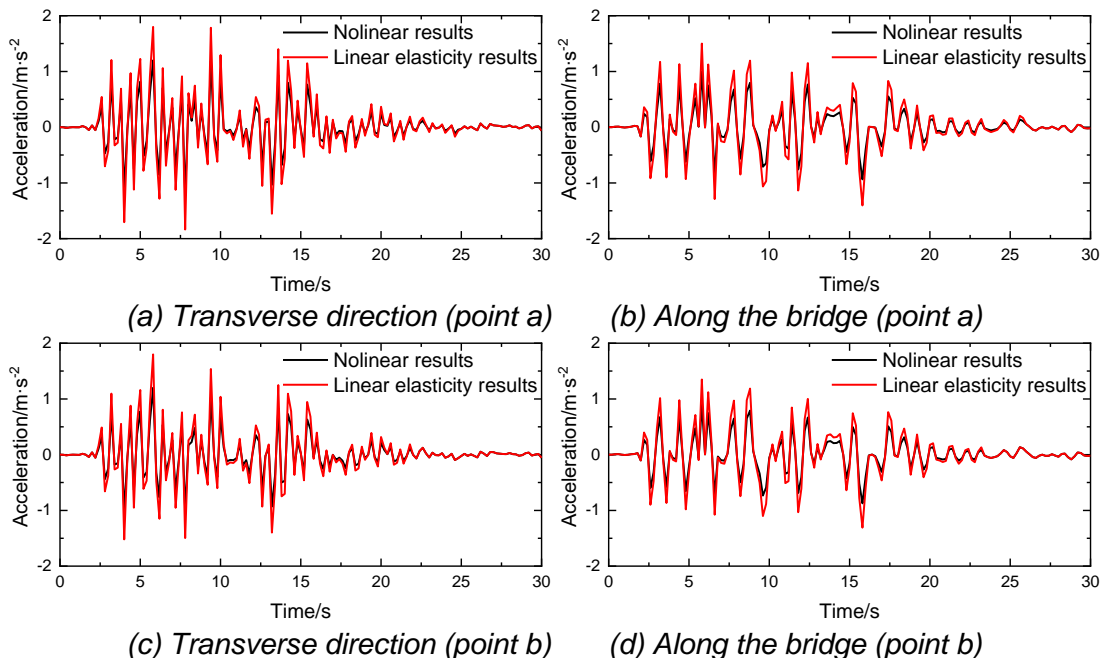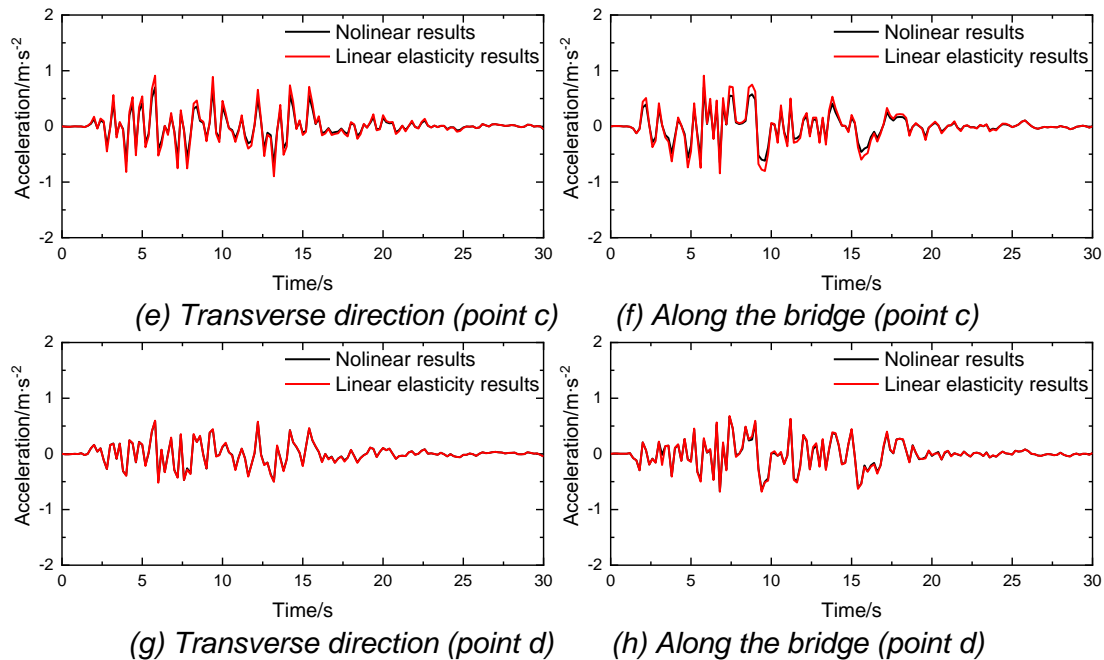nt horizontal peak acceleration considering plastic damage. Through this figure, we can see that: (1) Under earthquake action, when the time reaches about 6 s, the displacement of each characteristic point reaches the peak the first time. Seismic peak acceleration also appears at this time, and the occurrence time of these two peak times is the same. (2) The horizontal displacement along the bridge of each part is greater than the horizontal displacement across the bridge, which indicates that the stiffness of the structure across the bridge is greater, so we should pay attention to the change law of the displacement along the bridge. (3) With the gradual increase of peak acceleration, the displacement of each feature point is also large, because the structure has a large plastic deformation, indicating that the peak acceleration of seismic waves has a significant impact on the displacement of the bridge structure. (4) In the early stage of earthquake action, the bridge structure is still in the elastic state due to the small seismic excitation. Whether to consider the damage on the structural displacement response is not significant. In the later stage of the earthquake, as the peak acceleration of ground motion

gradually increases, the displacement response of the feature points to the structure has a certain displacement deviation relative to the foundation and gradually increases, mainly because the softening behavior of the concrete structure after damage can be described after the introduction of the CDP constitutive model. Irreversible plastic damage occurred in the structure during the earthquake.

(a) Transverse direction (point a)   *(b) Along the bridge (point a)*

(c) Transverse direction (point b)   *(d) Along the bridge (point b)*

(e) Transverse direction (point c)   *(f) Along the bridge (point c)*

(g) Transverse direction (point d)   *(h) Along the bridge (point d)*
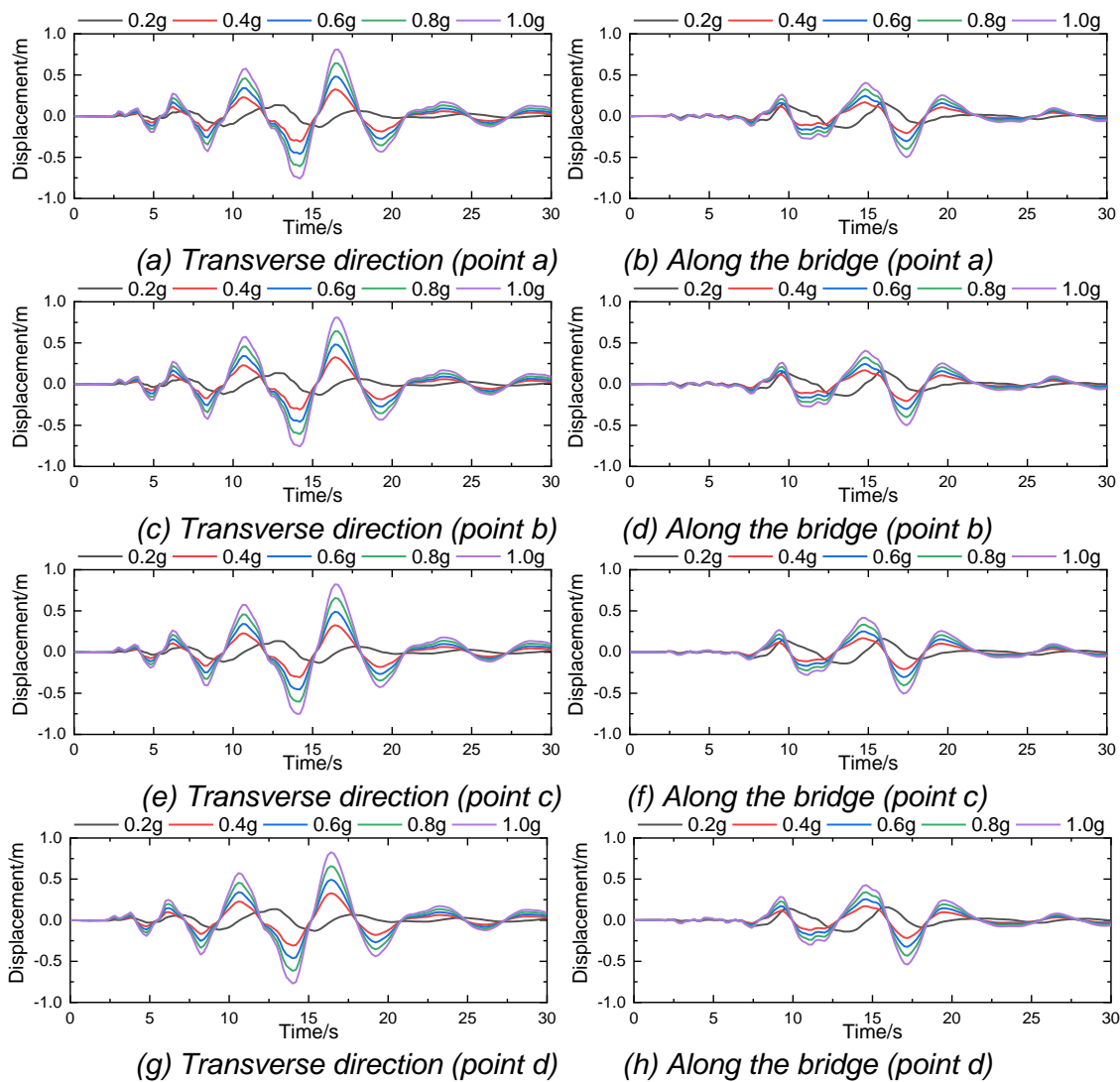
Fig. 7 - Comparison of the Displacement Time History of Each Feature Point

Dynamic damage mechanism of bridge structure

Figure 8, Figure 9 and Figure 10 describe the development process of bridge structure damage when the horizontal peak acceleration is 0.2 g, 0.4 g, and 0.6 g, respectively. Under the action of 0.2g and 0.4g horizontal peak acceleration, the damage was mainly distributed at the junction between the bottom of the box girder and the pier, the junction between the beam end and the pier, and the bottom of the pier. As the horizontal peak acceleration of the input gradually increases, the damage range of the pier column also gradually increases. At a horizontal peak acceleration of 0.6 g, in addition to damage to the pier column, damage also occurred to the bottom of the box girder.

From the perspective of damage development process, at 2.4 s, the bottom of the pier column appeared for the first time under the artificial wave of these three ground motion strengths，and then at 3.2 s, the damage appeared near the box girder near the pier support, as shown in the Figures 8 (a) ~ (b), 9 (a) ~ (b), 10 (a) ~ (b). In the duration of 3.2 s ~ 6.0 s, the damage range gradually extends from the top and bottom piers to the middle, as shown in the figure. 8 (b) ~ (c), 9 (b) ~ (c), 10 (b) ~ (c). During 6.0 s~11.2 s, the damage expands from the bottom of the box girder and the bottom of the pier to the middle of the pier, as shown in the figure. 8 (d), 9 (d), 10 (d). In the later stages of the earthquake, the loss is basically unchanged due to the decrease in the acceleration of the earthquake.

(a) t=2.4 s *(b) t=3.2 s*

(c) t=6.0 s *(d) t=11.2 s*
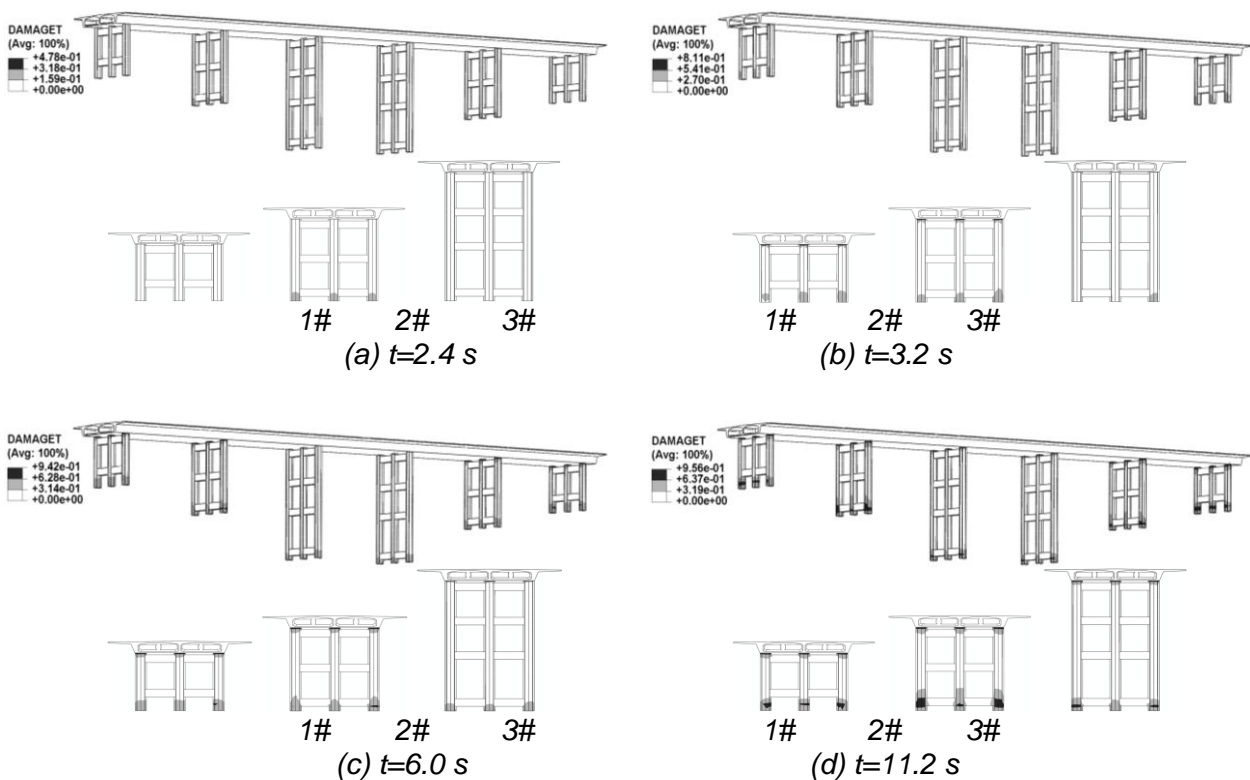
Fig. 8 - Developing Process of Bridge's Damage Under Earthquake(0.2g)

(a) t=2.4 s *(b) t=3.2 s*
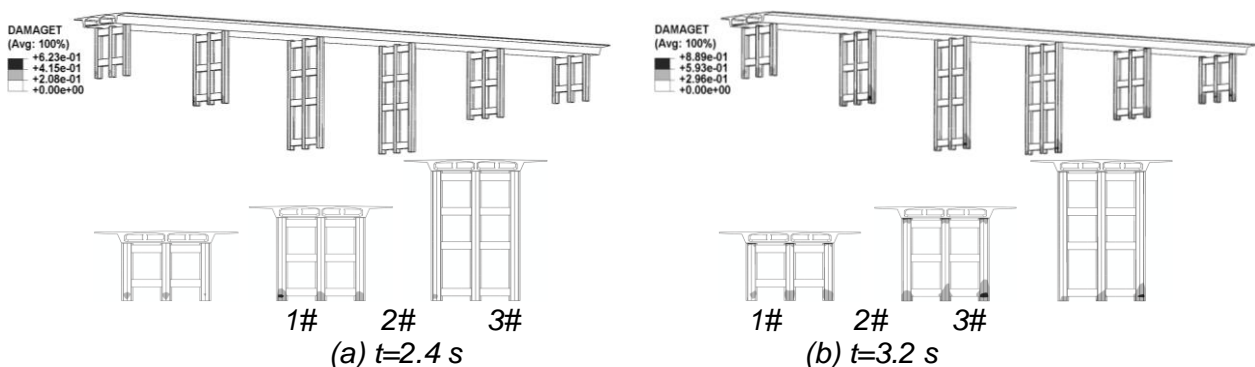
Fig. 9 - Developing Process of Bridge's Damage Under Earthquake(0.4g)
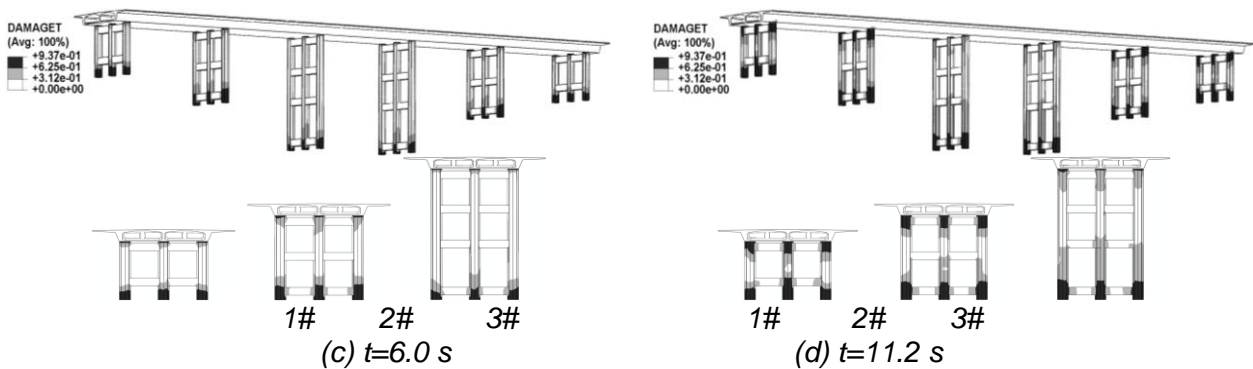
Fig. 9 - Developing Process of Bridge's Damage Under Earthquake(0.4g)
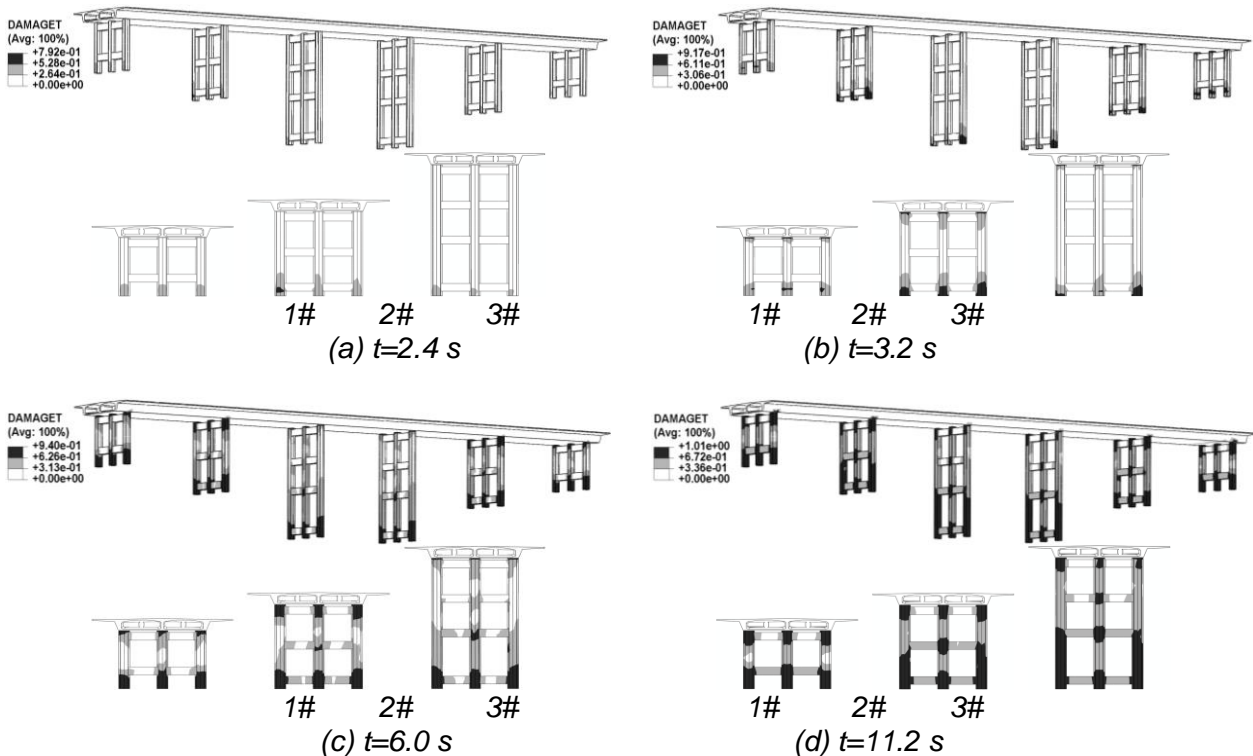
Fig. 10 - Developing Process of Bridge's Damage Under Earthquake (0.6g)

In order to further study, the damage process and development law of the bridge under the action of earthquake, the damage development process analysis of the feature points under different horizontal peak accelerations is carried out, and Figure 11 describes the development and change of the damage values of each feature point. Through this figure, we can see that: (1) The bottom of the pier column where the feature point D is located is the first to be damaged, and with the continuous action of seismic force, after the damage occurs at the bottom of the pier column, the damage range rapidly extends to the entire pier column. (2) Compared with the damage development time of each feature point, the damage rate of the bottom of the box girder where feature point A is located is obviously backward and the damage range is small, and the damage development rate at the bottom of the pier column where feature point D is located is the fastest and the damage value is large. (3) When the horizontal peak acceleration is 0.2g, only the feature

point d has obvious damage. (4) With the gradual increase of peak acceleration, the greater the damage of each feature point, and the damage peak of each feature point is reached in the range of 11 s~18 s, and the damage tends to be stable after 18 s. The bridge damage obtained above was obtained only for the manual records selected in the study.
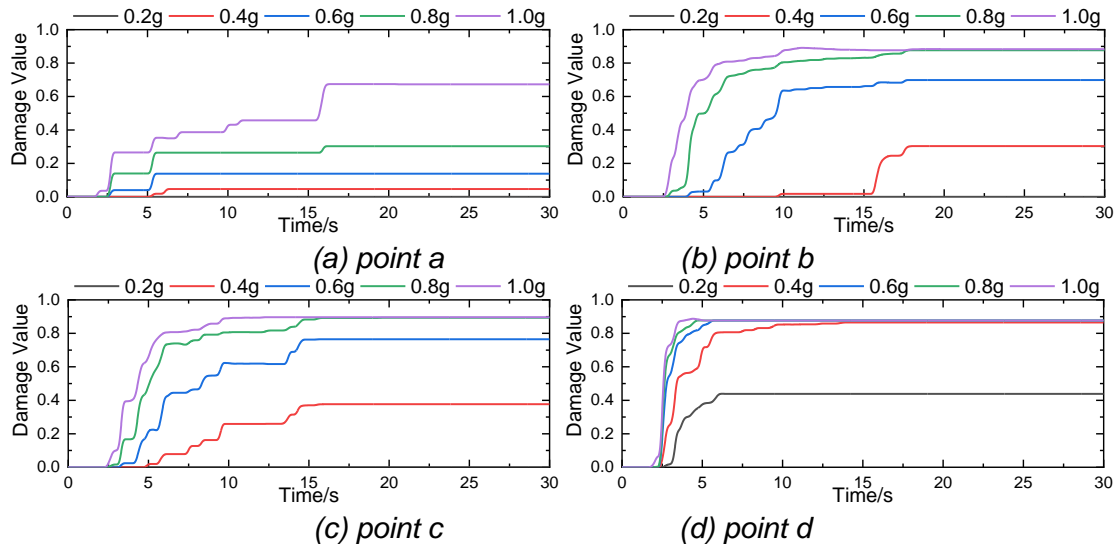
Fig. 11 - Feature point damage development process

CONCLUSION

In this study, the Wenchang Highway Bridge is taken as the actual engineering background to carry out the seismic response analysis. In the meantime, the seismic performance of the cross canal highway bridge is evaluated according to the design requirements. We get some conclusions as follows:

(1) The IEM boundary can well absorb the incident wave's energy and the results are accurate and reasonable. Compared with the viscous-spring boundary, the IEM boundary doesn't need to set a spring-damper system. At the same time, it can also simulate the case of zero displacement at infinity, which can make up for the lack of calculation due to the limitation of boundary conditions. It provides a new reference for the treatment of the boundary in the dynamic calculation of bridge structure.

(2) In the acceleration response analysis of bridge structures, the acceleration response increases with the increase of the height of the structure. The fluctuation of the nonlinear acceleration response curve of the characteristic points of the bridge structure was more obvious, and the nonlinear and linear elastic acceleration response results of the characteristic points of the bridge structure differ by 0.1% ~ 33.3%.

(3) Under the action of selected artificial waves, the damage location of the bridge mainly occurs in the following three parts: the connection of the box girder near the pier support, the bottom of the pier, and the connection between the pier column and the beam, which is the weak link of the bridge structure.

(4) In the analysis of the damage development process, under the action of the horizontal peak acceleration of 0.6g, in addition to the damage of the pier column, the bottom of the box girder also appeared damage. Therefore, when the horizontal peak acceleration of the seismic wave is greater than 0.6g, the failure of the bottom of the box girder is paid attention to.

ACKNOWLEDGEMENTS

REFERENCES

[1]   Long D., Yang W., Scanlon B.R., et al., 2020. South-to-North Water Diversion stabilizing Beijing's groundwater levels. Nature Communications, vol. 11: 1-10. http://doi.org/10.1038/s41467-020-17428-6

[2]   Xie W., Sun L. M., 2014. Study on Seismic Damage and Failure Patterns of Super Long-Span Cable-Stayed Bridge under Earthquake. Earthquake Engineering & Engineering Dynamics, vol.1 : 127-135. http://doi.org/10.13197/j.eeev.2014.06.127.xiew.017

[3]   Deng Y. L., Lei F., He X. J., 2015. Study on Effects of Pounding at Expansion Joints on Seismic Responses of Long-Span Cable-Stayed Bridges between Main Span and Multiple Approach Spans under Earthquakes. China Civil Engineering Journal, vol. 48: 87-95. http://doi.org/10.15951/j.tmgcxb.2015.02.013

[4]   Zhu X., Jiang H., 2009. Performance-Based Seismic Design Method for Rc Bridge Piers. China Civil Engineering Journal, vol. 42 ：85-92.

[5]   TONGAONKAR N. P., JANGID R. S., 2003. Seismic response of isolated bridges with soil–structure interaction. Soil Dynamics and Earthquake Engineering, vol. 23: 287-302. http://doi.org/10.1016/S0267-7261(03)00020-4

[6]   Shi Y., Zhang F. J., Han J. P., et al., 2020. Seismic damage analysis of a long-span continuous rigid frame bridge with high piers during typical construction stages. Zhendong yu Chongji/Journal of Vibration and Shock, vol. 39 : 89 - 95. http://doi.org/10.13465/j.cnki.jvs.2020.22.013

[7]   Guo W., Wang Y., Ge C. Y., et al., 2020. Seismic failure features of multi-span simply supported girder bridges of high-speed railway under near-fault earthquake. Zhendong yu Chongji/Journal of Vibration and Shock, vol. 39 : 210-218. http://doi.org/10.13465/j.cnki.jvs.2020.17.028

[8]   Wang J. Y., Yuan W. C., 2020. Numerical simulation of the response and damage of girder bridges subjected to the combined action of earthquake and blast. Harbin Gongcheng Daxue Xuebao/Journal of Harbin Engineering University, vol. 41 : 643-649. http://doi.org/10.11990/jheu.201812013

[9]   Farahmand-Tabar S., Barghian M., 2020. Seismic assessment of a cable-stayed arch bridge under three-component orthotropic earthquake excitation. Advances in Structural Engineering, vol. 24 : 227–242. http://doi.org/10.1177/1369433220948756

[10] Li C., Diao Y., Li H.-N. et al., 2023. Seismic performance assessment of a sea-crossing cable-stayed bridge system considering soil spatial variability. Reliability Engineering & System Safety, vol. 235: 109210. http://doi.org/ 10.1016/J.RESS.2023.109210

[11] Li J., Xu L., 2023. Seismic performance improvement of continuous rigid-frame bridges with hybrid control system under near-fault ground motions. Soil Dynamics and Earthquake Engineering, vol. 168: 107858. http://doi.org/10.1016/J.SOILDYN.2023.107858

[12] Chu Y., Li R., Li X., 2022. Analysis of Seismic Response of the Arch Bridge across Reservoir considering Fluid-Solid Coupling Effect. Shock and Vibration, vol. 2022. http://doi.org/10.1155/2022/3873935

[13] Deng Y., Ge S., Lei F., 2023. Effects of Pounding and Abutment Behavior on Seismic Response of Multi-Span Bridge Considering Abutment-Soil-Foundation-Structure Interactions. Buildings, vol. 13: 260. http://doi.org/10.3390/BUILDINGS13010260

[14] Addessi D., Gatta C., Nocera M. et al., 2021. Nonlinear dynamic analysis of a masonry arch bridge accounting for damage evolution. Geosciences, vol. 11: 343. http://doi.org/10.3390/GEOSCIENCES11080343

[15] LYSMER J., KUHLEMEYER R. L., 1969. Finite dynamic model for infinite media. Journal of the Engineering Mechanics Division, vol. 95 : 859-878. http://doi.org/10.1061/JMCEA3.0001144

[16] DEEKS A. J., RANDOLPH M. F., 1994. Axisymmetric time-domain transmitting boundaries. Journal of Engineering Mechanics, vol. 120 : 25-42. http://doi.org/10.1061/(ASCE)0733-9399(1994)120:1(25)

[17] Liu J. B., Lv Y. D., 1998. A Direct Method for Analysis of Dynamic Soil-Structure Interaction Based on Interface Idea. China Civil Engineering Journal, 1998. vol.83 : 3-5.

[18] He J. T., Ma H. F., Zhang B. Y., et al., 2010. Method and realization of seismic motion input of viscous-spring boundary. Journal of Hydraulic Engineering, vol.41 : 960-969.

[19] Liao Z. P., Huang K. L., Yang B, P., et al., 1984. A Transmitting Boundary for Transient Wave Analyses. Science in China Series A-Mathematics, Physics, Astronomy & Technological Science, vol. 27 : 1063-1076.

[20] UNGLESS R. F., 1973. Infinite finite element (University of British Columbia).

[21] Chow Y. K., Smith I. M., 1981. Static and periodic infinite solid elements. International Journal for Numerical Methods in Engineering, vol. 17 : 503-526. http://doi.org/10.1002/nme.1620170403

[22] BETTESS P., 1984. A new mapped infinite element for exterior wave problems. Numerical methods in coupled systems.

[23] Asheghabadi M. S., Ali Z., 2020. Infinite element boundary conditions for dynamic models under seismic loading. Indian Journal of Physics, vol. 94 : 907-917. http://doi.org/10.1007/s12648-019-01533-4

[24] Qi Y. L., Hisanori O., 2014. Study of Abaqus Dynamic Infinite Element Artificial Boundary. Rock and Soil Mechanics, vol. 35 : 3007-3012. https://doi.org/10.16285/j.rsm.2014.10.037

[25] Zhang C. H., Zhao C. B., 1987. Coupling method of finite and infinite elements for strip foundation wave problems. Earthquake engineering & structural dynamics, vol.15 : 839-851. https://doi.org/10.1002/eqe.4290150705

DESIGN OF AUTONOMOUS POSITION AND SECONDARY ESTIMATION OF ATMOSPHERIC PARAMETERS SENSOR USING LOW-COST GNSS

Lukáš Běloch

Czech Technical University in Prague, Faculty of Civil Engineering, Department of Geomatics, Thákurova 7, Praha 6, Czech Republic; lukas.beloch@fsv.cvut.cz

ABSTRACT

The article focuses on the design and implementation of a Low-cost GNSS device for autonomous position monitoring and for determining parameters of the atmosphere. The paper brings knowledge of the data quality of low-cost GNSS devices and components. From several components, there were assembled three GNSS devices and they have been thoroughly tested. The results offer insight into the device in terms of device cost, data quality, accuracy in determining a position, and tropospheric parameters. This is followed by a quality test of these collected datasets, there are shown device capabilities in several graphs. Some problems with components can be seen, but the causee was specified. The goal of this article is to describe in detail the behaviour of different parts of a low-cost GNSS device.

KEYWORDS

GNSS, U-Blox, Septentrio, Raspberry Pi, G-Nut, Low-cost receiver

INTRODUCTION

GNSS positioning is one of the most widely used technologies for determining position. We can find various types of GNSS devices used to track animals and vehicles or to navigate cars, boats, and even aero planes. High-accuracy GNSS equipment is frequently used in geodesy for measuring, point laying-out, monitoring land deformations and movements, or controlling autonomous vehicles, for example in agriculture. Less common is the determination of atmospheric parameters by this method.

The motivation to further determine the characteristics of low-cost GNSS devices is to use these devices instead of expensive professional GNSS equipment. This should lead to reducing the cost of this technology in the above cases and to expand into new branches.

Most of the measured parameters should be obtained using the software G-NUT. This software is commonly used in projects where data quality, atmospheric parameters, or position need to be addressed [1,2,3]. But it is designed and used to work with data from professional GNSS devices. For this reason, one of the goals of the paper is to run this software on a low-cost PC and work with data from the low-cost GNSS station.

The low-cost GNSS topic is now very popular, and a lot of research on this was done. The articles working with U-Blox, in the majority of cases used module ZED-F9P, mostly focusing on measuring in real-time positioning mode and position accuracy for surveying [4,5,6,7], or landslide monitoring [8,9,10,11].

The article [12] is dealing with the assembly of RTK measuring equipment using the ZED-F9P module and antenna ANN-MB-00. The resulting mean position of 1-hour observations for 24-hour error was 14 mm, but for 5-second fixed observations was mean position error 5 mm. This precision of the low-cost GNSS device is confirmed by the result from the article [13]. In this case,

was used U-Blox NEO-M8 receiver and ANN-MB-00 antenna, the final horizontal mean error was 5.5 mm and 11 mm for heights.

The work [14] shows that if some different components, better antennas, were used, in good conditions it is possible to achieve position precision very close to the precision of professional devices. The difference between the low-cost device position from the true value turned out to be 1.2 mm when using the DGNSS method.

A significant impact of GNSS antennas was shown in the article [15]. In the experiment, there were used triple-frequency Mosaix-X5 receiver and two types of antennas, low-cost ANN-MB-00 and geodetic TRM59800.00. The formal error of coordinates in some cases using ANN-MB-00 is about 80% higher than with using a TRM59800.00 antenna.

All the articles mentioned above are not involved in determining device qualities or errors except for position accuracy. Also, the papers are mostly focused on only one brand of low-cost GNSS receiver. The main goal of this article is to compare different GNSS components, and their properties and find errors so that the reader can choose the suitable configuration for their project.

METHODS AND MATERIAL

Sensor hardware design and realization

On the market, there are available a lot of low-cost receivers, antennas, and other usable components. In the first place was important to choose individual parts so that the final devices meet the following criteria. Ability to receive systems GPS, GLONASS, and Galileo at the same time, mutual compatibility of components, the possibility to use software G-Nut and RTKLIB, the possibility to connect to the internet, availability on the Czech market, low price. Chosen parts are listed in the tables below.

Components and connection

Tab. 1 - Receivers

Type	Manufacturer	Module	Price to 1. 12. 2022
simpleRTK2B-F9P	Ardusimple	U-Blox, ZED-F9P [17]	226,00 €
simpleRTK3B Pro	Ardusimple	Septentrio, mosaic-X5 [18]	575,00 €

Because both receivers have the same boards, it is possible and easy to replace these boards in the assembled devices. Mounted modules, which are from quite popular brands, meet the relevant criteria.

Tab. 2 - Antennas

Type	Manufacturer	Mounting	Price to 1. 12. 2022
ANN-MB-00	U-Blox	magnetic, screws	53,00 €
AS-ANT2B-SUR	Ardusimple	screw	89,00 €

The main reason for choosing these antennas is that their constructions differ significantly.

Tab. 3 - Minicomputers

Type	Manufacturer	Dimension	Price to 1. 10. 2022	Price to 1. 12. 2022
Zero 2 W	Raspberry Pi	60 x 30 x 5 mm	512 MB	17,00 €
4 Model B	Raspberry Pi	56 x 85 x 11 mm	2 000 MB	66,00 €

Received signals must be processed at a local device or distributed to another device. It is possible to use a computer, mobile phone, microcontroller, etc. We decided to choose the minicomputers Raspberry Pi for this project. They are running under the operating system Rasbian (Linux) and that allows the installation of required software. Raspberry Pi is also able to connect to the internet via Wi-Fi [19].

The connection between the receiver and the minicomputer can be done by USB ports, UART ports, I2C bus, and SPI interface. The first test of connection used a USB port, but later connections via a UART port turned out to be better. The link between components is stronger and is possible to divide streams into multiple ports using this connection.

Assembled devices

The following devices were assembled from all these components. They are similar to each other, it's because we can easily monitor the influence of individual parts on measured data.

Tab. 4 - GNSS sets

	Receiver	Antenna	Mini PC
GOPB	simpleRTK2B-F9P	AS-ANT2B-SUR	Raspberry Pi Zero 2 W
GOPC	simpleRTK2B-F9P	ANN-MB-00	Raspberry Pi Zero 2 W
GOPS	simpleRTK3B Pro	AS-ANT2B-SUR	Raspberry Pi 4 Model B

Sensor software design and realization

Used software

1. G-Nut/Anubis [20] - RTCM message processing and data saving to RINEX format and files of measurement quality (XML, XTR).
2. G-Nut/Tefnut [21] - calculation of tropospheric parameters.
3. gNut-Ntrip - providing data to an NTRIP caster.
4. RTKlib/STR2STR [22] - splitting the incoming data stream into multiple streams, providing data to an NTRIP caster.
5. RTKlib/RTKPOST [22] - postprocessing positioning.

Software design

Figure 1 shows a design of software and data flowing, there are three ways of data processing.

1. Network solution - The sensor is connected to the internet and provides data via an NTRIP caster. The remote server performs data processing.
2. Local solution - Data processing is performed by a local computer. The Final products are stored in data storage.
3. Complex solution - It is a combination of the designs described above.
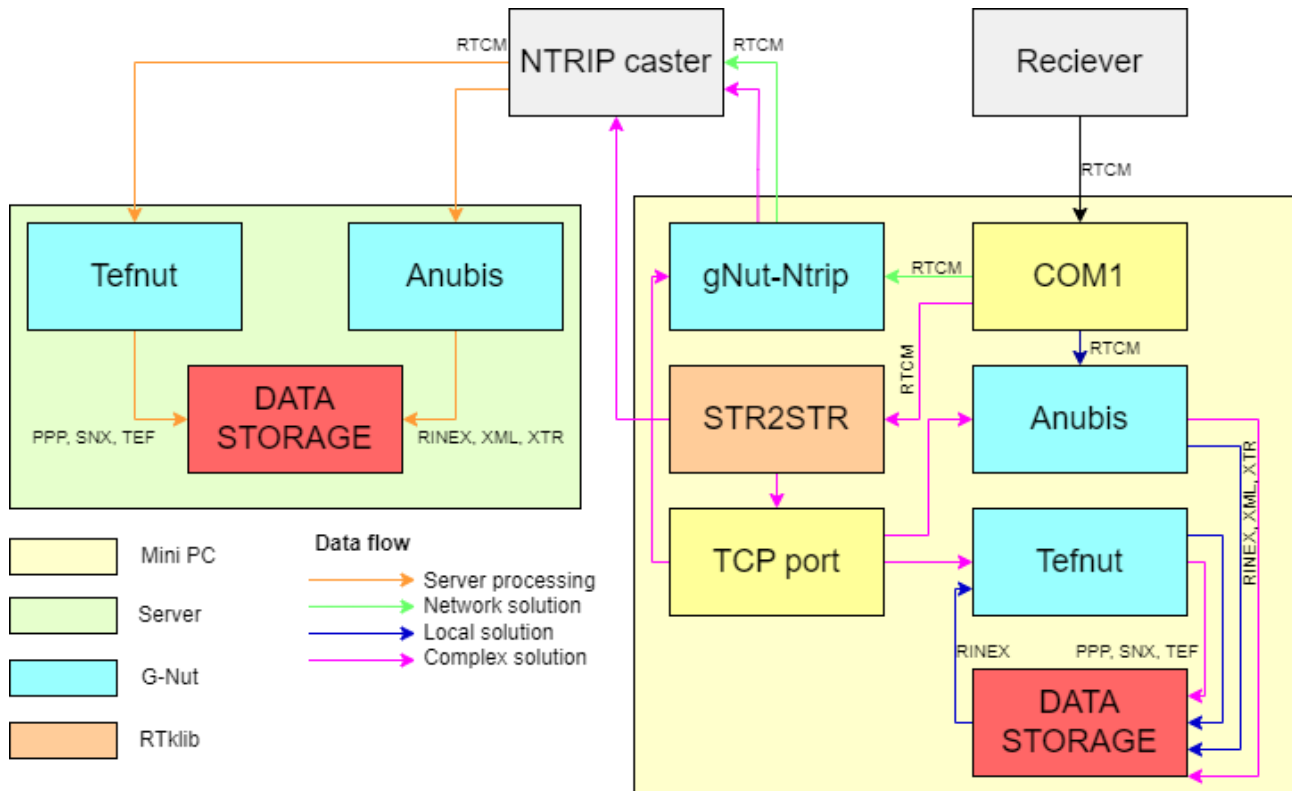
Fig. 1 - Software solution schema

Sensor testing

The first software design (Network solution) was selected for testing. The main testing parameters are described in Table 5.

Tab. 5 - Test parameters

	Location	Measurement date
GOPS	GO Pecný, reinforced chimney	2.3 - 2.4 2022
GOPC	GO Pecný, reinforced chimney	2.3 - present
GOPB	Prague - CTU, FCE, the roof of building B	17.3 - 2.4 2022

RESULTS

Raspberry Pi indicators

The software was run on the computers and basic parameters were monitored (CPU, RAM, temperature). This test was to prove the stability of the computers to prevent data loss. We can see that both devices are stable, and it is advisable to use them.
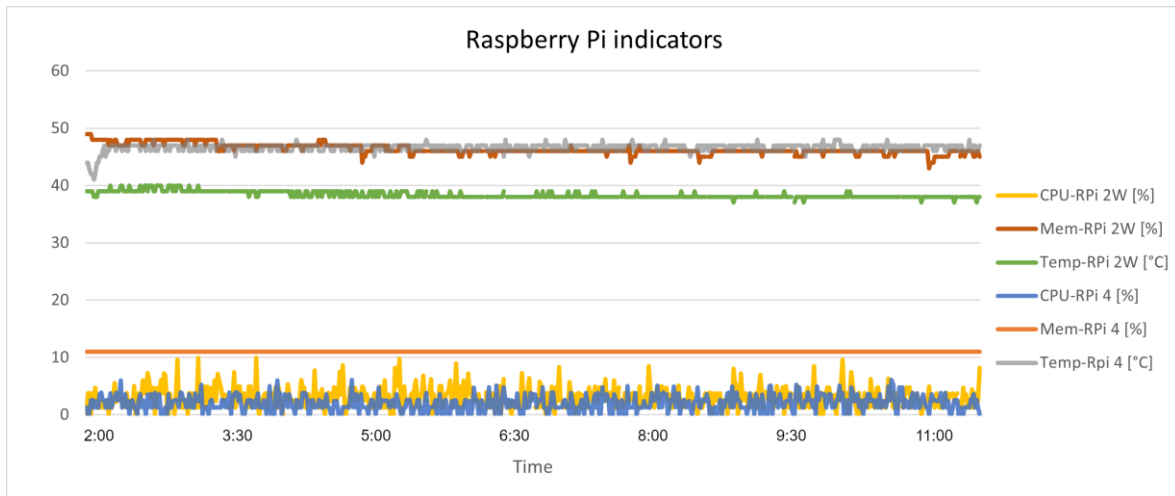
Fig. 2 - Raspberry Pi indicators

Parameters of data quality

Data quality rating retrieved from the G-Nut/Anubis was made from the following indicators.

1. MinEle - minimum elevation angle of viewed satellites.
2. GNSS - number of used satellite systems.
3. Ratio - a ratio of expected observations to measured observations.
4. URatio - a ratio of expected observations to measured observations over the elevation mask (10°)

Low-cost stations were compared with each other and with the GOPE reference station.
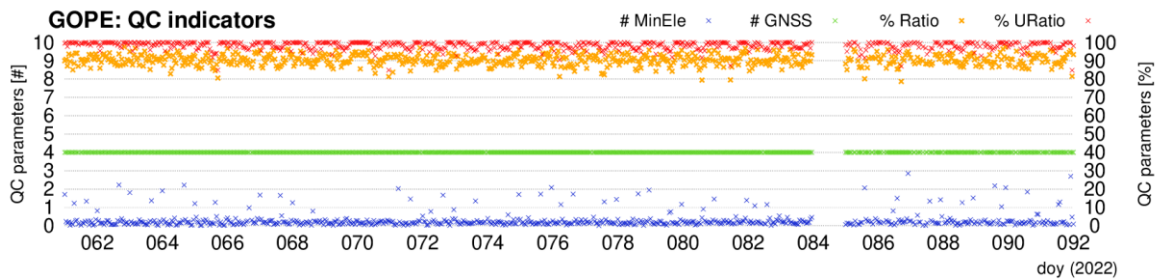
Fig. 3 - GOPE station parameters (GPS, GLO, BDS, GALILEO)
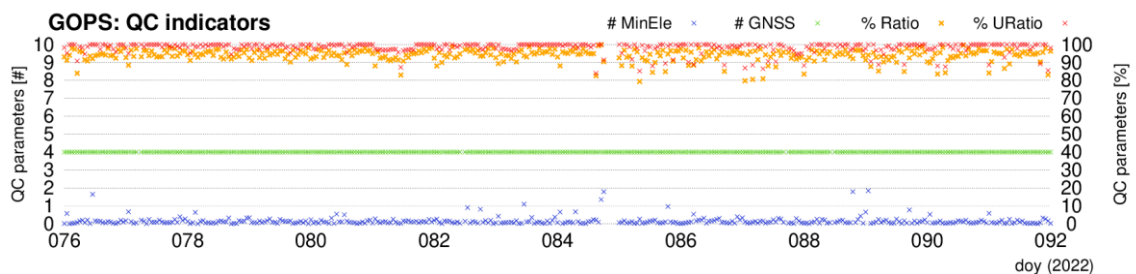
Fig. 4 - GOPS station parameters (GPS, GLO, BDS, GALILEO)
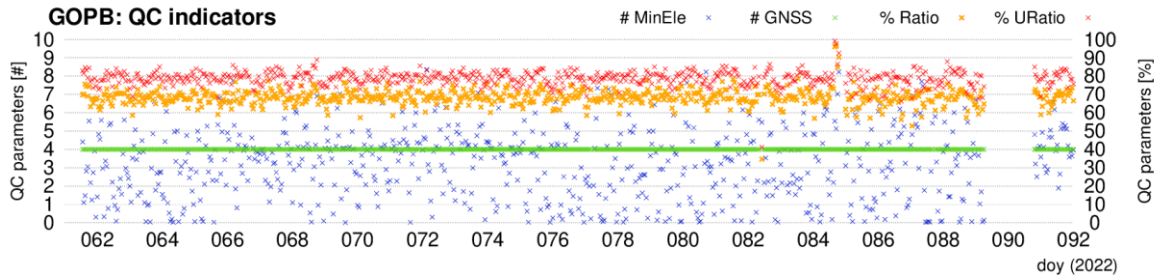
Fig. 5 - GOPB station parameters (GPS, GLO, BDS, GALILEO)
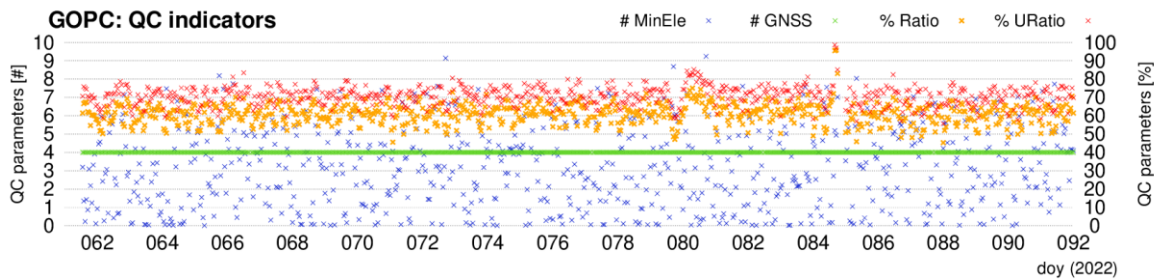
Fig. 6 - GOPC station parameters (GPS, GLO, BDS, GALILEO)

Identified problems

Antennas

1. AS-ANT2B-SUR - The results of GOPB (Figure 5) data quality may indicate some degradation of measured data caused by this antenna. However, it is refuted by the GOPS (Fig. 4) station indicators, and the visible problem is due to another part of the device.
2. ANN-MB-00 - Graph of GOPB (Figure 5) station compared to GOPC (Figure 6) station says that the choice of antenna is very important. In this case, ANN-MB-00 caused significant data degradation.

Receivers

1. simpleRTK3B Pro (Septentrio, mosaic-X5) - The graph of the GOPS station compared to the GOPE reference station (Figure 3) is very similar. It was assumed that the receiver would not cause any problems affecting data quality. This was confirmed in further work with the receiver.
2. simpleRTK2B-F9P (U-Blox, ZED-F9P) - This part is quite problematic. We can see several problems:

   a. The data from the GOPB station compared to the GOPE shows that the receiver affects the Ratio of the GNSS device, as we consider the antenna to be flawless. Analysis of the data quality files showed, as we can see from Figure 7, that the main problem was caused by U-Blox not being able to receive the BDS system correctly.
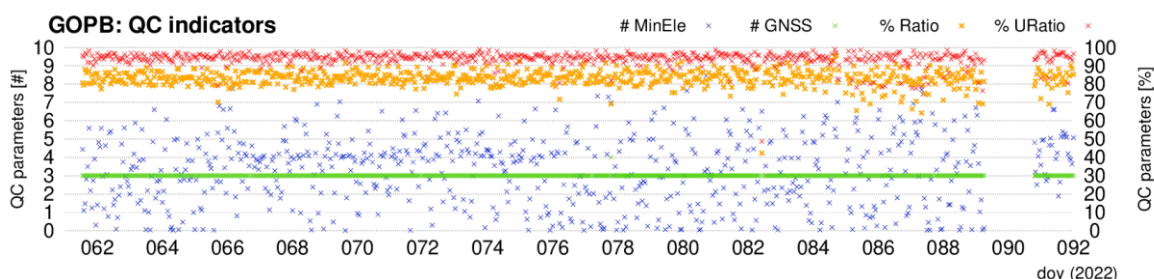
Fig. 7 - GOPB station parameters (GPS, GLO, GALILEO)

b. Even though we excluded the BeiDou system from further processing there was still a small data leak. The grey dots shown in Figure 8 indicate that the dataset is incomplete. The epochs of each system were sometimes different by 1 ms. The G-Nut software discards these different epochs.

c. Large variance of values shown in Figure 5 and Figure 6 is caused by the receiver's inability to receive signals with low SNR, as we can see from Figure 8.
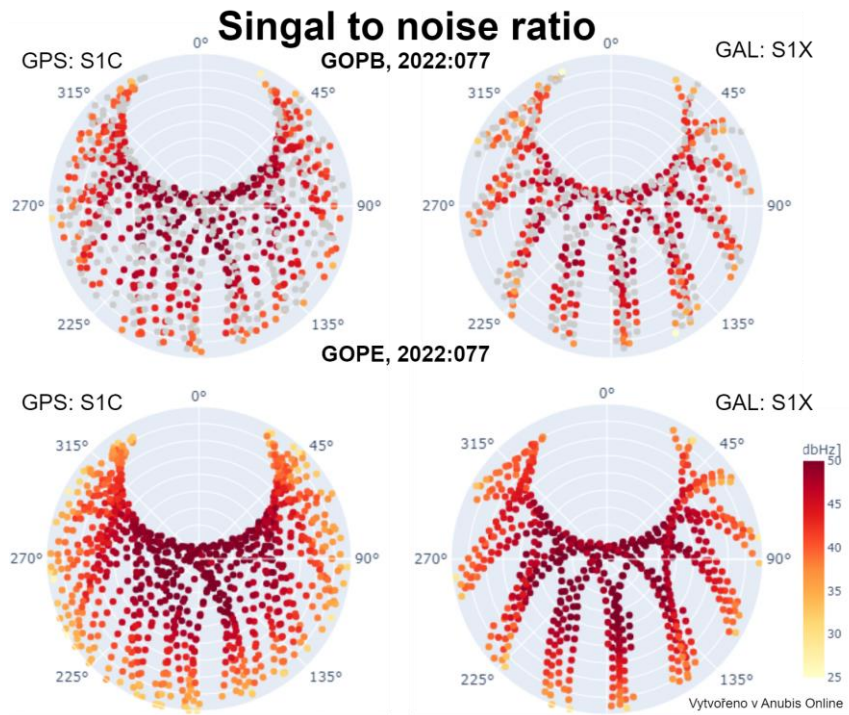
Fig. 8 - GOPB and GOPE SNR skyplot

Positioning

Position calculations were performed by a static method for hourly solutions using only the GPS and the Galileo system. There were used GOPE (GO Pecný) and CPRG (Cadastral Office Prague) reference stations from CZEPOS (Network of Permanent GNSS stations of the Czech Republic).

In Tables 7-9 there are calculated position and standard deviation of coordinate repeatability by RTKlib/RTKPOST. The fix is the ratio of fixed measurements to all measurements.

Tab. 6 - GOPB position

Reference station	Latitude - B [°, N]	Longitude - L [°, E]	Height - Hel [m]	σN [mm]	σE [mm]	σU [mm]	Fix [%]
GOPE	49° 54' 49.20491"	14° 47' 8.22001"	592.841	1.3	3.5	4	100
CPRG	49° 54' 49.20554"	14° 47' 8.21949"	592.787	4.0	7.9	15	54

Tab. 7 - GOPC position

Reference station	Latitude - B [°, N]	Longitude - L [°, E]	Height - Hel [m]	σN [mm]	σE [mm]	σU [mm]	Fix [%]
GOPE	49°54'49.20039"	14°47'08.19941"	592.653	2.8	2.0	6	26
CPRG	49°54'49.20097"	14°47'08.19694"	592.619	4.6	4.5	37	9

Tab. 8 - GOPS - position

Reference station	Latitude - B [°, N]	Longitude - L [°, E]	Height - Hel [m]	σN [mm]	σE [mm]	σU [mm]	Fix [%]
GOPE	50°06'14.01173"	14°23'16,21509"	305.384	4.3	7.2	20	61
CPRG	50°06'14.01206"	14°23'16,21523"	305.311	1.5	1.7	5	90

Troposphere parameters

This chapter examines the suitability of low-cost GNSS devices for determining atmospheric parameters.

ZTD (Zenith Total Delay) is calculated by G-Nut/Tefnut and low-cost stations results are primarily compared to the GOPE station. This software was developed and demonstrated in a long-term campaign involving 36 European and worldwide GNSS stations [2].

Article [3, p. 7], which focuses on European GNSS troposphere monitoring, says that a ZTD standard deviation of differences (daily) GOPE-GOP6 collocated stations is 3.44 mm.

1. GOPC - As we can see from Figure 9 calculated values are significantly different from other stations that are following a similar trend.
ZTD standard deviation of differences (daily) GOPE-GOPC is 11 mm.
2. GOPB - Figure 10 better shows a comparison of the GOPB station to the GOPE station. Here, the values from the low-cost station follow the values of the reference station very well.
ZTD standard deviation of differences (daily) GOPE-GOPB is 4.1 mm.
3. GOPS - Last, the parameters from two collocal low-cost stations were compared
(Figure 11). The results are unclear, and a new test needs to be done near the reference station
ZTD standard deviation of differences (daily) GOPS-GOPB is 11 mm.
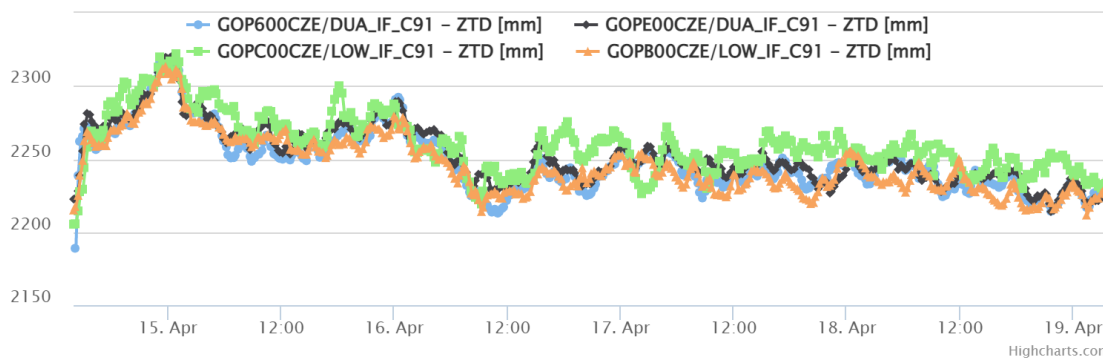
Fig. 9 - An assessment of the tropospheric characteristics of the stations situated at the Pecný Observatory.
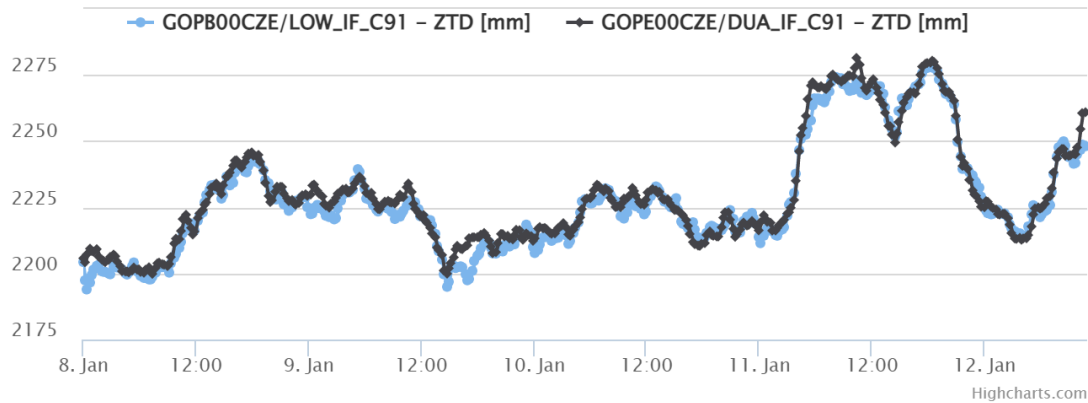
Fig. 10 - An assessment of the tropospheric characteristics of the GOPE and GOPB stations.
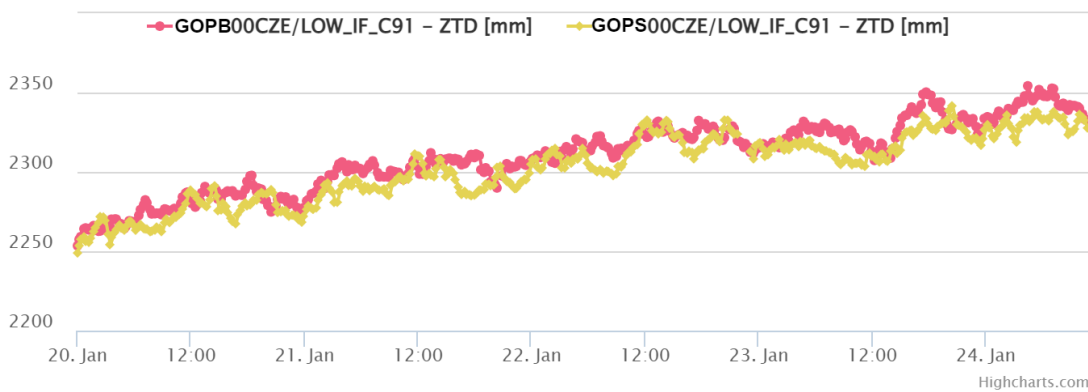
Fig. 11 - An assessment of the tropospheric characteristics of the GOPC and GOPB collocated stations.

CONCLUSION

Evaluation of the final sensor

Tab. 9 - Evaluation

	PC stability	Data quality	Position	Troposphere	Price
GOPS	+	+	+	?	+/-
GOPC	+	-	-	-	+
GOPB	+	+/-	+	+	+

All the results, summarize in Table 9 (+ satisfactory, - unsatisfactory, +/- acceptable), says that only the GOPC station is unsuitable for the intended purpose. The results from this device were significantly affected by antenna ANN-MB-00. This means that antenna selection is very important, and it would be interesting to try other antennas in the next projects.

The other two stations are suitable, from receiver datasheets and data quality results it would be expected that the GOPS station will perform better results than the GOPB station. However, that has not been confirmed.

The GOPB low-cost station is currently working. Surprisingly the weakest part of the device is Raspberry Pi, where the SD card with the operating system was often corrupted.

The main benefit of this paper is information on deeper characteristics of low-cost GNSS components. The identified properties and deficiencies of components are usually not listed in the manufacturer's documentation, and therefore all of these results can be used for setting up your own

GNSS device, not only for estimation of atmospheric parameters sensor but for a wide range of GNSS devices.

ACKNOWLEDGEMENTS

REFERENCES

[1]   VACLAVOVIC, Pavel; DOUSA, Jan; GYORI, Gabriel. G-Nut software library-state of development and first results. Acta Geodyn. Geomater, 2013, 10.4: 431-436.

[2]   DOUSA, Jan; VACLAVOVIC, Pavel. Real-time zenith tropospheric delays in support of numerical weather prediction applications. Advances in Space Research, 2014, 53.9: 1347-1358.

[3]   DOUŠA, Jan, et al. European GNSS troposphere monitoring for meteorological applications. In: IOP Conference Series: Earth and Environmental Science. IOP Publishing, 2021. p. 01205

[4]   Hohensinn, R.; Stauffer, R.; Glaner, M.F.; Herrera Pinzón, I.D.; Vuadens, E.; Rossi, Y.; Clinton, J.; Rothacher, M. Low-Cost GNSS and Real-Time PPP: Assessing the Precision of the u-blox ZED-F9P for Kinematic Monitoring Applications. Remote Sens. 2022, 14, 5100. https://doi.org/10.3390/rs14205100

[5]   Revert Calabuig, N.; Laarossi, I.; Álvarez González, A.; Pérez Nuñez, A.; González Pérez, L.; García-Minguillán, A.C. Development of a Low-Cost Smart Sensor GNSS System for Real-Time Positioning and Orientation for Floating Offshore Wind Platform. Sensors 2023, 23, 925. https://doi.org/10.3390/s23020925

[6]   Nie, Z., Liu, F. & Gao, Y. Real-time precise point positioning with a low-cost dual-frequency GNSS device. GPS Solut 24, 9 (2020). https://doi.org/10.1007/s10291-019-0922-3

[7]   Hamza, V.; Stopar, B.; Sterle, O.; Pavlovčič-Prešeren, P. Low-Cost Dual-Frequency GNSS Receivers and Antennas for Surveying in Urban Areas. Sensors 2023, 23, 2861. https://doi.org/10.3390/s23052861

[8]   Xue, Chenyu, Panos A. Psimoulis, and Xiaolin Meng. "Feasibility analysis of the performance of low-cost GNSS receivers in monitoring dynamic motion." Measurement 202 (2022): 111819. https://doi.org/10.1016/j.measurement.2022.111819

[9]   Biagi, L.; Grec, F.C.; Negretti, M. Low-Cost GNSS Receivers for Local Monitoring: Experimental Simulation, and Analysis of Displacements. Sensors 2016, 16, 2140. https://doi.org/10.3390/s16122140

[10]   Notti, D.; Cina, A.; Manzino, A.; Colombo, A.; Bendea, I.H.; Mollo, P.; Giordan, D. Low-Cost GNSS Solution for Continuous Monitoring of Slope Instabilities Applied to Madonna Del Sasso Sanctuary (NW Italy). Sensors 2020, 20, 289. https://doi.org/10.3390/s20010289

[11]   Heunecke, Otto, Jessica Glabsch, and Stefan Schuhbäck. "Landslide monitoring using low cost GNSS equipment n experiences from two alpine testing sites." Journal of civil engineering and architecture 5.8 (2011).

[12]   Zahradník, D., Vyskočil, Z., & Hodík, Štěpán. (2022). UBLOX F9P FOR GEODETIC MEASUREMENT. Stavební Obzor - Civil Engineering Journal, 31(1), 110–119. https://doi.org/10.14311/CEJ.2022.01.0009

[13]   GARRIDO-CARRETERO, María S., et al. Low-cost GNSS receiver in RTK positioning under the standard ISO-17123-8: A feasible option in geomatics. Measurement, 2019, 137: 168-178.

[14]   HAMZA, Veton; STOPAR, Bojan; STERLE, Oskar. Testing the performance of multi-frequency low-cost GNSS receivers and antennas. Sensors, 2021, 21.6: 2029.

[15]   STĘPNIAK, Katarzyna, et al. Applicability of recent low-cost GNSS receivers to deformation monitoring.

[16]   BĚLOCH, Lukáš. Design of autonomous position and secondary estimation of atmospheric parameters sensor with the use of low-cost GNSS. Praha, 2022, 82 s. Available from: https://dspace.cvut.cz/handle/10467/102815. Diploma thesis. CTU Prague, Faculty of Civil Engineering. Thesis leader Vyskočil Zdeněk. 458 (In the case of a contribution to proceedings)

[17]   ZED-F9P-04B: u-Blox F9 high precision GNSS module Datasheet [online]. s. 1-25 [cit. 2022-10-01]. Available from: https://content.u-blox.com/sites/default/files/ZED-F9P-04B_DataSheet_UBX-21044850.pdf

[18]   Mosaic-X5 [online]. s. 1-2 [cit. 2021-10-01]. Available from: https://www.septentrio.com/en/products/gnssreceivers/ receivers-module/mosaic#resources

[19]   Raspberry Pi 4 Model B: DATASHEET [online]. June 2019, p. 1-13 [cit. 2022-10-01]. Available from: https://datasheets.raspberrypi.com/rpi4/raspberry-pi-4-datasheet.pdf

[20]   DOUSA, Jan a Pavel VACLAVOVIC. G-Nut/Anubis [online]. p. 1-50 [cit. 2022-10-01]. Available from: https://gnutsoftware.com/themes/gnut/assets/files/anubis_manual.pdf

[21]   VÁCLAVOVIC, Pavel a Jan DOUSA. G-Nut/Tefnut [online]. p. 1-40 [cit. 2022-10-01]. Available from: https://gnutsoftware.com/themes/gnut/assets/files/tefnut_manual.pdf

[22]   TAKASU, Tomoji. RTKLIB ver. 2.4.2 Manual [online]. In: 29. April 2013, p. 99 [cit. 2022-10-01]. Available from: https://www.rtklib.com/prog/manual_2.4.2.pdf

STUDY ON THE DRIVING GAZE SHIFT CHARACTERISTICS OF VISION INTERESTING AREA ON MOUNTAINOUS ROAD

Yunwei Meng[1], Shibao Li[1], Kang Chen[2], Binbin Li[1], Guangyan Qing[3]*

1. *Chongqing Jiaotong University,College of Traffic and Transportation, Chongqing 400074, China; 514346081@qq.com,571187537@qq.com*
2. *Chongqing Jiaotong University, School of Civil Engineeing, Chongqing 400074, China; 2606011182@qq.com*
3. *China Merchants Roadway Information Technology (Chongqing) Co., Ltd, Chongqing, 400067, China; 379544277@qq.com*

ABSTRACT

Mountainous road landscape is the main source of driving information. The characteristics of two-lane mountainous road result in real-time dynamic changes in the driver's vision interesting areas. In order to explore the dynamic gaze characteristics, a driving experiment is conducted, and the gaze data of 10 drivers are collected. Markov chain is used to analyze the change process of the gaze. The results show that: (1) when the current gaze point is in the straight front area, different road landscape has no significant impact on the gaze shift probability; (2) when the current gaze point is in the near left area, next gaze will expand the search scope to obtain much more driving information; (3) when the current gaze point is in the near right area, there is a high probability that the driver's next gaze will return to the front area; (4) when the current gaze point is in the far right area, the gaze will move back and forth between the near right and the far right areas; (5) when the current gaze point is in the far left area, there is a high probability that the gaze will remain in current area; (6) the main source of traffic information obtained by the driver in mountainous road landscape is the straight front area in the vision field, and the gaze point constantly shifts between the far ahead and the near ahead. The research results can provide technical reference for the construction of landscape in mountainous two-lane road.

KEYWORDS

Mountainous road, Landscape, Shift of gaze while driving, Vision interesting area, Markov chain

INTRODUCTION

Mountainous roads often have many characteristics, such as complex alignment, many artificial structures, frequent spatial changes, etc. Drivers need to make correct driving operations in time to cope with changes in the driving environment. In addition, the form of traffic safety facilities is often very simple, and the variability of road landscape is often insufficient. These factors will cause the driver to have frequent eye movements when driving. From the perspective of traffic safety, the driver

should have excellent driving skills. Drivers should be able to receive and process external information timely and accurately. At the same time, the driver should also get appropriate feedback from the external driving environment, so as to maintain a good attitude, which is conducive to driving operation.

The landscape of mountainous roads can affect the driver's vision interesting area. There are rich landscape resources along mountainous road. Through reasonable landscape construction, the driving visual environment can be improved, and the driving direction can be guided by appropriate visual stimulation to improve the driving safety performance.

LITERATURE REVIEW

During driving, different drivers will have different visual loads due to the influence of environmental changes. Many scholars have studied the relationship between traffic safety and road landscape. A single road landscape is easy to cause negative driving psychology and visual fatigue [1]. XiaoLei Li et al. used simulation software such as UC-WIN to test the impact of road landscape environment color on driver vision, and found that red and yellow in the environment have a significant impact on drivers [2]. Meng YW et al. used the threshold segmentation method to process the visual image, obtained the calculation method of road landscape information, and established the regression relationship between comfort and landscape information [3]. Qin YQ summarized the factors affecting the driver's visual load, and pointed out that the road landscape had a great visual impact on drivers from the relationship between people, car, road and environment [4]. Jeong-Hun Mok et al. conducted statistical analysis of road traffic accidents in Texas, and found that the driver's visual perception was correlated with the road landscape [5]. After landscape improvement of some sections or roadside stops, the quantity of traffic accident significantly decreased.

The vision interesting area is located in the driver's vision field, which is the area with more gaze times and longer gaze time. With the aid of eye movement observation instrument, the distribution of visual gaze points can be obtained. A reasonable and effective division of the vision field helps to find the rules of the gaze points. By dividing the field of vision, the vision field will be divided into several zones. The number of gaze points and gaze time in each zone can be compared to determine where the vision interesting area is located. Therefore, it is important to divide the vision field. At present, there are three main methods to divide the vision field for deciding vision interesting area. (1) The method of statistical analysis for each frame, that is, researchers' playback the driving scene video frame by frame and record the position of the gaze point, and then superimpose the gaze point in the vision field according to the time sequence, so as to obtain the vision interesting area, i.e. the concentration of the gaze points. (2) Default partition method. Its main characteristic is to divide the vision field into several sub-regions before experiment. This method is relatively simple and has been widely used. Shan Bao et al. divided the vision field into 7 sub-regions: far left, near left, far right, near right, straight front, rearview mirror and others. The division of vision field is related to the gaze specific environment [6]. Yamada studies the visual recognition characteristics of drivers by dividing several regions with different weights [7]. (3) Clustering method of gaze points. It firstly selects several gaze point samples as the clustering center, then clusters according to the criteria, and continuously adjusts the clustering center until the clustering result is reasonable. Drusch et al. applied a clustering method based on Hausdorff distance to study the relationship between gaze

behavior and body behaviour [8]. Saha Bipin proposes a real-time eye gaze tracking interface based on an active appearance method using a simple web or smartphone camera in an unconstrained environment, where natural head movements have been taken into account [9].

Based on the comprehensive study of the gaze region, it can be found that the research results show that the driver's gaze points are mainly distributed in the middle and far ahead of the vision field, which is consistent with the visual characteristics while driving. With the change of driving, the gaze point will change dynamically.

Visual scanning behaviour can affect the role between attention and information acquisition from the driver's environment [10]. Stephan et al. introduced a new Hidden Markov models. This provides a new approach for the study of vision interesting area [11]. Nilsson introduced a type of gaze concentration effect, which analyzes the impact of cognitive load on driving visual characteristics by analyzing the movement path of gaze during driving. The research results help to understand and predict the safety related effects of cognitive load on car drivers [12]. Meng Y W et al. put forward a quantitative method of comprehensively considering the gaze position, gaze time and gaze times, which can better reflect the driver's gaze intensity on the vision interesting area [13]. He S M et al. analyzed the temporal and spatial characteristics of the driver's gaze behavior when entering the main line and ramp through the diversion region by real vehicle experiment [14]. Ghosal Deepanway et al. propose a transfer learning and attention mechanism based neural network model to predict visual interest & affective dimensions in digital photos. With various experiments they show the effectiveness of the proposed approach [15]. Morales Aythami et al. proposes a new algorithm based on LSTM networks and a fine-grained loss function for saccade landing point prediction in real-world scenarios [16]. For the weighted search area method, Christófano proposes a web application called PlaceProfile to perform visual profiling of city areas based on iconographic visualization and to label areas based on clustering algorithms [17].

Lee YC et al. used the simulating driving method to analyze the driver's gaze shift characteristics, and it pointed out that the short gaze away from the road may cause traffic safety accidents [18]. Shih-Hsuan Huang et al. established a visual attention evaluation framework based on the distribution principle of contribution, and it used the associated logit model to evaluate the driver's gaze shift probability, and it found that there was a wide range of scanning path process between the two fixations [19].

It can be seen that the driver's continuous multiple gaze at the vision interesting area is the guarantee of sufficient information sources. The landscape of two-lane mountainous roads has caused the dynamic shift of driver's attention. In this paper, the driving experiment is used to collect the driver's gaze data. From the perspective of time, the Markov chain is used to analyze the characteristics of dynamic shift and explore the main vision interesting area.

EXPERIMENT PROCESS

In this section, a driving experiment was carried out to explore the dynamic changes of driver's gaze area in two-lane mountainous road. The driving experiment mainly included recording the dynamic image of the road landscape, as well as the driver's visual response and other indexes.

Instruments

In the experiment, the experimental HONDA CR-V car was equipped with a camera. The eye-movement instrument called Dikablis was used to collect the driver's visual characteristic data. The data acquisition frequency is 60Hz. The tracking accuracy of the driver's pupils is 0.05°. The eye-movement instrument is shown in Figure 1. The instrument can record the eye movement trajectory and fixation time of participants. The vehicle-mounted CTM-8C non-contact vehicle speedometer was used to measure the speed and acceleration of the experimental car. The speed measurement range is 0-250km/h, with a baud rate of 9600.

Fig. 1 - Eye movement instrument and on-board data processing equipment

Process of experiment

Chongqing is famous for its mountain city, which has a wide range of mountain terrain, providing a rich site environment for experimental research. A section of road in Chongqing was selected as the experimental mountainous road. This road is located in Ba'nan District, Chongqing,China, and it is the provincial road S102. The geographical plan is shown below.
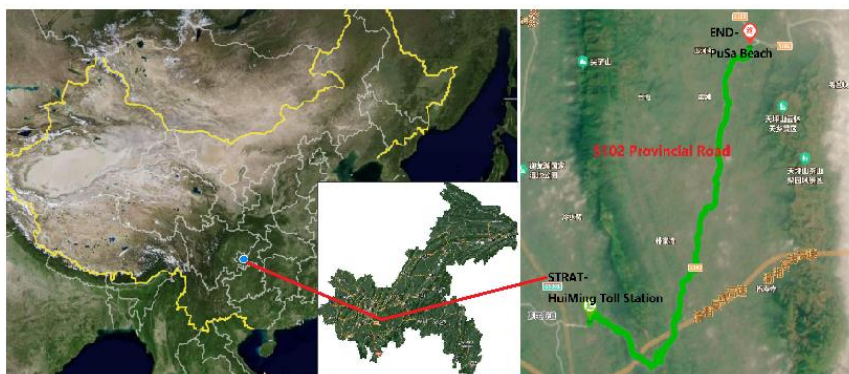
Fig. - 2 Plan of experimental section

The section length is about 25km, and the design speed is 60km/h. The width of the experimental road is 8.5m, of which 7.5m is the carriageway, and there are 0.5m wide hard shoulders on both sides. The pavement is asphalt concrete pavement. The minimum circular curve radius of mountainous roads is 40m, and the maximum longitudinal slope is 5%.

During the driving test, the traffic flow is in a free flow state. The weather is good. During the experiment, there was no obvious direct sunlight on the driver's eyes.

By recruiting online and selecting suitable volunteers, each person will receive 100 RMB and a commemorative cup. Ten subjects were selected as drivers for driving test, who were unfamiliar with

the experimental section and had corrected vision above 5.0. Among them, 5 were 20-30 years old and 5 were 30-40 years old. These drivers' occupations include 2 college students, 2 teachers, 1 company employees, and 5 general publics, all with over three years of driving experience. They are not professional drivers. And maintained normal physical condition before the experiment.

According to the acquisition frequency of the eye tracker, a total of 1.8 million pieces of data were collected. The data format includes timestamp files (TXT format), log files (LOG format), and finally imported into Excel for organization. It contains data on the driver's cardiac and physiological changes and the vehicle's movement status. For example, eye shift angle, acceleration, vehicle operating speed, etc.

The experimental process is as follows:

(1) On the experimental road section, the landscape types were selected in advance and marked at the boundary of the different landscape types.

(2) After the camera, eye tracker and other instruments were calibrated, the driver adjusts the height of the driving position. The driving test began. When the speed limit was not exceeded, the test driver could freely choose the driving speed he thinks is comfortable. During the whole process of the test, the tested driver could also adjust the speed according to the traffic conditions. The test driver drove continuously from the beginning of the experimental road section to the end, and the instrument recorded the driver's visual and physiological parameters. A trainman in the car records the range of stake numbers of different road landscapes for verification during data processing. After arriving at the destination, the test driver rested for 3 to 5 minutes to conduct the return test. The content to be recorded was the same.

(3) After a round trip, one test driver was replaced by another test driver, and the above driving test steps were repeated until 10 test drivers completed the whole test. The picture of a driver ready in the experimental car is shown in Figure 3. Figure 4 shows real-time recording of experimental data. Figures 3 and 4 describe the process of the experiment.

Fig.3 - The tested driver in the experimental car and data monitoring
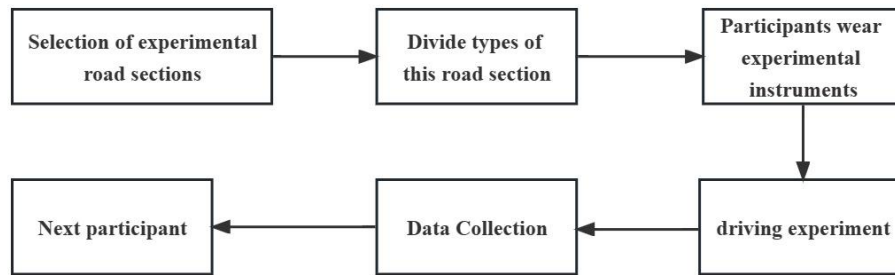
Fig.4 - Experimental process

Analysis model

The existing researchers on vision interesting areas are mainly focused on gaze behavior, including single-factor analysis of gaze indicators, cluster analysis of gaze location, etc. On the basis of the study, the dynamic clustering method is adopted in this paper to analysis the dynamic characteristics of the vision interesting area [20]. The range of driving visual interesting area was determined by the modified weighted search region calculation method.

Spatial Enclosure

When driving on the mountainous road, the driver's visual axis keeps the same direction with the tangent vector of the vehicle's motion path. At a certain speed, the driver's vision field is a nearly conical area. In landscape engineering, it believes that the driving speed, visual distance and scenery determine the degree of closed feeling brought by the landscape to the driver, which is called the space sense. The driver's space sense is expressed by the degree of space interface enclosure, and the evaluation index is the ratio H/D between the height H of the landscape or structure interface on both road sides and the horizontal distance D from the viewpoint to the roadside landscape or structure, as shown in Figure 5.
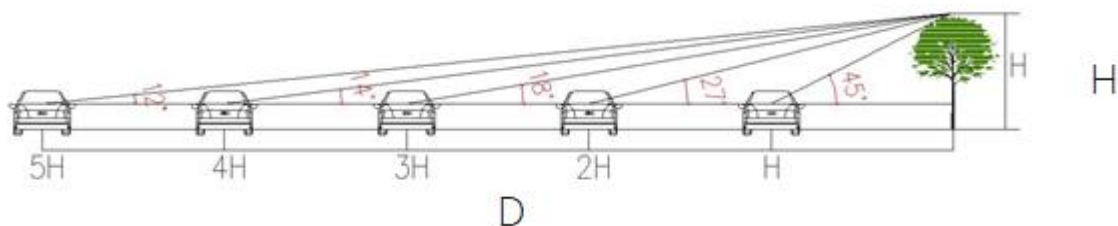
Fig.5 - the calculation of spatial enclosure

The impact of road landscape on driver visual comfort is mainly reflected in its spatial enclosure and color stimulation. In the field of landscape engineering, spatial enclosure is often used to represent the driver's sense of spatial closure, and road landscape is divided into three types——open, semi-closed, and closed, as shown in Table 1. The space enclosure is different, drivers get different feelings of space. When H/D<1:3, the driver's vision vertical angle is less than 18°, the sight line is less limited, and the vision field is relatively wide, so the driver can obtain an open space sense; when H/D>1:2, the driver's vision vertical angle is greater than 27°, and the vision field is

limited, which will produce a more closed space sense [21].

Tab. 1 - Parameters of different landscape types

Type	H/D	Vision vertical angle
Open space	≤1/3	<18°
Semi-closed space	1/3～1/2	18°～27°
Closed space	≥1/2	>27°

Markov chain theory

Set the random sequence *{X(n),n=0,1,2,…,n}* and the discrete state space be *E={0,1,2,…n}*. If for any *m* non-negative integers, $n_1, n_2, …, n_m$ (0< n_1< n_2<…< n_m) and natural number *k*, and any *{ $i_1, i_2, …, i_m$,},j∈E*. satisfy Equation 1,

$$p\left\{X\left(n_m+k\right)=j\middle|X\left(n_1\right)=i_1, X\left(n_2\right)=i_2,\cdots,X\left(n_m\right)=i_m\right\}$$
$$=p\left\{X\left(n_m+k\right)=j\middle|X\left(n_m\right)=i_m\right\}$$

（1）

{X(n),n=0,1,2,…,n} is called Markov chain.

Markov chain is a typical random process with no aftereffect, that is, the model state at time *t* is only related to its previous state time *t-1*, and independent from the previous state condition.

The driver's gaze point falls in different areas during driving. The next gaze point falls in which region is only related to the region where the current gaze located, which is a typical homogeneous Markov chain. Therefore, it is appropriate to use this theory to study the driver's gaze shift characteristics. The statistical estimation method is used to solve the driver's one-step shift probability matrix. The basic idea is to take each gaze region as a state of the Markov chain, and then calculate the shift probability between each state.

Set 1, 2, 3, 4 and 5 as the five states of the gaze point, and a_{ij} is the frequency of state *i* shiftring to state *j*. For example, a_{11} represents the frequency of the current gaze point in region 1 and the next gaze point still in region 1; a_{13} indicates the frequency of the current gaze point in region 1 and the next gaze point in region 3, and so on.

Set up

$$\sum_{j=1}^{n}a_{ij}=a_i \quad \left(i、j=1,2,\cdots,n\right)$$

(2)

then the shift probability from state *i* to state *j* is shown in Equation (3).

$$f_{ij}=\frac{a_{ij}}{a_i}, \quad \left(i=1,2,\cdots,n\right)$$

(3)

From the probability theory, when the theoretical distribution of state probability is unknown, if the sample capacity is large enough, the theoretical distribution of state can be approximately described by the sample distribution. The amount of data obtained in this vehicle test is large enough. Therefore, for the unknown gaze shift probability, the frequency can be used to approximate the shift probability. Therefore, the estimated value of shift probability from gaze region *i* to *j* is:

$$p_{ij} = \frac{a_{ij}}{a_i} \tag{4}$$

From this analysis, the shift probability matrix of the driver's gaze can be obtained by using the Markov chain.

SHIFT MODE OF DRIVING GAZE AREA

The driver's visual response characteristics are affected by the road landscape. When the road landscape is simple, the driver can easily obtain the information and have the ability to perceive the detailed landscape. When the road landscape is too complex, the driver's perception decreases, and the perception range decreases, which may ignore some important traffic information, and even cause traffic safety hazards. The driver's gaze feature is the visual psychological expression of the dynamic response to the road landscape. After screening the collected data, about 1.75 million pieces of valid data are retained for the analysis of the gaze shift characteristics of the driver's visual interesting area.

Division of driver's gaze region

Before studying the gaze shift characteristics, division of the gaze regions is needed. There are many ways to divide the gaze region of driver's vision field. In this paper, the dynamic clustering method is used to cluster the analytical coordinates of the gaze point location in the vision field. Through the analysis of the final clustering results, it is found that the distribution of driver's gaze points presents a certain clustering distribution rule. In the three types of road landscape, the distribution of gaze points is shown in Figure 5, which is placed in a two-dimensional coordinate system for quantitative analysis. It can be seen that the driver's gaze points are mainly concentrated in five regions. For each kind of road landscape, the range of the gaze point is calculated, as shown in Table 2.
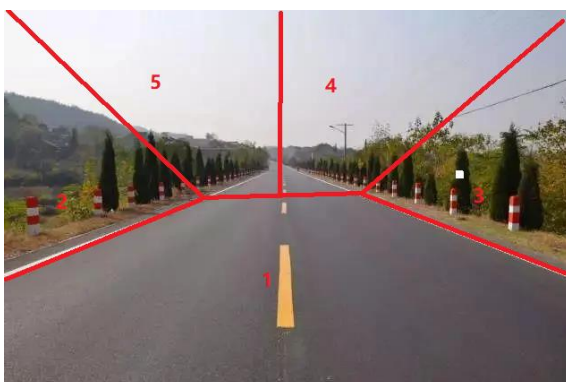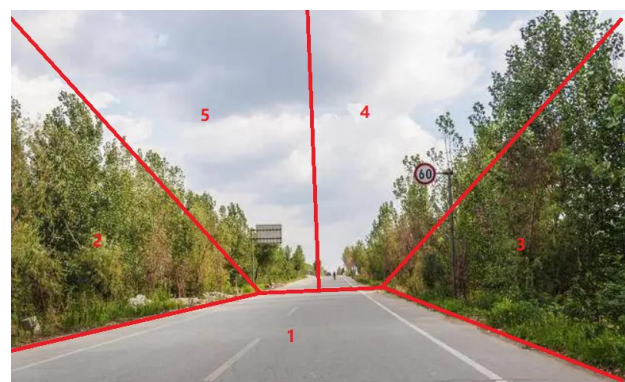
a) Open space   b) Semi-closed space

Fig.6 - Vision interesting areas
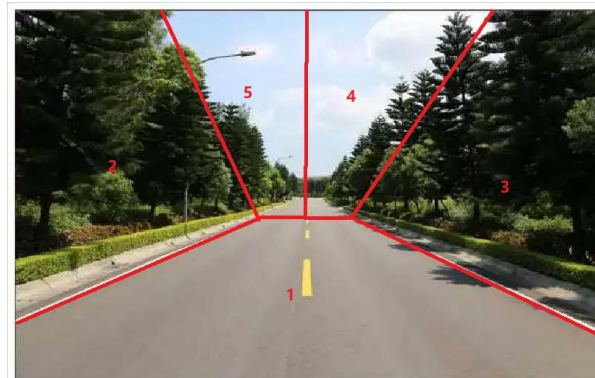
c) Closed space

Fig.6 - Vision interesting areas

Tab. 2 - Division of vision interesting areas

Number	Names for vision interesting areas	Coordinate range
1	Straight Front	$-12.36 \leq X \leq 5.42, -28.53 \leq Y \leq -12.36$
2	Near Left	$-42.62 \leq X \leq -25.81, -28.56 \leq Y \leq -7.43$
3	Near Right	$35.54 \leq X \leq 52.61, -28.46 \leq Y \leq -12.38$
4	Far Right	$0.52 X \leq 17.47, -10.88 \leq Y \leq 2.42$
5	Far Left	$-16.40 \leq X \leq -2.14, -11.37 \leq Y \leq -3.72$

The gaze data of 10 drivers in this experiment were selected for clustering and one-step Markov chain shift matrix solution. The following analyses the characteristics of gaze shift in the next step when the gaze is located in different regions.

(1) Current gaze point being in Region 1

Region 1 refers to the straight front of the driver's vision field. By analyzing the calculated data, it is found that if the driver's current gaze point is in Region 1, the probability of the next gaze point continuing to be in region 1 is the highest, and the probability of the open, semi-closed and closed landscapes is 0.829, 0.837 and 0.807 respectively, as shown in Table 3. The probability value of the next gaze point in Region 1 in the three kinds of landscapes is 0.824 on average, which means that no matter what kind of road landscape the driver drives in, most of his attention is in the straight front of the vision field, which also reflects that the straight front in the vision field is the main vision interesting area.

By comparing the probability of gaze shift in different road landscapes, it can be seen that when the current gaze is located in Region 1, different road landscape has no significant impact on the shift probability.

Tab. 3 - Probability of gaze region following current being in Region 1

	p_{11}	p_{12}	p_{13}	p_{14}	p_{15}
p	0.777	0.255	0.765	0.715	0.551
Open landscape(Average)	0.829	0.037	0.030	0.071	0.033
Semi-closed space(Average)	0.837	0.026	0.040	0.056	0.041
Closed space(Average)	0.807	0.050	0.040	0.052	0.051
Overall	0.824	0.038	0.037	0.060	0.042

(2) Current gaze point being in Region 2

Region 2 refers to the near left of the driver's vision field. Table 4 lists the results of the probability of gaze region following current gaze point being in Region 2 for three types of road landscape.

Tab 4 - Probability of gaze region following current being in Region 2.

	p_{21}	p_{22}	p_{23}	p_{24}	p_{25}
p	0.636	0.057	0.048	0.036	0.755
Open landscape(Average)	0.361	0.368	0.006	0.114	0.151
Semi-closed space(Average)	0.292	0.478	0.031	0.078	0.121
Closed space(Average)	0.288	0.564	0.013	0.048	0.138
Overall	0.314	0.470	0.017	0.080	0.137

From the Table 4, it is found that if the driver's current gaze point is in Region 2, the probability of the next gaze point is still in Region 2, and the probability of the open, semi-closed and closed landscape is 0.368, 0.478 and 0.564 respectively, with an average probability value of 0.470. If it considers the probability value of the next gaze point shifting to Region 1 (that is, $p_{21}+p_{22}$), the sum of probabilities from Region 2 to remaining and Region 1 is 0.784, the next gaze point is still basically located in straight front and near left, indicating that the driver pays more attention to the left and straight front in different road landscapes.

The one-way ANOVA of the gaze shift probability of three road landscapes was conducted, as shown in p (average value) of Table 4. It can be found that when the gaze point is located in region 2, the next gaze point is shifted to region 3 and region 4 with significant difference ($p_{23}=0.048<0.05$, $p_{24}=0.036<0.05$). For the case that the next gaze region is still in region 2, although the significance value is 0.057, it is very close to the significance level of 0.05. It can be considered that there are differences in the three types of road landscape. No matter what type of road landscape, when the current focus is in Region 2, for Region 5, that is, far from the left, the next gaze is very few, and the most focus is Region 1. The probability of gazing at Region 2, 3 and 4 next time will vary according to the landscape type. The probability of continuing to gaze on Region 2 in the closed landscape is the highest, the probability of shifting to Region 3 in the semi-closed landscape is the highest, and the probability of shifting to Region 4 in the open landscape is the highest. When located in Region 2, the driver will expand the search vision range to obtain various information beneficial to driving.

(3) Current gaze point being in Region 3

Region 3 refers to the near right of the driver's vision field. The results are shown as Table 5.

Tab. 5 - Probability of gaze region following current being in Region 3

	p_{31}	p_{32}	p_{33}	p_{34}	p_{35}
p	0.109	0.048	0.801	0.388	0.732
Open landscape(Average*)*	0.259	0.025	0.428	0.144	0.144
Semi-closed space(Average*)*	0.116	0.078	0.435	0.179	0.192
Closed space(Average*)*	0.127	0.107	0.407	0.201	0.158
Overall	0.167	0.070	0.423	0.175	0.165

From Table 5, it is found that if the driver's current gaze point is in Region 3, the probability of the next gaze point continuing to be in Region 3 is the highest, and the probability of the open, semi-closed and closed landscape is 0.428, 0.435 and 0.407 respectively, with an average value of 0.423. It indicates that the driver needs to repeatedly gaze on this region to obtain sufficient visual traffic information. If it considers the probability of the next gaze point shifting to Region 1, 4 and 5 ($p_{31}+p_{34}+p_{35}$), the average of the total probability sum in the three road landscape spaces is 0.507, indicating that the driver's gaze point will have a high probability of returning to the straight front after staying near right. It is verified that the driver's vision interesting area is mainly in the front region of the vision field.

The one-way ANOVA of the gaze shift probability of three road landscapes shows that when the gaze point is located in Region 3, there is a significant difference between the three landscapes when the next gaze point is shifted to Region 2 ($p_{32}=0.048<0.05$), that is, the dynamic attention of different landscapes on the left and right sides is different, and the next gaze point is shifted to other regions in different road landscape has no significant difference.

(4) Current gaze point being in Region 4

Region 4 refers to the far right of the driver's vision field. The results are shown as Table 6.

Tab. 6: Probability of gaze region following current being in Region 4

	p_{41}	p_{42}	p_{43}	p_{44}	p_{45}
P	0.589	0.010	0.678	0.039	0.567
Open landscape(Average*)*	0.290	0.155	0.053	0.348	0.154
Semi-closed space(Average*)*	0.216	0.200	0.035	0.379	0.170
Closed space(Average*)*	0.205	0.087	0.078	0.440	0.190
Overall	0.237	0.147	0.055	0.389	0.171

By comparing and analyzing the data in Table 6, it is found that if the driver's current gaze point is in Region 4, the probability of the next gaze point is still in Region 4 of the open, semi-closed and closed landscapes is 0.348, 0.379 and 0.440 respectively, with an average value of 0.389. If the probability values of the next gaze point shift to Regions 1, 4 and 5 are added ($p_{41}+p_{44}+p_{45}$), the average value of the sum of the probabilities is close to 0.8. It shows that the main source for drivers to obtain traffic information in the mountainous road landscape is the region in front of the vision field, and the gaze constantly shifts dynamically between the far ahead and the near ahead to obtain the required traffic information.

When the gaze point is located in Region 4, there are significant differences in the three landscapes while the next gaze point shifts to Region 2 and 4 ($p_{42}=0.010<0.05$, $p_{44}=0.039<0.05$).

When representing different landscape types, the dynamic attention to the central region is different. There is no significant difference in different landscape types when the next gaze shifts to other regions.

(5) Current gaze point being in Region 5

Region 5 refers to the far left of the driver's vision field. Table 7 lists the results of the difference experiment analysis of the three types of road landscape.

Tab. 7 - Probability of gaze region following current being in Region 5

	p_{51}	p_{52}	p_{53}	p_{54}	p_{55}
p	0.748	0.879	0.205	0.045	0.692
Open landscape(Average*)*	0.300	0.004	0.004	0.057	0.635
Semi-closed space(Average*)*	0.288	0.007	0.000	0.102	0.603
Closed space(Average*)*	0.246	0.013	0.031	0.178	0.532
Overall	0.278	0.008	0.012	0.112	0.590

If the driver's current gaze point is in Region 5, the probability of the next gaze point still in region 5 is the highest, and the probability of the open, semi-closed and closed landscapes is 0.635, 0.603 and 0.532 respectively, with an average value of 0.590. If the probability value ($p_{51}+p_{54}+p_{55}$) of the next gaze point moving to Regions 1, 4 and 5, the mean value of the probabilities sum in the three types of landscapes is 0.90, which shows that the probability of gaze shifting from the far ahead to the near left and right sides is small, indicating that the driver pays less attention to the roadside vision when driving normally.

The gaze shift probability of three type landscapes is analyzed by one-way ANOVA. From the test results, it can be found that when the gaze point is located in the Region 5, there is a significant difference in the three type landscapes when the next gaze point is shifted to the Region 4 ($p=0.045<0.05$), indicating that the dynamic adjustment of the gaze point in front of the vision field is different in different landscape. In the closed landscape, the probability of the next gaze region in Region 4 is the largest, which indicates that in the more depressed closed mountainous road landscape, the driver continues to seek useful driving information in the far left and the far right directions, reflecting the driver's desire to escape from this closed landscape.

ANALYSIS OF GAZE STATIONARY DISTRIBUTION

The driver's gaze moves back and forth between different vision interesting areas, and there is a time stay in each vision interesting region. So how to calculate the probability of stay in each region is also a quantitative content to determine the overall distribution. Therefore, the method of Markov stationary distribution is proposed.

Markov stationary distribution is a prediction method. It refers to that after a long time, the probability of gaze points assigned to each region can reach a stable value. After the gaze probability of each region is obtained by using the Markov chain, it is more convenient to calculate the stationary distribution vector of gaze shift according to the probability matrix and other data, so as to obtain the gaze probability of each region.

Markov chain stationary distribution

Set $\{X_n, n \geq 0\}$ be a homogeneous Markov chain, the state space is E, the shift probability is P_{ij}, and there exist probability distribution is $\{\pi_i, j \in E\}$, if Equation (5) is satisfied.

$$\begin{cases} \sum_{i \in E} \pi_j = 1, \ \pi_j \geq 0 \\ \pi_j = \sum_{i \in E} \pi_i p_{ij} \end{cases} \tag{5}$$

Then, $\{\pi_i, j \in E\}$ is the stationary distribution of the Markov chain.

Set Markov chain $\{X_n, n \geq 0\}$, finite state space $E=\{1,2,\dots,s\}$, if there is a positive integer n_0, so that there is $P_{ij}^{n_0}$ for all $i, j \in E$, then the Markov chain is ergodic. At this point, there is Equation (6).

$$\lim_{n \to \infty} p_{ij}^{n_0} = \delta_j \tag{6}$$

The ergodicity of the Markov chain shows that after a period of time, the system reaches a stable state, that is, for a certain state, the Markov chain starts from i at the initial time, and the probability of reaching j is close to δ_j through a long time shift.

According to the nature of the Markov chain, the Markov chain established for the gaze shift of 10 drivers in the driving experiment in this paper is irreducible and non-periodic, so its Markov chain has a stable distribution.

Solution of gaze stationary distribution

According to the definition of the stationary distribution of the Markov chain, the six-variable linear equation system can be established for the one-step shift probability matrix of each driver's gaze, as shown in Equation (7).

$$\begin{cases} \left\{ \left[P^T - diag\left(1,1,1,1,1,1,\right) \right] \right\} \pi = 0 \\ \sum_{i=1} \pi_i = 1 \end{cases} \tag{7}$$

Using the IML program of SAS statistics, it can solve the stationary distribution vector of gaze shift of drivers in different road landscapes. SPSS was used to conduct one-way ANOVA on the stationary distribution of gaze shift in three landscape types, as shown in Table 8.

Tab. 8 - Difference test of stationary distribution of gaze shift

	δ_1	δ_2	δ_3	δ_4	δ_5
p	0.099	0.527	0.280	0.002	0.438
Open landscape(Average)	0.447	0.100	0.112	0.150	0.191
Semi-closed space(Average)	0.418	0.093	0.105	0.189	0.195
Closed space(Average)	0.426	0.122	0.073	0.176	0.203
Overall	0.430	0.105	0.097	0.172	0.196

From the test results, it can be found that all drivers have the highest gaze probability in Region 1, that is, straight front of the vision field. The probability of open, semi-closed and closed landscapes is 0.447, 0.418 and 0.426 respectively, with an average value of 0.430. If the probability values of

gaze distribution in Region 1, 4 and 5 are considered at the same time, the average value of the sum of probability in the three landscapes types is close to 0.80, indicating that the main source of traffic information obtained by drivers in the mountainous road landscape is the area in front of the vision field. The gaze constantly shifts between the far ahead and the near ahead to search for traffic information.

When the gaze points are distributed in Region 4, there is significant differences among the three landscapes. The different landscape of the mountainous road affects the driver's gaze on the far right. There was no significant difference in the gaze point distribution of drivers in other regions.

CONCLUSION

The driver's gaze parameters in the mountainous two-lane road landscape are collected in driving experiments. Through the analysis of gaze dynamic shift, the following conclusions are obtained.

(1) When the gaze point is in the straight front, the average probability of no gaze shift in the open, semi-closed and closed landscapes is 0.824, which means that the driver's attention is mostly near the straight front of the vision field no matter what kind of landscape he drives in. This also reflects that the straight front of the driver's vision field is the main vision interesting area.

(2) If the driver's current gaze point is located in near left, the next gaze point is still basically located in straight front and near left, which means that the driver pays more attention to the left and straight front in different mountainous road landscapes.

(3) After the driver's gaze stays near right, the probability of returning to the straight front is high, which verifies that the driver's vision interesting area is mainly in the area in front of the vision field, and that the dynamic attention of the left and right sides in different road landscape is different. The gaze constantly shifts dynamically between the far ahead and the near ahead to obtain the required traffic information.

(4) The open landscape has the highest gaze probability for the straight front area and the near right area. The closed landscape has the highest gaze probability for the near left area and the far left area, while the semi-closed landscape has the highest gaze probability for the far right area. The different landscape types in the mountainous road area affect the driver's gaze on the far right.

ACKNOWLEDGEMENTS

REFERENCES

[1]   Thiffault P, Bergeron J. 2003 Monotony of road environment and driver fatigue: a simulator study[J]. Accident Analysis & Prevention, vol.35(3): 381-391.DOI:10.1016/s0001-4575(02)00014-3.

[2]   Xiaolei Li,Boming Tang,Qianghui Song. 2017. ANALYSIS ON THE INFLUENCE OF ACCUMULATION EFFECT OF LANDSCAPE COLOR ON TRAFFIC SAFETY IN THE FOGGY SECTIONS OF EXPRESSWAYS[J]. Civil Engineering Journal. 2017(3):222-236. DOI：10.14311/CEJ.2017.03.0020.

[3]   Meng Y.W, Cai H.Q, Chen L, et al. 2022, Research on driving visual comfort of two-lane mountainous road based on traffic safety evaluation[J]. Engineering Reports,e12561. DOI:10.1002/eng2.12561.

[4]   Qin Y.Q, Zhao P.Y, Xie J.M, et al. 2022, A Review of Research on Driver's Visual Load.[J]. Journal of Kunming University of Science and Technology(Natural Science) ,vol.47(06):137-153. DOI:10.16112/j.cnki.53-1223/n.2022.06.481.

[5]   Jeong-Hun M, Landphair H C, Naderi J R. 2006, Landscape improvement impacts on roadside safety in Texas. [J]. Landscape and Urban Planning, 78(3):263-274. DOI10.1016/j.landurbplan.2005.09.002.

[6]   Shan Bao, Linda Ng Boyle. 2009, Age-related differences in visual scanning at median-divided highway intersections in rural areas[J]. Accident Analysis and Prevention, 41(1): 146-152. DOI:10.1016/j.aap.2008.10.007.

[7]   Yamada T, Matsuura K, Takeuchi H, et al. 2022.TOWARD BETTER DRIVING WITH GAZE AWARENESS ENVIRONMENT SUPPORTED BY AREA SEGMENTATION[J]. Proceedings of the 19th International Conference on Cognition and Exploratory Learning in the Digital Age, CELDA 2022.49-56.

[8]   Drusch G, Bastien J M C, Dinet J. From gaze plots to eye fixation patterns using a clustering method based on Hausdorff distances[C]//Proceedings of the 23rd Conference on l'Interaction Homme-Machine. 2011: 1-7. DOI: 10.1145/2044354.2044356.

[9]   Saha B, Islam M J, Dipto A S, et al.2021. An Efficient Approach for Appearance Based Eye Gaze Estimation with 13 Directional Points[C]. IC4ME2. IEEE, 2021: 1-5. DOI:10.1109/IC4ME253898.2021. 9768643

[10]   Watling C N, Home M.2022. Hazard perception performance and visual scanning behaviours: the effect of sleepiness[J]. Transportation research part F: traffic psychology and behaviour,vol. 90: 243-251.DOI: 10.1016/j.trf.2022.08.020

[11]   Brueggemann S, Chan A B, Hsiao J H W.2016. Hidden Markov Modeling of eye movements with image information leads to better discovery of regions of interest[C].Proceedings of the 38th Annual Conference of the Cognitive Science Society, CogSci 2016.1032-1037, 2016.

[12]   Nilsson E J, Victor T, Aust M L, et al.2020. On-to-off-path gaze shift cancellations lead to gaze concentration in cognitively loaded car drivers: A simulator study exploring gaze patterns in relation to a cognitive task and the traffic environment[J]. Transportation research part F: traffic psychology and behaviour, vol.75: 1-15. DOI:10.1016/j.trf.2020.09.013

[13]   Meng Y.W, Chen L. 2020 ,Research on the calculation method of driving visual information on mountain roads [J]. Transportation System Engineering and Information, vol.20 (05): 45-50+63. DOI:10.16097/j.cnki.1009-6744.2020.05.007.

[14]   He S.M, Du Z.G, Han L, et al,2022, Research on driver's gaze behavior characteristics in urban tunnel diversion area [J]. Journal of Wuhan University of Technology (Traffic Science and Engineering Edition), vol.46 (02): 230-234+241.

[15]   Ghosal D, Kolekar M H. 2020. Visual Interest Prediction with Attentive Multi-Task Transfer Learning[J]. arXiv preprint arXiv:2005.12770. E-ISSN:23318422.

[16]   Morales A, Costela F M, Woods R L.2021. Saccade landing point prediction based on fine-grained learning method[J]. IEEE Access, vol.9: 52474-52484. DOI:10.1109/ACCESS.2021.3070511.

[17]   Christofano R M, Junior M, Estecio W, et al. 2021. PlaceProfile: Employing visual and cluster analysis to profile regions based on points of interest[C].//Proceedings Of The 23rd International Conference On Enterprise Information Systems (iceis 2021), Vol 1. Scitepress, 506-514. E-ISSN:21844992.

[18]   Lee Y C, Lee J D, Ng Boyle L. 2007, Visual attention in driving: The effects of cognitive load and visual disruption[J]. Human Factors, vol.49(4): 721-733. DOI:10.1518/001872007x215791

[19]   Shih Hsuan Huang, Jinn Tsai Wong.2015, A multinomial choice model approach for dynamic driver vision transitions [J]. Accident Analysis and Prevention, vol.74: 107-117. doi: 10.1016/j.aap.2014.10.010.

[20]   Meng Y W, Wen L, Liu T, et al. 2023, Research on catastrophe progression of driving load in mountainous road based on visual and environmental characteristics[J]. Engineering Reports,vol. 5(1): e12554.DOI:10.1002/ENG2.12554.

[21]   Deng Weidong, et al. 2011. Highway Landscape Planning and Cons [M]. China Communications Press.chapter 3.

EXPERIMENTAL STUDY ON REAL BRIDGE BEFORE AND AFTER SIMPLY SUPPORTED-CONTINUOUS REINFORCED CONCRETE HOLLOW SLAB

Bowen Hu[1], Jianxi Yang[1]*，Quansheng Sun[1]*，Chao Zhang[1]

1. Department of Civil Engineering, Northeast Forestry University, Harbin，
150040, China; sunquansheng @nefu.edu.cn

ABSTRACT

This article studies a concrete hollow slab simply supported-continuous actual engineering project in a certain city. Before the reinforcement of the bridge, there were cracks and exposed rebars, etc. In order to ensure the safe operation of the bridge, a reinforcement method of simply supported-continuous was adopted, prestressed steel strands are used to convert the simple-supported structure into a continuous structure, thereby improving the structural load-bearing capacity and overall integrity. Through conducting comparative analysis of load tests on a bridge before and after reinforcement, this article studies the improvement effect of the simply-supported-to-continuous reinforcement method on the bearing capacity of the bridge. A finite element model of the bridge was established, and comparative analysis was carried out before and after the reinforcement of the bridge. The bearing capacity and work performance of the bridge structure were evaluated. The research shows that the simply supported-continuous reinforcement method has a good improvement effect on the load-bearing capacity of the concrete hollow slab and can be used to improve the insufficient load-bearing capacity of the concrete hollow slab bridge in the city.

KEYWORDS

Concrete hollow slab, Simply supported-continuous, Old bridge strengthening, Finite element analysis, Static load test

INTRODUCTION

Current status of research

With the rapid development of economic construction, bridges have taken on increasingly heavy transportation tasks. The cost of bridge reinforcement and maintenance is 20% to 30%[1] of the cost of building a new bridge. Adopting a reasonable reinforcement method can not only effectively improve the bearing capacity of the bridge, but also has good economic and time benefits [2].

The prestressed concrete hollow slab beam bridge is widely used in China. Many of the bridges built in the early stage have cracks, damages, corrosion of steel reinforcement or strand, hinge joint failure and other bridge faults , resulting in bridge bearing capacity decreased. It cannot meet the needs of transportation development [3]. Therefore, adopting reasonable reinforcement measures to improve the bearing capacity and durability of the bridges and utilizing existing resources to ensure that the existing bridges with defects can still play their role is an important issue that engineers need to solve urgently.

Most of the time, the reinforcement measures are focused on the upper structure of the old bridges. The common reinforcement methods mainly include the steel plate bonding reinforcement method [4], the prestressed rod reinforcement method [5], changing structural system reinforcement method, etc. The "first simple support then continuous structure system" was proposed by the Portland Concrete Association through research on the arrangement of continuous steel bars in the bridge deck panel above the bridge pier and the concrete transverse partition between the two prestressed beams at the end of the precast beams [6]. The method is to transform the old bridge by setting up

temporary supports, pouring continuous segments, and then removing the temporary supports to achieve the transformation of the structure system. In order to improve the problem of insufficient bearing capacity of the bridge, this paper combines practical engineering to reinforce the hollow slab beam bridge by changing the structure system, converting its original simple support system into a continuous system, improving the stress status of the structure system, and enhancing the overall integrity of the structure. In order to study the performance of the reinforcement technology, a finite element analysis model of the whole bridge was established to compare the experimental results with the calculation values, analyze and evaluate the effect of the simply supported-continuous reinforcement technology on the improvement of the bridge bearing capacity.

Overview of the test bridge

The lower structure of a prestressed concrete hollow slab bridge in a certain city adopts a four-pillar concrete bridge pier and column bridge abutment, with pile foundations. The bridge has 21 plates per hole, and the span combination is 4x16m. The total width of the bridge is 20.5m, and the design load level adopts the China Bridge General Design Specification for highway-I Level Load. The bridge elevation view is shown in Figure 1.
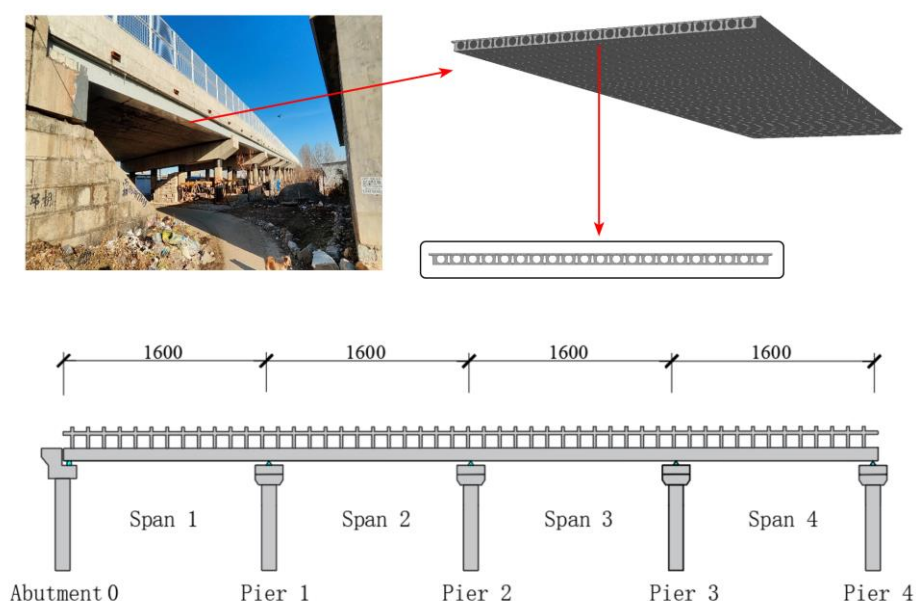
Fig.1 - Bridge type layout (unit: cm)

After many years of operation, the bridge has developed many diseases, such as multiple tensile cracks at the bottom of the beam, seepage and alkali, bearing disengagement, longitudinal cracks have appeared at the location of the negative bending moment at the top of the pier and at the mid-span position, scaling of concrete, water erosion at the corresponding drain hole of some edge plates, etc. Among them, the longitudinal cracks at the bottom of the hollow slab beam are shown in Figure 2.
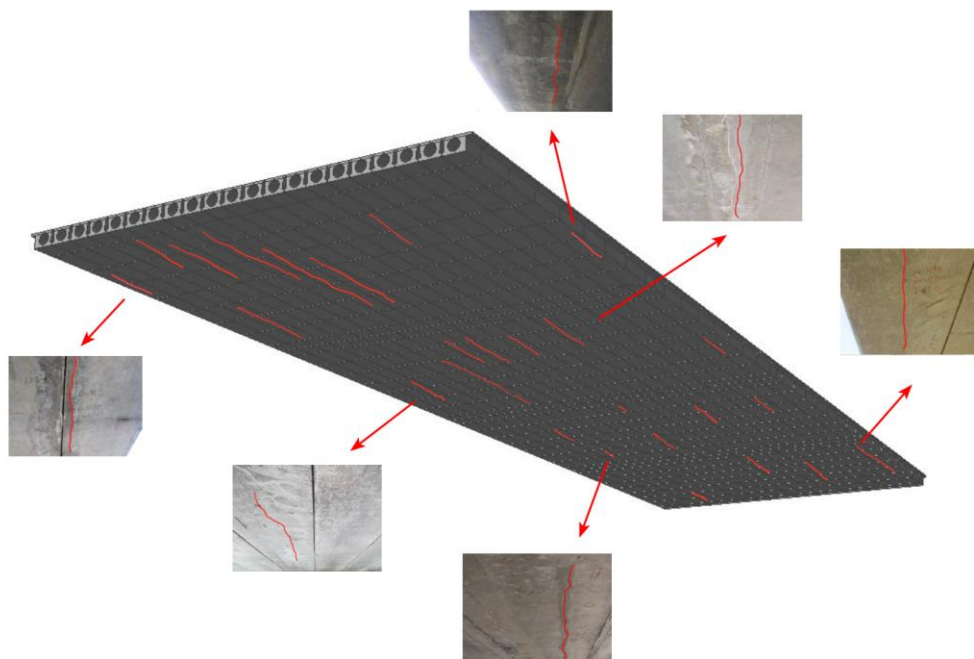
Fig.2 - Diagram of main crack diseases

There are 84 hollow slab beams in the bridge, of which 15.5% have longitudinal cracks at the bottom, with a length of 0.9m to 10m and a width of 0.06 to 0.15mm. The width does not exceed the limit value of the specification. Due to the long-term action of bending moments, concrete cracks of varying degrees may occur at the joints, but the resisting moment will also increase accordingly. Therefore, reinforcing or not reinforcing at the continuity joint may both lead to cracking[7]~[8]. 18% of the hinge joints have seepage and alkali diseases; 12 abutments have partial dislocation, there are 12 support abutments partial void in the whole bridge, 5% of the pier covers have vertical cracks at the top of the bending moment and mid-span position, with a length of 0.2 to 1m and a width of 0.06 to 0.20mm. The width does not exceed the limit value of the specification. The end position of the bent cap is subjected to water erosion, 10% of the bent cap end is concrete scaling, and the steel bars are corroded. Some piers have water erosion and steel bar corrosion expansion at the lower part, and vertical cracks in the concrete.

METHODS

Reinforcement measure

The reinforcement measures mainly aim to enhance the bridge's stability and strength by converting the hollow plates on both sides of the original bridge into solid plates, transforming the simple support system into a continuous structural system. Increasing the shear resistance of the cross-section and adding shear stirrups improve the shear capacity of the plate ends.

The main reinforcement method is to first remove the bridge pavement, chip away the concrete from the top slab and ends of the hollow slab, then insert reinforcement bars and thread prestressed steel strands into the hollow slab cavity, pour in concrete, and tension the prestressed steel strands after the concrete reaches the design strength. The prestressing steel used is high-strength low-relaxation galvanized steel strand with a tensile strength of 1860 MPa, nominal diameter of 15.2 mm, and nominal cross-sectional area of 140 mm. The prestressed steel strand N1 has a control stress of 1395MPa when anchored and pulled, and the prestressed steel strand N2 has a control stress of 1209MPa when anchored and pulled. The hollow slab cavity on both sides of the original bridge deck

is filled to become a solid slab, increasing the shear section and adding shear stirrups to improve the shear bearing capacity at the slab ends. The bridge deck is removed and relaid, and the concrete paving layer is thickened to improve the overall integrity of the structure and reinforce the transverse force of the bridge. The main reinforcement process is shown in Figure 3.
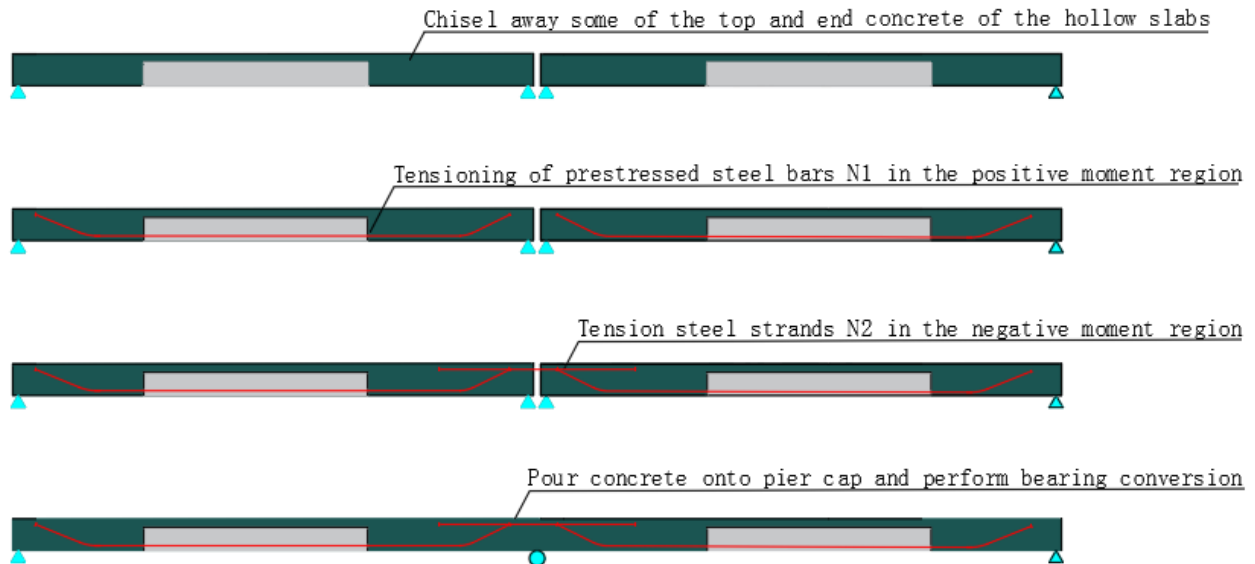
Fig.3 - Reinforcement process flowchart

The hollow slab at the top of the pier is connected with prestressed steel strands, converting the simple support system into a continuous structural system to improve the structural stress condition and increase the overall integrity of the structure. External pre-stressing is set inside the hollow slab cavity to increase the bearing capacity of the hollow slab. The cavity at the continuous end within a range of 5.5m on one side and at the simple support end within a range of 4m is filled with solid slab, converting the simple support system into a continuous system, reducing the bridge bending moment and improving the structure's shear resistance.
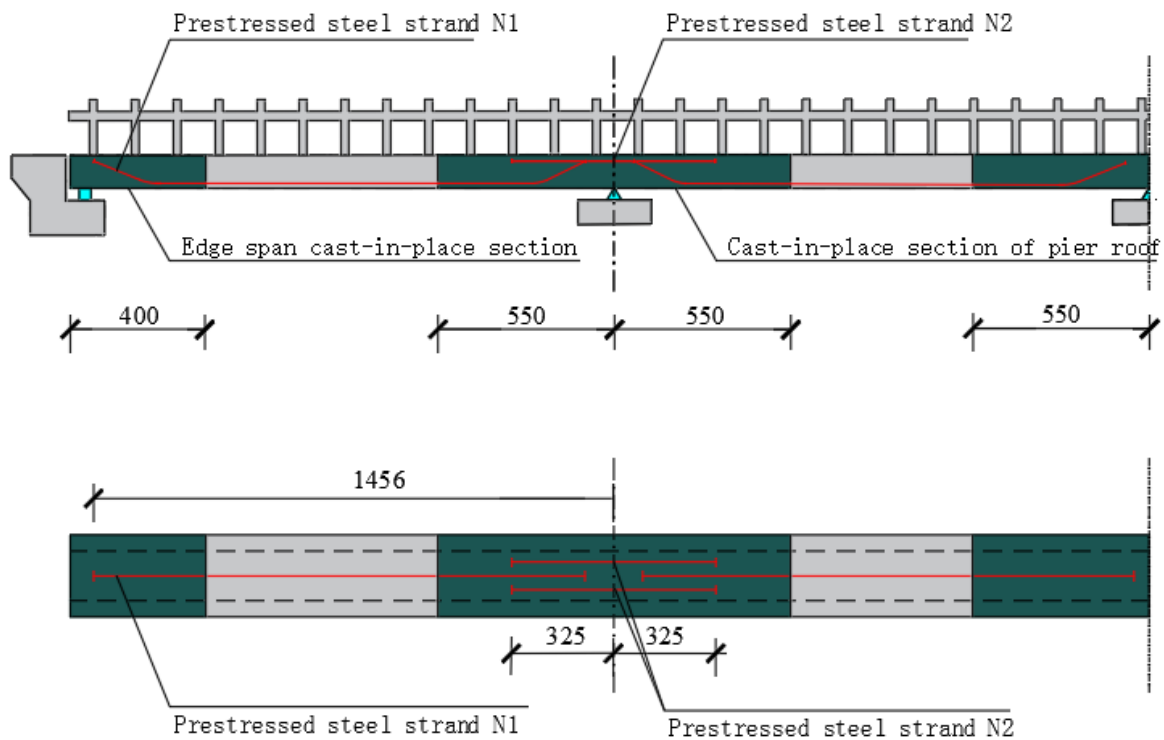
Fig.4 - Prestressed steel strand layout diagram (unit: cm)

Establishment of finite element model

Based on the original bridge design drawings, a three-dimensional finite element calculation model of the original bridge state was established through the finite element analysis software Midas/Civil, and a comparison was made between the new and old structures to perform simulation and analysis of the structure[9]. Before reinforcement, the 1x16m prestressed concrete simple-supported hollow slab was modelled with 597 nodes and 588 elements, as shown in Figure 5. After reinforcement, the 4x16m prestressed concrete continuous hollow slab was modelled with 1901 nodes and 2100 elements, as shown in Figure 6.
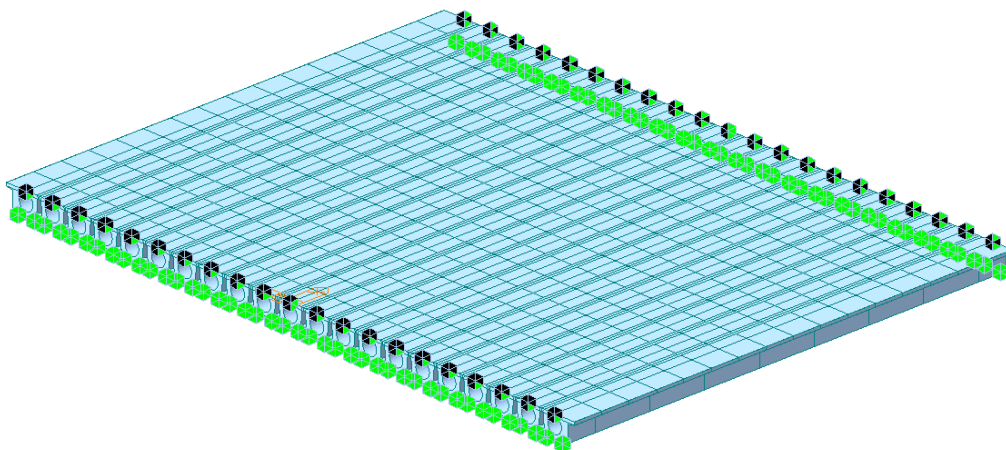
Fig.5 - Diagram of finite element model (before reinforcement)

6.
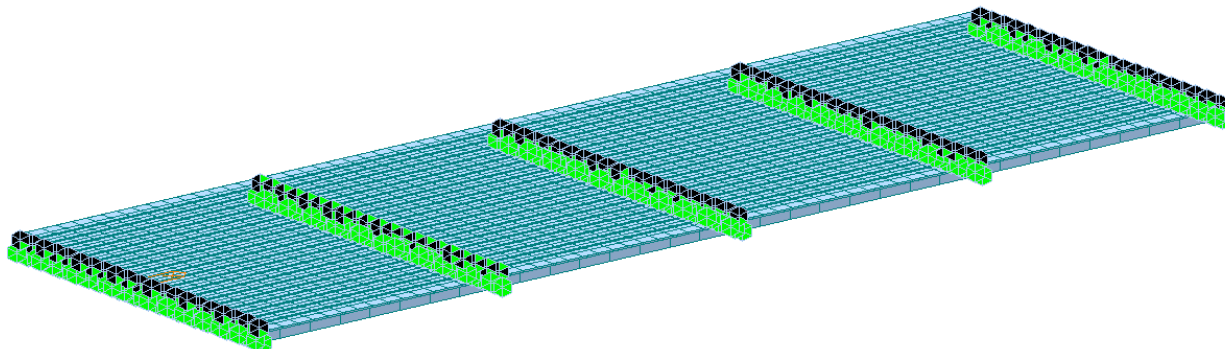
Fig.6 – Diagram of finite element model (after reinforcement)

The finite element software simulates the original bridge using material parameters and structural parameters provided by the completed bridge. The influence of highway- I level load design loads, total weight of the structure, second-phase dead loads, prestressed steel bars, shrinkage creep, non-uniform settlement, and temperature loads on the theoretical model is also taken into consideration. The material parameters can be found in Table 1.

Tab.1: Main material parameter table

Material	Volumetric weight（kN/m^3）	Elastic modulus（MPa）	Ratio
C40 concrete	25.0	3.5×10^4	0.15
prestressed steel strand	78.5	1.95×10^5	0.3

Comparative analysis of the model before and after reinforcement

Before reinforcement, the model is simulated using a damage calculation model. The damage calculation model simulates the actual damage state of the bridge by adjusting the rigidity of the bridge model and the prestress[10]. To accurately simulate the degree of damage to the bridge, the most representative bridge damage model of the actual state is determined by comparing different working conditions and the actual state of the bridge.

1.Selection of damage condition of model before reinforcement

According to the analysis of parameters, reliable impact parameters are selected and the following working conditions with different damage states are proposed. The experimental condition of span cracking can be seen in Table 2.

Tab. 2: Cracking damage condition

Condition	Damage state description
1	no damage, no stress reduction
2	stiffness reduction 10% + prestress reduction 10%
3	stiffness reduction 10% + prestress reduction 20%
4	stiffness reduction 10% + prestress reduction 30%
5	stiffness reduction 20% + prestress reduction 10%

All working conditions are in the same combination: dead load + secondary steel strand + secondary creep + secondary shrinkage + temperature load deflection values are compared with the actual measured deflection values to obtain a more realistic bridge damage model.

2. Determination of damage model

(1) Under the requirement of engineering survey level 2 conduct a composite level measurement and obtain the deflection value of each section by comparing the elevation difference between the measured elevation and the design elevation of each section. It can be seen from the data that the deflection at the mid-span of the bridge edge span is severe, and the maximum deflection value at the mid-span of the slight crack model reaches 12.7mm.

(2) Deflection analysis: Based on the damage calculation model, analyze the deflection under the same unfavourable loads. The deflection values of each calculated working condition are shown in Figure 7.
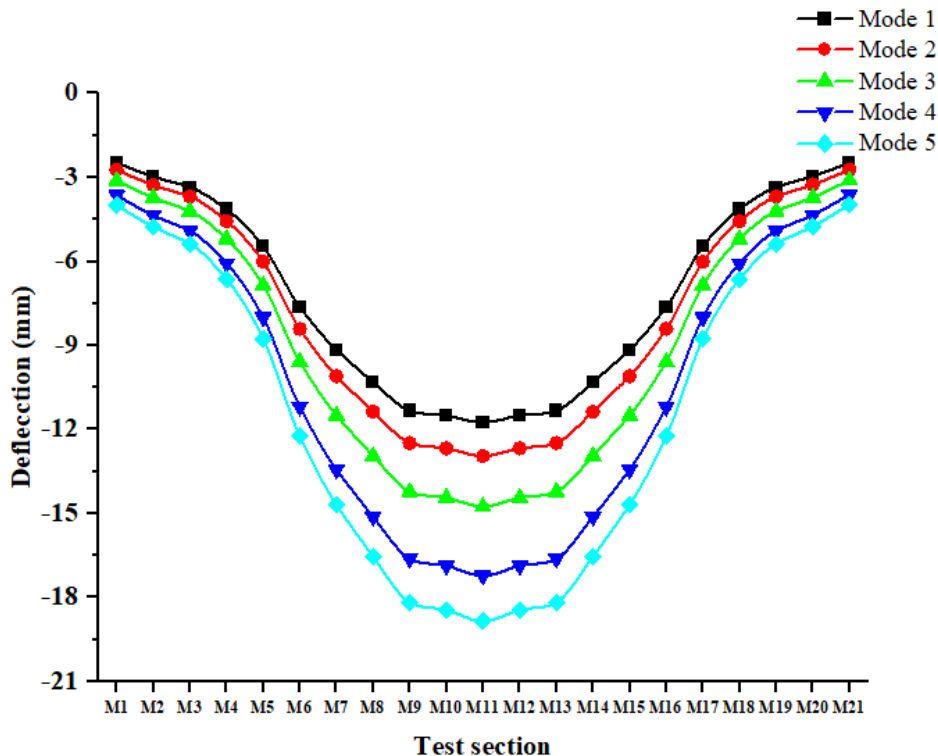
Fig.7 - Deflection value of cracking

As shown in Figure 7, under cracking conditions, the deflection value of the model in working condition two (10% reduction in stiffness + 10% reduction in prestress) is 14.09mm, which is more in line with the actual bridge situation. Therefore, working condition two (10% reduction in stiffness + 10% reduction in prestress) is adopted as the damage model of the bridge before strengthening in the cracking state.

2.Comparative analysis of theoretical values before and after reinforcement

In this section, a comparison analysis is made between the theoretical strain values and deflection values of the damaged model before reinforcement and the model after reinforcement. The result shows the improvement in the load-bearing capacity of the bridge after simple-support continuous reinforcement. The theoretical deflection values of the models before and after reinforcement can be seen in Table 3 and shown in Figure 8.

Tab.3: Comparison of results before and after reinforcement

/	Before (simple support beam)	After (continuous beam)	Ratio
Max bending moment/ (kN· m)	387.0	315.1	22.8%
Max shear /kN	5503.4	4566.9	20.5%
Max deflection/mm	12.94	8.72	32.6%

8.
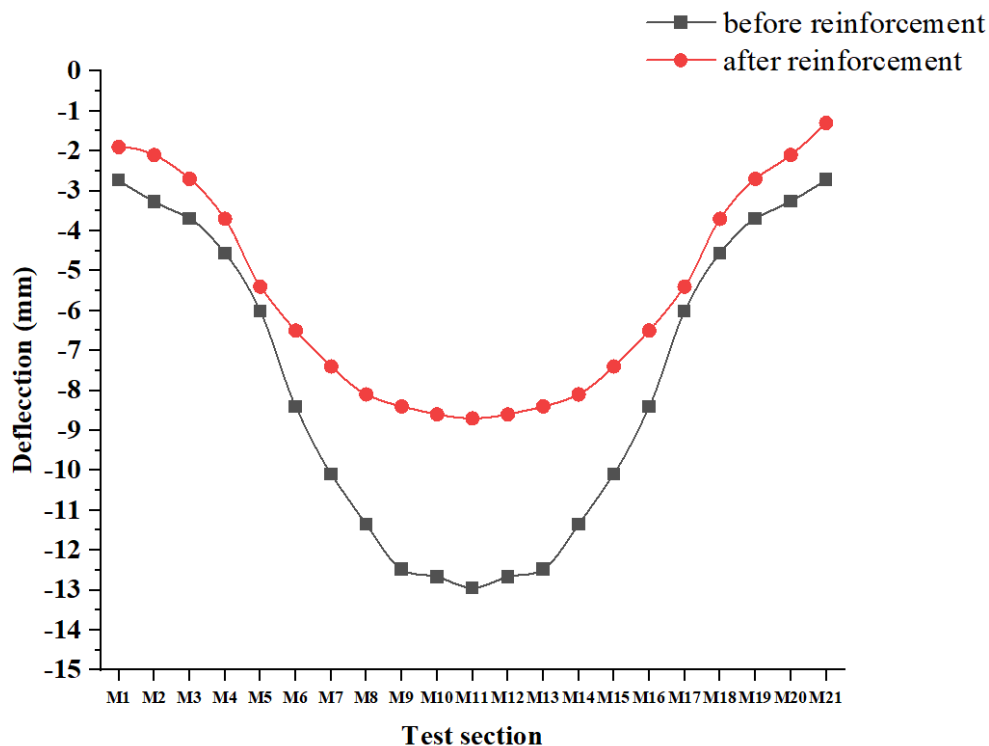
Fig.8 - Comparison chart before and after reinforcement

According to the comparison of the results in Table 3, it can be seen that the simple-supported to continuous reinforcement can effectively enhance the bearing capacity of the bridge, reduce the maximum deflection, and at the same time, the maximum shear force of the continuous beam is significantly increased compared to the simple support beam [11].

Static load test

In order to comprehensively evaluate the performance of the bridge under simple-supported to continuous reinforcement, static load tests are conducted on the bridge before and after reinforcement, respectively. This test measures the structural response of the bridge under static load and verifies the actual performance of the bridge structure [12]. By comparing the theoretical data before and after reinforcement with the experimental data, the actual stress state of the bridge is analyzed, and the improvement of the structural stress and the degree of improvement in structural performance after reinforcement are observed [13].

The static load tests are performed on the most unfavourable cross-section of the main beam under test load, using the JM3812 wireless static strain testing and analysis system and the SDL1X21S-C1 precision level instrument. The arrangement of test points is shown in Figure 9.9a and Figure 9.9b.

Static load test before and after reinforcement to measure the deflection and strain of main girder under test load. Dial indicator and digital strain gauge are used for testing. The arrangement of measuring points is shown in Figure 9.9c.
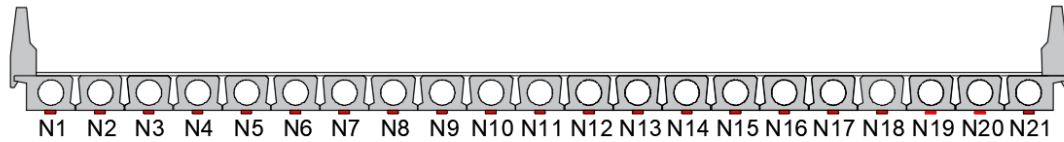
(a) The layout diagram of strain measuring points （▬ is strain measuring points）
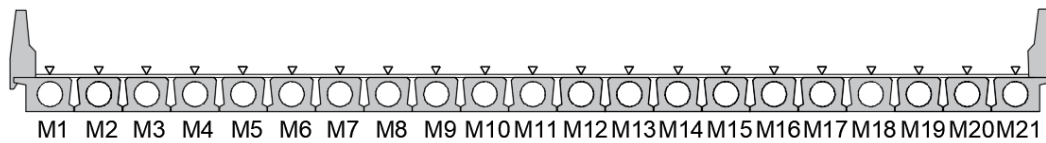
(b) The layout diagram of deflection measuring point （▽ is deflection measuring point)
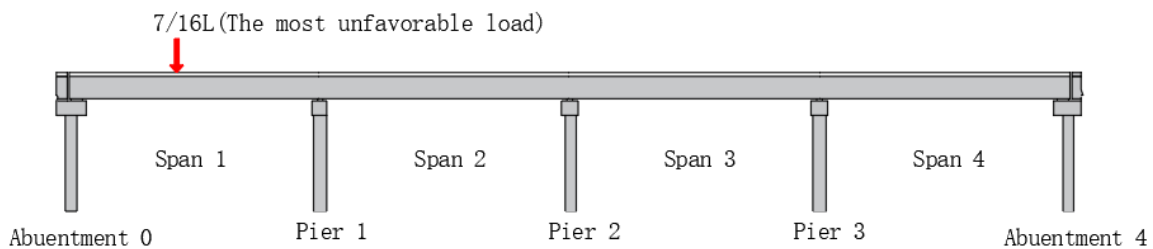
(c) Layout diagram of elevation measuring points

Fig.9 - Deflection and stress test sections

Two static load tests were conducted using the same model and tonnage of test vehicles. The most unfavourable effect of vehicle live load under controlled load should be simulated when selecting test vehicle tonnage. Since the design load of the bridge is highway- I level, highway- I level load is used as the control load in the test. Through the finite element software simulation calculation, it is proposed that four 45 tons vehicles be placed in parallel to simulate the effect of highway-I live load. The test load efficiency is calculated to be 1.01, which is in line with the loading efficiency range of 0.95~1.05 in the (Load Test Code for Highway Bridges) JTG/T J21-01-2015 [14]. Test is divided into medium load condition and partial load condition. Due to the similar conclusions, this paper only describes the medium load conditions[15]~[17], and the test conditions are shown in Table 5. The specific information of the loading vehicles is shown in Table 6, and the bridge load test schematic diagram is shown in Figure 10.

Tab.5: Test conditions

Condition	test conditions	loading position	load efficiency
1	the span 1 7/16L	Span 1 7m	1.01

Tab.6: Loading vehicle specification table (unit: kN)

Vehicle	Front axle	Middle axle	Rear axle	Total
1	90.1	180.2	180.2	450.5
2	90.0	180.2	180.1	450.3

Vehicle	Front axle	Middle axle	Rear axle	Total
3	89.8	179.6	179.5	448.9
4	90.1	180.3	180.1	450.5

10.
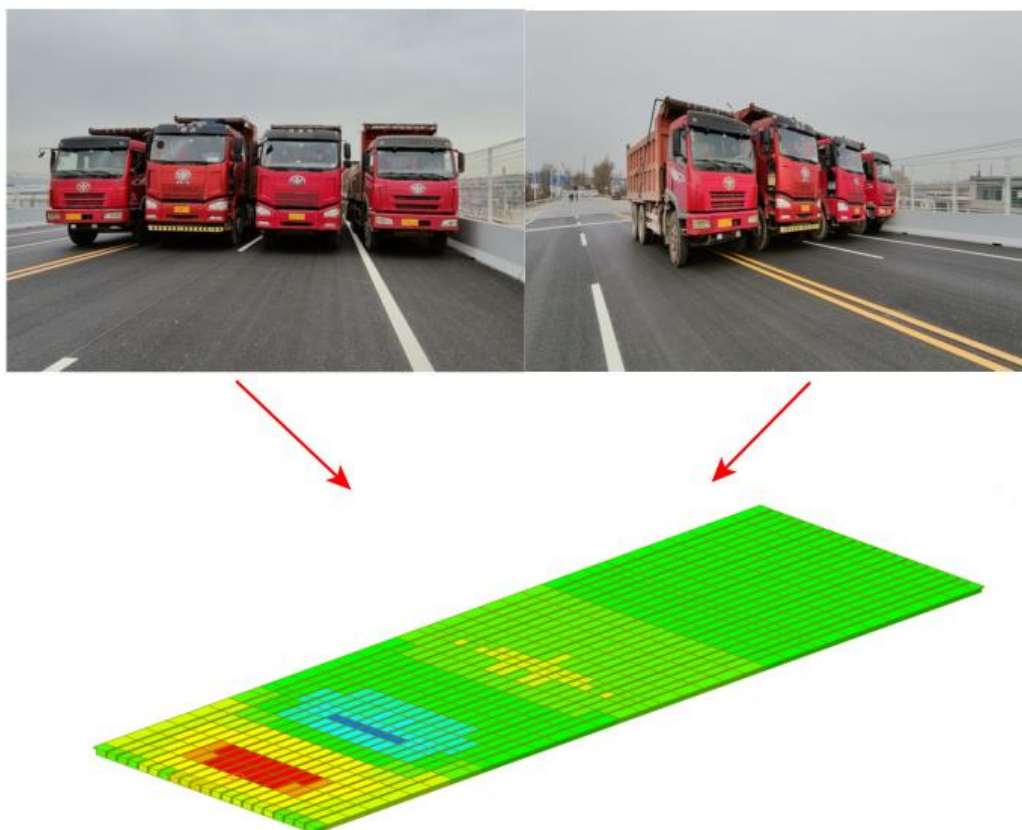
Fig.10 - Schematic diagram of bridge load test

The data acquisition device for bridge load test deflection is shown in Figure 11a).When the bridge is loaded and deflected, a corresponding displacement sensor placed on the deflection detector will measure the deformation displacement and transmit it to the terminal controller. The terminal controller will display the maximum and minimum deflection of the bridge bottom by processing the data with software. The data acquisition device for bridge strain is also shown in Figure 11b). By installing strain gauges at the force-bearing parts of the structure, the small deformation of the force-bearing parts can be measured, and the static strain under load of the structure can be obtained.

11.

a) deflection measurement

b) strain measurement
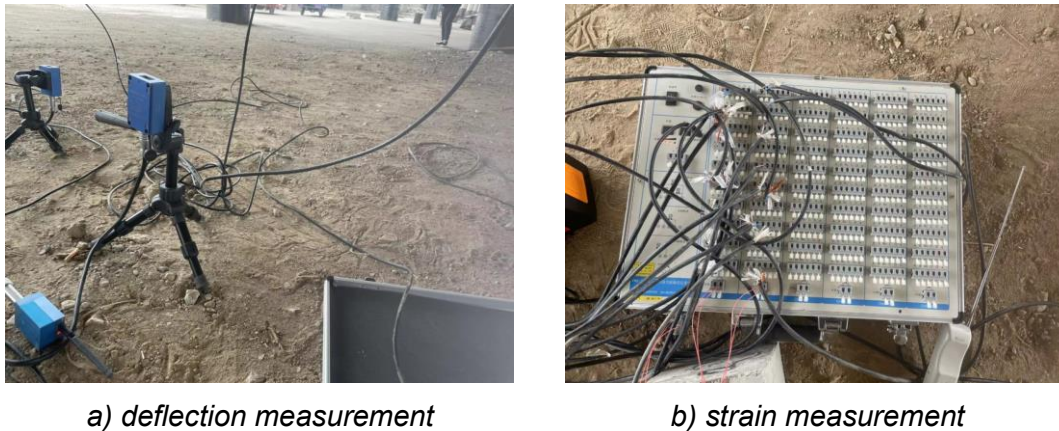
Fig.11 - Test measuring instruments

RESULTS

Analysis of deflection test results

Loading in the theoretical model and actual bridge, and analyze the change in the stiffness of the bridge before and after reinforcement through the analysis of the theoretical deflection values and actual measured deflection values at various test points. The comparison between the theoretical values obtained through finite element analysis and the actual measured values of the load test before and after reinforcement is shown in Figure 12.
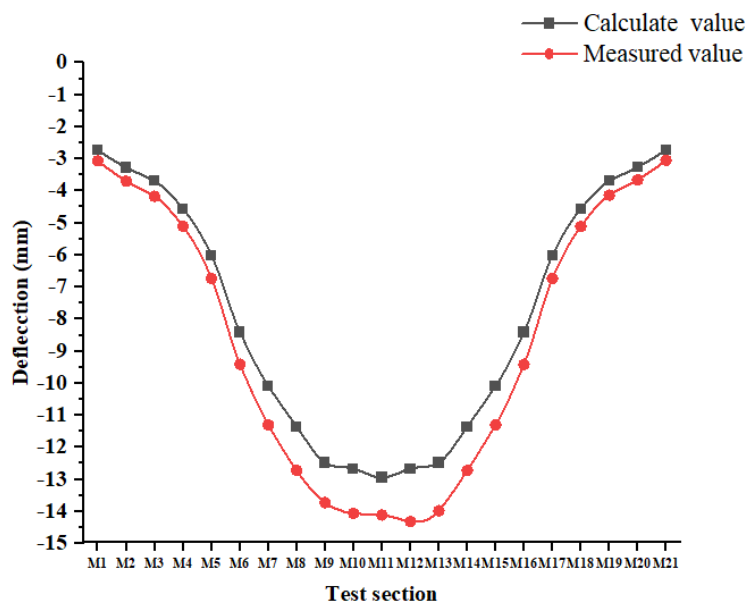
(a) Measured and theoretical deflection value at before reinforcement (Units: mm)
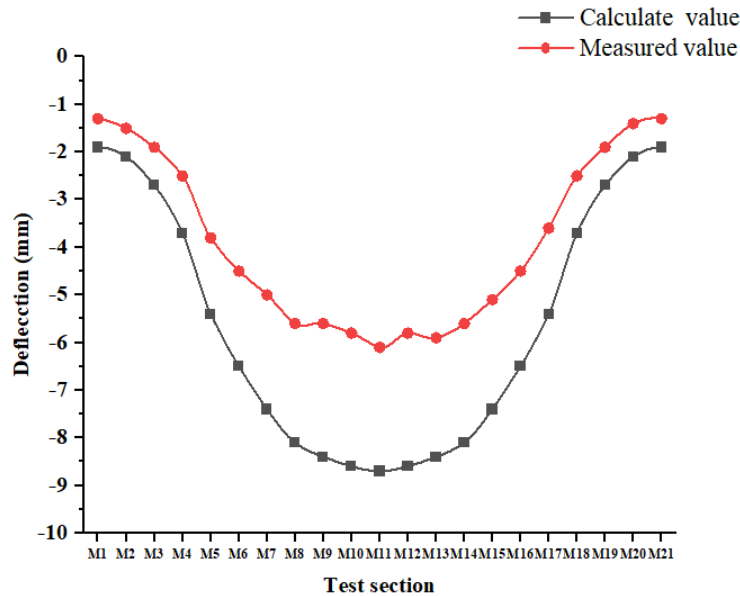
(b) Measured and theoretical deflection value at after reinforcement (Units: mm)

Fig.12 - Measured and theoretical deflection value (unit: mm)

As shown in Figure 12, before reinforcement, the check coefficient of the deflection of the 1# cross-section was 1.09 to 1.13, exceeding the theoretical calculation value, indicating that the stiffness of the structure could no longer meet the requirements for use. After reinforcement, the check coefficient of the deflection of the 1# cross-section was in the range of 0.67 to 0.70, and the deflection of each cross-section was smaller than the theoretical calculation value.

Tab. 7: Comparison of deflection test results

Measuring point		M7	M8	M9	M10	M11	M12	M13	M14	M15
Before	Theoretical value(mm)	-10.1	-11.4	-12.4	-12.7	-12.9	-12.6	-12.4	-11.4	-10.1
	Measured value(mm)	-11.1	-12.6	-13.7	-14.1	-14.1	-14.3	-13.9	-12.6	-11.0
	Coefficient	1.10	1.11	1.10	1.11	1.09	1.13	1.12	1.11	1.09
After	Theoretical value(mm)	-7.4	-8.1	-8.4	-8.6	-8.7	-8.6	-8.4	-8.1	-7.4
	Measured value(mm)	-5.0	-5.6	-5.6	-5.8	-6.1	-5.8	-5.9	-5.6	-5.1
	Coefficient	0.68	0.69	0.67	0.67	0.70	0.67	0.70	0.69	0.69

We can learn from Table 7 that the calculated values of bridge deflection obtained through finite element analysis after reinforcement have decreased compared to those before reinforcement., indicating that the structural stiffness has improved after reinforcement. The maximum improvement of the calibration coefficient after reinforcement is 0.46. This means that the structure's stiffness after reinforcement meets the required use and has some safety reserves, indicating that the reinforcement effect is obvious and the reinforcement method is reliable.

Analysis of strain test results

Stress and strain are key data that reflect the stress situation of the structure. By analyzing the stress response of the bridge structure, the stress situation of the structure can be clearly displayed [18]. The comparison between the theoretical values obtained through finite element analysis and the

actual measured values of the load test before and after reinforcement for the test cross-section is shown in Figure 13.
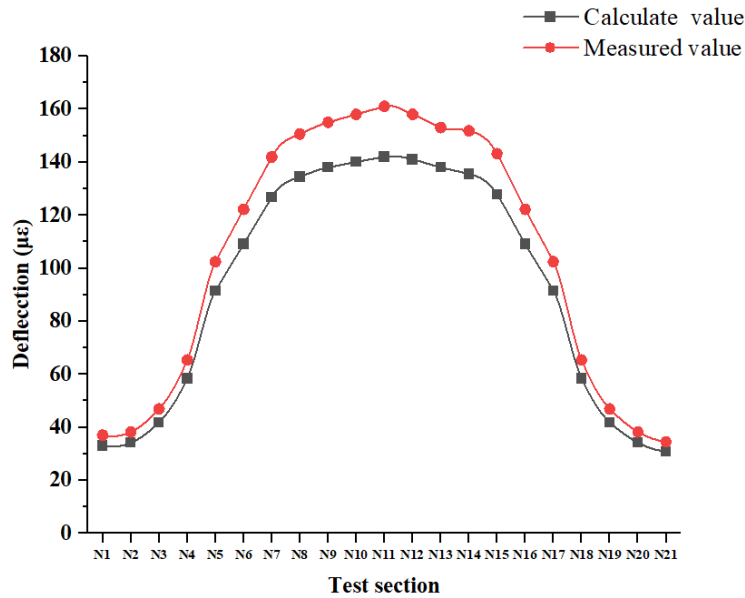
(a) Measured and theoretical strain value at before reinforcement
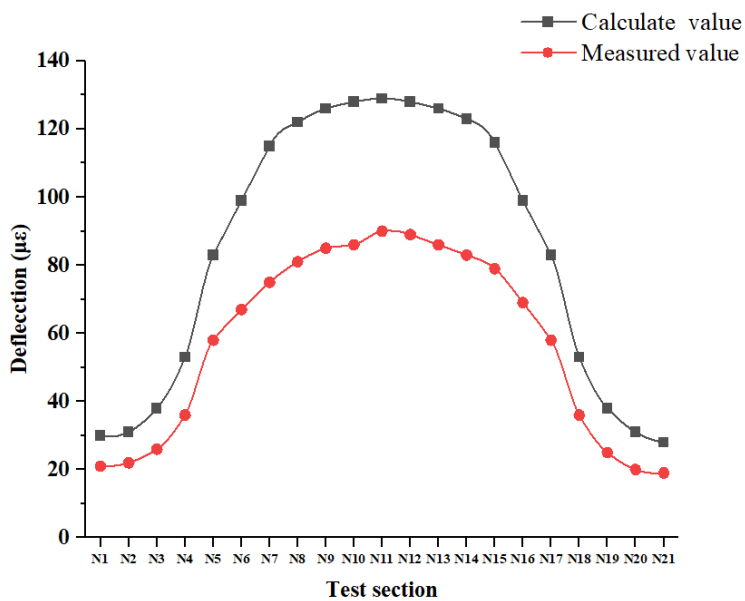
(b) Measured and theoretical strain value at after reinforcement

Fig.13 - Measured and theoretical strain value

The data in Figure 13 shows that the maximum calibration coefficient of deflection at section of span before reinforcement was 1.13, and section were greater than the theoretical calculation value, indicating poor overall integrity of the structure. After reinforcement, the maximum verification coefficient of deflection at each section was 0.70, and the deflection at each section was less than the theoretical calculation value.

Tab. 8: Comparison of strain test results

| Measuring point		N7	N8	N9	N10	N11	N12	N13	N14	N15
Before	Theoretical value(με)	127	134	138	140	142	141	138	134	127
	Measured value(με)	141	151	155	158	161	158	153	151	143
	Coefficient	1.11	1.12	1.12	1.13	1.13	1.12	1.11	1.12	1.13
After	Theoretical value(με)	115	122	126	128	129	128	126	122	115
	Measured value(με)	77	83	85	86	90	89	81	83	79
	Coefficient	0.67	0.68	0.67	0.67	0.70	0.70	0.64	0.68	0.69

As shown in Table 8, the theoretical strain values obtained through finite element analysis and the actual measured values of the load test after bridge reinforcement have decreased compared to before reinforcement, indicating that the overall integrity of the structure has improved after reinforcement. No new cracks have been found after reinforcement, and the structure is capable of meeting usage requirements and has a certain safety reserve.

CONCLUSION

This paper focuses on a prestressed hollow slab beam bridge in a certain city that has developed diseases such as longitudinal cracks due to long-term disrepair, which requires reinforcement treatment. The bridge was reinforced using the system transformation method, which converted the original simply supported hollow slab system into a continuous beam system, optimizing the structural mechanics of the bridge. The Midas/Civil finite element model was utilized to establish the model before and after reinforcement, and the theoretical values extracted from the finite element model were compared and analyzed with the actual measured values from the load test. The following conclusions were drawn:

(1) The calculated values of strain and deflection are in good agreement with the measured values, with small deviations and a basic similarity in the distribution of the measured and theoretical data for each test item.

(2) The reinforcement was most effective in the 7/16L of the 1st span, where the deflection decreased by 8.00 mm, a decrease of 56.7%, and the strain decreased by 71 $\mu\varepsilon$, a decrease of 44.0%. This greatly improved the load-bearing capacity of the bridge.

(3) Simply supported-continuous reinforcement technology can effectively improve the cracking performance of the main beam, reduce the deflection, and increase the structural stiffness and load-bearing capacity. This method is suitable for the reinforcement of hollow slab bridges in cities.

(4) The design method proposed in this paper significantly increases the load-bearing capacity and stiffness of the bridge, and the bridge operates well after reinforcement. The simply supported-continuous reinforcement method is not only suitable for the reinforcement of slab beams, but also for T-beams. Through the reinforcement and reconstruction method of the bridge, it provides a reference for similar bridge reinforcement and reconstruction in the future.

REFERENCES

[1] Lufei & Pengcheng. (2013). Analysis, comparison and application of common bridge reinforcement methods. Highway (10), 121-123.

[2] Zheng Zhaodong. (2013). Post-evaluation of bridge reinforcement. Scientific and technological information (15), 378 + 440.

[3] Wang Shichao, Wang Chunsheng, Wang Qian, Tian Xiaofeng & Duan Lan. (2018). Flexural behavior of full-scale prestressed concrete hollow slab beams strengthened with composite

reinforcement. Journal of Transportation Engineering (02), 31-41.doi : 10.19818 / j.cnki.1671-1637.2018.02.004.

[4] Hu Zhaofang, Chen Runshui. (2002). Research and examples of reinforcement and lifting technology of old highway bridges. Highway (02), 14-16.

[5] Yuan Quan, Zhang Song. (2003). Reinforcement design of a concrete cable-stayed bridge[J]. East China Highway ,(5):3-5.

[6] Shen Yuqiang. (2009).Mechanical analysis of structural continuous bridge system transformation after simply supported (master 's degree thesis, Chongqing Jiaotong University).https://kns.cnki.net/KCMS/detail/detail.aspx?dbname=CMFD2011&filename=2010160918.nh

[7] Maher K.Tadros, Joseth A.Ficenec. (1993). A new technique to continuity in pre-stressed concrete members [J]. PCI Joural, 38 (5):30-38

[8] Robert J.Peterman, Julio A. Ramirez. (1993). Behavior and strength of bridges with full-span pre-stressed concrete form panels [J]. PCI Joural ,43(3):80-91.

[9] Zhu Hanbing,Yang Yaxun & Fan Weiya.(2015).External Prestressing Bridge Reinforcement Technology Review. MATEC Web of Conferences.

[10] Zhao Guodong,Duan Shixin,Sun Bo & Yuan Xiaohua.(2021).Application on large-span reconstructed structure with external prestressing technology. Journal of Physics: Conference Series(4). doi:10.1088/1742-6596/1885/4/042042.

[11] Xin Lijuan, He Huanan & Chen Xu. (2013). Internal force analysis before and after the continuous reinforcement of the old bridge. Low temperature building technology (08), 67-69.

[12] JTG 3362-2018 Specifications for design of highway reinforced concrete and prestressed conc rete bridges and culverts [S]. P.R. China, Ministry of Communications, 2018.

[13] Sun Quansheng & Liang Daoyu. (2019). Analysis of the design effect of external prestressed r einforcement of urban low box girder. Low Temperature Building Technology (09), 56-59+98. d oi:10.13905/j.cnki.dwjz.2019.09.014.

[14] Liu Huichao. (2015). Research on Reinforcement Technology of Continuous Girder Bridge of Prestressed Concrete (Master's Thesis, Chang'an University)

[15] Kim SangHyun,Park JongSup,Jung WooTai,Kim TaeKyun & Park HeeBeom. (2021). Experimental Study on Strengthening Effect Analysis of a Deteriorated Bridge Using External Prestressing Method. Applied Sciences(6). doi:10.3390/APP11062478..

[16] Zhou Yongjun, Zhao Yang, Zhao Yu, Cao Qun & Li Zhen. (2021). Study on the impact coefficient of simple support girder bridge based on dynamic load test load efficiency. Vibration and Shock (20), 207-216. doi:10.13465/j.cnki.jvs.2021.20.026.

[17] Wang Ziqiang., 2019. Load Test of Prestressed Concrete Continuous Box Girder Bridge. The wind of science and technology, vol. 400(32), 119., doi.10.19392/j.cnki.1671-7341.201932099

[18] Kim SangHyun,Park JongSup,Jung WooTai,Kim TaeKyun & Park HeeBeom. (2021). Experimental Study on Strengthening Effect Analysis of a Deteriorated Bridge Using External Prestressing Method. Applied Sciences(6). doi:10.3390/APP11062478.

THE EFFECT OF RECYCLED RUBBER AGGREGATES AND DUNE SAND OF EL-OUED REGION ON THE COMPRESSIVE STRENGTH OF CEMENTITIOUS MORTAR: OPTIMIZATION USING TAGUCHI METHOD

Kaab Mohamed Zohaïr[1], Khelaifa Hamad[1], Athamnia Brahim[2],

Djedid Tarek[3] and Hima Abdelkader[4]

1. *University of El-Oued, Faculty of Technology, Department of Hydraulics and Civil Engineering, BP 789, El-Oued 39000, Algeria;*
   kaab-mohamed-zohair@univ-eloued.dz, khelaifahamad@gmail.com
2. *University of Tebessa, Faculty of Sciences and Technology, Department of Civil Engineering,Tebessa 12002, Algeria; brahim.athamnia@univ-tebessa.dz*
3. *Laboratory of exploitation and valorisation of Saharan energy resources " LEVRES " University of El-Oued, Faculty of Technology, Department of Hydraulics and Civil Engineering, BP 789, El-Oued 39000, Algeria; tarek-djedid@univ-eloued.dz*
4. *University of El-Oued, Faculty of Technology, Department of Electrical Engineering, BP 789, El-Oued 39000, Algeria; Abdelkader-hima@univ-eloued.dz*

ABSTRACT

This study optimizes the effect of recycled rubber aggregates and dune sand of El-Oued's region by maximizing the compressive strength of cementitious mortar using Taguchi's design experiments. The experiments were designed using an L9 orthogonal array to see the different relationships between the factors targeted in our research, namely: water/cement (W/C) ratio, rubber aggregates (RA) content, and dune sand (SD) content, with the levels of each factor in the mortar mixture. The samples were tested at 28 days in each of the nine trial conditions for two responses: compressive strength and ultrasonic pulse velocity. The results of the analysis of variation (ANOVA) show that RA content is the factor that has the largest effect on the two tests, and the second factor affecting the two tests is the W/C ratio. Then, the analysis shows that the SD content has no significant effect on the mechanical resistance of the mortar for the two tests. And from the mathematical models investigated in this study, we conclude that the factors RA content and W/C ratio have a negative influence on the responses of the compression test and the ultrasonic test together.

KEYWORDS

Rubber aggregates, Dune sand, Mortar, Compressive strength, Taguchi method

INTRODUCTION

The Algerian Sahara has a large supply of dunes sand, particularly in the El-Oued region, where there is a growing shortage of river sand for the production of cement mortar. Added to this is the factor of the remoteness of the Saharan regions from the supply points for aggregates, which makes the value of construction materials more expensive. From these facts, using local materials such as dune sand and recycled materials such as rubber granules from used tires could present an economic advantage to manufacturing sustainable building materials.

Over the past two decades, dune sand has become the subject of many studies in different countries [1-5]. In this context, several research projects have been established in Algeria for the solution to the problem of the depletion of natural resources by the valorization of dune sand in the field of construction [6-11], which presented this material as the material of the future.

The evolution of increasingly restrictive requirements regarding environmental protection as well as revision of economic standards inspired by sustainable development means that recycling and recovery of industrial by-products have become very important from an environmental and economic point of view [12-15]. All over the world, when it comes to the automotive industry, the use of rubber tires is increasing every year [13, 16, 17].

Experimental studies have been carried out by Liu et al. [18] to assess the behavior of concrete with recycled tire rubber particles. In addition, Kardos and Durham [19] conducted several studies to determine how recycled rubber particles affect the mechanical and environmental performance of rubber concrete, which showed that a substitution level up to 30% of fine aggregates using crumb rubber is acceptable. These results are consistent with those obtained by certain authors, concerning concretes and/or mortars based on rubber particles [20, 21], which show a clear lack of adhesion and a more extensive transition halo between the cementitious matrix and the rubber aggregates. Therefore, it is recommended to minimize the dosage of these to keep the mechanical resistance within an acceptable range. However, these results did not clarify the degree of contribution of each material to the mechanical and environmental properties. Consequently, to solve this issue and the valorization of dunes sand in the El-Oued region, the authors suggest using statistical analysis with the Taguchi method to find the best values for these materials, which affect the mechanical strength of mortar and as well as getting the significance level of each material through the analysis of variation (ANOVA) [22-25].

The studies reviewed above centered on assessing the usefulness of recycled tire rubber aggregates (RTRA) in improving the performance of mortar and concrete. The mechanical performances of recycled rubber aggregates mixed with dune sand in the mortar have rarely been examined, and the best percentages of these components, which give the best mechanical properties of the mortar, have not been defined. To this end, this study attempts to illustrate the best values and the effect level of the recycled rubber aggregates mixed with the dune sand of El-Oued's region on the mechanical behavior of rubber mortar by statistical analysis with the Taguchi method.

TAGUCHI'S METHOD

The design of experiments by Taguchi's method is an original procedure based on a statistical analysis of experimental results. This approach uses a robust experimental design derived from a few orthogonal arrays to find the most significant factors and predict the optimum responses in a short time and with fewer experiments [26, 27]. According to the characteristics of the response to be optimized, signal-to-noise (S/N) ratios could be selected for three goals, namely: larger is better if the maximum is the best with equation (1); smaller is better if the minimum value is the best with equation (2); and nominal is better if the nominal value is the best with equation (3), respectively [25, 28-30]. However, for this study, we calculate the optimum values on the basis that "larger is better."

Larger is better:
$$S/N = -10\log\left[\frac{1}{n}\sum Y^2\right] \quad (1)$$

Smaller is better:
$$S/N = -10\log\left[\frac{1}{n}\sum 1/Y^2\right] \quad (2)$$

Nominal is better:

$$S/N = 10\log\left[\frac{\overline{Y}^2}{S_Y^2}\right]$$

(3)

Where:

n and Y are the number of experimental tests and the experimental value, respectively.

$\overline{Y}$ and S_Y^2 are the average of data and the variation of data, respectively.

EXPERIMENTAL WORK

Materials

This study used two types of sand: dune and alluvial sand. The dune sand (SD) comes from the region of El-Oued (Figure1a) and the alluvial sand (SA) comes from the Djamaa sand pit, in the El-Oued Province (Figure1b). The physical properties of the sands are grouped in Table 1.

(a) Dune sand SD   (b) Alluvial sand SA

Fig. 1 – Types of sand used

In addition, the rubber granules used in our study are obtained from the mechanical crushing of waste tires (RTRA) and come from a rubber tire crushing plant located in Setif, Algeria. After the elimination of their metallic and textile parts, they are crushed mechanically to obtain the desired fineness (Figure 2). The granular class of the recycled rubber aggregates (RA) used in our composites is from 0 to 4 mm, and the physical characteristics of these are summarized in Table 1. Furthermore, the particle size distribution curves of sands and rubber aggregates are presented in Figure 3.

Fig. 2 – Rubber aggregates (0-4mm)

Tab. 1 - Physical properties of sands and rubber aggregates.

	SA*	SD**	RA***
Apparent density (g/cm^3)	1.64	1.56	-
Absolute density (g/cm^3)	2.70	2.64	0.94
Fineness modulus	1.87	1.20	-
Sand Equivalent (%)	80	85	-
Water absorption (%)	2.60	1.62	0.30
Granulometry (mm)	-	-	0-4

(*) Alluvial sand ;   (**) Dune sand ;   (***) Rubber aggregates.
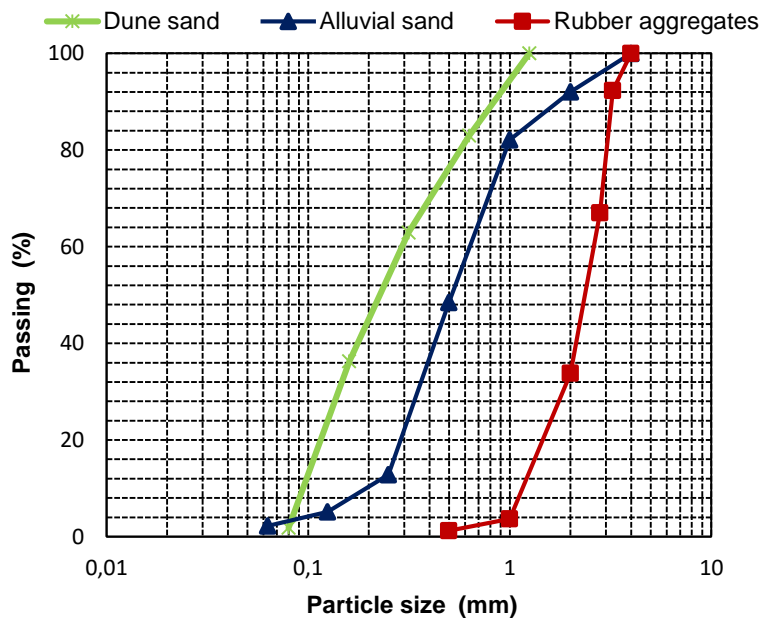
Fig. 3 – Particle size distribution curves of sands and rubber aggregates.

The cement used in all the experimental tests is a CEM II / B-L 42.5 N compound portland cement, it was manufactured at the LAFARGE cement plant in Algeria, and its physical and chemical properties are given in Table 2.

Tab. 2 - Physico-chemical properties of cement

Physical properties	Value	Chemical properties	Value
Specific gravity (g/cm^3)	3.08	Loss on ignition	8.0 ± 2.0
Blaine fineness (cm²/g)	3700 – 5200	Insolube residue	1.35 ± 0.65
Normal consistency (%)	26.5 ± 2.0	Sulphate content SO$_3$ (%)	2.5 ± 0.5
Expansion (mm)	≤ 3.0	Magnesium oxide content MgO (%)	1.7 ± 0.5
Shrinkage at 28 days (µm/m)	< 1000	Chloride content (%)	0.02 – 0.05
Initial setting time (min)	150 ± 30	C$_3$S	60 ± 3.0
Final setting time (min)	230 ± 50	C$_2$S	15 ± 3.0
Compressive strength at 2 days (MPa)	≥ 10	C$_3$A	7.5 ± 1.0
Compressive strength at 28 days (MPa)	≥ 42.5	C$_4$AF	11 ± 1.0

Design of mixtures

For statistical analysis, we applied Taguchi's method to model the effect of target factors in our research, namely: water/cement (W/C) ratio, rubber aggregates RA content, and dune sand SD content. wherein the levels of each factor were selected as shown in Table 3, based on a bibliographic search.

With a matrix of three factors at three levels, the experiments were designed using an L9 (3^3) orthogonal array as shown in Table 4.

Tab. 3 - The factors and levels targeted

Factor	Level		
	1	2	3
W/C ratio	0.55	0.60	0.65
RA content (%)	0	08	16
SD content (%)	0	10	20

Tab. 4 - Experimental design of the L9(3^3) orthogonal array

Trial	W/C ratio	RA content (%)	SD content (%)
01	0.55	0	0
02	0.55	8	10
03	0.55	16	20
04	0.60	0	10
05	0.60	8	20
06	0.60	16	0
07	0.65	0	20
08	0.65	8	0
09	0.65	16	10

Preparation of mixtures

We used a dosage of cement and sand corresponding to the dosage of the natural mortar according to EN 196-1. That is, one part of cement and three parts of sand. Then, the mortar formation used in our experimental study was carried out using RA and SD in two stages (Figure 4). In the first stage, we combined the rubber aggregates (0–4 mm) from recycled used tires in the volumetric replacement of alluvial sand SA with 0, 8, and 16% volume substitution. Whereas in the second stage, we incorporated the dune sand SD in substitution for alluvial sand SA volume with 0, 10, and 20% volume substitutions. In addition, we changed the W/C ratio for three cases: 0.55, 0.60, and 0.65.
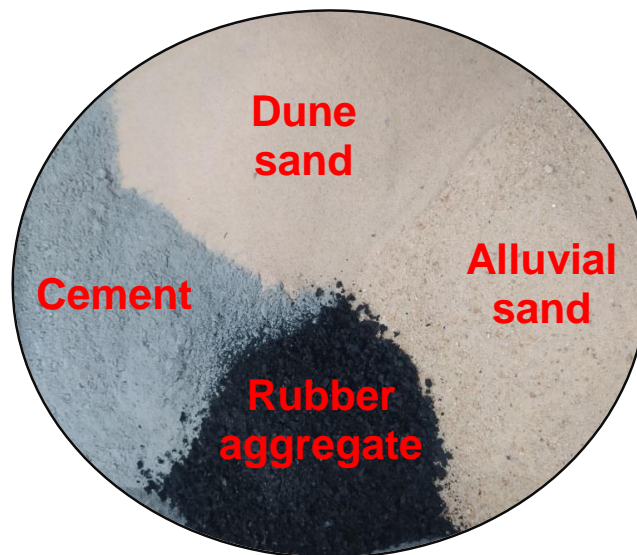
Fig. 4 –Preparation of mortar.

From these formulas, inspired by the design of the experimental (DOE), we launched the mortar formulations campaign incorporating the rubber aggregates and dune sand that we present in the following (Table 5). Knowing that the specimens produced in this study are prismatic in shape with dimensions of 40 x 40 x 160 mm according to EN 196-1. They were all put in a curing room in water at 20°C for 28 days before being submitted to compression and ultrasonic tests. It should be noted that for the different mortar mixtures, three specimens from each mixture were used to perform each test.

Tab. 5 - Composition of mortars used (kg/m^3)

Trial	Mixture designation	Cement (kg)	Alluvial sand (kg)	Rubber aggregates (kg)	Dune sand (kg)	Water (L)	W/C ratio
01	RA0 SD0	483.07	1449.22	/	/	265.69	0.55
02	RA8 SD10	483.07	1188.36	39.73	140.28	265.69	0.55
03	RA16 SD20	483.07	927.49	80.60	283.76	265.69	0.55
04	RA0 SD10	471.17	1272.15	/	136.83	282.70	0.60
05	RA8 SD20	471.17	1017.72	38.76	276.76	282.70	0.60
06	RA16 SD0	471.17	1187.35	78.61	/	282.70	0.60
07	RA0 SD20	460.03	1104.08	/	270.22	299.02	0.65
08	RA8 SD0	460.03	1269.69	37.83	/	299.02	0.65
09	RA16 SD10	460.03	1021.27	76.75	133.59	299.02	0.65

Testing

Compression test

The samples of the hardened mortar studied are subjected to an increasing load until failure, where the breaking load is the maximum load recorded during the test. The value of the resistance considered constitutes the average of the crushing stress of three specimens.

The compressive strengths were evaluated at 28 days (S_{28}) using a hydraulic compression testing machine equipped with a compression device for mortar molds.

Ultrasonic test

The ultrasonic velocity is a parameter that allows obtaining qualitative information on the materials. The speed of the ultrasonic waves results from the time taken by the waves to cross the prismatic specimens of hardened mortar, which depends enormously on the modulus of elasticity of the aggregates and their quantity in the mortar. In this study, the ultrasonic pulse velocity was evaluated at 28 days (U_{28}).

ANALYZE AND DISCUSS RESULTS

In the two tests performed in this study, the experiments were laid out using an L9 (3^3) array, and three samples were tested in each of the nine trial conditions. The results of the average of the three samples for each test are shown in Table 6.

Tab. 6 - Results of compressive strength and ultrasonic pulse velocity tests.

Trial	Mixture designation	Compressive strength (MPa)	Ultrasonic pulse velocity (m/s)
01	RA0 SD0	36.50	3587
02	RA8 SD10	33.12	3519
03	RA16 SD20	31.37	3448
04	RA0 SD10	34.62	3699
05	RA8 SD20	31.06	3477
06	RA16 SD0	27.75	3275
07	RA0 SD20	30.90	3600
08	RA8 SD0	32.25	3325
09	RA16 SD10	25.56	3125

Optimum values

The results of the analysis for S/N ratios are shown in Table 7 and Figure 5. Where determine the optimum levels for each factor and the best combination of factor levels. Consequently, from the results of the main effects for the S/N ratios, we find that the optimum results for each factor to give the optimum values for mechanical compressive strength are the following: W/C ratio 0.55, rubber aggregates content 0%, and dune sand content 0%. In addition, we find that the optimum results for each factor to give the optimum values for ultrasonic pulse velocity are the following: W/C ratio 0.55, rubber aggregates content 0%, and 20% from dune sand content.

Tab. 7 - Response table for signal-to-noise ratios

	W/C ratio	RA content	SD content
Level	Compressive strength		
1	30.53*	30.61*	30.09*
2	29.83	30.14	29.78
3	29.37	28.98	29.86
Level	Ultrasonic pulse velocity		
1	70.92*	71.19*	70.61
2	70.83	70.73	70.73
3	70.49	70.32	70.90*

(*) Optimum levels for each factor.
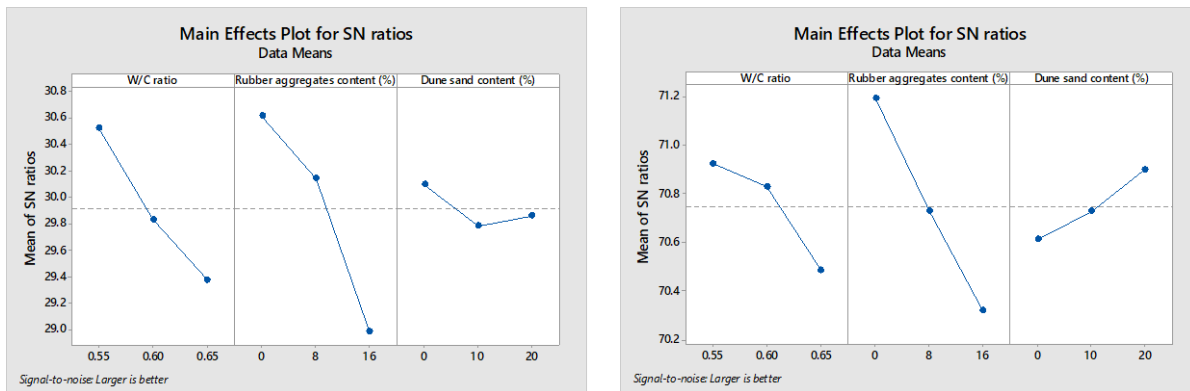
(a) Compressive strength   *(b) Ultrasonic pulse velocity*

Fig. 5 –Response plots for S/N ratios.

Analysis of variation (ANOVA)

The main objective of ANOVA is to show the factors that have the most effect on the responses of the experiments. The analysis is performed for a significance level α = 0.05, i.e., for a confidence level of 95%.

The ANOVA results of the two tests investigated are given in Table 8 and Figure 6. In this statistical technique, it is worth noting that a low probability (i.e., P-Value ≤ 0.05) indicates the statistical significance of the factor on the corresponding response, and the values of the contribution give the degree of influence of each factor on the response studied.

In the tests examined (Figure 6), analysis of contrast results showed that RA content is the factor that has the largest effect on the total variation of the two tests, which explains 57.06% of the contribution to compressive strength and 68.90% of the contribution to ultrasonic pulse velocity; the second factor affecting the two tests is the W/C ratio, with a 28.62% contribution to compressive strength and a 16.24% contribution to ultrasonic pulse velocity. Then, the analysis shows that the SD content has no significant effect on the overall variance of compressive strength and ultrasonic pulse velocity together. As a result, this statistical technique shows that the incorporation of the dune sand as a volume substitution for alluvial sand up to 20% has no effect on the mechanical resistance of the mortar. The thing that encourages the valorization of dune sand in the construction field and particularly in mortar preparation.

Tab. 8 - Analysis of variation results for the two tests.

Source	Degrees of Freedom	Sum of Squares	Mean Square	F-Value	P-Value	Contribution (%)	Remarks
Compressive strength							
Regression	3	76.92	25.64	11.76	0.011	/	/
W/C ratio	1	25.133	25.133	11.53	0.019	28.62	Significant
RA content	1	50.113	50.113	22.98	0.005	57.06	Significant
SD content	1	1.675	1.675	0.77	0.421	1.91	Insignificant
Error	5	10.902	2.180	/	/	12.41	/
Total	8	87.823	/	/	/	100.00	/
Ultrasonic pulse velocity							
Regression	3	240951	80317	20.40	0.003	/	/
W/C ratio	1	42336	42336	10.75	0.022	16.24	Significant
RA content	1	179574	179574	45.61	0.001	68.90	Significant
SD content	1	19041	19041	4.84	0.079	7.31	Insignificant
Error	5	19686	3937	/	/	7.55	/
Total	8	260636	/	/	/	100.00	/

(a) Compressive strength   *(b) Ultrasonic pulse velocity*
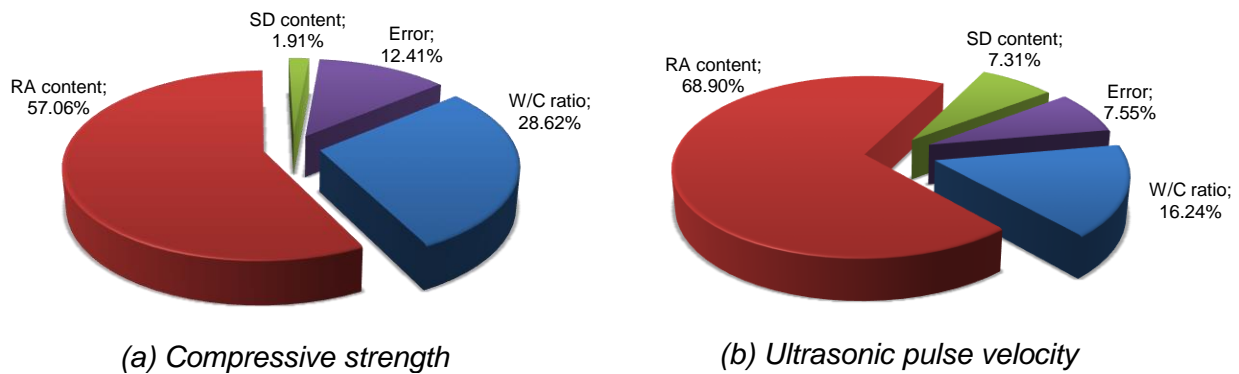
Fig. 6 – Contribution of each factor used in the experimental tests.

Mathematical models

In order to understand the effects of factors on the responses investigated. Regression analysis was used to develop the linear regression model. The mathematical models of the tests studied are the following:

$$S_{28} = 59.44 - 40.9\, W/C - 0.3612\, RA - 0.0528\, SD \tag{4}$$

$$U_{28} = 4575 - 1680\, W/C - 21.62\, RA + 5.63\, SD \tag{5}$$

Figure 7 presents the normal probability plots of the residuals of the models developed in this study. It is seen that the residuals fit in a straight line. In addition, the coefficient of determination (R^2) for the two models approaches unity, as shown in Table 9. As a result, we can conclude that the errors have a normal distribution and that the models developed are significant.

Tab. 9 - Coefficient of determination table.

Test	R^2 (%)
Compressive strength	87.59
Ultrasonic pulse velocity	92.45
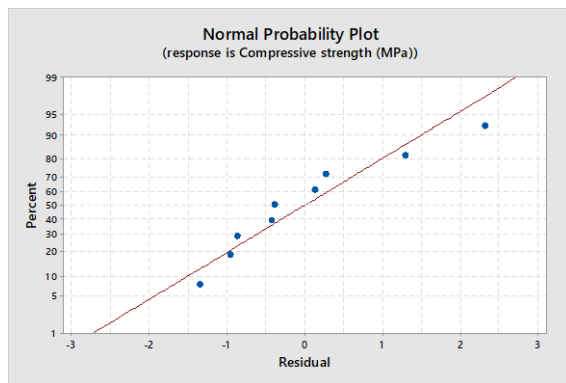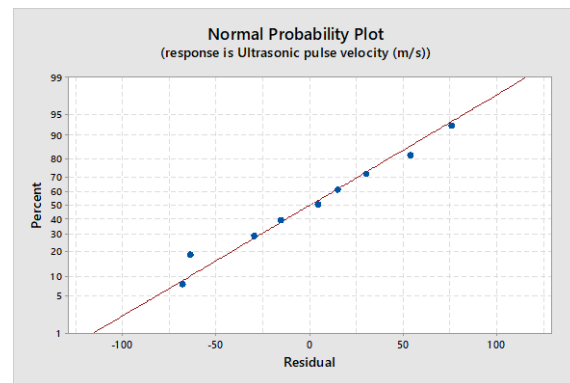
(a) Compressive strength   *(b) Ultrasonic pulse velocity*

Fig. 7 – Normal probability plots.

For the two mathematical models represented by equations (4) and (5), it was observed that the minus sign (–) indicates that the factors negatively affect the answers to the two tests. On the other hand, the plus sign (+) indicates that factors positively influence responses. Thus, we conclude that the factors W/C ratio and RA content have a negative influence on the responses of the compression test and the ultrasonic test together.

In addition, the reduction in the W/C ratio implies less water in the mixture, which results in an increase in the compressive strength and ultrasonic pulse velocity together. However, an increased percentage of RA content translates to the need for the mixture to contain a large amount of water. Consequently, this results in a reduction in mechanical resistance for the mortar.

CONCLUSION

The experimental and numerical work presented is part of the application of statistical analysis in the field of materials in civil engineering. More specifically, the object of the work is to apply Taguchi's design of experiments to see the different relationships between the factors targeted in our research (W/C ratio, RA content, and SD content) with the levels of each factor.

The Taguchi method uses a robust design that provides the most important factors in controlling the consistency of mortar quality with just a few experiments.

Predictive mathematical models are developed according to the tests carried out, which allowed us to understand the effect of the factors used in our work on the compressive strength and ultrasonic pulse velocity at 28 days. In order to determine the optimal values for each factor to give the best results for each response.

The optimal values for our mortar composite are as follows:

• Compressive strength at 28 days: 0.55 of W/C ratio at level1, 0% of RA content at level1, and 0% SD content at level1.

• Ultrasonic pulse velocity at 28 days: 0.55 of W/C ratio at level1, 0% of RA content at level1, and 20% SD content at level3.

Then, the results of the ANOVA analysis used in our work for each response allowed us to conclude that the RA content is the factor that has the largest effect of the two tests, which explains 57.06% of the contribution to compressive strength and 68.90% of the contribution to ultrasonic pulse velocity; the second factor is the W/C ratio, with a 28.62% contribution to compressive strength and a 16.24% contribution to ultrasonic pulse velocity. In addition, from the mathematical models, we conclude that the factors RA content and W/C ratio have a negative influence on the responses of the compression test and the ultrasonic test together. On the other hand, the ANOVA analysis shows that the SD content has no significant effect on the mechanical resistance of the mortar for the two tests.

REFERENCES

[1]   Abu Seif E.-S. S., Sonbul A. R., Hakami B. A. H, El-Sawy E., 2016. Experimental study on the utilization of dune sands as a construction material in the area between Jeddah and Mecca, Western Saudi Arabia. Bulletin of Engineering Geology and the Environment, vol. 75: 1007-1022. doi: 10.1007/s10064-016-0855-9

[2]   Chuah S., Duan W., Pan Z., Hunter E., Korayem A. H., Zhao X.-L., Collins F., Sanjayan J. G., 2016. The properties of fly ash based geopolymer mortars made with dune sand. Materials & Design, vol. 92: 571-578. doi: 10.1016/j.matdes.2015.12.070

[3]   Hadjoudja M., Khenfer M., Mesbah H. A., Yahia A., 2014. Statistical models to optimize fiber-reinforced dune sand concrete. Arabian Journal for Science and Engineering, vol. 39: 2721-2731. doi: 10.1007/s13369-013-0774-z

[4]   Haifeng L., Jurong M., Yiying W., Jianguo N., 2017. Influence of desert sand on the mechanical properties of concrete subjected to impact loading. Acta Mechanica Solida Sinica, vol. 30: 583-595. doi: 10.1016/j.camss.2017.10.007

[5]   Liu Y., Li Y., Jiang G., 2020. Orthogonal experiment on performance of mortar made with dune sand. Construction and Building Materials, vol. 264: 120254. doi: 10.1016/j.conbuildmat.2020.120254

[6]   Abadou Y., Mitiche-Kettab R., Ghrieb A., 2016. Ceramic waste influence on dune sand mortar performance. Construction and Building Materials, vol. 125: 703-713. doi: 10.1016/j.conbuildmat.2016.08.083

[7]   Amel C. L., Kadri E.-H., Sebaibi Y. S, Soualhi H., 2017. Dune sand and pumice impact on mechanical and thermal lightweight concrete properties. Construction and Building Materials, vol. 133: 209-218. doi: 10.1016/j.conbuildmat.2016.12.043

[8]   Djeridane M., Zaidi A., Lakhdari M. F., Krobba B., 2021. Theoretical and Experimental Flexural Behavior of Steel Bars-Reinforced Concrete Beams Strengthened with Cementitious Mortars Based on Dune Sands. International Journal of Civil Engineering, vol. 19: 623-634. doi: 10.1007/s40999-020-00591-8

[9]   Lakhdari M. F., Zaidi A., Bouhicha M., Krobba B., 2021. Sulfate Resistance of Cementitious Mortar Based on Dune and Alluvial Sands in Hot Region. Iranian Journal of Science and Technology, Transactions of Civil Engineering, vol. 45: 697-706. doi: 10.1007/s40996-021-00632-9

[10]   Mani M., Bouali M. F., Kriker A., Hima A., 2021. Experimental characterization of a new sustainable sand concrete in an aggressive environment. Frattura ed Integrità Strutturale, vol. 15: 50-64. doi: 10.3221/igf-esis.55.04

[11]   Mokhtari A., Kriker A., Guemmoula Y., Boukrioua A., Khenfer M., 2015. Formulation and characterization of date palm fibers mortar by addition of crushed dune sand. Energy Procedia, vol. 74: 344-350. doi: 10.1016/j.egypro.2015.07.624

[12]   Aiello M. A., Leuzzi F., Centonze G., Maffezzoli A., 2009. Use of steel fibres recovered from waste tyres as reinforcement in concrete: Pull-out behaviour, compressive and flexural strength. Waste management, vol. 29: 1960-1970. doi: 10.1016/j.wasman.2008.12.002

[13]   Eisa A. S., Elshazli M. T., Nawar M. T., 2020. Experimental investigation on the effect of using crumb rubber and steel fibers on the structural behavior of reinforced concrete beams. Construction and Building Materials, vol. 252: 119078. doi: 10.1016/j.conbuildmat.2020.119078

[14]   Medina N. F., Medina D. F., Hernández-Olivares F., Navacerrada M., 2017. Mechanical and thermal properties of concrete incorporating rubber and fibres from tyre recycling. Construction and Building Materials, vol. 144: 563-573. doi: 10.1016/j.conbuildmat.2017.03.196

[15]   Shahjalal M., Islam K., Rahman J., Ahmed K. S., Karim M. R., Billah A. M., 2021. Flexural response of fiber reinforced concrete beams with waste tires rubber and recycled aggregate. Journal of Cleaner Production, vol. 278: 123842. doi: 10.1016/j.jclepro.2020.123842

[16]   Girskas G., Nagrockienė D., 2017. Crushed rubber waste impact of concrete basic properties. Construction and Building Materials, vol. 140: 36-42. doi: 10.1016/j.conbuildmat.2017.02.107

[17]   Si R., Wang J., Guo S., Dai Q., Han S., 2018. Evaluation of laboratory performance of self-consolidating concrete with recycled tire rubber. Journal of Cleaner Production, vol. 180: 823-831. doi: 10.1016/j.jclepro.2018.01.180

[18]   Liu F., Zheng W., Li L., Feng W., Ning G., 2013. Mechanical and fatigue performance of rubber concrete. Construction and Building Materials, vol. 47: 711-719. doi: 10.1016/j.conbuildmat.2013.05.055

[19]   Kardos A. J., Durham S. A., 2015. Strength, durability, and environmental properties of concrete utilizing recycled tire particles for pavement applications. Construction and Building Materials, vol. 98: 832-845. doi: 10.1016/j.conbuildmat.2015.08.065

[20]   Baghban S., Mo K. H., Ibrahim Z., Radwan M. K., and Shah S. N., 2022. Effect of basalt and polypropylene fibers on crumb rubber mortar with Portland cement and calcium aluminate cement binders: Strength and artificial neural network prediction model. Progress in Rubber, Plastics and Recycling Technology, vol. 38: 99-124. doi: 10.1177/14777606211062912

[21]   Zaouai S., Tafraoui A., Makani A., and Benmerioul F., 2020. Hardened and transfer properties of self-compacting concretes containing pre-coated rubber aggregates with crushed dune sand. Journal of Rubber Research, vol. 23: 5-12. doi: 10.1007/s42464-019-00030-x

[22]   Tanyıldızı H., 2014. Post-fire behavior of structural lightweight concrete designed by Taguchi method. Construction and Building Materials, vol. 68: 565-571. doi: 10.1016/j.conbuildmat.2014.07.021

[23]   Tanyildizi H., Şahin M., 2015. Application of Taguchi method for optimization of concrete strengthened with polymer after high temperature. Construction and Building Materials, vol. 79: 97-103. doi: 10.1016/j.conbuildmat.2015.01.039

[24]   Boumaaza M., Belaadi A., Bourchak M., 2021. The effect of alkaline treatment on mechanical performance of natural fibers-reinforced plaster: Optimization using RSM. Journal of Natural Fibers, vol. 18: 2220-2240. doi: 10.1080/15440478.2020.1724236

[25]   Aeshah M. N. A. A., Kaplan G., 2022. Mechanical durability and microstructural properties of sustainable high strength mortars ıncorporated basalt fiber and copper slag: Taguchi optimization. Construction and Building Materials, vol. 339: 127815. doi: 10.1016/j.conbuildmat.2022.127815

[26]   Karthik K., Rajamani D., Manimaran A., Prakash J. U., 2020. Wear behaviour of hybrid polymer matrix composites using Taguchi technique. Materials Today: Proceedings, vol. 33: 3186-3190. doi: 10.1016/j.matpr.2020.04.133

[27]   Shaladi R. J., Johari M. A. M., Ahmad Z. A., Mijarsh M., 2022. The engineering properties and pozzolanic reaction kinetics of quaternary blended binder high strength mortars optimized by the Taguchi method. Journal of Building Engineering, vol. 54: 104582. doi: 10.1016/j.jobe.2022.104582

[28]   P. Vasanthi and S. S. Selvan, 2020. Optimization of mixing parameters in nanosilica toughened cement mortar using Taguchi-grey relational analysis. Silicon: 1-7. doi: 10.1007/s12633-020-00791-w

[29]   Arıcı E., Çelik E., Keleştemur O., 2021. A performance evaluation of polypropylene fiber-reinforced mortars containing corn cob ash exposed to high temperature using the Taguchi and Taguchi-based Grey Relational Analysis methods. Construction and Building Materials, vol. 297: 123792. doi: 10.1016/j.conbuildmat.2021.123792

[30]   Nasir M., Johari M. A. M., Adesina A., Maslehuddin M., Yusuf M. O., Mijarsh M., Ibrahim M., Najamuddin S. K., 2021. Evolution of room-cured alkali-activated silicomanganese fume-based green mortar designed using Taguchi method. Construction and Building Materials, vol. 307: 124970. doi: 10.1016/j.conbuildmat.2021.124970

STUDY ON THE SETTLEMENT LAW OF TUNNEL IN DIATOMITE STRATUM BASED ON STRAIN SOFTENING MODEL

Yan Li[1], Huijian Zhang[2], Gongning Liu[2, *], Yuchao Zheng[2], Wei Fang[1], Lichuan Wang[3]

1. China Railway Design Corporation, Tianjin, Hebei District, 300000, China; liyan@crdc.com; 2876568700@qq.com
2. Southwest Jiaotong University, Key Laboratory of Transportation Tunnel Engineering, Ministry of Education, Chengdu, No. 111, North Section, Second Ring Road, Jinniu District, 610031, China; huijianz@163.com; yczh@home.swjtu.edu.cn; 2995484603@qq.com
4. China Railway 18th Bureau Group Co., Ltd.,Tianjin, 300222, China; wlc773747@126.com

ABSTRACT

Nowadays, there is no precedent for building a high-speed railway in diatomite area. Due to the complex structure and poor mechanical properties of diatomite as well as the lack of relevant engineering experience, more attention has been paid to the proper constitutive model of the tunnel in diatomite layer using the numerical calculation method, while the traditional Elastoplastic calculation model is the most used yet. Therefore, relying on the Feifengshan tunnel, through FLAC[3D] software as well as the on-site monitoring, the analysis of the settlement law about tunnelling in diatomite stratum is carried out based on different constitutive models. The research results show that diatomite has obvious strain-softening characteristics. The calculated surface settlement and vault settlement based on the Strain Softening model is greater than that based on the Mohr Coulomb model. When compared with the on-site monitoring data, it is found that the Strain Softening model would more accurately show the settlement law of the tunnel in diatomite and has better applicability in the diatomite area. The above-mentioned research results may provide some references for the construction and design of tunnels in similar strata in the future.

Keywords

Diatomite, Strain-softening model, Tunnelling, Settlement, On-site monitoring

INTRODUCTION

Diatomite is a kind of sedimentary rock formed by the remains of single-celled algae after many years of deposition. It has the characteristic of large pores, low density, loose structure, well-developed joint, and large compressibility, it softens easily when in contact with water and the mechanical abilities will decrease sharply [1, 2]. Han [3] analyzed the engineering characteristics of diatomite based on field experiments, and compared the reinforcement effects of different pile types in diatomite area. Existing studies mainly focused on the selection of subgrade reinforcement in diatomite area, and evaluated the applicability of reinforcement scheme to diatomite geology from the perspective of pile forming effect, bearing capacity and construction, and selected the optimal reinforcement measures according to the comparison of test results [4-6]. Based on the calculation model and triaxial test of diatomite, the test results were compared with numerical simulation calculation, and it showed that the diatomite had obvious strain-softening characteristics [7-9]. In the research of tunnels in soft rock, the traditional Mohr-Coulomb model was often selected as the constitutive model when the numerical simulation method was used [10-15]. Nam and Bobet [16]

studied the variation law of the deformation amplitude of a circular tunnel using an elastic model and proposed corresponding analytical solutions. Wang and He [17] revealed the influence of the lining type and the stress release rate before the preliminary lining on the stability about tunnel, and proposed the related measures, such as systematic bolt or shotcrete lining, grouting after installation of preliminary lining, and 20% of stress release rate before the installation of preliminary lining.

It was found that many geotechnical materials had strain-softening characteristics, and the impact about the strain-softening characteristics on stability about tunnel should be considered [18]. Gao et al. [19] studied the difference in the contribution rate of advance reinforcement and preliminary lining on the control effect of the surface settlement of shallow-buried tunnels in diatomite. Zhao et al. [20] focused on the impact about parameter of strain-softening model on deformation of tunnel, and found the Elastic Modulus, Poisson's ratio as well as softening modulus had great influence on the tunnel deformation. The application of the strain-softening model in tunnel engineering was analysed adopting Hoek-Brown strength criterion, and some references for the optimization as well as stability analysis of the tunnel engineering were also provided [21-24]. The mechanical parameter about Mohr-Coulomb model used in the FLAC3D software is pre-set as constants, which not perfectly show the softening effect about surrounding rock led by the decrease in the strength parameter about surrounding rock in nonlinear phase [25]. With the rapid development of computing software, the strain softening phenomenon of rock mass can be well simulated, and the proposed strain softening constitutive model also provides an important reference for solving engineering problems [26, 27]. However, due to the differences in engineering properties of different soil qualities, the existing research results cannot be simply applied to guide engineering practice in diatomite. Also, there is no precedent for the construction about high-speed tunnel in diatomite before this project. For the numerical calculation of tunnel in diatomite, it is necessary to study the applicability of suitable constitutive models to the construction mechanics of tunnel in diatomite, which plays a vital role in guiding engineering practice.

Therefore, relying on the Feifengshan tunnel of the Hangzhou-Shaoxing-Taizhou Railway, on-site test about diatomite is carried out, and numerical calculation is also taken on for the tunnel in diatomite adopting different constitutive models. Then the calculation results difference is compared and analysed, and a proper constitutive model with better applicability is obtained through the comparison of on-site monitoring. The findings may be good references for the designing as well as construction about tunnels in similar strata in the future.

MECHANICAL CHARACTERISTICS OF DIATOMITE BASED ON THE ON-SITE DIRECT SHEAR TEST

Engineering background

In this paper, the Feifengshan tunnel of the Hangzhou-Shaoxing-Taizhou Railway is taken as the supporting project, and the tunnel is mainly in diatomite stratum. The tunnel width is about 9.0m, the clearance height is about 6.2m and the clearance area is 43.2m^2. The preliminary linings are made of C25 concrete and steel arch lining with a thickness of 23cm; secondary linings are made of C30 reinforced concrete with a thickness of 40cm, the detail is shown in Fig. 1. To further study the mechanics about diatomite, the on-site direct shear test about diatomite is further carried out on site.
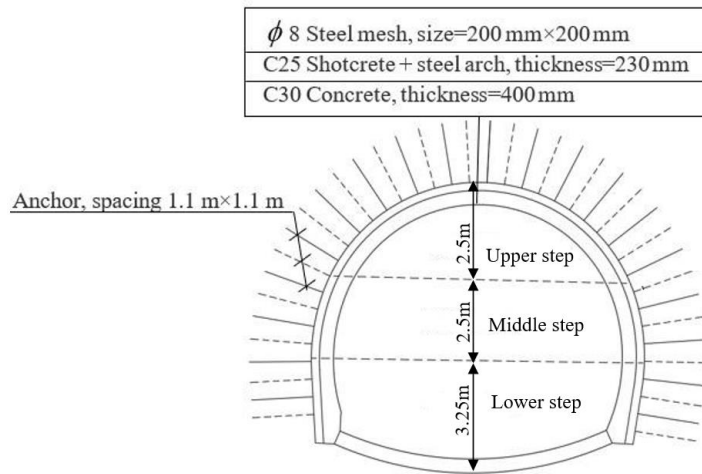
Fig. 1 - Design section about tunnel

On-site direct shear test of diatomite

The on-site shear test is conducted on a section of Feifengshan Tunnel, and a total of six specimens are tested. The size of each specimen is 50cm×50cm×50cm (the shearing area is 0.25m^2). During the test, a steel shear box with the same size as the specimen is used to fix the specimen. The normal force and shear force are applied by hydraulic jacks that are independent of each other, and the external reaction force device is loaded with sandbags. The measuring equipment for shear displacement and normal displacement is dial indicators, and the layout is presented in Figure 2. The normal displacement about specimen is the average value of indicators 1~4 and the shear displacement of the specimen is the average value of indicators 5~8. The purpose of this test is to obtain the on-site shear strengths of diatomite as a function of the normal stress on the shear face. The specimens are applied respectively with normal loads of 200kPa, 320kPa, 480kPa, and 680kPa.
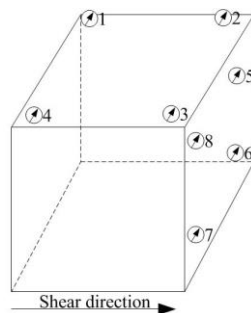
(a) Position of the dial indicator   (b) On-site dial indicator installation

Fig. 2 - Schematic diagram layout of the dial indicators

When the quick shear method is adopted in the test, the vertical loads are applied once, and the shear load is applied immediately. When the quick consolidation shear method is used for the test, the normal load is usually added to the predetermined load evenly in 4 to 5 grades, and then the normal stress remains unchanged. After each grade of the load is applied, the vertical deformation value should be measured immediately, then measured and recorded once for every 5 minutes. When the vertical deformation value does not exceed 0.05mm within 5 minutes, the next level of load is applied. After the last level of load is applied, the vertical deformation value is measured at the intervals of 5min, 10min, 15min, and 15min. When the cumulative value of vertical deformation for two sets of 15mins does not exceed 0.05mm, the vertical deformation value is

considered to stable and the shear load can be applied. The shear force is applied using the incremental loading method after the normal load is kept constant. It is usually applied gradually (at least in 10 steps) uniformly according to the estimated shear strength grades to control the shear displacement rate. At least 10 sets of readings are usually taken before the specimen reaches actual shear strength. When the peak value of shear stress is reached or the shear deformation increases sharply or the shear deformation is greater than 1/10 of the diameter (or side length) of the specimen, it is considered that the shear failure has occurred and the test can be stopped. The on-site direct shear test process and shear face are shown in Figure 3, and the corresponding shear force-shear displacement curve of the diatomite is presented in Figure 4.

As shown in Figure 4 that when the confining pressure is 200 kPa~680kPa, the diatomite all exhibits obvious "strain-softening" characteristics. During the elastic stage, shear force-shear displacements under different confining pressures all show a linear relationship, that is, the shear displacement increases with the shear force, and the difference between the slopes of different confining pressures is small. In the softening stage, the specimen fails when the shear displacement peak appears, the shear force gradually decreases, while the shear displacement continues to increase. In the residual stage, the shear force gradually decays and reaches a stable value, and the value fluctuation is small, but the shear displacement continues to accumulate.

(a) Test specimen

(b) Test loading

(c) Shear face

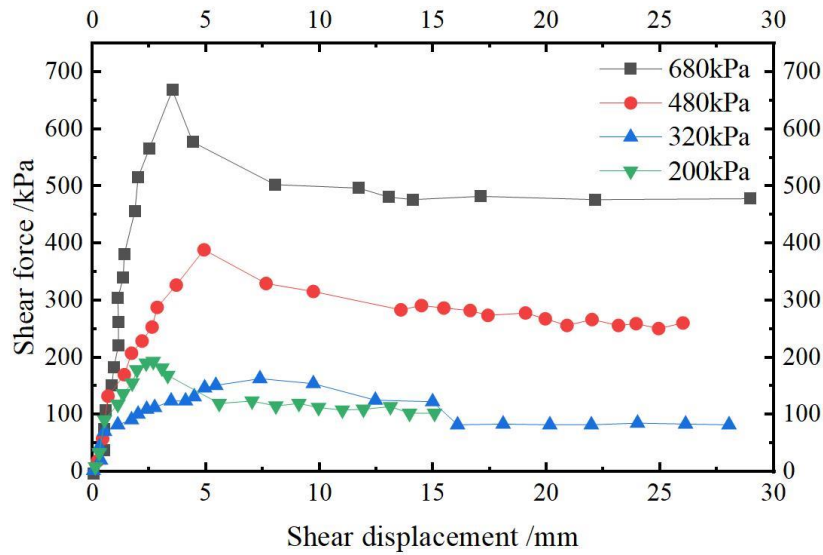*Fig. 3 - Test process of the diatomite*

Fig. 4 - Shear force-shear displacement curve of the diatomite under different confining pressures

## NUMERICAL SIMULATION ANALYSIS OF TUNNEL IN DIATOMITE BASED ON DIFFERENT CONSTITUTIVE MODELS

From the findings about on-site direct shear test of diatomite in the previous section, it can be found that the diatomite has obvious strain-softening characteristics. In practice, due to the limitation of test conditions, numerical simulation has gradually become an important means of the research. In this section, the numerical calculation method is used to further analyze the suitable constitutive model for diatomite, aiming to supply some reference for the tunnel with similar strata in the future.

Numerical calculation model

Calculation instruction

FLAC3D is adopted for the research. According to the theory about tunnel mechanics, the impacting ranges of tunnel's construction on surrounding rock are limited. When the distance is five times the tunnel diameter, then the calculation result error is less than 1%, and when the distance is three times the tunnel diameter, the calculation result error is less than 5%. Therefore, the boundary on the left-right sides about model is taken as 4 times the tunnel diameter. The dimension is presented in Figure 5(a) and the longitudinal excavation length is 40m.

To better simulate the calculation effect and reduce the boundary effect of the rear section [28, 29], the tunnel model extends 40m outward at the exit section (namely the longitudinal length is 80m). The model has a total of 308070 nodes and 296362 elements. The meshing diagram is shown in Fig. 5(b). Normal constraint is added to the front, rear, left, as well as right boundaries about model, and the bottom boundary is fixed [30]. The self-weight load is considered and the acceleration of gravity is taken as $10m/s^2$. Three-bench excavation method is adopted to simulate excavation process as the real project.
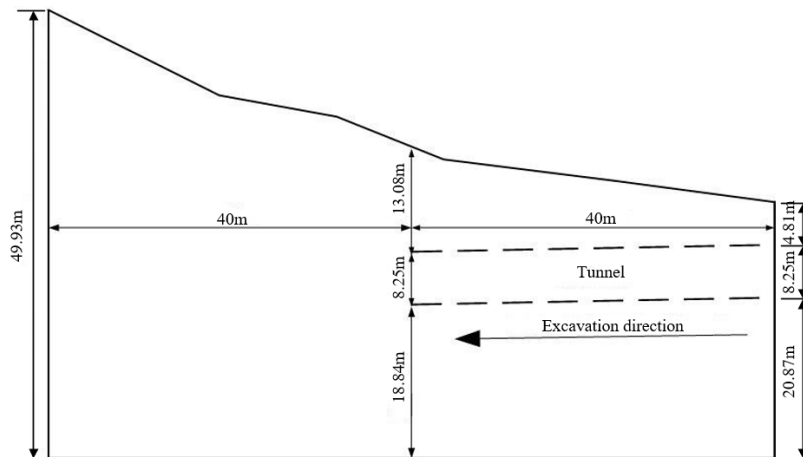
(a) Model size
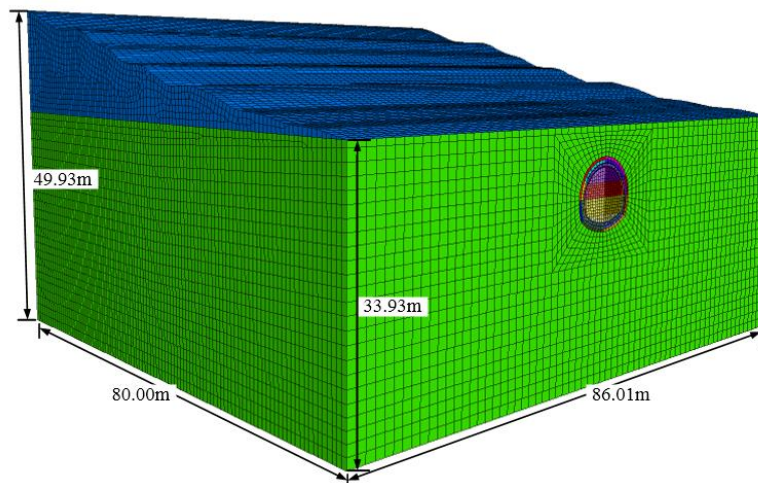
(b) Mesh division

Fig. 5 - Numerical model

Calculation parameter

Both the preliminary lining and secondary lining adopt solid element and follow the linear elastic criterion. The surrounding rock is diatomite, and its calculation parameter is selected based on geological survey data, as presented in Table 1. To improve the calculation efficiency, the lining effect about steel arch will be simulated by the equivalent method, namely, the elastic modulus about steel arch as well as steel mesh is converted into concrete.

Tab. 1 - Calculation parameters about surrounding rock and lining structures

Material type	Elastic Modulus E /MPa	Poisson's ratio μ	Density γ /(kN/m³)	Cohesion c /kPa	Internal friction angle φ /°
Surrounding rock	37.7	0.35	16.2	60.4	25.8
Anchor	200000	0.30	78.5	-	-
Preliminary lining	25500	0.30	25.0	-	-
Secondary lining	32000	0.30	25.0	-	-

Analysis of the constitutive model

It is assumed that the constitutive model about diatomite layer is the Mohr Coulomb (MC) model or Strain Softening (SS) model, and the analysis of numerical calculation about tunnel in diatomite is conducted.
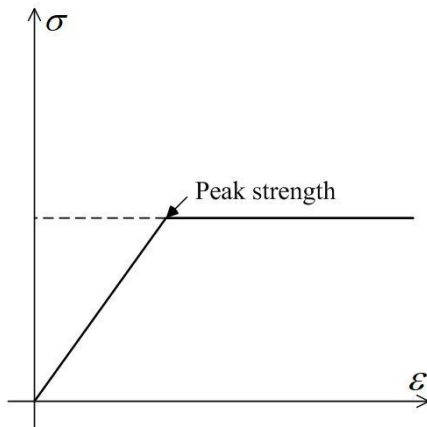
Fig. 6 - MC model
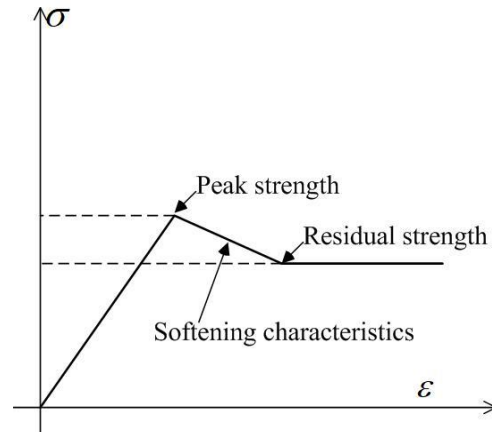
Fig. 7 - SS model
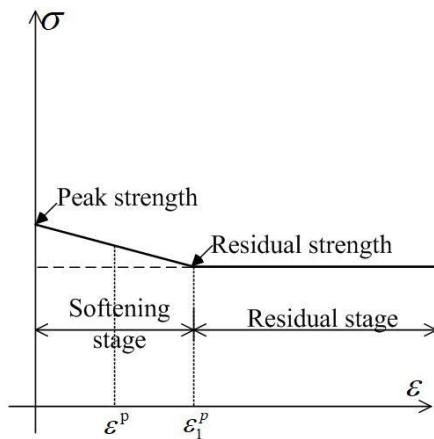
Fig. 8 - Reduction curve of the strength parameter

The curve of the MC model is presented in Figure 6, the curve of the SS model is presented in Figure 7, and the reduction curve about strength parameter is presented in Figure 8 (i.e., the detail of the curve after the peak strength in Figure 7). Obviously, the SS model is the special form about MC model. The difference is that the strength of the SS model will weaken after the plastic change begins. In FLAC3D software, the piecewise function of different strength parameters can be pre-set to represent the strain-softening phenomenon about material strength after the SS model enters the plastic stage, while the Mohr Coulomb model does not consider this weakening process. In FLAC 3D, the corresponding cohesion c and internal friction angles of different plastic shear strains can be preset in the table, so as to show the strain softening phenomenon of materials after plastic deformation. Therefore, the SS model is used as the calculation method (as shown in Figure 8) to express the softening phenomenon of material strength.

Taking cohesion as an example, its calculation equation is as followings after entering the strain-softening stage:

$$c = \begin{cases} c_0 \left[1 - \dfrac{(1-\eta_c)\varepsilon^p}{\varepsilon_1^p} \right], \left(0 \leq \varepsilon^p \leq \varepsilon_1^p \right) \\ c_0 \eta_c, \left(\varepsilon^p \geq \varepsilon_1^p \right) \end{cases} \qquad (1)$$

Where: ε^p is the plastic shear strain; $\eta_c = c_{cr} / c_0$ is the cohesion reduction rate, which reflects the degree of strength reduction after the peak; ε_1^p is the critical plastic softening coefficient, i.e., the plastic shear strain at the junction of the softening stage and the residual stage [25].

Calculation of strain-softening parameter

The key of strain softening model is to determine the law of strength parameter changing with the development of cumulative plastic shear strain [31]. The relationship between residual strength and peak strength and cumulative plastic shear strain can be determined by the direct shear test. Based on the direct shear test result of the third institution in the relying engineering project of this paper [32], using the least square method to fit the load and shear stress, the shear strength indexes of the tunnel in diatomite are obtained, as shown in Table 2. The cohesion reduction rate is η_c =48/105=0.457, and the reduction rate of internal friction angle is η_φ =35/41=0.854. The test also shows that the specimen typically undergoes three stages during the shearing process, and the typical shear force-shear displacement curve obtained from the on-site direct shear test is presented in Fig. 9. In Fig. 9, the plastic shear strain generated in the softening stage is $\gamma^p = L_{AB} / R$ =8.63/500=0.01726, R is the specimen diameter, taken as the field specimen size (namely, 500mm).

Tab. 2 - In situ direct shear test results of diatomite

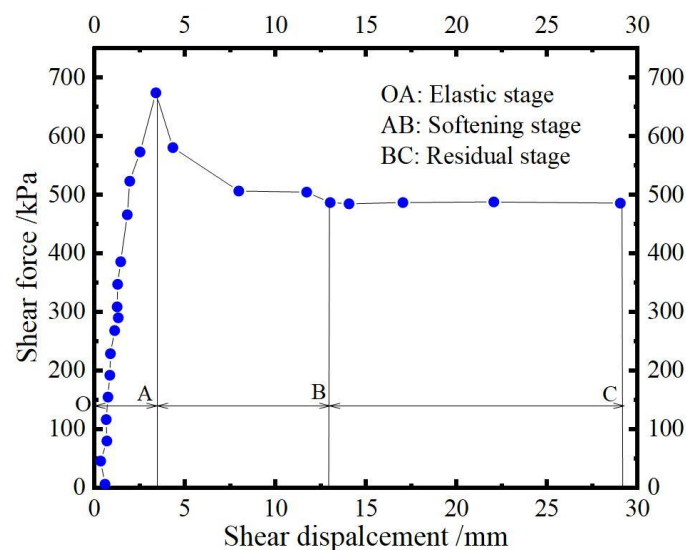| Name	c/kPa	φ/°
Peak strength	105	41
Residual strength	48	35

Fig. 9 - The relationship between the shear force and the shear displacement about diatomite

According to the literature [33], the relationship between the critical plastic softening coefficient ε_1^p and γ^p in FLAC^{3D} is:

$$\varepsilon_1^P = \frac{\sqrt{3}}{3} \cdot \frac{\sqrt{1+K_\psi + K_\psi^2}}{1+K_\psi} \cdot \gamma^P \tag{2}$$

Where $K_\psi = \frac{1+\sin\psi}{1-\sin\psi}$, ψ is the dilatancy angle of the soil. According to *Eq.* (2), when $\psi = 0$, $\varepsilon_1^p = \frac{\gamma^p}{2}$; even when ψ is very large, the relationship between ε_1^p and γ^p is close to the case of $\psi = 0$. Therefore, $\varepsilon_1^p = \frac{\gamma^p}{2}$ = 0.01726/2=0.00863 is taken in this paper.

Settlement law about tunnel in diatomite under different constitutive models

Surface settlement

The variation of surface settlement (10m, 20m, and 30m section away from the entrance of the tunnel) with excavation steps is shown in Figure 10.
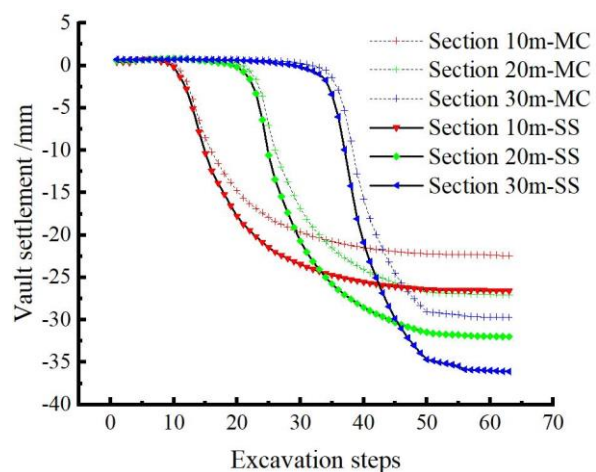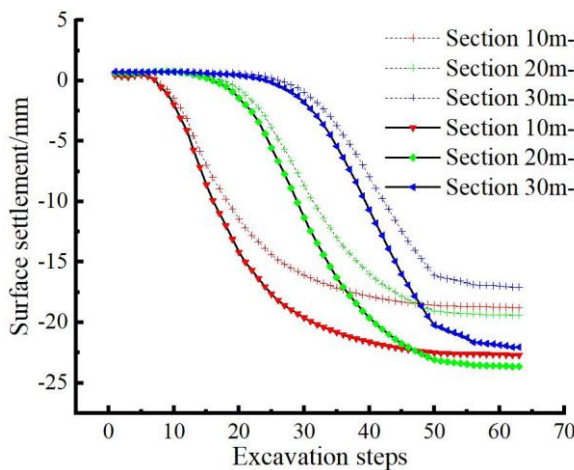
Fig. 10 - Variation curve about surface settlement with excavation step

Fig. 11 - Variation curve about vault settlement with excavation steps for each section

In Figure 10, the surface settlement trends under the two constitutive models are basically the same in a whole. When the tunnel excavation face has not been excavated to the vicinity of the target section, the surface settlement of the target section has not changed significantly. When the tunnel excavation face excavates to the vicinity of the target section, a large settlement occurs on the surface and it develops rapidly. With the increasing distance of the excavation face, the disturbance to the surface of the target section by the excavation face gradually decreases, and the surface settlement of the target section tends to be stable. It can be found that when using the MC model, the surface settlement values at the 10m, 20m, and 30m sections from the entrance of the tunnel are 18.79mm, 19.40mm, and 17.07mm respectively. Under the SS model, the surface settlement values at the 10m, 20m, and 30m sections from the entrance of the tunnel are 22.70mm, 23.64mm, and 22.05mm respectively, which are respectively 20.8%, 21.9%, and 29.2% higher than the calculation results under the MC model. It also shows that the settlement of diatomite is greater when the SS model is adopted and it is more conservative.

Vault settlement

The change law of the vault settlement of each target section under the calculation conditions of different constitutive models with excavation steps is shown in Figure 11. After the test tunnel is excavated, the change law of vault settlement along the tunnel axis is shown in Figure 12.

In Figure 11, the changing trend of calculation results of the vault settlement about the two constitutive models is basically the same, and the settlement increases rapidly with the progress of the excavation steps. However, after the excavation face passes through the target section, the settlement rate gradually slows down and eventually stabilizes. Under the MC model, the vault settlement values at 10m, 20m, and 30m sections from the tunnel entrance are 22.41mm, 27.04mm, and 29.70mm respectively. While under the SS model, the vault settlement values at 10m, 20m, and 30m sections from the tunnel entrance are 26.58mm, 31.98mm, and 36.07mm, which are 18.6%, 18.3%, and 21.4% larger than the calculation results under the MC model, respectively.
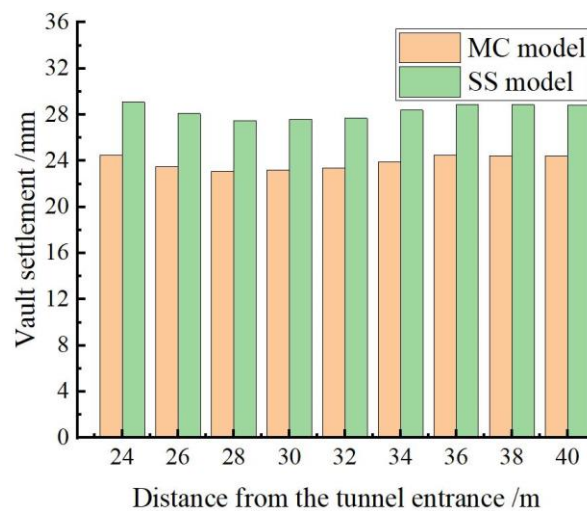
Fig. 12 - Schematic diagram of vault settlement along the tunnel axial direction

In Fig. 12, after the tunnel excavation, the vault settlement of the MC model and the SS model have similar distribution trends along the tunnel axis, and the vault settlement decreases with the progress of the excavation face. The calculation result of the SS model is even 18% higher than that of the former at the 24m section. Therefore, it is safer to use the SS model to reflect the excavation process about the tunnel in diatomite.

VERIFICATION OF THE SIMULATION THROUGH ON-SITE MONITORING

To further verify the suitable constitutive model for tunnels in diatomite, the vault settlement of the tunnel on site is monitored and measured. Some on-site monitoring pictures are shown in Figure 13.
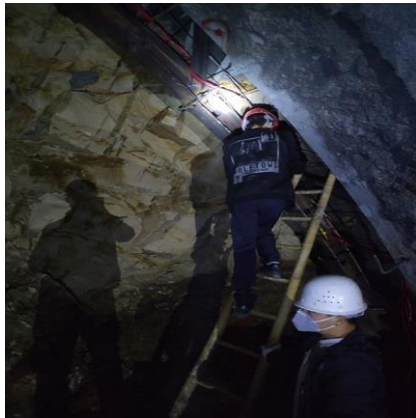
| (a) Measuring point layout | (b) Instrument installation |
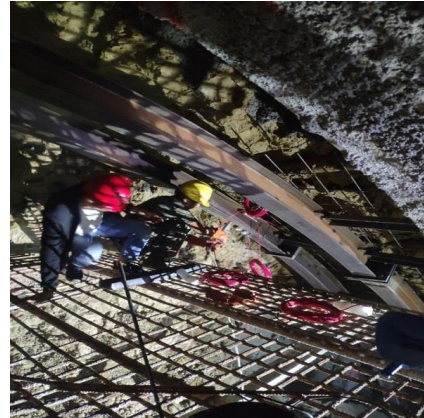
Fig. 13 - On-site monitoring pictures

When the on-site monitoring starts, the upper step has excavated to 26m, and the middle step has excavated to 24m. Based on the site conditions, the vault settlement values of measuring point A (12m from the tunnel entrance), measuring point B (15m from the tunnel entrance), and measuring point C (18m from the tunnel entrance) are selected, and the corresponding numerical calculation results of MC model and SS model are extracted and summarized, as shown in Table 3, and the specific layout of measuring points is presented in Figure 14.
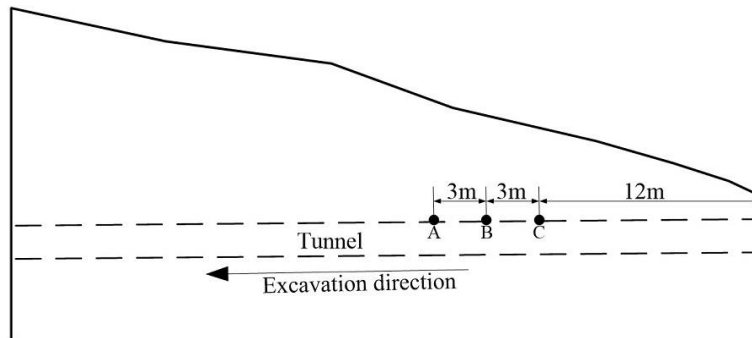
Fig. 14 - Schematic diagram about layout of measuring points along the tunnel axis

Tab. 3 - Comparison of the on-site measured values and numerical simulation values

Name		Vault settlement values of measuring points /mm		
		Measuring point A	Measuring point B	Measuring point C
Numerical simulation	MC	23.2	25.4	27
	SS	27.6	29.3	31.9
On-site measured values		29.8	31.5	33.3
Percentage difference to measured values		MC: 22.1% SS: 7.4%	MC:19.3% SS: 7.1%	MC:18.9% SS: 4.2%

It can be seen from Table 3 that when the SS model is used for calculation, the maximum percentage difference between the calculated results and on-site monitoring is only 7.4%, and the minimum is 4.2%. While the maximum percentage difference between the MC model and on-site monitoring is 22.1%. Therefore, from the above results, the simulated value under the SS model is closer to the measured value than the MC model. It also shows that for the numerical calculation of tunnel construction in the diatomite layer, the use of the SS model has higher applicability and can well reflect the settlement of surrounding rock. Taking safety into account, since the SS model

considers the influence about softening characteristic of the surrounding rock, the obtained settlement values are greater than the result of the MC model, so the SS model is closer to the actual situation and has a higher safety reserve.

CONCLUSION

Based on the Feifengshan tunnel, different constitutive models (MC model and SS model) are used to further study the settlement law about the tunnel in diatomite. Then the differences between the on-site test data and the numerical result of these two calculation models is compared and analyzed. The vital conclusions are listed below:

(1)   From the results of the on-site direct shear test of diatomite, it is concluded that the diatomite has obvious strain-softening mechanical characteristics. In the softening stage, the shear force gradually decreases after the peak shear force appears, while the shear displacement continues to increase. In the residual stage, the shear force gradually reaches a stable value, but the shear displacement continues to accumulate.

(2)   By comparing the numerical calculation results about surface settlement and vault settlement of the MC model and the SS model, it is concluded that the settlement change law of the two models with the excavation steps is similar, namely, the settlement increases rapidly with the progress of excavation steps. After the excavation face passes through the target section, the settlement rate gradually slows down and eventually stabilizes. However, it is also found that the settlement value under the SS model is much larger than that of the MC model and it is safer.

(3)   By comparing the settlement values about MC model and SS model with the on-site measured values, it is concluded that the results of the SS model are closer to the measured results than the MC model. The reason is that the MC model does not fully consider the softening characteristics of the material and cannot well reflect the softening characteristics of diatomite. Therefore, the SS model has better applicability for the numerical analysis about tunnel construction in diatomite.

ACKNOWLEDGMENTS

Competing interests

The authors have no relevant financial or non-financial interests to disclose.

DATA AVAILABILITY

All data, models, and code generated or used during the study appear in the submitted article.

REFERENCES

[1]   Day, R.B.,1995. Engineering properties of diatomaceous fill. Journal of Geotechnical Engineering, Vol. 121, 908 − 910. https://doi.org/10.1061/(ASCE)0733-9410(1995)121:12(908)
[2]   Fang, Y.Y., 2019. Study on behavior of Shengzhou diatomite considering structural effects. Master's thesis, Zhejiang University, Hangzhou.
[3]   Han, J.W., 2021. Experimental study and measures on engineering characteristics of diatomite subgrade in Shengzhou. American Journal of Traffic and Transportation Engineering, Vol.6, 95-106. https://doi.org/10.11648/j.ajtte.20210603.14
[4]   Yang, M.Y., Liu, B., 2021. Study on experimental scheme of different types of pile diatomite foundation treatment for high-speed railway. Subgrade Engineering, 85-91. https://doi.org/10.13379/j.issn.1003-8825.202106004

[5]   Li, Y., Jiang, Z.Y., Gao, W.S., et al., 2022. Field test study on reinforcement method of diatomite tunnel base. Subgrade Engineering, 89-93. https://doi.org/10.13379/j.issn.1003-8825.202011053

[6]   Chen, C., 2021. Experimental study on multi-pile reinforcement effect of diatomite foundation for highspeed railway. Master's thesis, Southwest Jiaotong University, Chengdu.

[7]   Yin, J.H. and Graham, J., 1999. Elastic viscoplastic modeling of the time-dependent stress-strain behavior of soils. Canadian Geotechnical Journal, Vol. 36, 75-105. https://doi.org/10.1051/jp4:2005129032

[8]   Liao, H.J., Su, L.J., Yin, J.H., 2004. 3-D elastic viscoplastic modeling analysis of a diatomaceous soft rock. Rock and Soil Mechanics, Vol. 25, 337-341. https://doi.org/10.16285/j.rsm.2004.03.001

[9]   Zhang, Y.S., Guo, C.B., Qu, Y.X., et al, 2012. Discovery of swelling diatomite at Tengchong, Yunnan Province and its implication in engineering geology. Journal of Engineering Geology, Vol. 20, 266-275.

[10]   Xiang, Q.M, Gao, Y.Q, Su, J.X., et al, 2022. Strata subsidence characteristics of shield tunneling in coastal soft soil area. Stavební obzor-Civil Engineering Journal, 31(3), 444-455. https://doi.org/10.14311/CEJ.2022.03.0033

[11]   Luo, J.W., Zhang, D.L., Fang, Q., et al, 2021. Mechanical responses of surrounding rock mass and tunnel linings in large-span triple-arch tunnel. Tunnelling and Underground Space Technology, Vol. 113, 103971. https://doi.org/10.1016/j.tust.2021.103971

[12]   Nguyen, T.T., Do, N.A., Karasev, M.A., et al, 2021. Influence of tunnel shape on tunnel lining behaviour. Proceedings of the Institution of Civil Engineers-Geotechnical Engineering, Vol. 174, 355-371. https://doi.org/10.1680/jgeen.20.00057

[13]   Qi, W.Q., Yang, Z.Y., Jiang, Y.S., et al, 2021. Structural deformation of existing horseshoe-shaped tunnels by shield overcrossing. KSCE Journal of Civil Engineering, Vol. 25, 735-749. https://doi.org/10.1007/s12205-020-0599-8

[14]   Zheng, Y., Wu, K., Jiang, Y.J., et al, 2023. Optimization and design of pre-reinforcement for a subsea tunnel crossing a fault fracture zone. Marine Georesources and Geotechnology, Vol. 41, 36-53. https://doi.org/10.1080/1064119X.2021.2009602

[15]   Pan, H.S., Tong, L.Y., Wang, Z.S., et al, 2022. Effects of soil-cement mixing wall construction on adjacent shield tunnel linings in soft soil. Arabian Journal for Science and Engineering, Vol. 47, 13095-13109. https://doi.org/10.1007/s13369-022-06705-9

[16]   Nam, S.W., Bobet, A., 2007. Radial deformations induced by groundwater flow on deep circular tunnels. Rock mechanics and rock engineering, Vol. 40, 23-39. https://doi.org/10.1007/s00603-006-0097-4

[17]   Wang, H.D., He, S.T., 2022. Stability analysis of surrounding rock of shallow-buried subway tunnel with small spacing under different working conditions. Geotechnical and Geological Engineering, Vol. 40, 5065-5079. https://doi.org/10.1007/s10706-022-02200-y

[18]   Huang, X., Jia, S.D., Yao, C.F., et al., 2022. Settlement analysis of dense buildings under-passed by shield tunnel considering stratum strain softening. Railway Engineering, Vol. 62, 111-116.

[19]   Gao, W.S., Wang, L.C., Zhang, H.J., et al., 2021. Analysis of the contribution of face support and primary support to the surface settlement control of shallow tunnel. Journal of Railway Science and Engineering, Vol. 18, 720-727. https://doi.org/10.19713/j.cnki.43-1423/u.t20210097

[20]   Zhao, Y., Li, X.H., Lu, Y.Y., et al., 2008. Orthogonal design of mechanical parameters in a strain softening model for deeply-buried tunnels. Journal of Chongqing University, 716-719.

[21]   Lu, Y.L., Wang, L.G., Yang, F., et al., 2010. Post-peak strain softening mechanical properties of weak rock. Chinese Journal of Rock Mechanics and Engineering, Vol. 29, 640-648.

[22]   Sun, C., Zhang, X.D., Liu, J.H., 2013. Application of strain softening model to tunnels based on Hoek-Brown strength criterion. Rock and Soil Mechanics, Vol. 34, 2954-2960. https://doi.org/10.16285/j.rsm.2013.10.029

[23]   Sun, C., 2013. The research on the strain-softening behavior of the deep joints rock and the interaction between the surrounding rock and the supporting structure. PhD thesis, Liaoning Technical University, Fuxin.

[24]   Su, Y.H., and Zou, Y.H., 2020. Stability analysis of support structure based on HOEK-BROWN strain-softening model. Journal of Central South University, Vol. 51, 453-463. https://doi.org/10.11817/j.issn.1672-7207.2020.02.019

[25]   Wang, H.B., 2014. Application of strain softening model in numerical simulation of shallow-buried soil tunnel. Master thesis, Huazhong University of Science and Technology, Wuhan.

[26]   Wang, D.Y., Tang, H., Yin, X.T., et al., 2019. Preliminary study on the progressive failure of tunnel-type anchorage based on strain-softening theory. Chinese Journal of Rock Mechanics and Engineering, Vol. 38, 3448-3459. https://doi.org/10.13722/j.cnki.jrme.2017.1497

[27] Yang, Y.B., Zheng, J.J., Zhang, R.J., et al., 2015. Comparative study on construction schemes of shallow tunnel in soft rock considering strain-softening behavior. Journal of Hydraulic Engineering, Vol. 46, 303-308. https://doi.org/10.13243/j.cnki.slxb.2015.S1.055

[28] Shi, Y.F., Cao, C.W., Tan, Y.F., et al., 2022. Study on dynamic response and long-term settlement of water-saturated weathered soft rocks at the base of subway tunnels. Modern Tunnelling Technology, Vol. 59, 86-95. https://doi.org/10.13807/j.cnki.mt.2022.02.011

[29] Qiu, J.L., Fan, F.F., Zhang, C.P., et al., 2022. Response mechanism of metro tunnel structure under local collapse in loess strata. Environmental Earth Sciences, Vol. 81, 164. https://doi.org/10.1007/s12665-022-10256-5

[30] Bai, W., Ning, M.Q., Guan, Z.C., 2023. Surface settlement characteristic of shield tunnel excavation under asymmetrical terrain condition. Journal of Fuzhou University, Vol. 51, 205-212. https://doi.org/10.7631/issn.1000-2243.22410

[31] Qiao, C.Z., 2021. Stability analysis of tunnel in water-rich and weakly consolidated conglomerate strata based on strain softening model. Master thesis, Beijing Jiaotong University, Beijing.

[32] Report of in situ direct shear test of diatomite rock on Hangzhou-Shaoxing-Taizhou Railway. Civil Engineering Testing Center of Zhejiang University, 2017, 9-12. (In Chinese)

[33] Alonso, E., Alejano, L.R., Varas, F., et al., 2003. Ground response curves for rock masses exhibiting strain-softening behaviour. International Journal for Numerical and Analytical Methods in Geomechanics, Vol. 27, 1153-1185. https://doi.org/10.1002/nag.315

STUDY ON THE REASONABLE RSR OF ARCH AND ITS INFLUENCING FACTORS IN METRO USING THE PBA METHOD

Jing Sun

Guangzhou Metro Design & Research Institute Co., Ltd, Guangdong Guangzhou 510010, China; 1011480859@qq.com

ABSTRACT

In this paper, based on the numerical calculation, the reasonable rise-span ratio (RSR) and its influencing factors of the arch in the pile-beam-arch (PBA) method are compared and analyzed, and the mechanical properties of the arch under different influencing factors (RSR, lateral pressure coefficient (LPC), and structure thickness) is further obtained. The results show that the deformation and bending moment of the arch structure decreases first and then increases with the increase of the RSR, that is, optimal RSR exists. Different LPCs have a great influence on the stress of arch structure, and the deformation and bending moment of arch structure decrease with the increase of LPC. The increase in arch structure thickness can effectively reduce structural deformation but may also lead to an increase in structural stress due to the increase in self-weight. At the same time, the comprehensive factors show that the optimal RSR increases with the increase of LPC and structure thickness, and it is suggested that the reasonable RSR should be 0.2-0.3. The rationality of the calculation is also verified by the application status of the station RSR with the PBA method in China.

KEYWORDS

Subway, PBA method, RSR, LPC, Structure thickness, Deformation law

INTRODUCTION

The PBA method is widely used in subway construction all over the country [1-3]. The main construction steps include small pilot tunnel excavation, pile-beam-column construction, initial lining, buckle arch of secondary lining, and main project excavation [4]. Among them, the arch structure is the key part of the main force system of the station. The force conversion mechanism of the structure at this position is complex, and the force conversion mainly occurs at the arch. The arch's structural form will also have a great influence on the structural force. The arch's structural form is mainly reflected in the RSR [5-7], and its safety and stability are of great significance to the entire station. Fang [8] analyzed the structural section of a subway station and concluded that for the underground excavation structure, the principle is that the arch should be arched as much as possible, and the RSR of the arch should not be greater than 1/3. Fu [9] analyzed the influence of the RSR of the inverted arch in the expansive rock stratum on the mechanical properties of the secondary lining and pointed out that the RSR of the inverted arch had the greatest influence on the inverted arch and side wall of the secondary lining. The larger the RSR, the bending moment of the secondary lining at the inverted arch and the side wall, and the axial force of the wall foot all showed a decreasing trend. Zheng et al [10] took the arch structure of the station with the PBA method as the research object and obtained the stress characteristics and surface deformation law of steel pipe columns with different RSR. Liu [11] studied the difference in the mechanical performance of bridge arch structures under different RSR. Fang *et al* [12] studied the mechanical characteristics of the tunnel and proposed some vital suggestions for practical engineering. Ma et al [13] suggested that the RSR of tunnel invert should be 1/6-1/8 in the heavy-haul railway tunnel. Based on the case of a metro collapse project in Beijing, Li et al [14] found that the failure form of a shallow buried tunnel was

related to the overburden span ratio and RSR of the tunnel, and analyzed the distribution of the plastic zone and the failure process of the tunnel. Xu et al [15] found that geological strength index has the greatest influence on the minimum RSR of long-span cavern, and the better the rock mass quality, the smaller the minimum RSR. The relationship between minimum RSR and LPC and buried depth is not linear. Huang et al [16] pointed out that the floor heave of an invert decreases with the increase of the RSR, and the larger the RSR is, the smaller the reduction is. The reasonable RSR is suggested to be 0.125 ~ 0.25. Song [17] analyzed the relationship between the stress on the invert structure and the RSR of the weakly expansion-contraction high-speed railway tunnel, and found that the maximum axial force on the invert structure was inversely proportional to the RSR, and the greater the RSR, the more significant the influence on the stress on the arch foot.

The above research mainly reflects the importance of arch structure, or mainly focus on the RSR of the tunnel invert, but there are few systematic studies on reasonable RSR and its influencing factors of arch in underground engineering. It can be seen from the engineering practice that the selection of the RSR has a great influence on the stress, construction convenience, and economy of the structure. Therefore, further exploration of the reasonable RSR can provide some guiding suggestions for the project. Therefore, based on the Tianhedong subway station project of Guangzhou Metro Line 11, the mechanical performance difference and deformation law of the arch structure of the station under different influencing factors (RSR, LPC, and structure thickness) is analyzed, and a reasonable RSR is obtained, which provides some vital reference for subsequent related research.

THEORETICAL ANALYSIS

Investigation of the station RSR with the PBA method in China

This paper collects the side span RSR ρ of the station using the PBA method in China, as shown in Table 1 and Figure 1. In Table 1 and Figure 1, the range of the side span RSR of the station with the PBA method is between 0.21 ~ 0.33, and the station with the RSR of 0.27 is the majority, which also shows that the selection of RSR in the actual project has a certain regularity.

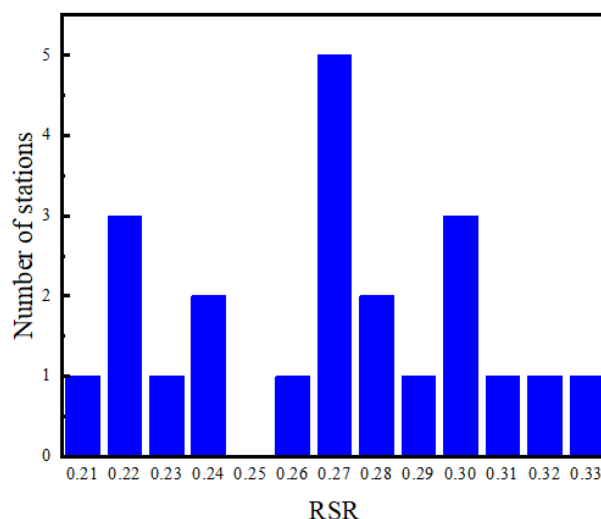

Fig. 1 - The distribution of stations number under different RSR

Theoretical analysis

The force of arch structure is simplified as shown in Figure 2. It is assumed that the arch structure is subjected to horizontal load and vertical uniform load on both sides. Since the weak point of the arch is generally at the vault, the bending moment as well as axial force at vault C is calculated

to obtain its variation with RSR (ρ= f/l). It can be seen from Figure 2 that the influencing factors of the force of vault C mainly include RSR, LPC, and structure thickness.

Tab. 1 - Application of station RSR with PBA method

Station name	ρ	Station name	ρ
Guangzhou Shahe Station	0.24	Beijing Xiangheyuan Station	0.27
Beijing Dongdaqiao Station	0.30	Guangzhou Tianhe East Railway Station	0.27
Beijing Puhuangyu Station	0.30	Guangzhou Huajing Road Station	0.22
Beijing Yonganli Station	0.29	Beijing Tiananmen West Railway Station	0.22
Beijing Financial Street Station	0.28	Beijing Chaoyang Park Station	0.28
Beijing Tuanjiehu Station	0.30	Dalian Labour Park Station	0.24
Beijing Liaogongzhuang Station	0.31	Urumqi Wangjialiang Station	0.21
Beijing Wangfujing Station	0.23	Shenyang Youth Street Station	0.22
Beijing Niujie Station	0.32	Harbin Provincial Government Station	0.27
Guangzhou Liuhua Road Station	0.33	Shenyang Chongshan Road Station	0.26
Beijing Mudanyuan Station	0.27	Shenyang Youth Park Station	0.27

The bending moment and axial force about the vault change with RSR, and the change range is determined by the coefficient K [18]. Assuming that the LPC is a, that is, $q_2 = aq_1$, the bending moment and axial force about the vault can be obtained, as shown in *Eqs.* (1) ~ (2).
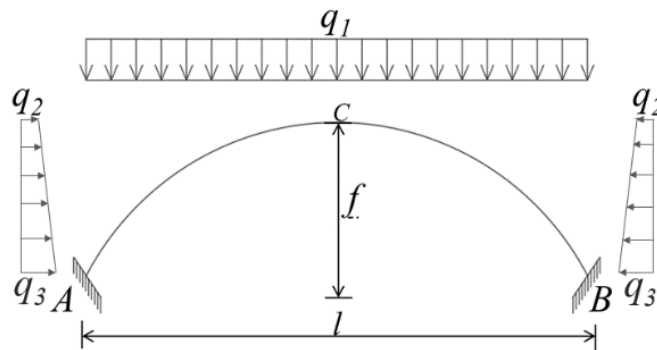
Fig. 2 – Stress diagram of the Arch

$$M_c = l^2 q_1 \left(K_1 + a\rho K_2 \right) = K_M l^2 q_1 \tag{1}$$

$$N_c = l q_1 \left(K_3 + \left(K_4 + 1 \right) a\rho \right) = K_N l q_1 \tag{2}$$

Among them, K_1, K_2, K_3, and K_4 are the coefficients that change with RSR. In addition, K_M and K_N are the coefficients of bending moment and axial force of the vault respectively. The relationship between them and RSR can be obtained by checking the table [18], as shown in Figures 3 ~ 4 (assuming that the LPC is 0.4). Note: from Table 1, it can be seen that the range of the side span RSR of the domestic PBA station is between 0.21~0.33, so the range of the RSR discussed in this paper is 0.1 ~ 0.5.

From Figures.3~4, the bending moment about the vault increases with RSR, and the axial force of the vault decreases with the increment of RSR. It also shows that for the arch structure, the selection of RSR can effectively improve the structural force and the safety of the structure.
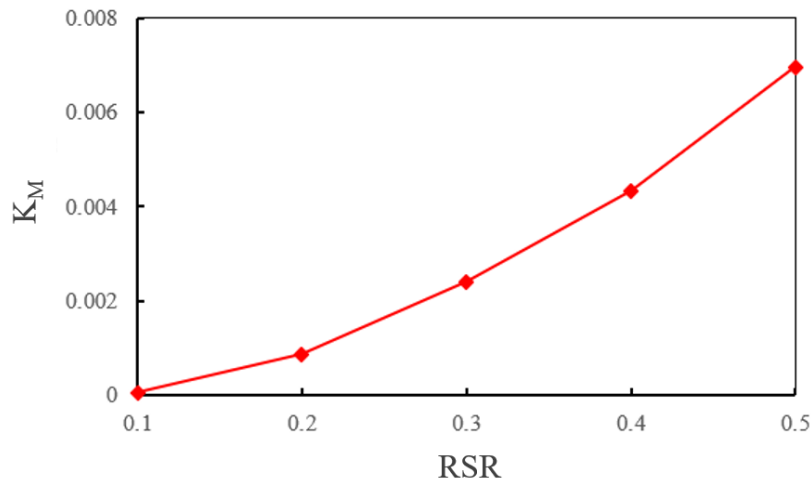
Fig. 3 - Curve of bending moment coefficient of the vault with RSR
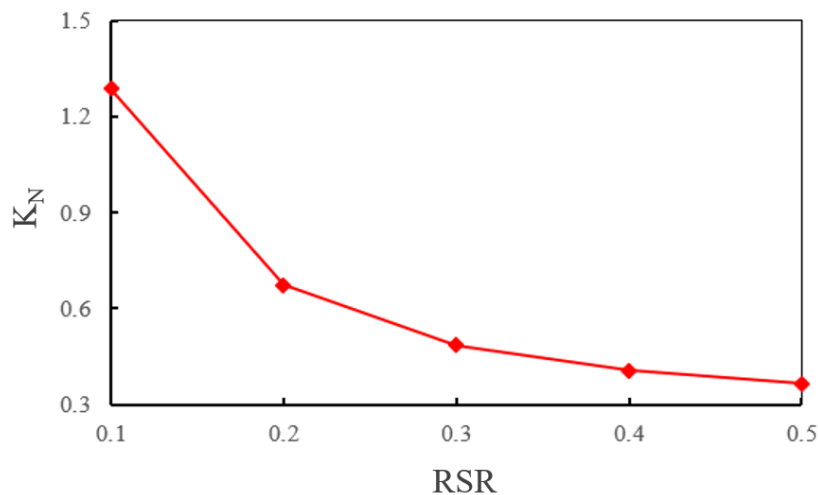
Fig. 4 - Curve of axial force coefficient of the vault with RSR

NUMERICAL CALCULATION ANALYSIS

Calculation instruction

For the arch structure, there are many factors affecting the force of the arch. Based on the theoretical analysis, this paper mainly discusses the influence of RSR, LPC, and structure thickness on the stress and deformation of arch structures. Load-structure model is adopted for this paper. ANSYS software is used for numerical calculation and analysis, the calculation model is presented in Figure 5. For the numerical simulation, the arch structure is modeled adopting the beam structure element, and the interaction between the arch structure and surrounding rock is realized by spring element. Note that the interaction springs around the arch structure can only bear compressive load, and the force of spring will set to zero when tensions appear, the outer end of the spring is fixed. The vertical load q = 400 kPa and the single arch span l= 10 m are fixed, and the horizontal load changes with the change of the LPC, and the arch height f is determined by the corresponding RSR.
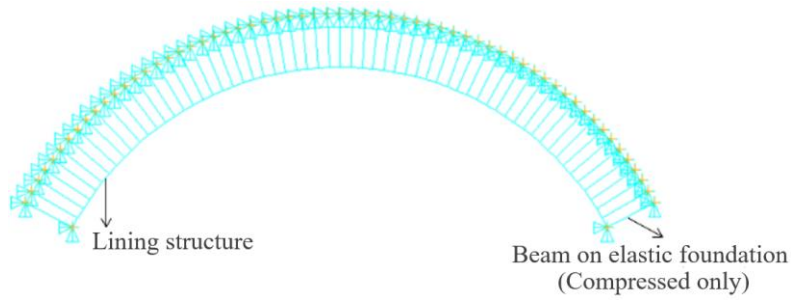
Fig. 5 - Calculation model

Calculation results and analysis

The influence of RSRs

To further explore the influence of the RSR on the arch deformation and stress, the fixed LPC and arch thickness are 0.4 and 0.35 m respectively, and the arch height *f* is 1m, 2m, 3m, 4m, 5m (i.e., the corresponding RSR is 0.1, 0.2, 0.3, 0.4, 0.5, respectively),
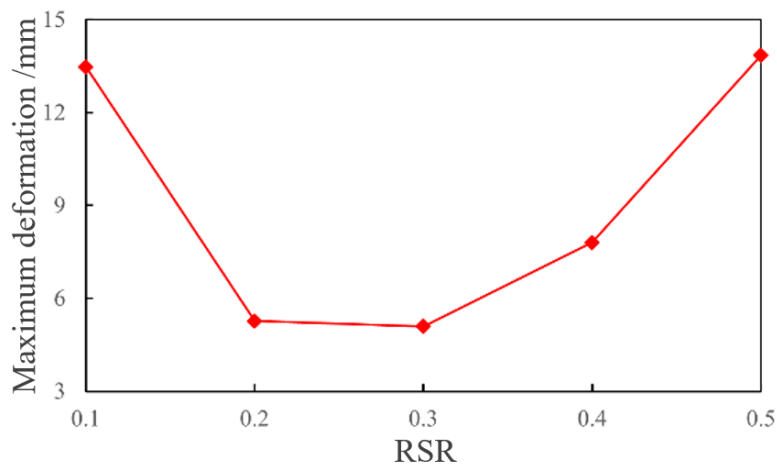
Fig. 6 - Curve of the maximum deformation of arch structure with RSR
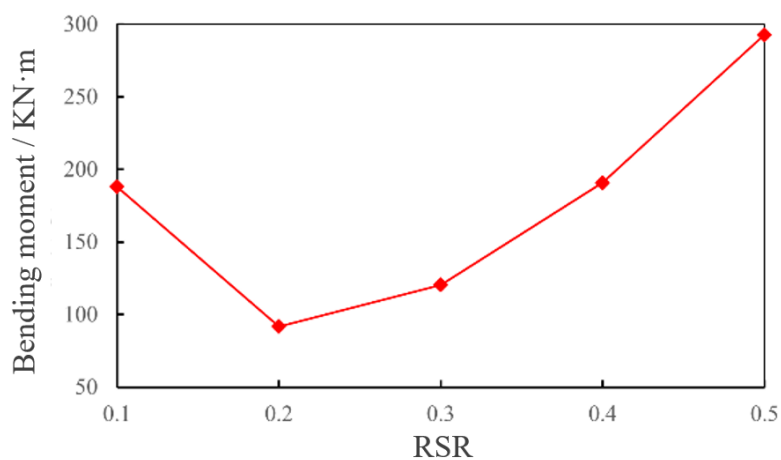
Fig. 7 - Curve of the bending moment of the vault with RSR
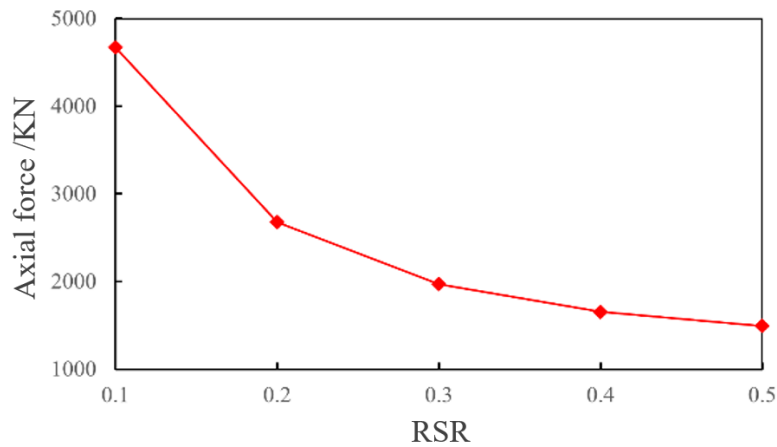
Fig. 8 - Curve of the axial force of vault with RSR

The variation law of the maximum deformation of the arch structure with RSR is presented in Figure 6, and the distribution of internal force about the vault is shown in Figures 7 ~ 8. From Figures 7~ 8, the maximum deformation and bending moment of the arch structure decrease first and then increase with RSR (i.e., from flat arch to sharp arch). When RSR is 0.5, the maximum arch deformation is 13.85 mm. When the RSR is 0.3, the maximum arch deformation is only 5.10 mm, and the reduction rate is 63.17 %. At the same time, the maximum and minimum values of the bending moment of the vault at different RSRs are 292.78 kN·m and 91.79 kN·m, respectively, and the difference reaches 68.65 %, indicating that the RSR greatly influences the deformation and stress of the arch structure. There exists optimal RSR making the stress as well as deformation about arch structure relatively minimum. Under this condition, the reasonable RSR is between 0.2 and 0.3, which is consistent with the investigated 0.21-0.33 in the previous section.

Besides, the axial force of the vault gradually decreases with the increase of RSR, and there is a sharp downward trend at RSR = 0.2, indicating that the increase of the RSR can also effectively improve the axial force of the arch structure.

The influence of LPCs

Fix the RSR and structure thickness at 0.3 and 0.35m respectively, and the LPCs are taken 0, 0.2, 0.4, 0.6, and 1.0 respectively, the influence of LPC on the deformation and stress of the arch is studied. The distribution of maximum deformation and internal force of arch structure under different LPCs are calculated, as shown in Figures. 9 ~ 11.
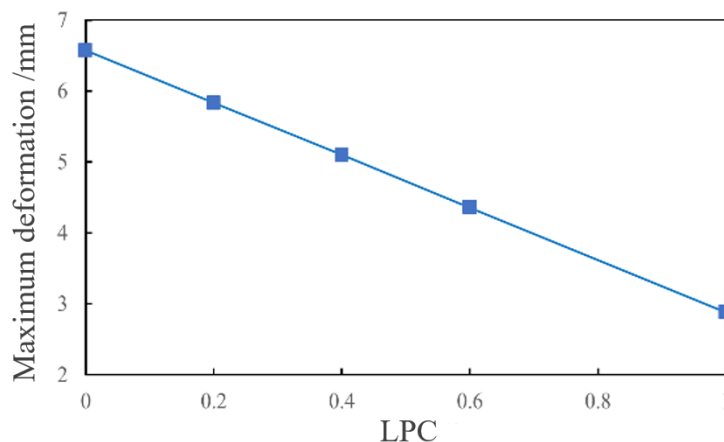
Fig. 9 - Curve of maximum deformation of arch structure with LPC
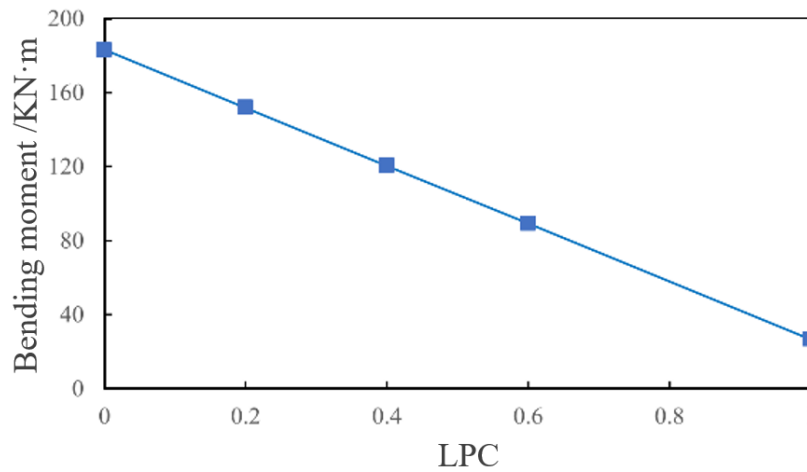
Fig. 10 - Curve of the bending moment of the vault with LPC
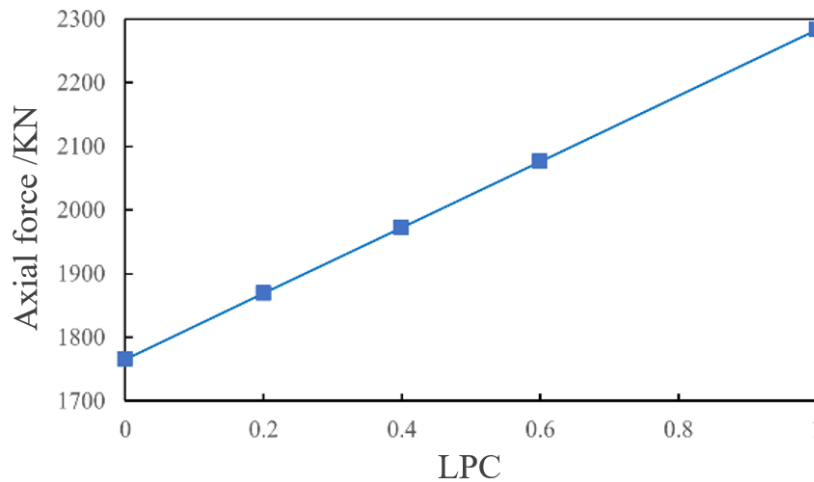
Fig. 11 - Curve of the axial force of vault with LPC

From Figures 9~11, the deformation and bending moment of the arch decrease with the increase of the LPC, while the axial force of the vault increases gradually and is linearly related. When the LPC is 0~1, the maximum deformation values of the vault are 6.57 mm and 2.88 mm, the bending moment values are 183.14 kN·m and 26.66 kN·m, and the axial force is 1765.44 kN and 2283.51 kN. It shows that LPC greatly influences the arch structure, and LPC is closely related to the surrounding rock conditions. Therefore, more attention should be paid to the surrounding rock conditions in the design of the station structure to improve the force as well as the deformation of the structure.

The influence of structure thicknesses

Fix RSR and LPC at 0.3 and 0.4 respectively, and the structure thickness is taken as 0.35m, 0.5m, 0.65m, 0.8m, 1m, and 1.2m respectively to study the impact of structure thickness on the deformation and stress of arch. The calculation results are shown in Figures 12~14.
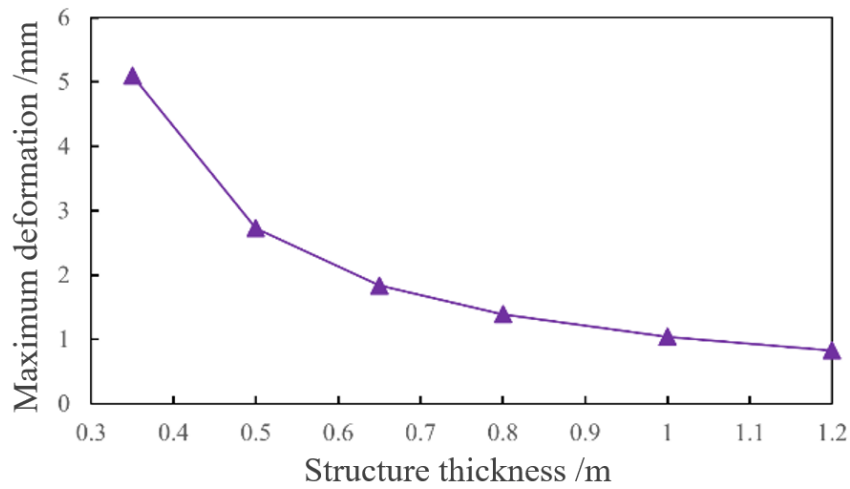
Fig. 12 - Curve of the maximum deformation of arch structure with structure thickness
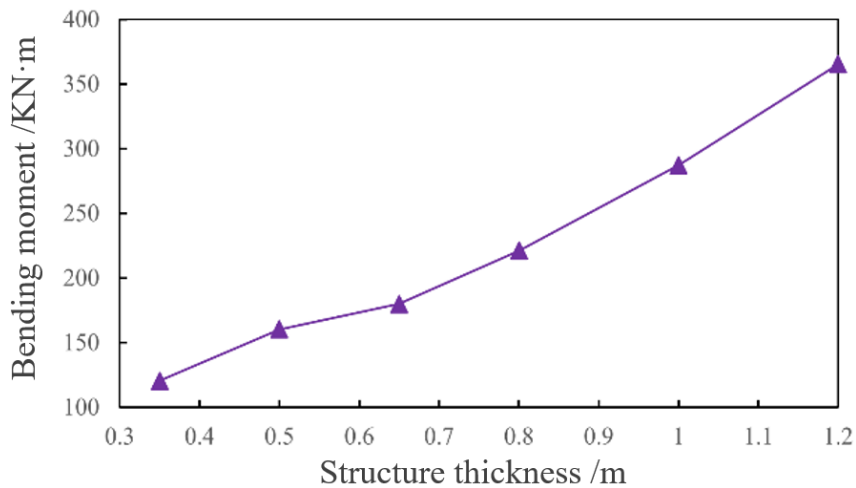
Fig. 13 - Curve of bending moment of the vault with structure thickness
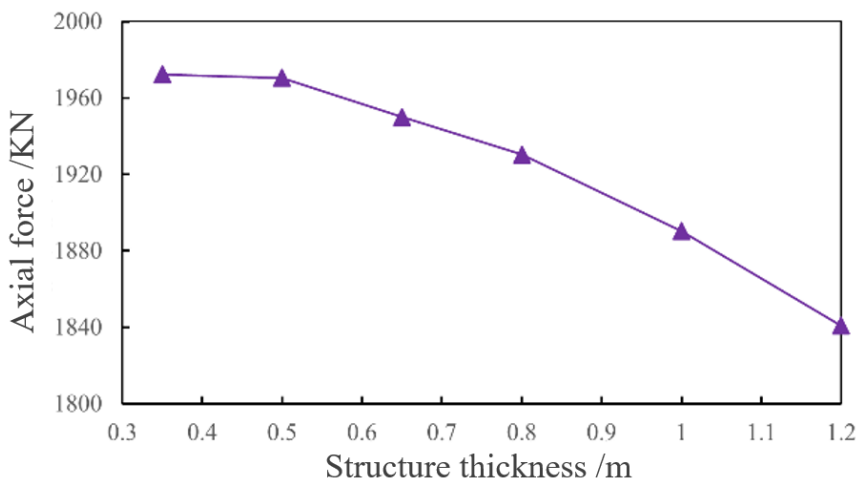
Fig. 14 - Curve of the axial force of vault with structure thickness

From Figures 12~14, as the thickness of the arch structure increases, the deformation of the arch structure gradually decreases, and the bending moment about the vault gradually increases. Since the structural stiffness increases with structure thickness, which can effectively reduce the deformation of the structure. However, the increase in structure thickness also leads to the increase

of structure self-weight and increases its vault bending moment, and has no significant effect on the axial force of the vault.

Comprehensive analysis

To further study the influence of RSR, LPC, and structure thickness on the safety of the arch, the influence of LPC-RSR and RSR-structure thickness on the safety factor of the vault are discussed respectively. The following is the variation law of the safety factor of the vault of the LPC =0 ~ 1.0 and the structure thickness = 0.35m ~ 1.2m when RSR is 0.1 ~ 0.5.

When the fixed structure thickness is 0.35 m, the safety factor of a vault under different RSRs and LPC conditions is calculated, as shown in Figure 15.
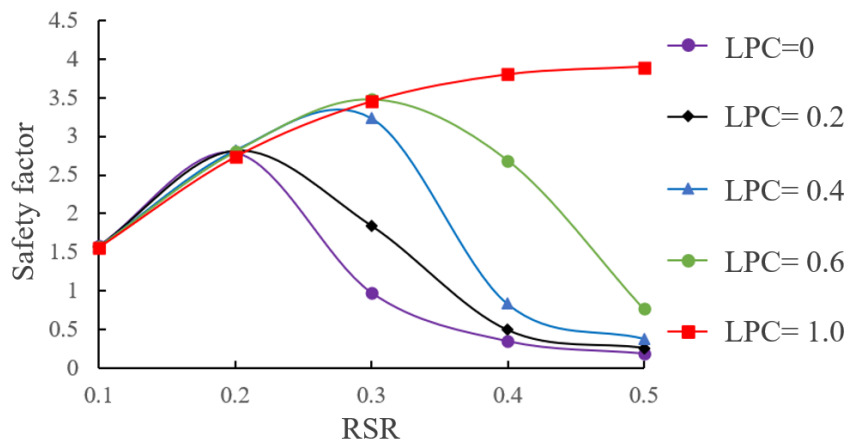
Fig. 15 - Curve of the safety factor of the vault with RSR (different LPC)

From Figure 15, within the range LPC=0-0.6, the safety factor about the vault increases first and then decreases with RSR. When LPC=1.0, the safety factor about the vault increases with RSR. It can be also found that with the increase of LPC, the largest safety factor about the vault needs larger RSR, and even no largest safety factor appears when LPC=1.0. The safety factor varies greatly with different LPCs. The larger the LPC, the greater the safety factor of the vault. It can also be seen that the larger the RSR, the greater the influence of LPC on the safety factor of the vault. In general, when RSR is between 0.2~0.4, the vault safety is high.
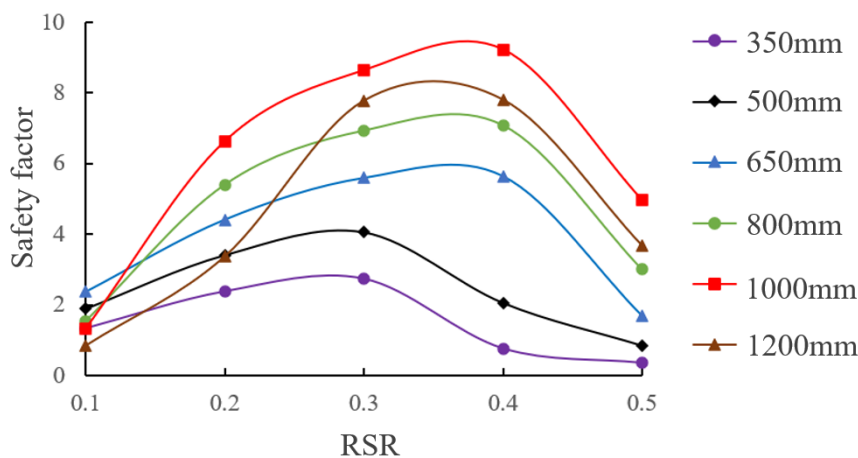
Fig. 16 - Curve of the safety factor of vault with RSR (different structure thickness)

When the LPC is fixed at 0.4, the safety factor of the vault under different RSRs and structure thickness is calculated, as presented in Figure 16. The vault safety factor increases first and then decreases with RSR, and when the structure thickness is no more than 1 m, vault safety factor increases with structure thickness. The safety factor at the structure thickness = 1.2 m is less than

that of the structure thickness = 1 m, indicating that increasing the structure thickness after the structure thickness reaches 1 m does not continuously increase the safety of vault. At the same time, it can be seen that the greater the structure thickness, the greater the RSR corresponding to the maximum safety factor, indicating that when the structure thickness increases, the better RSR can be also increased.

CONCLUSIONS

(1)   When the structure thickness and LPC are fixed, the deformation and bending moment of the arch structure decrease first and then increase with RSR. The difference in deformation and bending moment under different RSRs is 63.17 % and 68.65 % respectively, which shows that RSR greatly influences the deformation and stress of arch structure, and there exists optimal RSR making the bending moment and deformation of arch structure relatively minimum. It is suggested that the reasonable RSR is 0.2 ~ 0.3.

(2)   When the structure thickness and RSR are fixed, the deformation and bending moment of the arch decrease with the increase of the LPC, and the axial force of the vault increases gradually and linearly. When LPC is 0~1, the deformation of the arch structure and the bending moment of the vault are reduced by 56.16 % and 85.45 % respectively, indicating that LPC has a great influence on the arch structure. LPC is closely related to the surrounding rock conditions, so attention should be paid to the surrounding rock conditions when designing the station structure.

(3)   When RSR and LPC are fixed, the deformation about arch structure decreases with the increase of structure thickness, and the bending moment of the vault gradually increases. This is mainly because the structure stiffness increases with structure thickness, which can effectively reduce the structural deformation. However, the increase in the structure thickness increases the structure 's self-weight, thus increasing the bending moment of the structure itself, while the influence on the axial force is not significant.

In addition, LPC can improve the optimal range of RSR to a certain extent, and the influence law of structure thickness is similar to that of the LPC.

Competing interests

The authors have no relevant financial or non-financial interests to disclose.

DATA AVAILABILITY

All data, models, and code generated or used during the study appear in the submitted article.

REFERENCES

[1]   Fang, X., 2013. Research on construction mechanical behavior of subway station with PBA cave-pile method and space-crossing structure. Master thesis, Southwest Jiaotong University, Chengdu.

[2]   Yu, L., Zhang, D.L, Fang, Q., et al, 2019. Surface settlement of subway station construction using pile-beam-arch approach. Tunnelling and Underground Space Technology, Vol. 90: 340-356. https://doi.org/10.1016/j.tust.2019.05.016

[3]   Huang, B., Du, Y.H, Zeng, Y., et al, 2022. Study on stress field distribution during the construction of a group of tunnels using the pile-beam-arch method. Buildings, Vol. 12: 300. https://doi.org/10.3390/buildings12030300

[4]   Luo, F.R., Wang, Y.H., Hao, Z.H., 2015. The key technology of tunnel pile design and construction of subway station, 29-65 (China Railway Press).

[5]   Zhong, Z.L., Liu, A.R., Pi, Y.L., et al, 2020. In-plane dynamic instability of a shallow circular arch under a vertical-periodic uniformly distributed load along the arch axis. International Journal of Mechanical Sciences, Vol. 189: 105973. https://doi.org/10.1016/j.ijmecsci.2020.105973

[6]   Hu, C.F., Pi, Y.L., Gao, W., et al, 2018. In-plane non-linear elastic stability of parabolic arches with different rise-to-span ratios. Thin-Walled Structures, Vol. 129: 74-84. https://doi.org/10.1016/j.tws.2018.03.019
[7]   Vo, D., Nanakorn, P., 2019. Large displacement analysis of pinned-fixed circular arches with different rise-to-span ratios using an isogeometric approach. In: Proceedings of the 16th East Asian-Pacific Conference on Structural Engineering and Construction. Singapore, 951-960. https://doi.org/10.1007/978-981-15-8079-6_89
[8]   Fang, Z.B., 2016. Reasonable section form design of underground excavation entrance and exit of subway station. China Water Transport, Vol. 16: 230-232.
[9]   Fu, Y.P., 2018. Influence of rise-span ratio of double track tunnel inverted arch on mechanical properties of secondary lining in swelling rock stratum. Railway Engineering, Vol. 58: 64-66. https://doi.org/10.3969/j.issn.1003-1995.2018.08.16
[10]   Zheng, L.G., Chang, L.F., Jiang, H., et al, 2022. Stress characteristics of concrete-filled steel tubular column and surfacedeformation in pile-beam-arch station with different rise-span ratios of arch:a case study of Xiangheyuan Station on Beijing Metro Line 17. Tunnel Construction, Vol. 42: 174-182. https://doi.org/10.3973/j.issn.2096-4498.2022.S1.020
[11]   Liu, H., 2015. Research on the design of rise-span ratio in arch structures. Master thesis, Changsha University of Science and Technology, Changsha.
[12]   Fang, W., Zhang, H.J., Gao, S.F., et al, 2022. Mechanical characteristics and deformation law of tunnel in diatomite considering various softening conditions. Stavební obzor-Civil Engineering Journal, Vol.31: 504-515. https://doi.org/10.14311/CEJ.2022.03.0038%20
[13]   Ma, W. B., Chai, J. F., Han, Z. L., et al, 2020. Research on design parameters and fatigue life of tunnel bottom structure of single-track ballasted heavy-haul railway tunnel with 40-ton axle load. Mathematical Problems in Engineering, Vol. 2020: 3181480. https://doi.org/10.1155/2020/3181480
[14]   Li, S., Zhang, D.L., Li, Z.J., 2012. Study on mechanism of collapse based on shallow buried subway tunnel of Beijing. Journal of Beijing Jiaotong University, Vol. 36: 24-29.
[15]   Xu, Q., Wu, J.Y., Chu, W.J., 2021. The research on the smallest rise-span ratio of large span cavern. Journal of Chongqing University, Vol. 44: 119-130. https://doi.org/10.11835/j.issn.1000-582X.2021.01.013
[16]   Huang, H., Yu, Y., Yang, C.Y., et al, 2021. Research on the deformation regularity and treatment measures of tunnel floor heave in gently inclined layered surrounding rock. Journal of Railway Engineering Society, Vol. 38: 72-78.
[17]   Song, F., 2021. Research on causes of floor heave and invert arch structure of weakly swelling-shrinking tunnels for high-speed railway. Journal of Xi'an University of Science and Technology, Vol. 41: 481-489. https://doi.org/10.13800/j.cnki.xakjdxxb.2021.0313.
[18]   Yao, J., 2014. Practical manual for static calculation of building structures, 241-286 (China Architecture and Building Press).

FUNCTIONAL USE OF THE AREA OF PRAGUE CASTLE WITH EMPHASIS ON THE NORMALIZATION PERIOD

Martin Šnorbert

Czech Technical University in Prague, Faculty of Civil Engineering, Department of Architecture, Prague, Thákurova 7, 166 29 Prague 6 - Dejvice, Czech Republic; martin.snorbert@fsv.cvut.cz

ABSTRACT

This paper deals with individual typological parts and units in the Prague Castle area. It also focuses on the urban and historical development, as it is significantly influenced by the situation in the period under study. It focuses more closely on the period of the second half of the 20th century, and especially the period of normalization - the 1970s and 1980s.

Prague Castle was and still is the seat of the monarch, or today the President of the Czech Republic. The historical context has had a considerable influence on the shape of the Castle (the succession of ruling personalities from different dynasties, the transformation from the position of the seat of the Habsburg monarchy and therefore the most important center in Central Europe to the position of the summer residence of the ruling family, etc.). Also the concentration of the main buildings of secular and ecclesiastical power in one area is unprecedented. The castle is a huge complex, combining morphological assumptions with the result of the work of a huge number of people. A number of foreign artists worked here, reaching world-class standards and both understanding and supporting the local genius loci. There are also many contrasts - political and constructional. For example, the imprints of monarchy and republic, church and secular power, ancient and modernist architecture, contrasts among the smallest buildings of houses and the largest palaces.

On the basis of archival research and the study of expert literature, the reader is introduced to the progressive changes in the layout of the Castle complex and the associated changes in the functional use of the buildings and spaces in the aforementioned complex.

KEYWORDS

Prague Castle, Urban development, Functional use, Typological units, Normalization

INTRODUCTION

At the beginning of this article, for the better imagination of the readers and understanding of the discussed issues, an orthophoto (Figure 1) with the position of Prague Castle within the capital city of the Czech Republic - Prague - is attached. The picture next to it (Figure 2) shows the area of the Prague Castle from an aerial view. For even better orientation within the Castle grounds, an official map from the Prague Castle Administration with the marking of individual objects is attached (Figure 3).
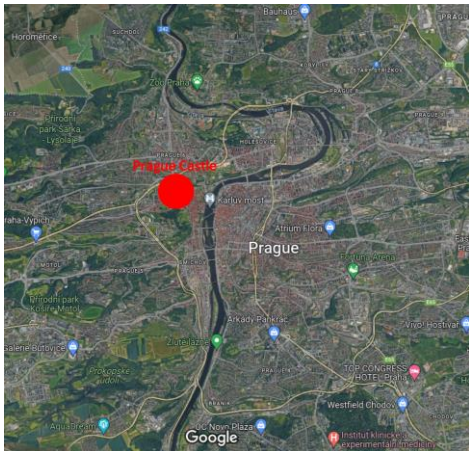
Fig. 1 – Marking of the Prague Castle on the basis of orthophoto [1]

Fig. 2 – Prague Castle from an aerial view [2]

Fig. 3 – The area of Prague Castle on the official map for tourists with marking of accessible objects [2]

The Prague Castle is a magnificent complex where every visitor and user can find his or her own: authentic historical environment, precious architectural monuments, rich art collections, awe-inspiring silence of the temple interiors, beautiful and romantic corners, remarkable exhibitions or concerts, relaxation in the gardens, spectacular show during the changing of the castle guard and breathtaking views of the city. In addition to this, it can also be seen the manifestations of efforts to preserve this beautiful area. Complex renovations, costly and demanding maintenance, restoration

work, archaeological and building history research are and have been continuously taking place at the Castle.

The Prague Castle is a very exceptional case of the use of a castle, a former monarchist residence, as a presidential seat. Much more often we encounter the typological unit of the presidential palace [3], which is usually mono-functional. In the immediate vicinity, we can mention a Slovak example (Grasalkovič Palace) and a Hungarian example (Sándor Palace). A very famous example is the Elysee Palace in France.

A similar theme of the functional use of castles and palaces has been dealt with in a number of academic articles, but mostly with reference to the reuse of these spaces, as their maintenance has been neglected. The old spaces are being renovated and new tourist attractions are being created, often related to the original use of the premises such as museums, galleries [4], [5]. Some articles point to a completely different use of the rooms - the conversion of a palace into a nursing home [6].

The functional use of the Prague Castle was recently explored by Elena Fialková, who, while studying at UMPRUM (University of Arts and Crafts in Prague), examined the current use of the Castle and also sought to redefine this space to serve democracy in the 21st century. She wrote her diploma thesis entitled Redefining Prague Castle and several articles on this topic have been published in the Czech press. The topic even resurfaced before the last presidential election, when the national media (Czech TV; Czech radio; Czech news websites as Aktuálně.cz, Seznam Zprávy; national daily and weekly newspapers) focused on the possibility of moving the president's seat from the Prague Castle to another suitable space.

NORMALIZATION AND ITS IMPACT ON ARCHITECTURE

Normalization is a period of Czechoslovak history from the violent suppression of the Prague Spring in August 1968 to the Velvet Revolution in November 1989. After the violent entry of Warsaw Pact troops into Czechoslovakia in August 1968, a Czechoslovak political delegation went to Moscow to negotiate with the Soviets on the way forward. The Moscow Protocol was signed there. Later, the Central Committee of the Communist Party of Czechoslovakia (1970) approved the document Lessons from the Crisis Development in the Party and Society after XIII. Congress of the Communist Party of the Soviet Union. "In this document, the Czechoslovak leaders expressed their determination to achieve the normalisation of conditions in our country on the basis of Marxism-Leninism, to restore the leading role of the Party and the authority of the state power of the working class, to eliminate counter-revolutionary organisations from political life and to strengthen the international ties of the Czechoslovakia with the Soviet Union and other socialist allies. Husák, V. Biľak and other politicians taking clear class internationalist positions." [8]

The normalization of conditions in many cases meant repressive measures against inconvenient persons, purges in the Communist Party (reformist Communists were removed), dismissals from employment, the restoration of censorship, and the dismantling of inconvenient interest and political associations and organizations. [9] The same was happening in the field of architecture. After August 1968, there were purges and checks in the Union of Architects, and some architects were expelled. Fortunately, unlike in the 1950s, they did not end up in prison, but very often lost their jobs. The ban on publishing and participating in architectural competitions was a huge blow to their freedoms. This culminated in 1971 when the independent Union of Architects of the Czechoslovakia was dissolved. A year later, a new pro-communist Union of Architects of the Czechoslovak Republic was established, which at its first meeting approved the Analysis of the Activities of the Former Union. This Analysis criticized the activities before January 1968 and during the crisis period of 1968-1971, and listed 26 architects who, although they could continue their work, were removed from public life [10].

TYPOLOGICAL UNITS IN HISTORY

Over the course of several centuries, the layout and the functional use of the area of the Castle changed. However, since the pre-Slavic settlement (the hillfort) we can find here typological types related to the administration of the area and later the whole territory of the Bohemian lands. This function was first provided by a wooden princely palace, later by a stone castle [11]. To this we can add the dwelling of the castellan, the houses of the prince's (king's) retinue, courtiers and servants. The palace thus also contained office and storage space (the great development of this function came in the Classical period and was associated with the rebuilding of Nicola Pacassi), but also representative spaces - first one large hall where entertainment took place - for example, jousting, musical recitals and audience with the prince (later king).
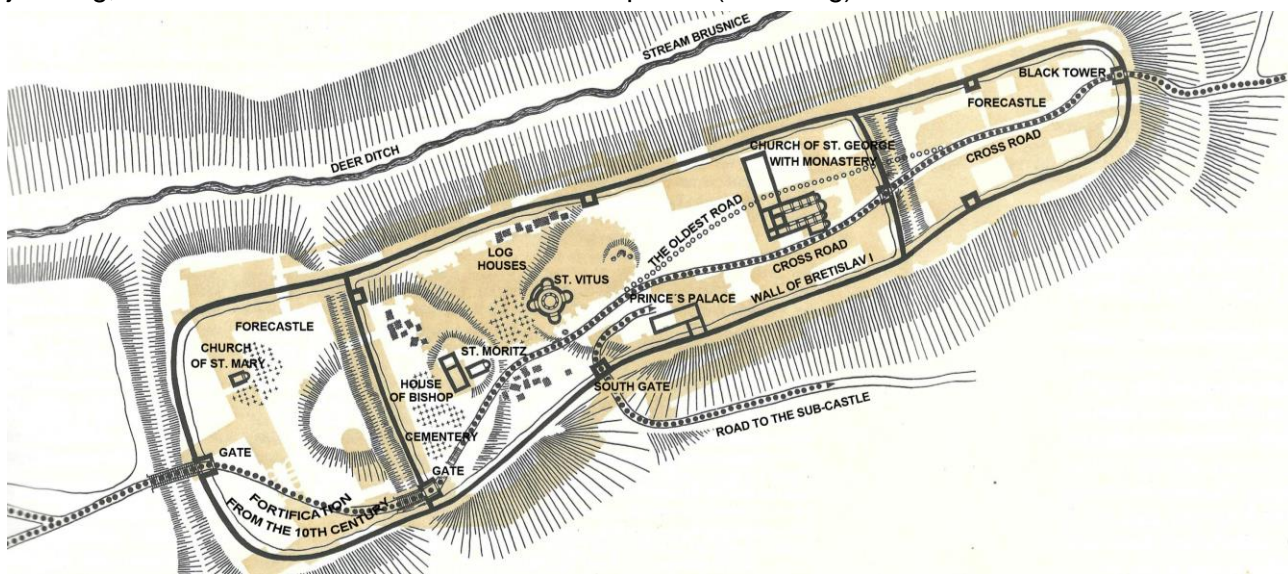
Fig. 4 – Reconstruction of a pre-Romanesque hillfort - the predecessor of today's Castle. The main buildings are the princely palace, the rotunda of St. Vitus, the three-nave basilica of St. George, the bishop's house with the chapel of St. Moritz, several towers and gates, log buildings of peasants and servants, cemeteries. Colour suite according to the stable cadastre of 1879 [12], page 62

In the course of further development, the number of representative halls and rooms increased (for example, under Rudolf II the present Spanish Hall and Rudolf's Gallery were built, under the Jagiellonians the Vladislav Hall - the throne room, Vladislav's Bedroom - the audience hall). Other rooms (typological types) also appeared in the palace - royal rooms, palace rooms, later the president's apartment, the Chamber of Deputies, the governor's offices, the gallery for collections of rarities and curiosities (again, the personality of Emperor Rudolf II should be mentioned), the Institute of Noblewomen (it was an institute headed by an abbess, it served for the education, care and training of young ladies from noble families) [13].

The Castle was also the ecclesiastical center of the whole region - the rotunda of St. Vitus (later the basilica, and even later the cathedral of St. Vitus, Wenceslas and Vojtěch), the basilica of St. George, to which a women's monastery with a paradise court was attached, and above all the building of the bishop's palace with the chapel of St. Moritz. Some church buildings have disappeared over the centuries (St. Bartholomew's Church, St. Mary's Church, various chapels, bell towers). There were also other associated buildings and structures, such as the purgatory building, the St. Vitus Chapter House, the canons' dwellings and court, and the servants' houses. During the Baroque period, the Archbishop's Palace moved outside the Prague Castle grounds, but remained in its immediate vicinity on Hradčany Square. The cathedral remained unfinished for a long time, the first initiative was taken under Charles IV, the construction was stopped by the Hussite wars, then there were two attempts to continue the construction - under Vladislav Jagellonsky the foundations of the northern tower were laid, Leopold I had the pillars of the baroque triple tower built (in 1673). In the

interior, more changes took place. In the second half of the 19th century, the final completion began, which ended in 1929.

Of course, there were also farm buildings and yards in the area, the Royal Garden was founded during the Renaissance under the Habsburgs, and other gardens were gradually established. The restoration led by Josip Plečnik contributed to the increased interest in these gardens; he enriched the interconnected gardens with views, pavilions and small architecture. Some of the gardens used to grow vegetables and fruit. Vineyards could be also found here. Rudolf II built a game preserve for deer in the gorge of the Brusnice stream. At his instigation, he also built a brick Lion Court (for breeding lions and other beasts), a pheasantry, a pond, an aviary, an orangery, a fig tree and a summer riding arena. The castle also had stables, greenhouses and Rudolf II built vaulted Renaissance stables in the north wing for Spanish horses. The premises are currently adapted for exhibition purposes. The grounds also included a bear farm for a period of time. The grounds were also occupied by craftsmen, the last remnant of their small dwellings being the Golden Lane. In the 16th century goldsmiths lived here (the original name was Goldsmith's Alley). The houses were demolished when the walls were repaired under Rudolf II. The Emperor allowed the castle archers to demolish the dwellings here. There used to be a carpenter's corral in the Riding Yard, gradually other stables and residential and economic buildings were built here - for example, a hunter's house, a falconer's house, a stable with a forge. The stable yard included a mason's house (formerly the dwelling of the ballroom keeper), a gardeners' house and a Renaissance house. The foundry yard was adjacent to the castle foundry, which was built during the reign of Rudolf II. [14]

Especially at the beginning, the defensive function was also important, so we can find several buildings serving this purpose - for example towers, gates, bastions, barracks, armouries, gunpowder stores, artillery laboratory (in the Classical period in the building of the summer palace), gun bastions and gun towers (during the Jagiellonian period). The Romanesque White Tower was used as a prison in the Middle Ages, Rudolf II had moved the prison to the so-called New White Tower at Golden Lane. There is also a well-known legend connected with the tower called Daliborka. Mention must also be made of the reign of Joseph II, which brought about quite a lot of unfortunate interventions in the area in question. The Emperor put the Great Ballroom, the Royal Summer Palace, the Riding School and the Monastery of St. George at the disposal of the army, which damaged these objects by improper treatment. He even auctioned off the remains of the Rudolphine collection. The government of Joseph II, however, was much more comprehensive, and his reformist Enlightenment efforts in particular have been positively evaluated. [15].

PRAGUE CASTLE AT THE BEGINNING OF THE 16TH CENTURY

1 West Gate
2 West Palace
3 White Tower
4 Chapter Provost´s Office
5 St. Vitus Cathedral
6 Foundations of the North Tower
7 Royal Palace
8 Church of All Saints

9 Mihulka (Tower)
10 Basilica and Monastery of Saint George
11 New White Tower
12 Purgatory
13 Daliborka (Tower)
14 Black Tower
15 Barbican
16 Cannon Bastions
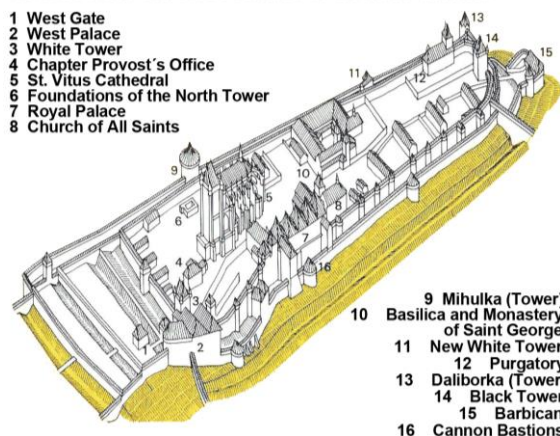
Fig. 5 – Prague Castle during reign of Vladislav Jagellonsky (early 16th century [16], page 14

PRAGUE CASTLE AT THE BEGINNING OF THE 17TH CENTURY

1 West Gate
2 Wicked for New Castle Stairs
3 Powder Bridge
4 White Tower
5 Mathematical (Bishop´s Tower)
6 Rudolph's Palace (Sommerhaus)
7 North Wing
8 St. Vitus Cathedral
9 Foundry
10 Mihulka (Tower)

11 Royal Palace
12 Church of All Saints
13 Basilica and Monastery of Saint George
14 Rožmberk Palace
15 Pernštejn Palace
16 New White Tower
17 Daliborka (Tower)
18 Black Tower
19 Garden of Eden
20 Burgler´s Tower

Fig. 6 – Prague Castle during reign of Rudolf II (early 17th century) [16], page 16

In the considered area there were (some still are) objects and spaces used for recreation, entertainment and sports. The Queen Anne's Summer Palace with the adjacent Royal Garden is a prime example. Other gardens with their fountains and pavilions were also used for relaxation and

tranquillisation. The Great Ball House was built between 1567-69, by which time it was the third building used for ball games. In the Baroque period it was converted into a riding hall and stables. The Riding Hall and the Riding Court were also built in the same period. These buildings were built during the stay of Emperor Leopold I in Prague (1679-1680). During these years, the castle came alive with festivities, balls and theatrical performances. The lion court with wild beasts was mentioned earlier. Rudolf's game preserve used to be in the Deer Moat. There was also an opera theatre (burnt down in 1747) and other theatres in the castle grounds, and in the second half of the 20th century the Summer Stage was built here. The St. John's Day festivities held on the occasion of the canonization of St. John of Nepomuk (the patron saint of the Czech lands) must also be mentioned. During the preparations, a chapel of this saint was built at the Basilica of St. George.

As the centre of the whole kingdom, this area also had a certain commercial function. The most important market in the early Middle Ages was located in the sub-castle of Prague Castle.

Prague Castle is also associated with art and since the 19th century with tourism - since the time of Rudolf II, art objects and works of art have been collected and exhibited (e.g. in the Rudolf Gallery, in the Castle Picture Gallery, in the Treasury - for the Crown Jewels, for various treasures).

TYPOLOGICAL UNITS IN THE STUDIED PERIOD

The communist regime preached revolution, but at the same time its representatives were aware that they had to symbolically continue history, and therefore the residence of President Gottwald had to remain at Prague Castle, and no new government building was considered. Despite its proclaimed openness and accessibility to the common people, the Gottwald government tended to close it down. This complex was perceived primarily as the residence of the President and a space of state representation. Fortunately, this attitude changed after 1953.

The period of the second half of the 20th century is characterised by adaptations, conversions and reconstructions of existing buildings. Many new buildings were not built here - an exception is the construction of garages and car workshops of the Office of the President of the Republic on the site of the former open summer riding hall. Another example is the modern extension of the entrance wing and atrium at the Supreme Burgrave´s Hou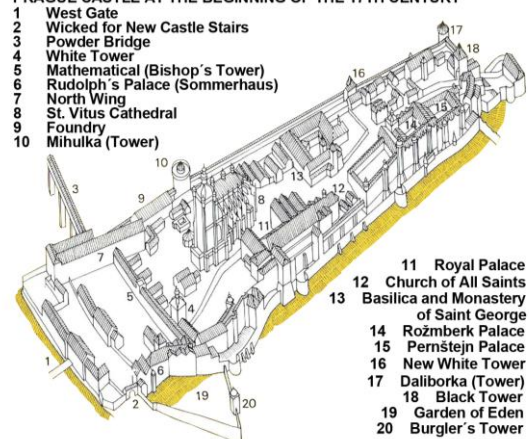se, which became the so-called House of Czechoslovak Children (unfortunately, the new building has not survived to this day, and the building of the Supreme Burgrave´s House housed the Leica Gallery after the Velvet Revolution; today it houses the Toy Museum). Similarly generous (but unrealised) projects such as the House of Czechoslovak Children were the Avenue of Socialism and the planned conversion of the Lobkowicz Palace into the Palace of Labour. The aforementioned Alley was conceived as a practical but monumental link between the Castle and Letná, which was to become the new city centre. Adaptations and reconstructions often had an ideological basis - for example, due to the influence of desacralization (and the associated ideas and proposals for the reconstruction of the Monastery of Saint George into a Memorial to the History of the Czechoslovak People) or the celebration of labour (the aforementioned project of the Palace of Labour, which was to show that the Castle also belonged to the working people and to create an exhibition that was to celebrate the work of workers, their influence on the development of socialist society and to highlight the history of workers). In some cases these were necessary modifications because the buildings no longer fulfilled their original function (e.g. the Hunter's House, the Falconer's House, the Lion's Court, the Foundry Court). Most of the changes were reflected in the interiors, while the exterior remained very similar since Paccasi's reconstruction. The period under review also saw many steps taken to make the Castle a centre of the exhibition industry. We observe several new interventions in the complex only with the activity of President Havel and the people who surrounded and worked with him. Based on the archival material [17], [18], the following chapters discuss the different typological units.

Representative spaces

First of all, attention will be paid to spaces that were not open to the public and were also important for the party - these are representative spaces. These were located in all wings on the first-floor level. In the Old Royal Palace, the following rooms were used for representational purposes: the antechamber and the Green Room, the small audience hall (incorrectly referred to as Vladislav's Bedroom), Vladislav Hall. The west wing (the wing facing Hradčany Square) contained the Column Hall (Plečnik), the Rothmayer Hall, the Spanish Hall dressing room. The north wing was (and still is) dominated by the Spanish Hall. The most representative rooms could be found in the south wing - for example, the Brožík Salon, the Habsburg Salon, the Throne Room, the Mirror Salon, the Music Salon [7]. At one point, the project to build a monumental access to the Spanish Hall even became a priority construction project for the Office of the President of the Republic. The project under the direction of architect Rothmayer was completed in 1954 (Wedge Corridor, Rothmayer Hall). The entrance areas (among other things, the cloakroom) to this hall were also designed in the 1970s (the collective of architects Döbert, Firbas, Pirout, Švábová). The Spanish Hall was the meeting place of the party's central committee. In the Vladislav Hall some presidential elections or last farewells to the highest representatives of the state took place. Great emphasis was placed on the festive decoration of these halls. The monumental granite staircase inserted into Plečnik Hall has been preserved and is still functioning today, and the furnishings in the Spanish Hall have been replaced several times.

Fig. 7 – Plečnik Hall, into which a monumental granite staircase was built in the 1970s, connecting the entrance from the Matyáš Gate with the Spanish Hall [19], page 81
Fig. 8 – A meeting of the Central Committee of the Communist Party of Czechoslovakia in the Spanish Hall in 1977. The hall was equipped with furnishings designed by architect Ladislav Vrátník [19], page 87
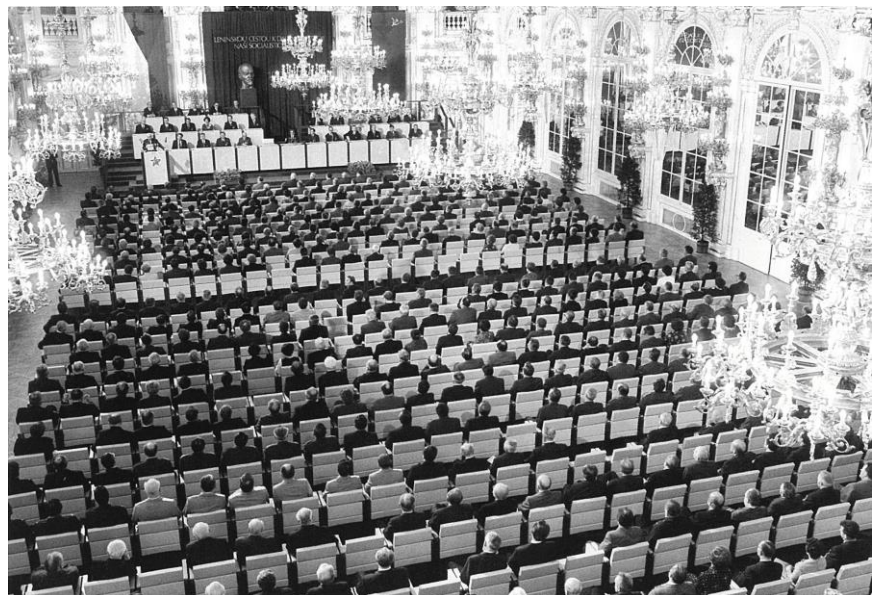
Many rooms and spaces were used by the Office of the President of the Republic - for example, on the 2nd and 3rd floors of the middle wing. This involved building alterations for new elevator shafts, a telephone switchboard (project 1971-1972), sanitary facilities and kitchenettes for the staff. These offices and rooms of the Prague Castle Archives are still used at the Castle today. The south wing still houses the Prague Castle Archives, for which construction work was carried out between 1933 and 1971. One of the depositories was located in the former black kitchen. An apartment for President Masaryk (under the direction of architect Plečnik) was built on the border between the south and middle wings. At the end of the 1950s, the apartment was furnished according to the ideas of communist presidents. In the 1970s, the library of this apartment was converted into the office of President Husák. In 1993, the room was reconstructed to the condition of the period of

our first president. President Beneš and later also Gottwald had the garden house in the Royal Garden converted into a presidential residence (1948-1950, architect Janák, Studený, interiors designed by Nový byt). In the 1970s, under President Husák, the presidential residence underwent another reconstruction - the kitchen preparation room was remodelled, a balcony, sauna and swimming pool were added (architects Döbert and Prokůpek were involved).

Sacral spaces

If one focuses on the church buildings, this period brought a process of desacralisation. The spaces were to serve other than ecclesiastical purposes. This was to symbolically contribute to the separation of the state from the church. The cathedral began to be referred to as a mere burial place for Czech kings, and there were even thoughts of transferring the crown jewels to other places. A Memorial to the History of the Czechoslovak People was to be built in St. George's Monastery (considerations began in 1959, the project ran from 1961-1967), but due to construction complications this project was never completed. Eventually, between 1969-1975, the monastery was adapted for exhibitions of the National Gallery. The main architects of this reconstruction were František Cubr and Josef Pilař. This beautiful exhibition dedicated to old Czech art from the Middle Ages to the end of the Baroque period was moved to other buildings of the National Gallery in the 1990s and the building began to deteriorate, later it was transferred to the use of the Church and a new use for the Archbishop's Museum is being considered. Another example was the conversion of the Chapel of the Holy Cross into a jewellery store (1960 - architect Studený). In 1991, the entrance and information operation in this chapel was redesigned (architect Burian was in charge of this). Most of the sacral spaces were newly designed for exhibition purposes - for example, the Chapel of St. Anne (1973 - the implementation project led by architects Cubr and Pilař). During the reconstruction of the Ursuline Monastery in 1964, new functions were created - a car repair shop, a laundry in the basement and a heavy warehouse. The reconstruction project was led by architects Hölzel and Firbas. Another example was the reconstruction of the refreshment chapel in the Kajetán Garden (1966 - detailed design by architect Hrubý). A cultural house was set up in the building of the Old Rectory - a new typological element supported by the communist regime.

Fig. 9 – View of the exposition in the monastery of St. George – Gothic part [20]

Fig. 10 – View of the exposition in the monastery of St. George – Baroque part [21]

Spaces for economic activities

Some farm buildings and yards changed their functional use during this period. The Stable Yard still had stables, but some rooms were converted into apartments between 1946 and 1953 (architect Pichlík). In the same period of time, the Lion's Court was adapted to create flats and a tobacco shop (Janák, Neumann). Between 1968 and 1971, the reconstruction of this courtyard was carried out by the architects Hlavatý and Kunca. The tobacco shop was modified and a new cafeteria was built in these spaces. Nowadays it houses a restaurant, which underwent a reconstruction and

interior modification after the Velvet Revolution. In 1976, a garage with a fuel warehouse was built here (Burian).

The houses in Golden Lane were adapted for the installation of a museum (1953 - Tintěra, 1985 - Prokůpek). Related to this was the creation of public toilets (1955 - Tintěra, 1985 - reconstruction - Fenclová), a ticket office at the entrance to the Golden Lane (1957 - Voříšek) and a souvenir shop (1969). In 1986, the entrance exposition in house no. 23 was redesigned (Šmejkal).

In the Foundry Yard, changing rooms and washrooms were built in the 1950s. In 1968 a project for the gymnasium space was created. The creation of a meeting hall was also considered. In 1967-1971, an architectural study was made under the direction of architect Pirout. At the end of the 1980s, the reconstruction of the aforementioned hall was addressed under the leadership of architects Burian, Jordák and Petříková. At the beginning of the 1970s, in the premises of the houses No. 40 and No. 198 in Vikářská Street, new surgeries were set up and furnished (Matičková), and in 1975 a photo studio was completed (Brotáková, Kříčková, Bláhová). These spaces are not used in this sense today, they have been restored to the state of the times of President Masaryk.

In the area of the former pheasantry, a greenhouse (1951-1952 - Studený), a boiler house (1951), a flower cold store (1953 - Skála) and a storage building (1976 built, 1996 demolished) were newly built. Houses Nos. 34, 35 and 36 were converted into flats and a factory canteen between 1953 and 1955, with a cloakroom and potato store. In 1975 a shop was built here. The factory canteen and kitchen was rebuilt three more times - from 1964 to 1969, from 1981 to 1986 and in 1991. It was also rebuilt in a later period and is now a café. In the house No. 34, depositories for the National Gallery and Prague Castle were built (1968 study - Pilař, 1979 construction - Pisch).

Between 1972 and 1974 the falconer's house was converted into a bistro, café and confectionery (Slach). The hunter's house was adapted for contemporary housing (1976 interior study, 1982 project completion). The riding hall of Prague Castle was adapted to exhibition space according to the project of architect Janák in 1949. An upholstery workshop was also built in this space between 1953 and 1954 according to a project by the architect Neudörfl. From 1982 to 1985, some spaces were redesigned - the porter's lodge and vestibule, the cloakroom in the basement, the battery station, the laundry and the fire hose drying room (Burian, Borovičková and Šefl). Partial modifications were carried out in this building under President Havel, but the building is still used for exhibition purposes.

In the Riding Yard, workshops and a paint shop were being renovated (1957 to 1958 - Studený). In the 1970s, the carpentry workshop was reconstructed (1970 to 1971 - Žatečka and Stýblo) and the paint shop was reconstructed (1972 to 1973 - Suchan). In 1989 a warehouse for printed materials was established (Nesvačil). And in 1991-1992, a police station was built on the Powder Bridge. The Prague Castle Garage (garage yard) was one of the few new buildings built in the early 1950s under the direction of architect Janák, near the Riding School. A petrol station, a car lift and an oil shed were also built here. In 1964, these premises were reconstructed (by Arnautov, Ulman and Kníže). In 1976-1981 a warehouse for cleaning and mechanisation equipment was built (Sobota, Dufek). Furthermore, modifications were made to the existing welding shop (1986-1987 - Dufek) and a new design of the pumping station (1988). It is worth mentioning the youngest new building at Prague Castle - it is a modern Orangery. It was built on the site of the old greenhouse (old orangery) in 1999 according to the project of architect Eva Jiřičná. The credit for the creation of this building goes to the then First Lady Olga Havlová.

Some of the buildings have been supplemented with related facilities. To the old orangery building were added a flower store, a winter garden (1959 - Studený), a propagation room and a study in the central space (1965 - Studený). The greenhouses in the gardens were renovated and rebuilt. A dressing room for employees was built near the utility garden (1951-1953, 1963 extension of the dressing room - Studený). A boiler house (1951 - Studený), a woodshed with a sawmill (1952-1953, Studený) were also built here. The houses in Jelení Street were supplemented with wood sheds and sheds in the yard (1955 and 1958). The farm premises on the northern outskirts of the Prague Castle were supplemented in 1976 with maintenance workshops, gardening, central

warehouses and a construction yard (Tatíček). In 1988, the construction of a utility horticulture in the so-called Utility Garden was considered (Kovalčíková).

Spaces with defensive function

Compared to previous periods, the Castle lost its defensive function, so the buildings underwent conversions in the period under study. The Mihulka Tower was modified for exhibition purposes - as early as in 1958 the placement of shelves was addressed (Studený), at the end of the 1960s the entrance from the courtyard to the underground was modified, an elevator tower was built and the ground floor was reconstructed (1969 - Veldem) and the loopholes were reconstructed (1970 - Muk). In 1971, a more extensive and complex implementation project was created (SÚRPMO - Růžičková, Nejedlý). In 1982, the State Enterprise Exhibition and the architects Ulrich, Páter and Tykva created museum exhibitions. After the revolution (1993), the DAM studio headed by Petr Malinský created the Rudolfinum exposition. A similar fate awaited the White Tower. In 1953 and 1954, the architect Studený designed the building plans and details concerning the modification of the fireplace on the ground floor and the hooks for hanging the tortures. He designed the torture chamber and the vault bars in 1960. The black tower was first modified in 1956 and 1957. In the following year it was decided to locate the museum in this building (Studený). A refreshment stand and garden landscaping were also designed (Studený). Later (1971), the tower was renovated and an elevator was installed. There are still exhibition and museum spaces in the towers, but with different scenarios and exhibits.

Recreational, catering and cultural spaces

The focus will now shift to facilities for leisure, entertainment, culture and sport. A facility called the House of Culture was part of the emerging regime and its political engagement, education and entertainment, and a facility of this type was also established at the Castle. It was established in the building of the Old Provost's Office. In 1949, the interior furnishings were designed - a library, walls for coats (Křička). Later (1951) public toilets were established at the cultural house, the project was led by architect Rothmayer. There was also an information centre (1956 - Moravec). Two years later, the dividing wall at the treasurer's office and the doctors' office was solved (Tintěra). In 1976, a redesign of the polling place was proposed (Procházka). In October 1963 (implementation project from 1961 to 1963 - SÚRPMO - Hlavatý) the House of Czechoslovak Children was inaugurated. During the project, the staircase in the Romanesque tower, the entrance hall and the stairs, the vestibule, the atrium galleries, the ceramic fountain, the glazed wall to the dining room, the wall between the dining room and the kitchen, the interlaced wall in the preparation room were designed, kitchen lift, stage facilities, auditorium, lounge, foyer, clubhouse, exhibition space, furniture, display panels, display cases, display counter, refrigerated display cases, concierge, coat check. The building was designed for children ages 6 to 15 only. Children were to be exposed to political education (without parents present). The building was to serve mainly non-Prague children, who would be dropped off by their parents and could quietly explore the extensive exhibitions at Prague Castle. It was also to be a meeting place for children to meet interesting personalities, to host exhibitions of children's creations (related to the Castle) and various performances. Several rooms have survived unchanged, but now serve a different purpose (the Toy Museum). The new glass communication hall made of steel profiles adjoining the reconstructed premises of the historic building was highly appreciated at the time of its construction, but unfortunately it has not survived to this day (the building was on the verge of life, the roof leaked, condensation on the glass in winter and overheating in summer, so it was demolished in 2015).

The planned Palace of Labour was to have a similar content (but for a different age group). A museum dedicated to the celebration of work was to be created there. It was also to be linked to the Memorial to the History of the Czechoslovak People - thus embracing the period after the Second World War (the era of the construction of socialism). The conceptual proposal of 1960 states the following content: "The mission of the Palace of Labour is to celebrate the creative work of workers,

cooperative peasants and the working intelligentsia and its outstanding results, to depict the magnificent development of our society, to document the fact that socialism has triumphed in our country, and to show convincingly the perspective of communist development. An effort will be made to show that for all our achievements we must pay tribute to the great struggle, diligence and initiative of our people who, under the leadership of the Communist Party, in indissoluble friendship with the Soviet Union, are building their socialist homeland." [22]

The ballroom had not served its original purpose in the previous period, and in 1946 the architect Janák drew up a study of its use - an apartment and lounges were to be built in the building. In 1947-1950 the same architect rebuilt the building, added a cellar and created a projection booth. Since this adaptation, the Ballroom has been used as a space for art exhibitions, concerts and important social events. In the garden of Na Baště, in 1960, the paving and drainage was repaired (SÚRPMO), in 1979 the garden was reconstructed (Tobiášek) and between 1983 and 1984 the paving was repaired (Prokůpek, Hejl). The Queen Anne's Summerhouse has been used for exhibition purposes since the second half of the 20th century. From 1940 to 1955, the garden was renovated (the architects Sokol and Janák were in favour of reconstructing the original Renaissance appearance, but unfortunately, they were not heard in the end). Between 1952 and 1955, details were addressed - the modification of the entrance to the gallery, the bars for paintings, the curtain rods and the flagpoles (Tintěra). Later (1976) a study of the use of the complex was made by the architect Burian. At the end of the 1980s (1986 to 1987), "improvements were made to the structural and technical condition of the Summerhouse". Architect Pekarová was in charge of the interiors, architect Švábová dealt with the architectural and structural part (the floor in the engine room, the flagpole). She was followed by architects Jordák and Hlaváčková, who designed the change of the basements and the modifications in the gardener's house. In the Royal Garden the roads were repaired (1950 - Matěna), fence walls (1946 to 1956 - Studený). The fountains were designed - Hercules (1949 to 1950 - Hlavatý) and Neptune (1951 to 1960 - Studený). These spaces still serve the same purpose today.

Information about the Riding Hall and its adaptation can be found above. This conversion created a new recreational space, which is still not well known, although it is open to the public. It is a garden on the terrace of the Riding School. The architects Janák and Tintěra were responsible for the modifications of the terrace. In Phase I (1953 to 1954), a preliminary design of the fountain was created, a section of the pool with the fountain, an irrigation system, a pumping station, a station under the terrace, a station with a reserve tank and the supporting structure of the fountain were designed. Phase II was carried out between 1956 and 1957 and involved mainly landscaping, detail of the fountain surround, fountain with spotlights, baroque vases and mats in front of the gallery entrances. These buildings still serve the same purpose today.

A new intervention in the Lower Deer Ditch after 1950 was the construction of a shelter under the Castle with an entrance from the bottom of the ditch. In 1967 the roads were addressed (Jelinek). In the 1970s (1976 to 1977), fencing (Straka, Smolka), ditch bridging (Horák), pedestrian walkways (Junek) and a footbridge (Paulus) were designed. Construction activity took place in the Upper Deer Ditch, especially in the 1950s. Between 1955 and 1956, the roads were modified for accessibility (Studený, Neudörfl), and a treasury for the National Gallery was being designed (Studený, Stavoprojekt). The bear nursery and the well were restored. The architect Studený also designed the fruit chamber (fruit cold store) - a freight elevator and a space for vegetables were built.

In 1965, architect Hölzel made a study of the use of the space under Plečnik's staircase in the Paradise Garden. He examined the location of a cafeteria, lapidarium, toilets for 1000 spectators, dressing rooms and toilets for actors. An interesting project in the Middle Wing was the construction of a cinemascopic cinema in 1961. In 1976, the entrance to the projection booth of the cinema was designed (Švábová), and in the 1980s the electrical wiring in the cinema was reconstructed (Fenclová). Another area that was landscaped was the garden Na Valech. Improvements to the garden were designed in 1953 (Matka) and in 1961 (Kunca). The reconstruction of the roads was started in 1959 (Kříž). In the same year, a collective of architects and civil engineers (Kos, Jeřábek, Herda and Roos) designed the reconstruction of the music pavilion. The surroundings of the music

pavilion were also designed (Tintěra), as well as the total reconstruction of the garden (Šimůnek) and the connection with the Lesser Town gardens (Hlavatý). The architects Kunca and Kupka were in charge of the second stage of the landscaping - garden landscaping, details, a circular viewing terrace, and the construction part of the music pavilion. Between 1980 and 1981, the reconstruction of the aforementioned pavilion (Matičková) and the podium (Šmejkal) were designed. At the end of the 1980s, the South Gardens came into focus. From 1988 to 1990, the architect Burian led the renovations in these gardens. At first, the concept of the view terrace, the reconstruction of the perimeter structures (Burian, Jakoubek), surface treatments (Burian, Šimko), and the summer scene (Burian, Petříková) were designed. The stage in the Na Valech garden, the entrance to the museum and the addition to the summer stage were designed by architects Burian and Crickettová. Nowadays, these gardens have been restored to the state designed by the outstanding architect Jože Plečnik for President Masaryk.

Another object discussed is the Pohořelec Riding School. In 1962, the orchard was landscaped (Ondřejová), in 1979 the fencing and the construction part - stairs to the warehouse, landscaping (Burian) was designed.

Spaces for exhibitions, art and tourism

During the previous regime, there was a great effort to build the Castle into an exhibition centre, but also a space for tourism (the most important Czechoslovak monument). In general, museums and galleries played a great role in the formation of the modern state, serving to educate a large number of people, but also to present the ruling regime. Contemporary and socialist art was to be shown in these spaces, with an emphasis on the heroic stories of working class leaders. The exhibitions were used by the Communist Party to legitimize the new order after Victory February (1948). The link with the past was emphasised, but at the same time the differences of the new regime from the capitalist establishment were pointed out.

The Museum of Prague Castle was established in the Royal Palace. The floor plans and numbering of the rooms were designed by the architect Studený in 1951. The tour routes were designed by architects Sokol (1966) and Burian (1978). In the West Wing, the Treasury was designed for this purpose (1956 - Studený). The same architect designed a new ticket office, complete with a catalogue shop in 1959. Visitor routes were also created in the cathedral. In 1954, the design of the ticket office was presented (Janák, Moravec). The new ticket office was designed by the architect Beránková in 1982. There were also several changes in the interior. I can mention the changes in the treasury (1959 - Studený), in the crown chamber (1974 - Procházka, Burian) and in the tomb of the Czech kings - a new tour route was created (1975 - Lukášová, Tatíček). In the north wing, the Picture Gallery of the Prague Castle was created, or rather restored - the initial project and studies of the modifications were created in 1963 (KPÚ - Cubr, Hrubý). Many paintings from the original inventory were returned to the Castle. In the Teresian Wing, construction work was carried out between 1989 and 1990 to install the museum. Recently, the Picture Gallery has undergone another renovation, and this space has been closed for several years. The Museum of Prague Castle still operates today in an almost unchanged form.

In the 1950s, the Ballroom was adapted and used as a space for art exhibitions, concerts and important social events. The Riding Hall of Prague Castle was adapted into an exhibition space according to a project by the architect Janák in 1949. In the 1950s a museum was established in the houses in Golden Lane. Expositions were also set up in the Black Tower, Mihulka, the White Tower and St. Anne's Chapel. After the reconstruction of the Lobkowicz Palace according to the project by the architect Hlaváčková from 1981 to 1982, a historical exposition was also created in these premises (1983 to 1984 - Makula, Fejk). Between 1969 and 1975, the Monastery of St. George was adapted for the National Gallery's exhibitions.
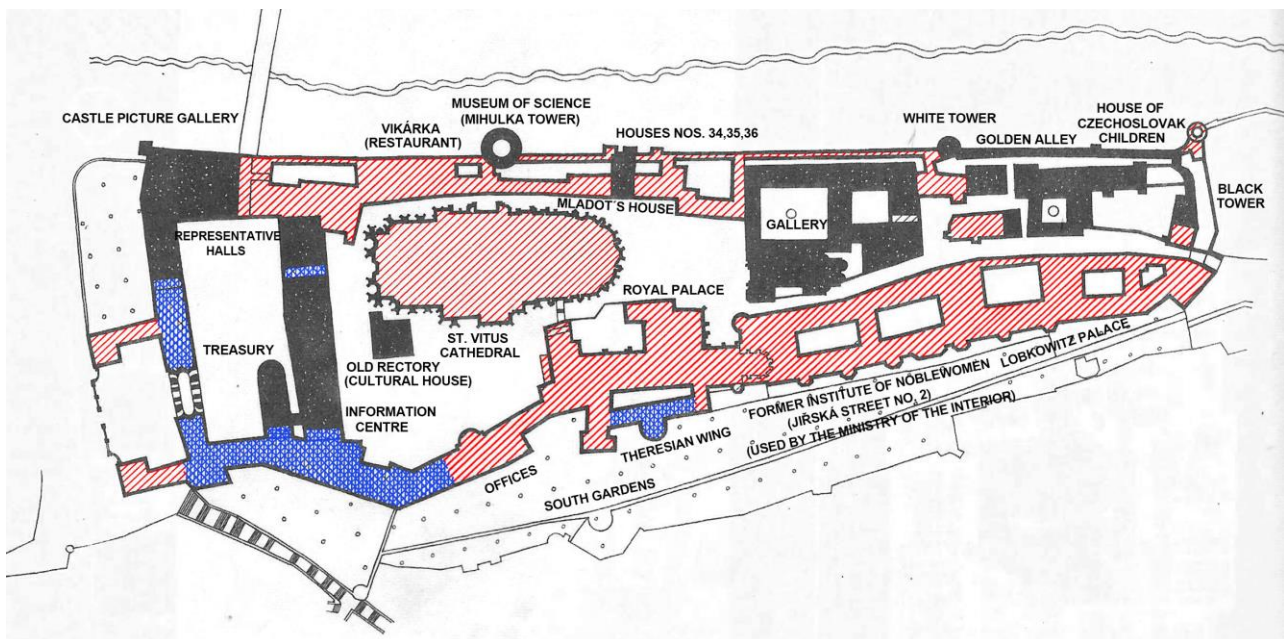
Fig. 11 – Diagram of the main reconstructions and modifications of the Castle from the period of the First Republic after 1920 and from the period of the Socialist Republic after the Second World War until 1972 [12], page 130.
Marking of the period of modifications:
simple hatching (red colour) - until 1918, the original state essentially unrebuilt, but in many cases subject to archaeological investigation; cross-hatching (blue colour) - 1st Republic period;
full area (black colour) - modifications from 1945 to 1972

In Jelení Street, houses No. 197, 199 and 200 were reconstructed in 1986 and during these modifications a hostel for 30 people was created (Malinovský). Later this project was converted into a hotel. There are no other accommodation facilities in the Castle grounds, but there are several in the immediate vicinity.

The tourism industry undoubtedly includes catering facilities and several of them were established in the Castle area during the period under study. The Vikárka restaurant was established in the houses No. 38, 39 and 40. The first project was created in 1956 under the direction of the architect Moravec. Three years later another study of the Vikarka (Lácha) was made. In 1964, the houses were reconstructed and on this occasion a restaurant was built (Hölzel, Čapek, Jelínek). The interior furnishings were designed by the duo Firbas and Kníže. In 1966, a wine cellar was opened in Vikárka, designed by architect Šolcová and the interiors were designed by architect Firbas. A year later, lounges (Michálková), a preparation room (Jenčová) and in the fateful year of 1968 a dry warehouse (Setíkovská) were added. The Vikárka restaurant was closed from 2014 to 2022. It was undergoing extensive reconstruction and the original furnishings were replaced.

The architect Moravec also worked on the restaurant Na Baště. Already in 1950 he created a volumetric study, but he did not prepare the initial project until 1957. It was realised between 1957 and 1959. The counter, kitchen facilities and the entrance from the garden were designed. A

cafeteria was built in the House of Czechoslovak Children in 1974 (Hlavatý). A cafeteria was also to be built at the entrance to the Palace of Labour (unrealised study 1964 - Hölzel). In 1971, a project for the interior of the cafeteria in the Lion Court was created (Hlavatý, Kunca, Mošna). In the house No. 8 (next to Daliborka) a project for a snack bar was created in 1964. Architects Firbas and Šimoníková designed the dining tables, benches, clothes rack, bar chairs, bar counter facilities, cabinet for the waiter and counter facilities, washroom and storage, serving window, chairs for the terrace and tables for the terrace. A refreshment stand was designed at the Black Tower in 1958 (Cold). The refreshment room was part of the implementation project for the renovation of St. George´s Monastery for the National Gallery (1972 to 1973 - Pilař). According to a study by the architect Hölzel, a refreshment stand was to be built in the Paradise Garden (1965). In 1966, an implementation project was created for the adaptation of the chapel for refreshments in the Kajetán Garden (Hrubý), which was implemented by 1970. At present, this garden is inaccessible to the public and relatively deserted. Only the terrace with a café, which was created from a building designed by the architect Hrubý, is in use.

Technological spaces

It is necessary to mention the technological background, which is part of the whole complex. In the individual buildings we can find various technical rooms, boiler rooms, air-conditioning machinery rooms, transformer stations, collectors, rooms for spare sources, freight elevators, rooms for television and radio transmissions and a telephone exchange. In the 1970s and 1980s, a complete renovation of the technological facilities was carried out, a renovation that required significant interventions that affected the Castle site not only underground but also on the surface. Some of the buildings had to be demolished and then rebuilt - for example, the joinery building (1978 to 1986). At the end of the 1980s, the construction of the energy centre became the most important action in the area. As early as 1984, a project was drawn up for a centralised heat supply system for the Prague Castle area (Nesvačil). The same problem and the related collector were solved by a team of engineers (Skalický, Hošek, Pospíšil and Petráň) between 1986 and 1987. It required the demolition of some buildings and a fence was designed on the Powder Bridge. A boiler house and a retaining wall under the collector were designed.

In 1988, the project for the 400 Energy Centre was created. Engineers Cibulka, Stehlíková, Petráň, Butkaiová and Nováková participated in the architectural and construction part. They solved the upper construction - park arrangement, construction modifications in the diesel generator, air handling chamber, addition of steel structures in the refrigeration plant, garage doors, freight elevator NGS 100, construction and layout modifications of the guardhouse, exhausts of the refrigeration plant, location of the incubator, modifications of the kitchen layout at the guardhouse (all in 1988), construction modifications of the maintenance workshop (1989). During 1988 and 1989, building 312 was also designed - security of the excavation pit, plan of retaining walls, plan of modifications (Petráň). In the revolutionary year, object 382.1 - construction modifications of the cable shaft relocation in Jiřská Street was also realized. Between 1989 and 1990 the project of the energy centre was completed - construction modifications of the HVAC system, HVAC penetrations, connection of the energy centre (EGC) to the existing garages, noise insulation of the HVAC system (Cibulka).
There are also a number of underground passages (tunnels) in the area. As already mentioned, the communist presidents had an underground bunker built with access from the Deer Ditch. It was marked as object K110. In 1998 a project for its reconstruction and use was created - first a project for the building permit (Tomášek, Jonášová), then a project for the construction (Jonášová). The same engineer drew up the final building design in 1999.

The collectors and the energy centre are still in operation today. The current planners are glad that it was built back then, because they are reaping the benefits of that solution. From a technical point of view, it was certainly a necessary thing, from a conservation point of view it was problematic and from an archaeological point of view it was basically a big devastation because a lot of strata disappeared and could not be sufficiently explored.

CONCLUSION

From the very beginning, Prague Castle was a large complex that was constantly changing. The Slavic fortress with few buildings surrounded by wooden walls expanded, grew, filled with power and new life of prince, king, emperor and president, bishop and archbishop. It expanded across the Deer Moat, raising walls, buildings and churches. Noble families and the highest administrative authorities found their seat here. The central seat of power was moved to other buildings and filled with new functions. The black kitchen in the Castle was transformed into offices, the monastery into an art hall, the stables into a picture gallery, the sports ballroom into a meeting hall, the offices into a museum, etc.

The breadth of typologies in the Prague Castle area is immense. There are typological units related to the administrative function of the Castle, to tourism, to the religious center of the whole country, but also to the function of permanent or temporary housing and recreation.

For most of the second half of the 20th century, Prague Castle evoked more the seat of a totalitarian power that did not like to communicate with the public. Despite the proclaimed opening of the Castle, various parts of the Castle grounds were gradually closed to the public. After a partial relaxation in the 1960s (for example, the House of Czechoslovak Children was built here and the Palace of Labour was considered to attract the working class to Prague Castle), normalization (1970s and 1980s) brought further closures. A more positive period for Prague Castle and public access came after the fall of communism and the election of President Václav Havel.

The 1950s and especially the 1960s brought new building activity to the Castle, which was also connected with new functional use of some of the premises. The Second Courtyard, the central wing of the New Palace, St. Vitus Cathedral and the aforementioned transformation of the Supreme Burgrave´s House into the House of Czechoslovak Children were modified. Compared to the previous period, the period under review is characterised by reconstructions and renovations of the internal and external areas of the Castle, but these interventions were of lesser quality. They did not manifest themselves much externally and did not fundamentally change the architectural form or function of Prague Castle. Unfortunately, ideologically inappropriate elements were also removed - for example, interior decorations from the period of President Masaryk. The most significant modifications with the insertion of a new function into the castle premises in this period were the reconstruction of St. George's Monastery for the needs of the National Gallery (completed in 1976) and the creation of the historical exposition of the National Museum in the Lobkowicz Palace (1987). However, these two interventions met the same fate as most of the building modifications of the period under review after the Velvet Revolution, namely gradual destruction, reconstruction or return to the form of the First Republic. A minimum of modifications have survived to the present day. The Prague Castle Archive and some minor interior interventions and office spaces can be mentioned. Some of the buildings have been adapted from the period under review, only the content of the exhibited objects has changed. The exhibition spaces of the Lobkowicz Palace are now used as a museum and picture gallery, while the Spanish Hall is still used for ceremonial gatherings at the highest level. However, the furnishings from the 1970s can no longer be found there.

After the Velvet Revolution, most of the castle's spaces were opened to the public and considerable investment was made in renovations and refurbishments. New construction activity has also resumed here and several award-winning architectural buildings have been created (the orangery by architect Eva Jiřičná, the Powder Bridge passage created by architect Josef Pleskot.

ACKNOWLEDGEMENTS

REFERENCES

[1]   Google Maps (online). (cit. 2023-05-01). Available from
https://www.google.com/maps/@50.0910966,14.3990416,571m/data=!3m1!1e3?hl=en

[2]   Pražský hrad pro návštěvníky (Prague Castle for visitors) (online). (cit. 2023-05-01). Available from https://www.hrad.cz/file/edee/cs/prazsky-hrad-pro-navstevniky/mapa-hradu/hrad-plan-hradu.pdf

[3]   Presidential palace – Wikipedia (online). (cit. 2023-05-01). Available from
https://en.wikipedia.org/wiki/Presidential_palace

[4]   Assessment of The Adaptive Reuse of Castles As Museums: Case of Cyprus – Witpess.com
(online). (cit. 2023-05-01). Available from https://www.witpress.com/elibrary/sdp-volumes/11/2/1096

[5]   Adaptive Reuse of Historical Buildings: The Case of Qishla Castle in Koya City – Research Square
(online). (cit. 2023-05-01). Available from https://www.researchsquare.com/article/rs-1468778/v1

[6]   The Adaptive Re-Use of Historic Manor Buildings in Poland. The Maciejewo (Matzdorf) Palace in
Western Pomerania, as a Specific Case – MDPI Open Access Journals (online). (cit. 2023-05-01). Available
from https://www.mdpi.com/2076-0752/10/4/87

[7]   Fialková E., 2017. Redefinícia Pražského hradu (Redefining Prague Castle), diplomová práce
(diploma project), Vysoká škola umělecko-průmyslová ((University of Arts and Crafts in Prague). Vedoucí
práce Roman Brychta (Project supervisor Roman Brychta).

[8]   Poučení z krizového vývoje ve straně a společnosti po 13. sjezdu KSČ: schváleno plenárním
zasedání ÚV KSČ 11. prosince 1970 (Lessons from the crisis in the Party and society after the 13th
Congress of the Communist Party of Czechoslovakia: approved by the plenary session of the Central
Committee of the Communist Party of Czechoslovakia on 11 December 1970) Praha (Prague) (ÚV KSČ =
CENTRAL COMMITTEE OF THE COMMUNIST PARTY OF CZECHOSLOVAKIA), 1971, 16 pp.

[9]   Kolář P., Pullmann M., 2017. Co byla normalizace? Studie o pozdním socialismu (What was
normalisation? A Study of Late Socialism), (Nakladatelství Lidových novin = Lidové noviny Publishing
House) 224 pp.

[10]   Šnorbert M., 2022. Architektonické intervence v areálu Pražského hradu v 70. letech 20. století
(Architectural Interventions in the Area of Prague Castle in the 70s of the 20th Century) in in M. Peřínková,
S. Jüttnerová, L. Videcká, 14. Architektura v perspektivě 2022 (14th Architecture in Perspective 2022),
Ostrava: Vysoká škola báňská – Technická univerzita Ostrava, Fakulta stavební (Ostrava: Technical
University of Ostrava, Faculty of Civil Engineering), pp. 189-196 (online). (cit. 2023-05-01). Available from
http://otto.vsb.cz/data/proceeding_2022.pdf

[11]   Borkovský I., 1969. Pražský hrad v době přemyslovských knížat (Prague Castle during the Time of
Premyslid Princes), 51 (Academia = Academia Publishing House) 162 pp.

[12]   Vančura J., 1976. Hradčany, Pražský hrad (Hradčany, Prague Castle), (SNTL = State Publishing
House of Technical Literature) 320 pp.

[13]   Stefan O., 1964. K dějepisným otázkám naší renesanční architektury (To the Historical Questions of
Our Renaissance Architecture), in Umění XII (Art XII), pp. 428-432.

[14]   Mencl V., 1969. Praha (Prague), page 109 (Odeon = Odeon Publishing House) 378 pp.

[15]   Novotný Ant., 1949. Praha v květu baroka (Prague in Bloom of Baroque), 54 (Atlas = Atlas
Publishing House) 462 pp.

[16]   Chotěbor P., 1994. Pražský hrad – podrobný průvodce (Prague Castle - Detailed Guide), (Pražské
nakladatelství Jiřího Poláčka = The Prague Publishing House of Jiří Poláček) 184 pp.

[17]   Archiv Pražského hradu. Nová plánová sbírka, 1918-2001, ev. č. 14 (Archive of Prague Castle. New
Plan Collection, 1918-2001, ev. no. 14).

[18]   Archiv Kanceláře prezidenta republiky. Funkční řešení objektů Pražského hradu, květen 1986. Č.j.
402.131/86 (Archive of the Office of the President of the Republic. Functional Solution of the Prague Castle
Buildings, May 1986. No. 402.131/86).

[19]   Halmanová K., 2007. Pražský hrad ve fotografii 1939-1989 (Prague Castle in Photographs 1939-
1989), Praha (Prague) (Správa Pražského hradu = Prague Castle Administration) 176 pp.

[20]   Archiv Národní galerie, Dokumentace výstav Národní galerie, 1976–1980, Sbírka starého umění
(stálá expozice) (1980) – karton č.1, i.č. 7, foto Marie Šonková (National Gallery Archives, Documentation of
National Gallery Exhibitions, 1976-1980, Collection of Old Art (permanent exhibition) (1980) - card no. 1,
i.no. 7, photo Marie Šonková).

[21]   Archiv Národní galerie, Dokumentace výstav Národní galerie, 1976–1980, Sbírka starého umění (stálá expozice) (1980) – karton č.1, i.č. 7, foto Vladimír Fyman (National Gallery Archives, Documentation of National Gallery Exhibitions, 1976-1980, Collection of Old Art (permanent exhibition) (1980) - card no. 1, i.no. 7, photo Vladimír Fyman).

[22]   Archiv Pražského hradu. Spisový znak 400.000, 1948-1964, Ideový návrh Paláce práce, inv. č. 176, sg. 404 730/64, k.33, č.j. 404.802/60 (Archive of Prague Castle. File mark 400.000, 1948-1964, Conceptual Design of the Palace of Labour, inv. no. 176, pg. 404 730/64, k.33, no. 404.802/60).

RESEARCH ON THE PREDICTION OF RIGID FRAME-CONTINUOUS GIRDER BRIDGE DEFLECTION USING BP AND RBF NEURAL NETWORKS

Liu Jingyang, Wu Hexiang and Sun Quansheng

Department of Civil Engineering, Northeast Forestry University, Harbin，150040, China; 1258362856@qq.com; whx2015@nefu.edu.cn; sunquansheng@nefu.edu.cn

ABSTRACT

To solve the problem of excessive deflection in the post-operation process of a rigid frame-continuous girder bridge and provide a basis for the setting of its initial camber, this paper, based on the results of finite element analysis, uses three methods to predict and verify the deflection of a rigid frame-continuous girder bridge. The results show that the average deflection method can be used to fit the average deflection value for a relatively long period of time and predict the average deflection value for the next longer period of time. Both the back-propagation (BP) neural network model and the radial basis function (RBF) neural network model can predict deflection well, but the RBF neural network model has higher prediction accuracy, with a mean absolute error (MAE) of 2.55 $\times 10^{-5}$ m and a relative error not exceeding 1%. The prediction model established by the RBF neural network has higher stability, better generalization ability, and better overall prediction performance. The established model has some reference significance for similar engineering projects and can achieve the optimization of structural parameters.

KEYWORDS

Rigid frame-continuous girder bridge, BP neural network, RBF neural network, Deflection prediction, Structural parameter optimization

INTRODUCTION

Current status of research

With the advancement of transportation and building technology, highway construction has expanded into hilly regions. The severe terrain characteristics, such as high mountains, deep ravines, and steep slopes, increase the prevalence of rigid frame-continuous girder bridges with tall piers and extended spans. Typically, rigid frame-continuous girder bridges are constructed using the cantilever-symmetrical casting method, which is influenced by a number of variables, and the variation of internal forces and displacements is very complex. With the increasing service life of rigid frame-continuous girder bridges constructed with cantilever casting, it has been discovered that the mid-span deflection of these bridges is generally too great, or even cracking is observed, which not only severely affects the use and safety of the bridges but also limits the development and breakthrough of this bridge type to larger spans. To ensure that the bridge can be closed normally, that the bridge line shape and stress meet the design specifications, and that the structure is safe, it is necessary to monitor and control the deformation, stress, and safety during the construction process, thereby accurately predicting the mid-span deflection. Currently, the most popular approaches for making predictions include the least-squares method, the gray system theory, the Kalman filtering method, the artificial neural network method, etc. Since the influencing parameters of the construction of rigid frame continuous girder bridges, such as volume weight of concrete, elastic modulus, concrete shrinkage and creep, and temperature load, are subject to random

variations, artificial neural networks have been rapidly developed in recent years as an integral part of the rapidly developing artificial intelligence. Neural networks, as a technique for nonlinear data modelling, may rapidly determine the functional relationship between input parameters and output parameters [10]. Recently, academics have become interested in the optimization of construction-related factors using neural networks. The two most commonly employed neural networks are BP (back propagation) and RBF (radial basis function). The BP network is a multi-layer feedforward network trained using error backpropagation with an input layer, a hidden layer, and an output layer [11]. During backpropagation, the weights and offsets are changed continuously to bring the actual output of the network closer to the expected output [12]. The alteration of weights and offsets influences the output of the BP network; hence, the BP neural network is a "universal approximation" of the nonlinear mapping [13]. The RBF neural network has a similar structure to the BP neural network, but the input parameters are directly transferred to the hidden layer without weight connections, and the radial basis function is used as the neuron activation function for the hidden layer[14]. Non-linear is the transformation from the input layer to the hidden layer, whereas linear is the transformation from the hidden layer to the output layer [15]. It has the "local mapping" attribute since the output of the RBF network is only dependent on a few adjustment factors. In light of this issue, this work applies the average deflection approach for a single-factor deflection prediction analysis on a bridge with a rigid frame continuous girder bridge that is currently under construction. A rigid frame-continuous girder bridge deflection prediction model is developed utilizing a BP neural network and an RBF neural network. In order to optimize structural characteristics and advance construction control technology, the prediction results are compared and studied in order to select the approach with the highest prediction accuracy and greatest effect.

Engineering overview and finite element modeling

The background of this paper is a rigid-continuous beam bridge, which is a prestressed concrete semi-rigid-continuous box beam bridge with a span of (70 + 120 + 70) m and a cantilever casting construction method. The total length of the bridge is 1046 meters. The total width of the bridge deck is 11.5 meters (anti-collision guardrail). The transverse slope of the bridge deck is 1.5% in both directions. The design speed is 80 kilometers per hour, the vehicle load grade is highway-I standard, and the design safety level is one level.

Using Midas/Civil, the finite element model of the underpinning engineering was developed. The model construction stage was segmented based on the engineering design documents and adjusted in real time based on the actual construction situation on the job site. The construction of the model was divided into twelve stages.

The primary bridge consists of 127 distinct nodes and 122 simplified units. The pier beams are simulated by beam elements, with rigid connections between the 18-foot main beam and the main pier and elastic connections between the 19-foot seat beam and the main beam. The section and material parameters are selected based on the bridge's design document and modified based on field measurements. Given that the bridge is cast using the cantilever method, the bracket is simulated using node general support (only compression); the corresponding finite element model is depicted in Figure 1.
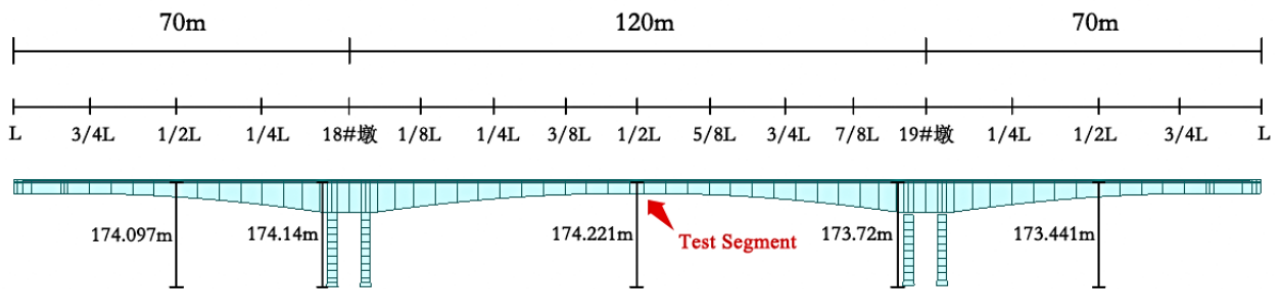
Fig. 1 – Graph of the Finite Element Model

METHODS

Analysis of single-factor deflection prediction

In this section, the measured deflection values at the 1/4L position of the second span of Pier 18, based on the engineering dependency, from late August 2022 to early January 2023, are selected. The deflection data is then fitted and predicted using the least squares method. Divide each month into two periods (every 15 days is one period), calculate the average measured deflection value of the two periods, create a new sample point, fit the sample of the first five months (1~10 periods) using the least squares method, and use the sample of the sixth month (11~12 periods) to predict deflection. The average mean value of deflection (AMVOD), the minimum value of deflection (mVOD) and the maximum value of deflection (MVOD) are shown in Table 1. The line graph of the measured average deflection is depicted in Figure 2.

Using Matlab software and the principle of least squares [16], the relationship between the average value of the mid-span deflection f (mm) and the time (period) can be fitted by a third-order polynomial.

$$f = 0.00929t^3 - 0.1725\ t^2 + 0.01547\ t - 1.186 \tag{1}$$

Where f is the Average deflection and t represents The number of periods. Each month is divided into two halves, one each in the first and second halves. Figure 3 depicts the deflection's fitting curve. The fitting curve is close to the average value of the measured deflection between the measured deflection minimum curve and the measured deflection maximum curve, and it has a high degree of fitting.

Tab. 1 - Measured average deflection table

| Numbers	Time	AMVOD/m	mVOD/m	MVOD/m
1	Aug.16th-30th	-1.36×10^{-3}	1.06×10^{-3}	-3.78×10^{-3}
2	Sept.1st-15th	-1.735×10^{-3}	0.74×10^{-3}	-4.21×10^{-3}
3	Sept.16th-30th	-2.43×10^{-3}	0.32×10^{-3}	-5.18×10^{-3}
4	Oct.1st-15th	-3.27×10^{-3}	-0.52×10^{-3}	-6.02×10^{-3}
5	Oct.16th-30th	-4.465×10^{-3}	-1.82×10^{-3}	-7.11×10^{-3}
6	Nov.1st-15th	-5.13×10^{-3}	-2.87×10^{-3}	-7.39×10^{-3}
7	Nov.16th-30th	-5.92×10^{-3}	-3.31×10^{-3}	-8.53×10^{-3}
8	Dec.1st-15th	-7.885×10^{-3}	-5.81×10^{-3}	-9.96×10^{-3}
9	Dec.16th-30th	-8.335×10^{-3}	-6.32×10^{-3}	-1.035×10^{-2}
10	Jan.1st-15th	-8.925×10^{-3}	-6.47×10^{-3}	-1.138×10^{-2}
11	Jan.16th-30th	-9.18×10^{-3}	-7.47×10^{-3}	-1.089×10^{-2}
12	Feb.1st-15th	-9.97×10^{-3}	-7.93×10^{-3}	-1.201×10^{-2}
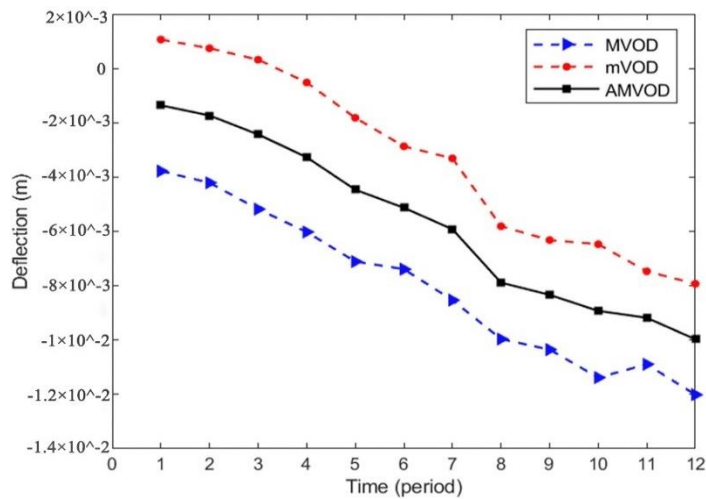
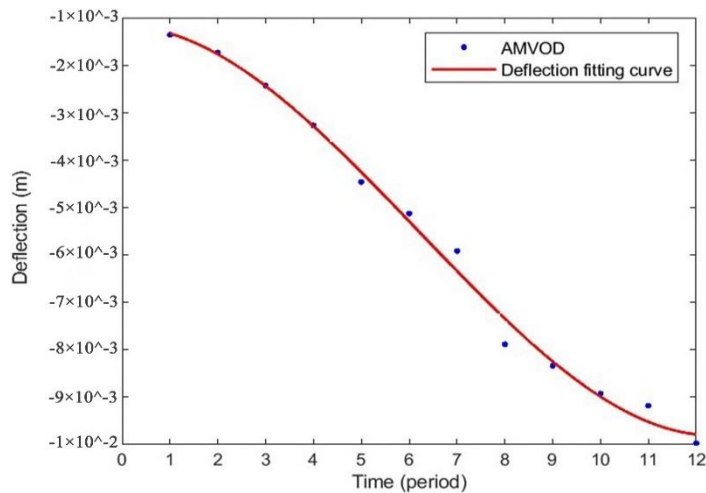*Fig. 2 – The line graph of the measured average deflection*

Fig. 3 – Diagram of the deflection fitting curve

Table 2 depicts the relative error between the measured average deflection and the fitted value for the first five months, i.e. the first through tenth period.

Tab. 2 - Relative error fitting deflection

Numbers	Measured Value/m	Predicted Value/m	Relative Error/%
1	-1.360×10^{-3}	-1.334×10^{-3}	1.91
2	-1.735×10^{-3}	-1.771×10^{-3}	2.07
3	-2.430×10^{-3}	-2.441×10^{-3}	0.45
4	-3.270×10^{-3}	-3.290×10^{-3}	0.61
5	-4.465×10^{-3}	-4.260×10^{-3}	4.59
6	-5.130×10^{-3}	-5.297×10^{-3}	3.26
7	-5.920×10^{-3}	-6.344×10^{-3}	7.16
8	-7.885×10^{-3}	-7.346×10^{-3}	6.84
9	-8.335×10^{-3}	-8.247×10^{-3}	1.06
10	-8.925×10^{-3}	-8.991×10^{-3}	0.74

The predicted deflection values for the sixth month, i.e. the 11th and 12th periods, are -9.523×10^{-3} m and -9.787×10^{-3} m, which are close to the measured values of -9.180×10^{-3} m and -9.970×10^{-3} m, indicating that the prediction model is accurate. The relative error between measured and predicted values is displayed in Table 3.

Tab. 3 - Prediction relative error of deflection

Numbers	Measured Value/m	Predicted Value/m	Relative Error/%
11	-9.180×10^{-3}	-9.523×10^{-3}	3.74
12	-9.970×10^{-3}	-9.787×10^{-3}	1.84

The above calculation demonstrates that the average deflection method can be used to fit the average deflection value over a longer time period and predict the average deflection value over the next longer time period.

Analysis of multi-factor deflection prediction

Experimental program

In order to ensure that the experiment is effective and to examine the influence of elastic modulus, volume weight of concrete, concrete shrinkage strain, and temperature load on deflection, elastic modulus (EM), volume weight of concrete (VWOC), material age (MG), and minimum temperature (MT) are used as input variables. Based on the calculation results of the Midas/Civil finite element model. The EM is set to 3.53×10^{4} MPa~3.57×10^{4} MPa; the VWOC is 23KN/m³~27KN/m³; the MG is 5~9 days; and the MT is -51℃~-55℃. The four factors and five levels are coded according to Table 4. During the construction process, the tensioning of prestressed tendons exerts an upward force on the beam segment, causing it to lift. As time progresses, the deflection of the beam segment also gradually increases. In this study, the deflection of the beam segment after the prestressing of segment 12 of Pier 18, measured using Midas/Civil software, was used as the evaluation criterion. Based on the data in Table 4, a single-factor control variable method was employed to investigate the influence of parameters on the deflection of the main beam. Twenty sets of experiments were designed as training samples, as shown in Table 5. Twenty sets of experiments were designed as training samples. As shown in Table 6, eight sets of experiments are designed as test verification based on the experiment's general principle. The experimental flowchart is depicted in Figure 4.

Tab. 4 - Structure parameter factor coding level table

Numbers	EM/MPa	VWOC/(KN/m³)	MG/days	MT/°C
1	3.53×10^4	23	5	-51
2	3.54×10^4	24	6	-52
3	3.55×10^4	25	7	-53
4	3.56×10^4	26	8	-54
5	3.57×10^4	27	9	-55

Tab. 5 - Training samples

Numbers	EM/MPa	VWOC/(KN/m³)	MG/days	MT/°C	Deflection/m
1	3.53×10^4	23	9	-55	2.8730×10^{-2}
2	3.54×10^4	23	9	-55	2.8660×10^{-2}
3	3.55×10^4	23	9	-55	2.8600×10^{-2}
4	3.56×10^4	23	9	-55	2.8530×10^{-2}
5	3.57×10^4	23	9	-55	2.8472×10^{-2}
6	3.57×10^4	23	9	-55	2.8472×10^{-2}
7	3.57×10^4	24	9	-55	2.6929×10^{-2}
8	3.57×10^4	25	9	-55	2.5387×10^{-2}
9	3.57×10^4	26	9	-55	2.3844×10^{-2}
10	3.57×10^4	27	9	-55	2.2302×10^{-2}
11	3.57×10^4	23	5	-55	2.8474×10^{-2}
12	3.57×10^4	23	6	-55	2.8474×10^{-2}
13	3.57×10^4	23	7	-55	2.8473×10^{-2}
14	3.57×10^4	23	8	-55	2.8473×10^{-2}
15	3.57×10^4	23	9	-55	2.8472×10^{-2}
16	3.57×10^4	23	9	-51	2.9199×10^{-2}
17	3.57×10^4	23	9	-52	2.9017×10^{-2}
18	3.57×10^4	23	9	-53	2.8835×10^{-2}
19	3.57×10^4	23	9	-54	2.8654×10^{-2}
20	3.57×10^4	23	9	-55	2.8472×10^{-2}

Tab. 6 - Testing samples

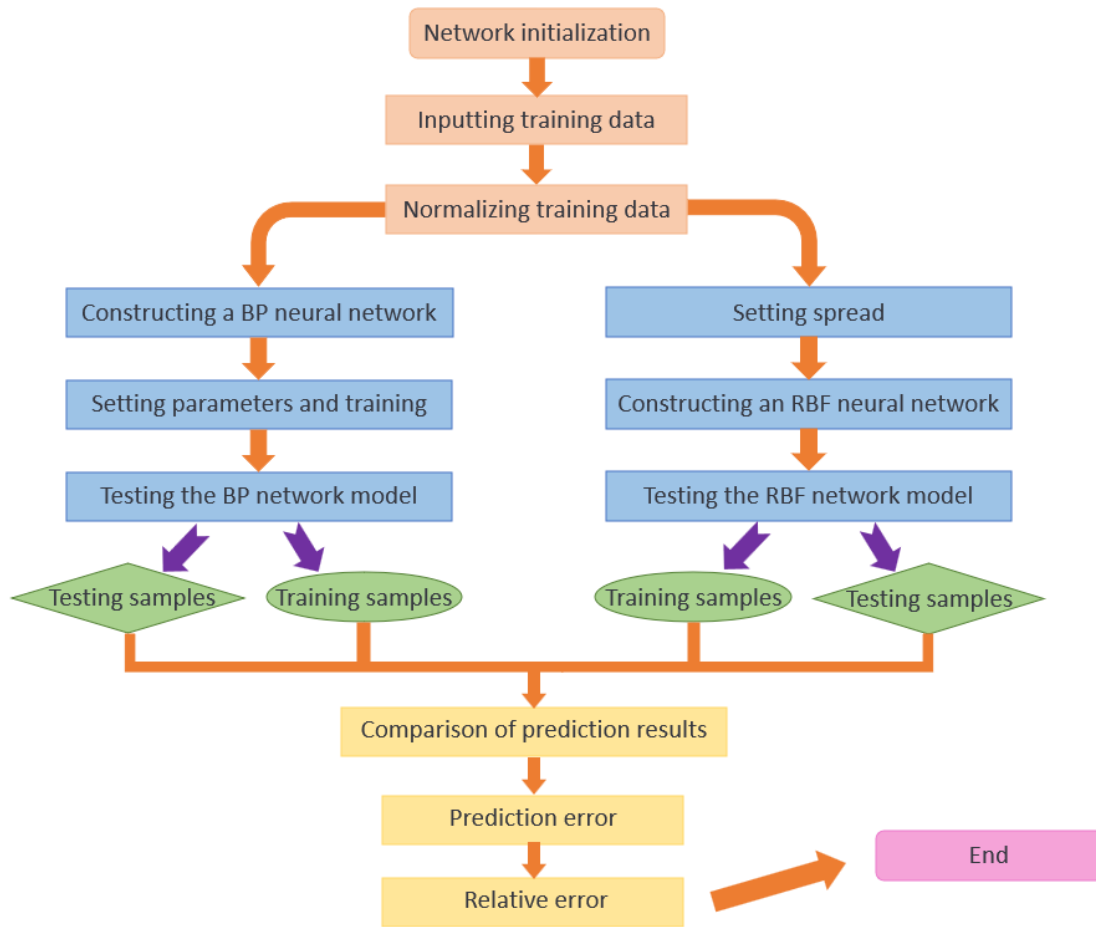| Numbers	EM/MPa	VWOC/(KN/m³)	MG/days	MT/°C	Deflection/m
1	3.55×10^4	24	9	-55	2.7049×10^{-2}
2	3.55×10^4	24	5	-55	2.7051×10^{-2}
3	3.55×10^4	25	7	-55	2.5500×10^{-2}
4	3.55×10^4	25	9	-55	2.5499×10^{-2}
5	3.55×10^4	26	5	-55	2.3952×10^{-2}
6	3.55×10^4	26	7	-55	2.3951×10^{-2}
7	3.55×10^4	27	5	-55	2.2402×10^{-2}
8	3.55×10^4	27	7	-55	2.2401×10^{-2}

Fig. 4 – Experimental flowchart

BP neural network model construction

A three-layer BP neural network is used to establish a prediction model, with elastic modulus (EM), volume weight of concrete (VWOC), material age (MG), and minimum temperature (MT) as input variables and deflection value as output. Therefore, the constructed neural network model has 4 nodes in the input layer and 1 node in the output layer. The BP neural network is a multi-layer feed-forward network trained by error backpropagation, which consists of an input layer, a hidden layer, and an output layer. By continuously modifying the weights and offsets, the actual output of the network is closer to the desired output. The model operation feeds back the output results to the output layer through backpropagation of the input variables (EM, VWOC, MG, MT) so as to obtain the output result, that is, the deflection prediction value, and the number of nodes in the hidden layer is also One of the key factors affecting the BP neural network model is that if there are too many nodes in the hidden layer, it will increase the network training time, and it is easy to overfit during the training process. If the number of nodes in the hidden layer is small, the neuron training is insufficient and cannot achieve. The intended target of the network. In this study, the mean square value of the error is aimed at, and the optimal number of neurons in the hidden layer is mainly obtained through trial and error. After repeated training, when the number of nodes in the hidden layer is 4, the mean square value of the error is the smallest, and the prediction performance of the BP neural network is the best. Using 28 sets of experimental data samples for analysis, the data were normalized so that the model sample data fell between [0, 1], and the function used was following:

$$xi \ = \ (x - min(xi))/(max(xi) - min(xi)) \tag{2}$$

Where he normalized data is xi, where $min(xi)$ and $max(xi)$ are, respectively, the smallest and largest numbers in the data. The training samples from the experimental data are used to construct the prediction model, while the test samples are used to evaluate the model's generalization ability. The hidden layer transfers functions "tansig" and "purelin" are selected, and the training function "trainlm" is selected. Using the newff function, a neural network model is created. Maximum training time is 400 seconds, target mean square error is 0.001, and learning rate is 0.05. The model is trained and validated to obtain prediction results.

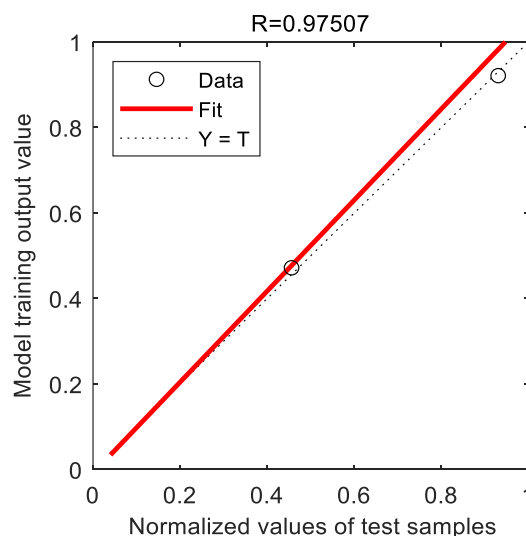### RBF neural network model construction

The RBF neural network is similar to the BP neural network in structure, but it uses radial basis functions as activation functions for the hidden layer neurons. The input parameters are directly mapped to the hidden layer without requiring weight connections. The output of the RBF network is only dependent on a subset of adjustable parameters, making it possess the characteristic of "local mapping". Using an RBF neural network to normalize 28 sets of data and then develop a prediction model, the number of input and output nodes is the same as that of the BP neural network, but the number of hidden layer nodes achieved a better approximation effect with 20 neurons. Build a neural network model using the "newrbe" function. In the RBF neural network model, the expanding coefficient has a significant impact on the RBF model's prediction accuracy. After multiple trials, it is set to 1, the mean square error target is set to 0.001, and experimental data is trained and evaluated.

RESULTS

To validate the prediction performance of BP and RBF neural network models, the fitting degree of the two network models was compared, and the fitting regression of the sample values and the model training output values on the training samples and test samples was obtained, as depicted in Figure 5. The fitting correlation coefficients for the two network models are all up to 0.99, indicating a high degree of fit to the training samples. When the normalized sample value equals the training value of the model, that is, when the fitting line Y=T, the fitting correlation coefficient (R) value is 1. The greater the correlation between the actual output and the expected output, the closer the R value is to 1. On the test sample, the BP neural network model's fitting correlation coefficient is 0.97507, and the predicted output deviates from the target output. The RBF neural network model has an appropriate correlation coefficient of 0.9991. Based on the preceding analysis, it is clear that both network models have good prediction capabilities, but the RBF neural network outperforms the other in terms of prediction accuracy for the input sample.
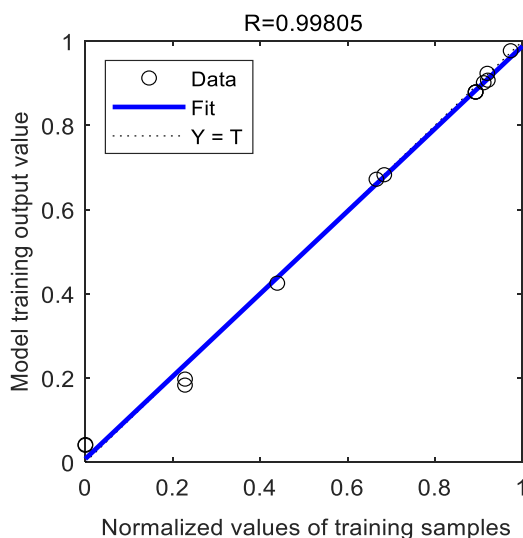
(a) Training samples of BP network   *(b) Testing samples of BP network*
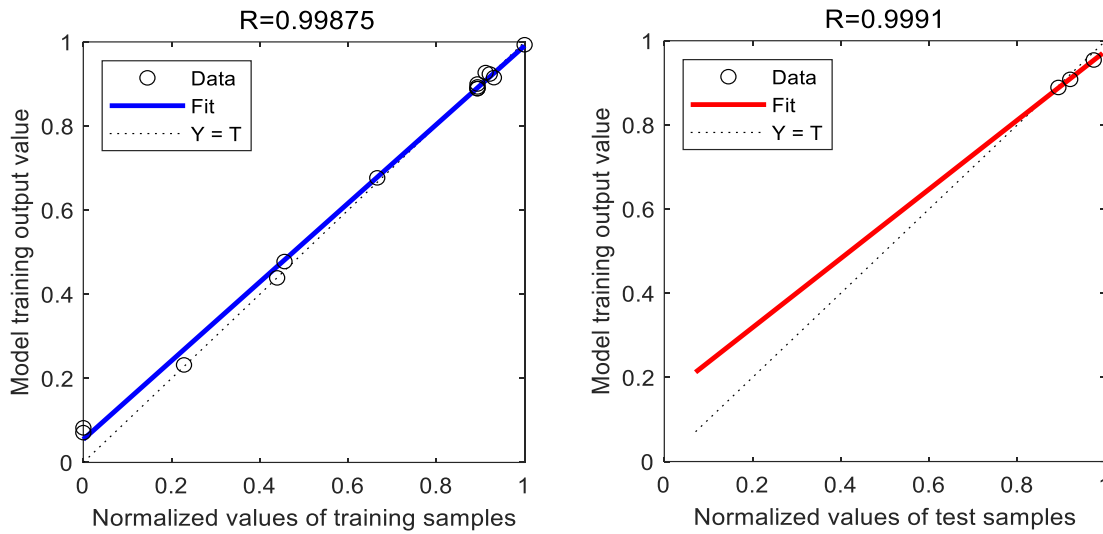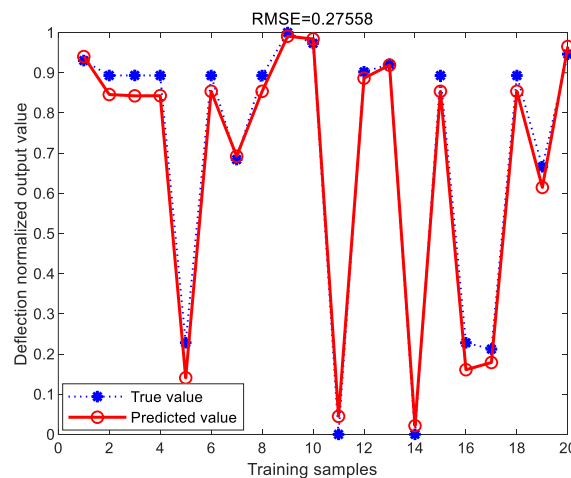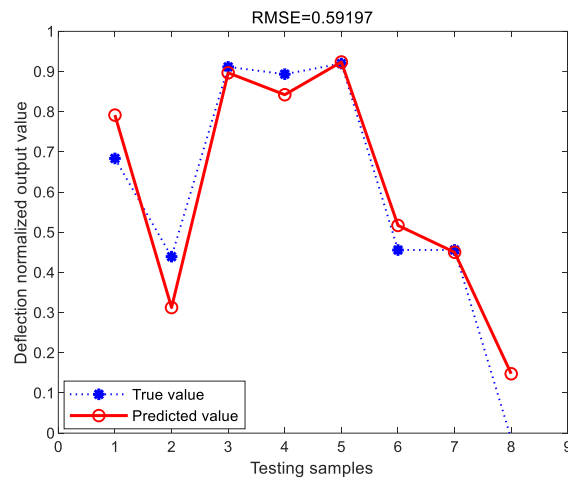
(c) Training samples of RBF network   *(d) Testing samples of RBF network*

Fig. 5 – The prediction and fitting curves of BP and RBF neural network models' performance

To further validate the prediction performance, the BP and RBF neural network models were developed to predict the deflection, and the normalized output values of the deflection on training samples and test samples were obtained, as depicted in Figure 6. For the training samples, the predicted values of the BP and RBF constructed network models are essentially consistent with the actual values, and both neural network models do an excellent job of approximating the samples. Although there is a certain amount of error when comparing the test samples to the predicted samples, the overall prediction effect is good, and the predicted deflection falls within the acceptable error range. As shown in the figure, the BP neural network has a higher prediction accuracy only in the seventh group of test samples, and the prediction result is superior to that of the RBF neural network but inferior to that of the RBF neural network in the other groups of test samples. The root mean square error (RMSE) of the RBF neural network is significantly smaller than that of the BP neural network, indicating that the RBF neural network has a smaller deviation between the predicted value and the actual value.
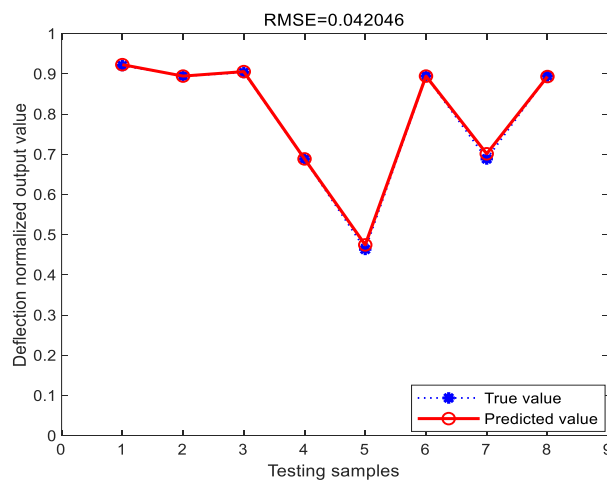

(a) Training samples of BP network

(b) Testing samples of BP network
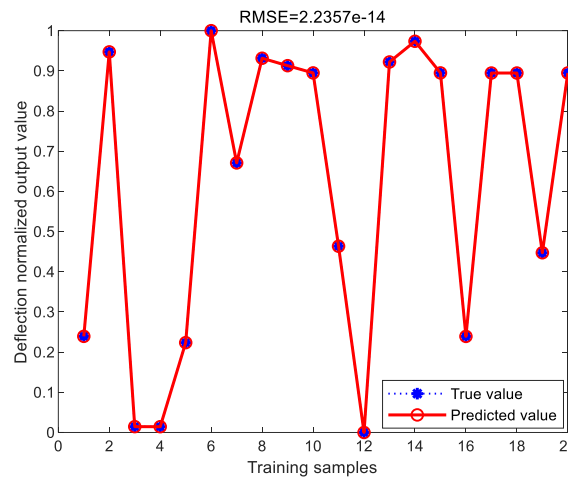
(c) Training samples of RBF network

(d) Testing samples of RBF network

Fig. 6 The deflection prediction curves of the BP and RBF neural networks

By comparing the deflection values of the Midas/Civil finite element model with the measured values on site after the completion of the pouring and post-tensioning of pier segment 12 in pier 18, as shown in Table 7, it can be concluded that the model has good predictive capability.

Tab. 7 - Comparison table of model values and measured values

| Construction phase	Deflection values of the model/m	Measured deflection values/m	Error/m	Relative error/%
Completion of pouring for pier segment 12 of pier 18.	3.464×10^{-2}	3.500×10^{-2}	3.600×10^{-4}	1.03%
Completion of post-tensioning for pier segment 12 of pier 18.	2.551×10^{-2}	2.670×10^{-2}	1.190×10^{-3}	4.45%

The prediction error of the neural network model reveals the model's precision. To more intuitively illustrate the difference between the predicted value and the actual value in the test sample, the original quantity scale of the data is restored using the inverse normalization function, and the prediction error and relative error of the two network prediction models are computed.

$$Error = Ri - Pi \tag{3}$$

$$Relative\ error = (Ri - Pi)/\ Ri \tag{4}$$

Where Ri is the true value; Pi is the predicted value.

According to Figure 7, The prediction error of the BP neural network model varies from 4×10^{-5} m to 4.5×10^{-4} m, with a maximum error of 4.1×10^{-4} m and a maximum relative error of 1.6%; the prediction error of the RBF neural network model extends from 2×10^{-5} m to 2.5×10^{-4} m, with a maximum error of 2.3×10^{-4} m and a maximum relative error of 1%. In the third round of test samples, both BP and RBF neural networks exhibit higher mistakes. For other groups of test data, RBF neural networks have prediction errors ranging between 2×10^{-5} m to 2×10^{-4} m, and their prediction performance is clearly superior to that of BP neural networks. Compared to the BP model, the RBF model provides greater prediction accuracy and greater stability.
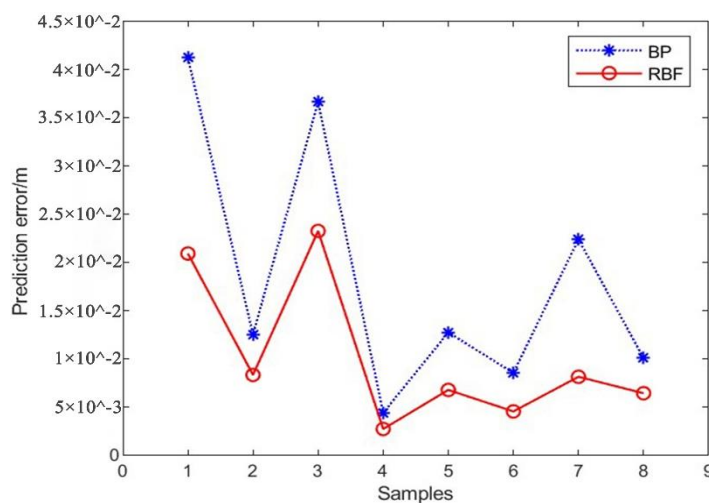
(a) Prediction error
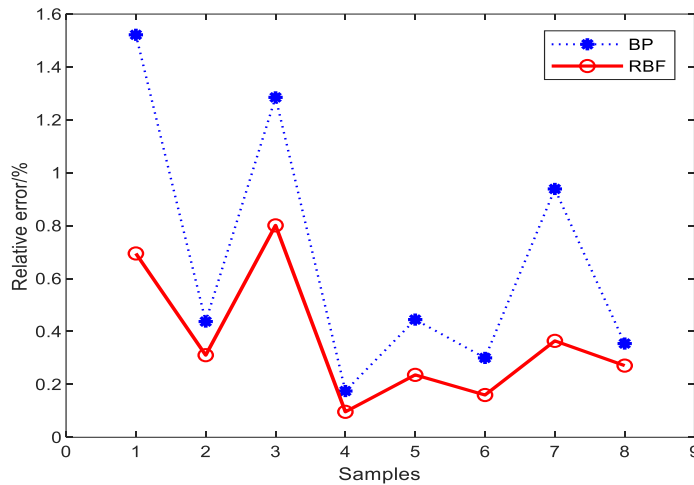
(b) Relative error

Fig. 7 - Error analysis of BP and RBF neural networks

The accuracy of the prediction model is measured using the mean absolute error (MAE) by comparing the predicted values to the actual values. The MAE of the BP model for the training sample is 2.117×10^{-4} m, while the MAE for the test sample is 6.551×10^{-4} m; the MAE of the RBF model for the training sample is 1.6×10^{-17} m, and the MAE for the test sample is 2.55×10^{-5} m; both models demonstrate excellent prediction performance. The average absolute error of the RBF model on training and test samples is less than that of the BP model, and the RBF model has a smaller deviation between training and test samples, indicating that the RBF neural network model has superior generalization ability and prediction effect.

CONCLUSION

This research examines the effect of elastic modulus, volume weight of concrete, material age, and temperature load on the deflection of a rigid frame-continuous beam bridge, using measured values from the building site to fit the deflection curve with the average deflection technique. Four major parameters constitute input variables, while deflection is an output variable. Using MATLAB, the BP and RBF neural network methods are implemented to predict the deflection of the rigid frame-continuous beam bridge, and the following conclusions are drawn.

(1)   Based on the principle of least squares and using the average deflection method, fit the deflection curve function at 1/4L of Pier 18 of the supporting structure from late August 2022 to early January 2023, $f = 0.00929t^3 - 0.1725 \ t^2 + 0.01547 \ t - 1.186$, based on the Least Squares Principle, and its accuracy was confirmed. The Average Deflection Method can be used to fit and predict the average deflection value over a longer time period and the average deflection value over the next longer time period.

(2)   The prediction models established by the RBF neural network and the BP neural network have a high fitting correlation coefficient under the same conditions, and both neural networks can accurately predict the deflection values under various influencing parameters, providing a basis for the selection of influencing parameters.

(3)   Comparing the prediction models of RBF neural network and BP neural network reveals that RBF neural network is more stable; the average absolute error of training samples is 1.6×10^{-17} m, whereas the average absolute error of test samples is 2.55×10^{-5} m; the generalization ability of the model is superior; the training is more stable; and the prediction effect is superior.

(4)   Comparing the prediction models of the RBF neural network and the BP neural network, it was discovered that the prediction error of the RBF neural network model ranged from 2×10^{-5} m to 2.5×10^{-4} m, with a maximum error of 2.3×10^{-4} m and a relative error that did not exceed 1%. Clearly,

the prediction performance was superior to that of the BP neural network. Compared to the BP model, the RBF model has greater prediction accuracy and greater stability.

ACKNOWLEDGEMENTS

REFERENCES

[1] Editorial Department of China Journal of Highway and Transport, 2021. 'Review on China's Bridge Engineering Research:2021', China Journal of Highway and Transport, vol. 34(02):1-97. doi. 10.19721/j.cnki.1001-7372.2021.02.001

[2] Meng Lingxing, 2008. Research on Construction Control of Long-span Prestressed Continuous Rigid Frame Bridge. Master 's degree thesis of Shandong University.

[3] Yuan Zengren, 1999. Artificial Neural Networks and Its Applications, Tsinghua University Press.

[4] Jiang Zongli, 2001. Introduction to Artificial Neural Network, Higher Education Press.

[5] Yan Pingfan, Zhang Changshui, 2005. Artificial Neural Networks and Simulated Evolutionary Computation, Tsinghua University Press.

[6] Hou Yuanbin, Du Jingyi, Wang Mei, 2007. Neural Network, Xi 'an University of Electronic Science and Technology Press.

[7] Chen Ming, 2013. Principles and Examples of MATLAB Neural Networks, Tsinghua University Press.

[8] Liu Xiaoyao, Xu Yue, 2011. Design Manual for Highway Bridges and Culverts: Beam Bridges (2nd Edition), China Communications Press.

[9] Sun Quansheng, Wu Tong, 2010. Application of BP Neural Network in the Cable-replacing Construction Control of Cable-stayed Bridge, China Safety Science Journal, vol. 2010,20(07):21-25. doi. 10.16265/j.cnki.issn1003-3033.2010.07.012

[10] Peng Binbin, Yan Xianguo, Du Juan, 2020. Research on Surface Quality Prediction Based on BP and RBF Neural Network, Surface Technology, vol. 2020,49(10):324-328,337. doi.10.16490/j.cnki.issn.1001-3660.2020.10.038

[11] Wang Ting, 2019. Study on mathematical model and fractal properties of porosity of electrospun nanofiber membrane, Tiangong University.

[12] Kang Le, Liu Yuankun, Wang Liping, Gao Xiaoping, 2021. Preparation of electrospun nanofiber membrane for air filtration and process optimization based on BP neural network, Materials Research Express, vol. 2021,8(11):115010. doi.10.1088/2053-1591/ac37d6

[13] Kang Le, Wang Lizhi, GAO Xiaoping, 2022. Process optimization of polyvinylidene fluoride/polypropylene gradient composite filter material based on BP neural network, Acta Materiae Compositae Sinica, vol. 2022, 39(08):3776-3785. doi.10.13801/j.cnki.fhclxb.20210913.005

[14] Zhou Jinhua, Ren Junxue, Cai Ju, 2018. Prediction of milling residual stress of aviation blade based on RBF neural network, Computer Integrated Manufacturing Systems, vol. 2018, 24(02):361-370. doi. 10.13196/j.cims.2018.02.008

[15] Tao Jili, Yu Zheng, Zhang Ridong, Gao Furong, 2021. RBF neural network modeling approach using PCA based LM–GA optimization for coke furnace system, Applied Soft Computing, 111:1076. doi. 10.1016/j.asoc.2021.107691

[16] Feng Jianhu, Che Gangming, Nie Yufeng, 2006. Numerical Analysis Principles, Science Press.

[17] Hossein Mohammad Khanlou, Ali Sadollah, Bee Chin Ang, et al, 2014. Prediction and optimization of electrospinning parameters for polymethyl methacrylate nanofiber fabrication using response surface methodology and artificial neural networks, Neural Computing and Applications, vol. 2014, 25(03):767-777. doi. 10.1007/s00521-014-1554-8

[18] Komeil Nasouri, Hossein Bahrambeygi, Amir Rabbi, et al, 2012. Modeling and optimization of electrospun PAN nanofiber diameterusing response surface methodology and artificial neural networks, Journal of Applied Polymer Science, vol. 2012, 126(01):127-135. doi. 10.1002/app.36726

[19] Lei Junqing, 2009. Analysis of deflection causes of long-span prestressed concrete continuous rigid frame bridge, Master Degree Thesis of Beijing Jiaotong University.

[20] Zhan Jianhui, Chen Hui, 2005. Cause analysis of main beam deflection and box girder crack of large span continuous rigid frame, Journal of China & Foreign Highway, vol. 2005, 25(01):56-58. doi. 10.14048/j.issn.1671-2579.2005.01.015

[21]   Li Qiao, Bu Yizhi, Zhang Qinghua, 2009. Whole-procedure adaptive construction control system based on geometry control method, CHINA CIVIL ENDINEERING JOURNAL, vol. 2009, 42(07):69-77. doi. 10.15951/j.tmgcxb.2009.07.014

[22]   Xing Yun, Wu Xun, 2007. Study on the Excessive Long-Term Deflection of Large Span Prestressed Concrete Girder Bridges, Structural Engineers. doi. 10.15935/j.cnki.jggcs.2007.05.003

[23]   Li YunXi, Liu Yongjian, 2008. Study on the Influence Factors of Long-term Deflection for Prestressed Concrete Continuous Box-girder Bridge. Modern Transportation Technology, vol. 2008, 05(05).

[24]   Xie Jun, Wang Guoliang, Zheng Xiaohua, 2007. State of Art of Long-term Deflection for Long Span Prestressed Concrete Box-girder Bridge. Journal Highway and Transportation Research and Development, vol. 2007, 24(01):47-50.

[25]   Wang Fei, 2007. Construction monitoring and shrinkage and creep effect analysis of continuous rigid frame bridge, Master Degree Thesis of Beijing Jiaotong University.

[26]   Vitek J.L, 1997. Long-term deflections of large prestressed concrete bridg, Progress Report CEB Bulletin, No235.

[27]   Pan Z, Fu C.C, Lu Z, 2010. Impact of longitudinal tendons on long-term deflections oflong-span concrete cantilever bridges, Bridge Maintenance, Safety, Management and Life-Cycle Optimization-Proceedings of the 5th International Conference on Bridge Maintenance, Safety and Management. Philadelphia, PA, United states. doi. 10.1201/b10430-349

[28]   Piotr Gwoździewicz, Bruno Jurkiewiez, Jean-François Destrebecq, 2000. Long Term Serviceability of Concrete Structures with Regards to Material Behaviors and Cyclic Loading, Proceedings of the 2000 Structures Congress-Advanced Technology in Structural Engineering, Philadelphia Pennsylvania USA:ASCE. doi. 10.1061/40492(2000)159

[29]   Huang Zhongwen, 2011. Research on reducing deflection technology of long-span prestressed concrete beam bridge, Engineering Master's thesis of Chongqing Jiaotong University.

[30]   Cao Qingsong, Zhou Jihui, 2004. Application of MATLAB in Neural Network Design, JOURNAL Of EAST CHINA JIAOTONG UNIVERSITY, vol. 2004, 21(04):86-88.

[31]   Li Qiaoru, Liu Guixin, Chen Liang, et al, 2023. Short-term traffic flow prediction based on adaptive BAS optimized RBF neural network, Journal of Harbin Institute of Technology, vol. 2023, 55(03):93-99. doi. 10.11918 /202108096

PREPARATION OF THE COMPOSITE ASPHALT MATERIAL AND ITS PERFORMANCE IN ROAD REHABILITATION

Tiezeng Zhu and Xudan Li

Highway College, Henan College of Transportation, Zhengzhou, Henan 450000, China; buzhu60957@yeah.net

ABSTRACT

Asphalt materials have a very wide range of applications in roads, but with the increase of traffic pressure and the intensification of cracking and rutting in traditional asphalt pavements, there is an urgent need to further improve the performance of asphalt materials. In this paper, composite asphalt materials containing 10%, 20%, and 30% trinidad lake asphalt (TLA) and 0%, 2%, 3%, and 4% styrene-butadiene rubber (SBR) were prepared. Their basic properties and the properties of the mixes used for road rehabilitation were analyzed. It was found that the addition of TLA and SBR caused a decrease in the penetration degree of the material, but significantly increased the softening point of the material, TLA was detrimental to the ductility of the material, and SBR could improve the ductility. From the analysis of the performance of road rehabilitation mixes, the comprehensive performance of 20% TLA+3% SBR was good, its dynamic stability reached 3,712.66 times/mm, its water stability was also good, and its stiffness modulus was 3,332.64 MPa. The results prove the improvement of TLA and SBR for asphalt performance, and this method can be applied in practical projects.

KEYWORDS

Composite asphalt, Road rehabilitation, Styrene-butadiene rubber, Trinidad lake asphalt

INTRODUCTION

With the development of society, the scale of road networks has been expanded [1]. Asphalt is a very widely used material in road construction [2], with the advantages of friction resistance and levelling [3], but this material is easily softened at high temperature and rutting [4], and easily cracked at low temperature. Under the influence of increasing traffic [5], the phenomenon of cracking and depression of asphalt roads is becoming more and more serious [6], which has a great impact on the quality of roads [7]. In order to improve the performance of pavements using asphalt materials in road rehabilitation, composite asphalt materials obtained by adding modifiers to the base asphalt have received considerable attention from researchers [8]. Sembiring et al. [9] mixed asphalt with silica in a ratio of 1:2 and obtained a composite material after calcination at 200-450 °C. Their study showed that with increasing calcination temperature, the density and strength of the material were improved, and the material could be used as a roofing material. Choudhary et al. [10] added waste glass powder (GP) and glass-hydrated lime (GL) in different proportions to asphalt concrete and found that the GL and GP mixes had better rutting and fatigue resistance, the GP mix had poor adhesion, the GL mix had good moisture resistance, and the use of GL and GP could effectively reduce the material cost. Kashfi et al. [11] studied nanomaterials and styrene-butadiene rubber (SBR). They found that nanomaterials could improve the resistance of the mix, reduce the amount of wear, and improve rutting resistance, loosening, etc. One et al. [12] found that the use of portland composite cement (PCC) and Buton granular asphalt (BGA) could improve the indirect tensile strength of the mix through indoor tests and P1.5B8 and P2B8 had the best performance. This paper studied both trinidad lake asphalt (TLA) and SBR. Composite asphalt materials mixed with different

content of TLA and SBR were designed, and their performance in road rehabilitation was analyzed to find the best preparation of the material to improve the effect of asphalt materials in engineering applications.

MATERIALS AND METHODS

Test materials

The matrix asphalt used in the study was 70# asphalt (Qingzhou Xintong Asphalt Technology Co., Ltd., China), and its basic properties are shown in Table 1.

Tab. 1 - Basic properties of matrix asphalt

Technical specifications	JTGF40-2004 specification requirements	Actual measurement results
Penetration degree (25 °C, 5 s, 100 g)/0.1 mm	60-80	68.41
Penetration index (PI)	-1.5-1.0	-1.46
Softening point/°C	≥ 46	48.12
Rotational viscosity (135 °C)/(mPa·s)	< 3000	421
Density (15 °C)/(g/cm^3)	Actual measurement	1.037
Ductility (10 °C, 5 cm/min)/cm	≥ 15	36.37
Ductility (15 °C, 5 cm/min)/cm	≥ 100	> 100
Penetration ratio/%	≥ 61	63.4

TLA is a natural asphalt with a long history [13], which has excellent resistance to oxidation, acid, and alkali compared with conventional asphalt [14]. The mixture of TLA and asphalt can effectively improve the performance [15]. The TLA used in the study was from Gangfeng Global Group Limited, and its basic properties are shown in Table 2.

Tab. 2 - Basic properties of TLA

Technical specifications	JT/T860.5-2014 specification requirements	Actual measurement results
Penetration degree (25 °C, 5 s, 100 g)/0.1 mm	0-5	2.5
Softening point/°C	≥ 90	97.3
Ash content/%	33-38	36.1
Density (25 °C)/(g/cm^3)	1.3-1.5	1.43
Residual penetration ratio/%	≥ 50	96

The current study shows that TLA has slightly poor performance at low temperatures. In order to improve the performance of composite asphalt materials at low temperatures, SBR is added to it for modification. SBR has excellent anti-aging and anti-friction properties [16], which has good effect on improving the crack resistance at low temperatures. The SBR used in the study was from Jinan Yuanbolai Chemical Technology Co., Ltd. and its basic properties are shown in Table 3.

Tab. 3 - Basic properties of SBR

Technical specifications	Actual measurement results
Ash content/%	≤ 0.5
Organic acid/%	4.50-6.75
Bound styrene/%	22.5-24.5
Raw rubber Menny viscosity ML(1+4)100 °C	44-56
300% tensile stress at a given elongation (MPa) 145 °C, 35 min	20.6 ± 2.5
Tensile strength (145 °C × 35 min), MPa	≥ 24.5

The coarse and fine aggregates used in the study were basalt (Shijiazhuang Deze Mineral Products Co., Ltd., China), and the filler was mineral powder (Foshan Sanshui District Jiachangyuan Building Materials Business Department, China). Their basic properties are shown in Table 4.

Tab. 4 - Basic properties of aggregates and fillers

Technical specifications		JTGE42-2005 specification requirements	Actual measurement results
Coarse aggregate	Crushing value/%	≤ 26	13.3
	Apparent relative density/(g/cm^3)	≥ 2.6	2.73
	Water absorption/%	≤ 2	0.78
	The content of elongated and flaky particles/%	≤ 15	7.68
	< 0.075 mm particle content/%	≤ 1	0.4
	Los Angeles wear value/%	≤ 28	11.7
Fine aggregate	Apparent relative density/(g/cm^3)	≥ 2.5	2.87
	Silt content/%	≤ 3	1.32
	Methylene blue value/(g/kg)	≤ 25	23
Filler	Apparent density/(t/m^3)	≥ 2.5	2.58
	Water content/%	≤ 1	0.42
	Hydrophilic coefficient	< 1	0.65
	Plasticity index	< 4	2.2

Composite asphalt material preparation

Since TLA is easier to melt with the matrix asphalt and SBR is more difficult to melt, the following steps are used to prepare the composite asphalt material.

(1)　The matrix asphalt was preheated to 160 °C in an oven, and the TLA was preheated to 180 °C to make them in a flowing state.
(2)　SBR was added to the matrix asphalt and stirred in a stirrer at a speed of 1,000 r/min for ten minutes.
(3)　The temperature was maintained for ten minutes to allow the SBR to develop and swell.
(4)　After raising the temperature to 155 °C, TLA was added to the mixture and sheared using a high-speed shear apparatus at a speed of 5000 r/min for one hour.
(5)　The temperature was maintained, and the mixture was stirred under 155 °C at a speed of 1000 r/min for ten minutes.
(6)　The preparation was completed.

Referring to the existing research results [17], the mixing proportion of TLA was set as 10%-30%, and the mixing proportion of SBR should not be too high because it is not easy to melt with the matrix asphalt, so the mixing proportion was set as 0%, 2%, 3% and 4%. The preparation scheme of the composite asphalt material is shown in Table 5.

Tab. 5 - Composite asphalt material preparation schemes

Preparation scheme	TLA mixing proportion/%	SBR mixing proportion/%
1	0%	0%
2	10%	0%
3	10%	2%
4	10%	3%
5	10%	4%
6	20%	0%
7	20%	2%
8	20%	3%
9	20%	4%
10	30%	0%
11	30%	2%
12	30%	3%
13	30%	4%

Basic property analysis of composite asphalt materials

According to JTGE20-2011, the following basic properties of composite asphalt materials were analyzed.

(1)   Penetration degree/0.1 mm: it reflects the consistency of the material, measured at 25 °C in this paper.

(2)   Softening point/°C: it reflects the viscosity of the material as well as its high temperature stability.

(3)   Ductility/cm: it reflects the plasticity of the material, measured at 10 °C in this paper.

Composite asphalt mix preparation

According to the existing engineering experience, the test used continuous gradation AC-13, and the best oil to stone ratio was set at 5%. The mixture preparation process is as follows.

The aggregates were well mixed, placed in an oven, and heated for 4-6 hours.

The composite asphalt material was melted and set aside.

The mixing sequence was: aggregate + asphalt → mineral powder, and the mixing was performed in a mixing pot.

Road rehabilitation performance analysis

(1)   High temperature stability

Asphalt pavements are prone to deformation in high temperature environments. High-temperature stability refers to the ability of the mixture to resist plastic deformation under the combined effect of wheel load and temperature. The rutting test [18] was conducted to analyze the high-temperature stability of the composite asphalt mixture in road rehabilitation. The size of the test specimen was 30 × 30 × 5 cm, and the temperature was set as 60 °C. The specific steps are shown below.

① The rutting plate was kept at a constant temperature of 60 °C for five hours.
② The specimen was fixed in the center of the rutting meter, and the device door was closed.
③ The rutting meter was turned on to start the test.

The dynamic stability of the specimen (times/mm) is:

$$DS = \frac{N \times (t_2 - t_1)}{d_2 - d_1} \times C_1 \times C_2,$$ (1)

where:

N: the walking speed of the wheel, 42 times/min,

t_1: 45 min,

t_2: 60 min,

d_1: rutting depth at time t_1,

d_2: rutting depth at time t_2,

C_1: the correction factor for tester type, whose value was 1 when the crank connecting rod drives the loading wheel to do round-trip operations,

C_2: the coefficient of the test specimen, whose value was 1 when the specimen with a width of 30 cm is prepared in the laboratory.

(2)　Water stability

When water enters the mix, it affects the bond between the asphalt and the mineral aggregate, resulting in structural damage to the mix. Water stability refers to the bond between the asphalt and the mineral aggregate. The analysis of water stability consisted of two tests.

The first test was the water immersion Marshall test [19].

① 　Two groups of standard Marshall specimens were prepared. The specimen had a diameter of 101.6 mm ± 0.2 mm and a height of 63.5 mm ± 1.3 mm. There were eight specimens, and they were divided into two groups, four each group.

② 　The first group was placed in a constant temperature water bath at 60 °C for 30-40 min. The upper and lower squeeze heads of the Marshall tester were also put into the bath and dried after being taken out. The specimen was put above the lower squeeze head and covered by the upper squeeze head. The Marshall stability was measured.

③ 　The second group adopted the same method, but the constant temperature water bath was extended to 48 h. Then, the Marshall stability was measured.

④ 　The residual stability was calculated:

$$MS_0 = \frac{MS_2}{MS_1} \times 100\%, \tag{2}$$

where:

MS_1: 30-40 min stability,

MS_2: 48 hours stability.

The second test was the freeze-thaw splitting test [20].

① 　Two groups of Marshall specimens were prepared by 50 times of double-sided compaction.

② 　The first group was placed in a water bath for two hours at 20 °C, and maximum damage load P_{T1} was measured.

③ 　The second group was placed in a water bath for 30 min under vacuum conditions, and after a freeze-thaw cycle, maximum damage load P_{T2} was measured.

④ 　The splitting tensile strength of the two groups of specimens was calculated:

$$R_{T1} = \frac{0.006287P_{T1}}{h_1}, \tag{3}$$

$$R_{T2} = \frac{0.006287P_{T2}}{h_2}, \tag{4}$$

where:

h_1: the height of the specimen in the first group,

h_2: the height of the specimen in the second group.

⑤ 　The residual intensity was calculated:

$$TSR = \frac{R_{T2}}{R_{T1}}. \tag{5}$$

(3)   Low-temperature crack resistance

In low-temperature environments, asphalt pavements tend to harden and crack easily under load. Low temperature crack resistance refers to the crack resistance of the mixture in low temperature environment. The low-temperature crack resistance of composite asphalt mixtures in road rehabilitation was analyzed by means of a small beam bending test [21] using specimens with a size of 250 × 30 × 35 mm, as follows.

① The specimen was placed at a constant temperature of -10 °C for more than three hours.
② The specimen was fixed by a bending fixture.
③ Open the testing machine and keep applying the load until the specimen is destroyed.

The flexural-tensile strength when the specimen is damaged is:

$$R_B = \frac{3 \times L \times P}{2 \times b \times h^2}. \tag{6}$$

The maximum flexural-tensile strain is:

$$\varepsilon_B = \frac{6 \times h \times d}{L^2}. \tag{7}$$

The flexural-tensile stiffness modulus is:

$$S_B = \frac{R_B}{\varepsilon_B}. \tag{8}$$

In the above equations, L is the span of the specimen, P is the maximum load when the specimen is damaged, b is the width of the midspan cross-sectional specimen, h is the height of the midspan cross-sectional specimen, and d is the midspan deflection of the specimen at the time of damage.

ANALYSIS OF RESULTS

The penetration degree (25°C) of the composite asphalt materials prepared by different schemes is shown in Figure 1.
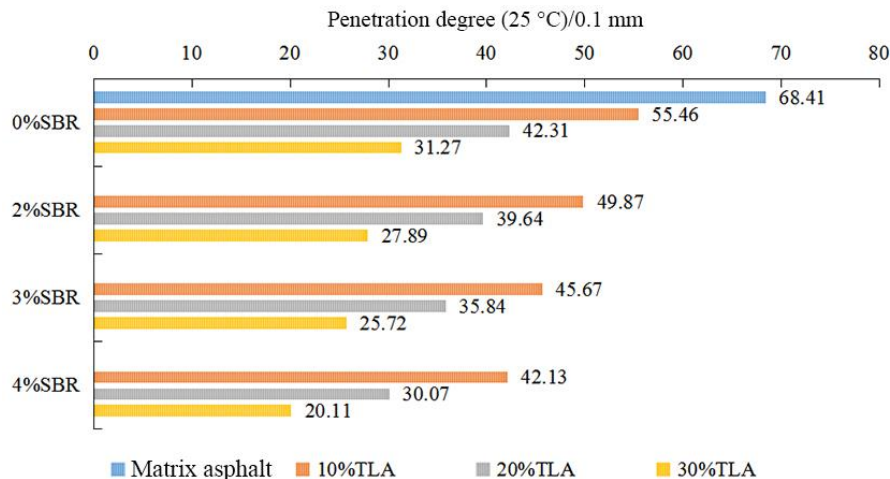

Fig. 1 – Penetration degree analysis

From Figure 1, the degree of penetration of the matrix asphalt was 68.41/0.1 mm at 25 °C. Without the addition of SBR (0% SBR), the penetration degree decreased continuously with the increase of TLA mixing proportion, and the penetration degree of 10% TLA, 20% TLA, and 30% TLA decreased by 12.95/0.1 mm, 26.1/0.1 mm, and 37.14/0.1 mm, respectively, compared to the matrix asphalt.

When the mixing proportion of TLA was fixed, the addition of SBR also decreased the penetration degree, but the decrease was small. For example, in the case of 10% TLA, the penetration degree was 49.87/0.1 mm after the addition of 2% SBR, which was 5.59/0.1 mm lower

than that of 0% SBR; after the addition of 3% SBR, the penetration degree was 9.79/0.1 mm lower than that of 0% SBR; after the addition of 4%, the penetration degree was 13.36/0.1 mm lower than that of 0% SBR. The comparison between TLA and SBR showed that the effect of TLA on the penetration degree of the material was greater.

A comparison of the softening points of the composite asphalt materials prepared by different schemes is shown in Figure 2.
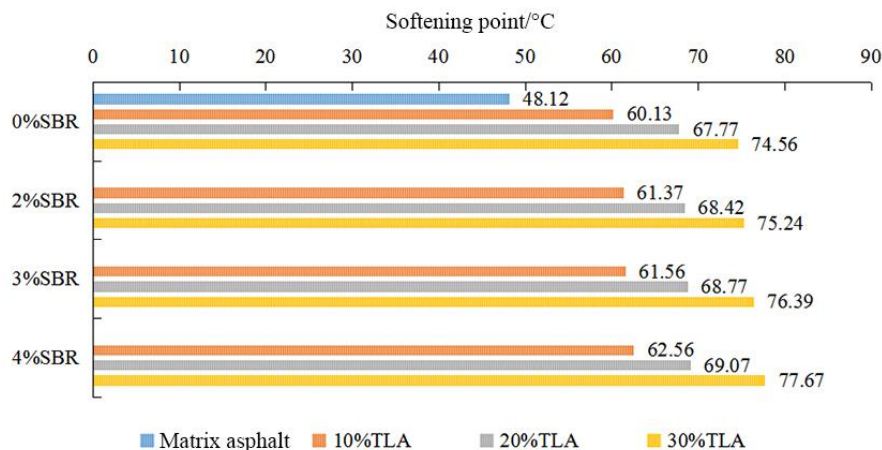

Fig. 2 – Softening point analysis

From Figure 2, the softening point of the matrix asphalt was the lowest, 48.12 °C, indicating that the quality of the matrix asphalt was easily affected under high temperature conditions. After the addition of TLA and SBR, the softening point of the material showed a significant increase. First, in the absence of SBR addition (0% SBR), the softening point of the material added with 10% TLA was 60.13 °C, which was 12.01 °C higher than the matrix asphalt, and the softening points of the materials added with 20% TLA and 30% TLA were 19.65 °C and 26.44 °C higher than the matrix asphalt, respectively, proving the effectiveness of TLA in improving the high temperature performance of the material.

When the mixing proportion of TLA was fixed, the addition of SBR further improved the softening point of the material. For example, when the mixing proportion of TLA was fixed at 10%, the addition of 2%, 3%, and 4% SBR resulted in an increase in softening point of 1.24 °C, 1.43 °C, and 2.43 °C, respectively, compared to 0% SBR, demonstrating the improved high temperature stability of the material with the combined effect of TLA and SBR.

The ductility (10 °C) of the composite asphalt material prepared by different schemes is shown in Figure 3.
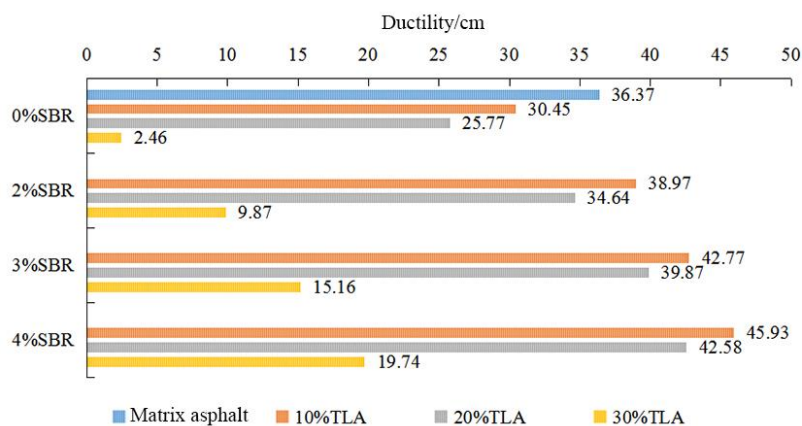

Fig. 3 – Ductility analysis

From Figure 3, the ductility of the matrix asphalt was 36.37 cm, and there was a significant decrease in the ductility of the material from 10% TLA, 20% TLA to 30% TLA. Without the addition of SBR (0% SBR), the ductility of the material added with 10% TLA, 20% TLA, and 30% TLA were 30.45 cm, 25.77 cm, and 2.46 cm, respectively, which was 16.28%, 29.14%, and 93.24% lower than that of the matrix asphalt, indicating that the addition of TLA resulted in a decrease in the ductility of the material under low temperature conditions, i.e., the material was more easily broken, which was detrimental to its use in road rehabilitation.

When the mixing proportion of TLA was fixed, SBR had an improving effect on the material ductility. Taking 10% TLA as an example, the ductility of the material increased by 27.98%, 40.46%, and 50.84% after adding 2% SBR, 3% SBR, and 4% SBR. Therefore, in actual use, if the content of TLA was high, the content of SBR should also be high to improve the ductility of the material.

Based on the above analysis of the performance of composite asphalt materials prepared by different schemes, only the following schemes were compared in the mix performance analysis.

①   10% TLA+2% SBR

②   10% TLA+3% SBR

③   20% TLA+2% SBR

④   20% TLA+3% SBR

The analysis of the dynamic stability of the different mixes when applied to road rehabilitation is shown in Figure 4.
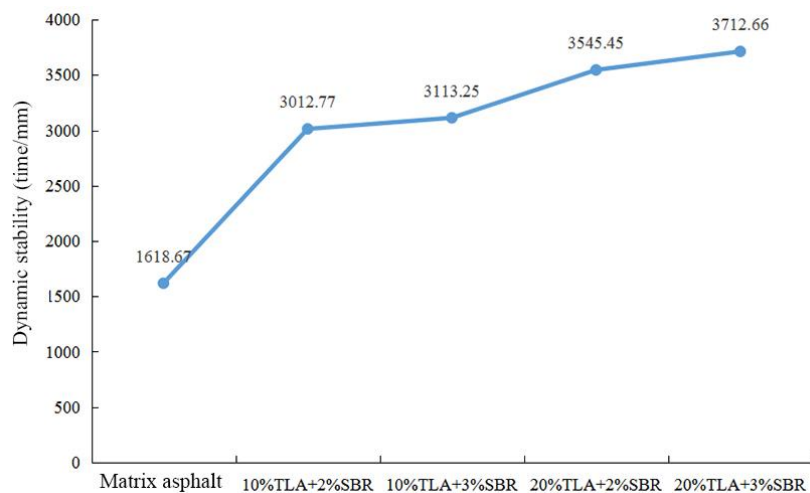

Fig. 4 – Dynamic stability analysis

From Figure 4, the dynamic stability of the matrix asphalt was the worst, 1,611.25 times/mm, while the dynamic stability of the mixes was sufficiently improved after the addition of TLA and SBR. Compared to the matrix asphalt, the dynamic stability of the 10% TLA+2% SBR mix was improved by 86.13%, and the 10% TLA+2% SBR mix was improved by 92.33%. The comparison between 10%TLA+2%SBR and 10%TLA+2%SBR showed that the amplitude of increase in dynamic stability was small. The dynamic stability was further improved in the material added with 20%TLA+2%SBR, which was doubled compared to the matrix asphalt. Similarly, the increase amplitude of the dynamic stability of 20%TLA+3%SBR was also not large. The results showed that the addition of TLA could significantly improve the dynamic stability of the mix and the effect of SBR was relatively small.

When applied to road rehabilitation, the water stability analysis of different mixes is shown in Figure 5.
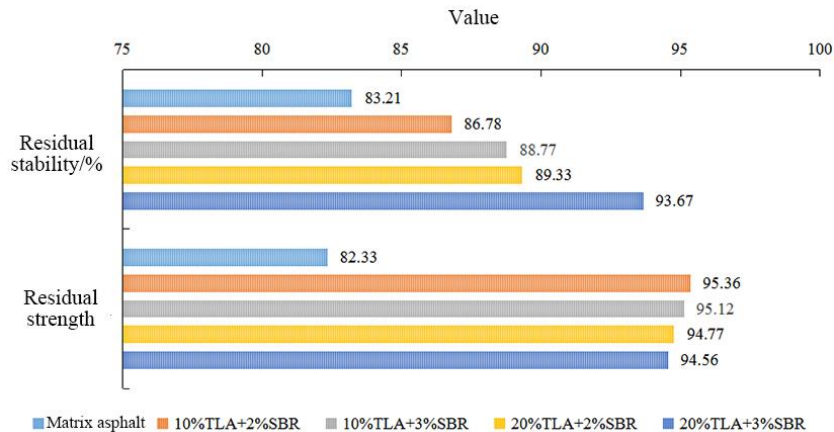
Fig. 5 – Water stability analysis

According to Figure 5, first, in terms of residual stability, the matrix asphalt was the lowest, 83.21%, and the addition of both TLA and SBR improved the residual stability of the mixes. Compared to the matrix asphalt, the four mixes improved by 3.57%, 5.56%, 6.12%, and 10.46%, respectively. In the mixes after the addition of TLA and SBR, the adhesion between asphalt and aggregate was improved, which strengthened the water stability of the mixes.

Then, in terms of residual strength, the value of the matrix asphalt was 82.33, and after the addition of TLA and SBR, the residual strength of the mixes all reached above 90. In comparison, the residual strength of 10% TLA + 2% SBR had the highest value, 95.36, while the residual strength of the remaining three mixes decreased slightly, but were still significantly better than the matrix asphalt, indicating that the composite asphalt material could effectively improve the splitting strength of the mixes in road rehabilitation.

Finally, a comparison of the low-temperature crack resistance of different mixes when applied to road rehabilitation is shown in Figure 6.
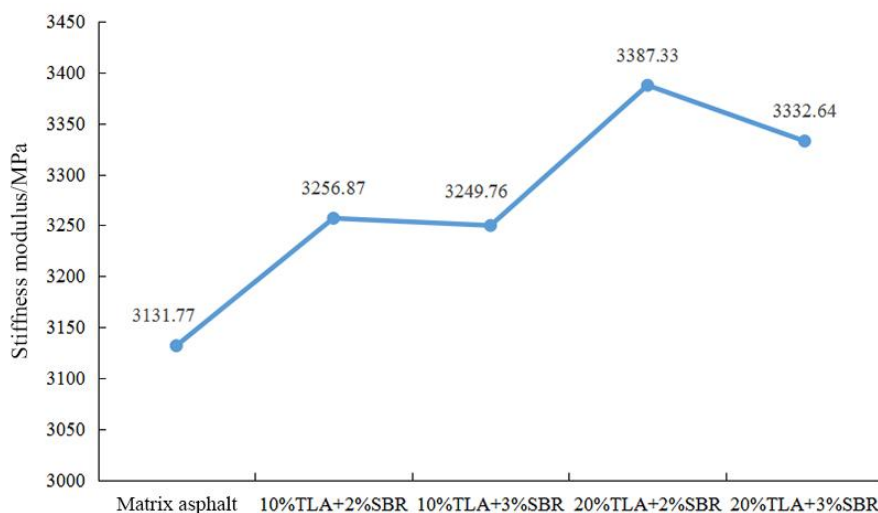

Fig. 6 – Low-temperature crack resistance analysis

From Figure 6, the stiffness modulus of the matrix asphalt was 3,131.77 MPa, and the stiffness modulus of the mix was greatly increased after the addition of TLA and SBR. In comparison, the stiffness modulus of the mix containing 20% TLA was higher than that of the mix containing 10% TLA, while the stiffness modulus of the mix containing 3% SBR was slightly lower than that of the mix containing 2% SBR. Under low-temperature conditions, the addition of TLA made the mix stiffer and brittle, while the addition of SBR improved the deformation capacity of the mix to some extent, which is consistent with the performance analysis of composite asphalt materials.

The comprehensive results showed that the asphalt prepared with 20% TLA and 3% SBR had good performance in all properties, so the mix prepared by this scheme can be used in the actual road rehabilitation.

CONCLUSION

In this paper, TLA and SBR were used to optimize the performance of asphalt materials. The composite asphalt materials were prepared by different schemes, and their basic properties and performance in road rehabilitation were analyzed. The results showed that increasing the mixing proportion of TLA and SBR could reduce the penetration degree, and the effect of TLA on the penetration degree was greater. After the addition of TLA and SBR, the softening point and ductility of the materials were improved. From the perspective of the performance in road rehabilitation, the dynamic stability of 20% TLA+3% SBR was 3,712.66 times/mm, the residual stability was 93.67%, the residual strength reached 95.56, and the stiffness modulus was 3,332.64 MPa, all of which were significantly improved compared with the matrix asphalt, so it can be applied in practical engineering.

REFERENCES

[1]   He W., Song H., Yao Y., Jia X., 2021. A Multiscale Method for Road Network Extraction from High-Resolution SAR Images Based on Directional Decomposition and Regional Quality Evaluation. Remote Sensing, vol. 13: 1-20.

[2]   Chang X., Xiao Y., Long Y., Wang F., You Z., 2022. Temperature dependency of VOCs release characteristics of asphalt materials under varying test conditions. Journal of Traffic and Transportation Engineering (English Edition), vol. 9: 280-292.

[3]   Jadidi K., Esmaeili M., Kalantari M., Khalili M., Karakouzian M., 2021. A Review of Different Aspects of Applying Asphalt and Bituminous Mixes under a Railway Track. Materials, vol. 14: 1-22.

[4]   Allateef E.A., Abedali A.H., 2021. Improvement the Shear strength of Asphalt Mixture by using crumb tire Rubber. Journal of Physics: Conference Series, vol. 1973: 1-12.

[5]   Ene N.M., Rcnel C., 2021. The influence of characteristics of aggregates on performance of asphalt mixtures. IOP Conference Series: Earth and Environmental Science, vol. 664: 1-9.

[6]   Yang K., Li R., Castorena C., Underwood B.S., 2022. Correlation of asphalt binder linear viscoelasticity (LVE) parameters and the ranking consistency related to fatigue cracking resistance. Construction and Building Materials, vol. 322: 1-13.

[7]   Kamenchukov A., Yarmolinsky V., Pugachev I., 2018. Evaluation of road repair efficiency in terms of ensuring traffic quality and safety. Transportation Research Procedia, vol. 36: 627-633.

[8]   Andronov S.Y., 2018. Influence of Method for Basalt Fibers Introduction on Physical-Mechanical Indicators of Composite Asphalt Concrete Mixes. Stroitel'nye Materialy, vol. 750: 71-73.

[9]   Sembiring S., Riyanto A., Junaidi I.F., Situmeang R., 2021. Effect of calcination temperature on silica-asphalt composite properties using amorphous rice husk silica. Journal of Physics: Conference Series, vol. 1751: 1-13.

[10]   Choudhary J., Kumar B., Gupta A., 2021. Utilization of Waste Glass Powder and Glass Composite Fillers in Asphalt Pavements. Advances in Civil Engineering, vol. 2021: 1-17.

[11]   Kashfi S.S., Tanzadeh J., Gilani F.R., 2021. Laboratory Investigation of the Composite of Slurry Seal Asphalt Reinforced by Hybrid Nanomaterials and Fiber. Journal of Testing and Evaluation: A Multidisciplinary Forum for Applied Sciences and Engineering, vol. 49: 1-17.

[12]   One L., Tjaronge M.W., Irmawaty R., Hustim M., 2020. Effect of portland composite cement and buton granular asphalt on indirect tensile strength of emulsified asphalt cold mix using limestone aggregate. IOP Conference Series: Earth and Environmental Science, vol. 419: 1-7.

[13]   Mohammed S., Maharaj R., Ali R., White D., 2020. Reusing Clay Based Spent Filter Media to Modify Trinidad Asphaltic Materials. Clay Research, vol. 39: 23-30.

[14]   Yilmaz M., Qeloglu M.E., 2013. Effects of SBS and different natural asphalts on the properties of bituminous binders and mixtures. Construction & Building Materials, vol. 44: 533-540.

[15]   He R., Zheng S., Chen H., Kuang D., 2019. Investigation of the physical and rheological properties of Trinidad lake asphalt modified bitumen. Construction and Building Materials, vol. 203: 734-739.

[16]   Refay H., Sanad M.H., Eyssa H.M., 2022. Enhancement of the thermal and physicochemical properties of styrene butadiene rubber composite foam using nanoparticle fillers and electron beam radiation. Radiochimica Acta, vol. 110: 205-218.

[17]   Feng X.J., Hao P.W., Zha X.D., 2007. Research on Proportioning Design of TLA Modified Asphalt Mixture. Highway, vol. 194-196: 170-176.

[18]   Jeong J., Underwood B.S., Kim Y.R., 2021. Rutting performance prediction using index-volumetrics relationships with stress sweep rutting test and Hamburg wheel-track test. Construction and Building Materials, vol. 295: 1-11.

[19]   Usman K.R., Hainin M.R., Satar M., Warid M.N.M., Abdulrahman S., 2020. Modified Marshall Test assessment for emulsified asphalt cold mixes. IOP Conference Series: Earth and Environmental Science, vol. 498: 1-8.

[20]   Zhang K., Li W., Han F., 2019. Performance deterioration mechanism and improvement techniques of asphalt mixture in salty and humid environment. Construction & Building Materials, vol. 208: 749-757.

[21]   Zhang H., Sun J., Gong M., 2022. Study on anti-aged durability of HMA based on inherent and improved performance. Multidiscipline Modeling in Materials and Structures, vol. 18: 54-69.